

# Nanostructured Materials for Energy Storage and Conversion

by

Xiulei Ji

A thesis  
presented to the University of Waterloo  
in fulfillment of the  
thesis requirement for the degree of  
Doctor of Philosophy  
in  
Chemistry

Waterloo, Ontario, Canada, 2009

© Xiulei Ji 2009

## **AUTHOR'S DECLARATION**

I hereby declare that I am the sole author of this thesis. This is a true copy of the thesis, including any required final revisions, as accepted by my examiners.

I understand that my thesis may be made electronically available to the public.

---

Xiulei Ji

## **Abstract**

Efficient, cost effective, and environmentally friendly energy storage and conversion systems are highly desirable to meet ever increasing demands. Nanostructured materials have attracted great interest due to their many superior characteristics in these energy applications. These materials, typically nanoporous or nanostructured, exhibit faster charge transports, better contact, and sometimes new electrochemical reactivity, which leads to their high energy density, high power and/or great catalytic performances. A series of functional nanostructured materials have been fabricated with new synthetic schemes. Nanoporous materials technology and solid state electrochemistry have been attempted to be integrated in this study.

New functional nanoporous materials have been sought for electrochemical purposes. By employing a simple dilution strategy, homogeneously sized, ordered mesoporous silica nanorods (SBA-15), spanning about 10 porous channels in width and ranging from 300 to 600 nm in length were prepared. By employing SBA-15 nanorods as a template, ordered mesoporous carbon (OMC) CMK-3 nanorods were prepared. These porous nanorods exhibit enhanced mass transfer kinetics in their applications owing to their short dimensions. To improve the electronic conductivity of OMC and exploit otherwise wasted copolymer surfactant cross-linked in the channels of as-synthesized SBA-15, direct graphitic mesoporous carbon (termed as DGMC) were synthesized from the copolymer surfactant by employing transition metals (Fe, Co, Ni) as a catalyst. DGMC exhibit three orders higher conductivity and better thermal stability than non-graphitic OMC materials.

A series of nanostructured composites were fabricated by employing OMC as structure backbones and/or electronic conduits. DGMC/MoO<sub>2</sub> as a Li ion battery anode exhibits a reversible capacity more than twice the value that a graphite anode can provide. Due to the confined and nanosized dimensions of the MoO<sub>2</sub>, the composite exhibits a cycle life with no capacity fading. Polymer modified OMC/sulfur interwoven nanostructures were prepared and applied as a cathode in Li-S batteries. The nanostructure displays all of the benefits of confinement effects at a small length scale. The nanostructure provides not only high electronic conductivity but also great access to Li<sup>+</sup> ingress/egress for reactivity with the sulfur. The tortuous pathways within the framework and the surface polymer strongly retard the diffusion of polysulfide anions out from the channels into the electrolyte and minimize the loss of active mass in the cathode, resulting in a stabilized cycle life at reasonable rates. The Li-S batteries can supply up to near 80% of the theoretical capacity of sulfur (1320 mA·h/g). This represents more than five times the specific capacity of conventional intercalation Li ion batteries. The assembly process for OMC/S is simple and broadly applicable, conceptually providing new opportunities for materials scientists for tailored design that can be extended to many different electrode materials.

Size-controlled supported metal and intermetallic nanocrystallites are of substantial interest because of their wide range of electrocatalytic properties. These intermetallics are normally synthesized by high temperature techniques; however, rigorous size control at high temperature is very challenging. A simple and robust chemically controlled process was developed for synthesizing size controlled noble metal, or bimetallic nanocrystallites,

embedded within the porous structure of OMC. The method is applicable to a wide range of catalysts, namely bimetallic PtBi but also including Pt, Ru, Rh and Pd. By using surface-modified OMC, nanocrystallites are formed with monodisperse sizes as low as 1.5 nm, that can be tuned up to 2 and 3.5 nm (equivalent to the channel size of OMC) by thermal treatment. The method is also tailored for the deposition of catalysts on conventional fuel-cell carbon supports. OMC-PtBi nanohybrids were investigated as catalysts for formic acid oxidation for the first time. OMC-PtBi catalysts show an absence of CO poisoning. The excellent catalytic properties can be attributed to the successful catalyst preparation and the faithful practice of the “ensemble effect” at the nanoscale level.

A new agitation-friction methodology was developed to prepare the nano-OMC/S composite. The method is completely different from any conventional impregnation which requires the voluntary molecular mobility of guest phases. The method relies on frictional forces, and the hydrophobic attraction of the mixing components. This is the first example of a nanoporous solid which can be infiltrated by another solid phase at room temperature. The C/S nanocomposite exhibits not only better Pt ion sorption kinetics than its bulk counterpart, but also a higher pseudo-second-order rate constant than chitosan sorbents.

## **Acknowledgements**

I would like to express my most sincere gratitude to my supervisor Professor Linda F. Nazar. She has been a mentor to me. Her dedication to science greatly influences me. From her, I began to learn the scientific logic and scientific communication skills. With her guidance, support and encouragement, I have been enjoying my research originated from my interest and curiosity.

I would like to thank my committee members, Professor Holger Kleinke, Professor Sonny C. Lee, and Professor Marcel Schlaf for their kindness and advice during my study. I would also thank Professor Jeffery Dahn from Dalhousie University and Professor Zhongwei Chen from the Chemical Engineering department for their time being the external committee members.

I would like to extend my sincere thank you to Dr. Herle Subramanya, Dr. Kyu Tae Lee, Dr. Young-Ho Rho, Dr. Shih-Chieh Yi, Dr. Denise Corsil-Gosselink, Brian Ellis, Donglin Han, Mike Makahnouk, and many other lab members for all of their help and collaboration.

I am greatly thankful to all of our collaborators. I would like to thank Dr. JiuJun Zhang and Dr. Lei Zhang in National Research Council for their help in the electrochemical studies of the fuel cell catalysts. Dr. Neil Combs in University of Toronto and Dr. Gianluigi Botton in McMaster University, thank you for your wonderful TEM imaging work.

I would like to thank my beautiful wife Wei. Honey, without you, I could not have achieved so much. You are amazing! Thank you so much!

## Table of Contents

List of Figures .....	xv
List of Tables .....	xxiii
Glossary .....	xxiv
Chapter 1 Introduction .....	1
1.1 Brief overview of energy problems.....	1
1.2 Rechargeable batteries.....	3
1.2.1 Basic concepts .....	3
1.2.2 History of rechargeable batteries.....	4
1.2.3 How to evaluate a Li (ion) battery electrode .....	6
1.2.4 Cathodes in Li (ion) batteries .....	7
1.2.4.1 Insertion cathodes .....	7
1.2.4.1.1 Layered structures .....	7
1.2.4.1.1.1 Lithium cobalt oxide, LiCoO <sub>2</sub> .....	8
1.2.4.1.1.2 Lithium nickel oxide, LiNiO <sub>2</sub> .....	9
1.2.4.1.2 Spinel structure.....	9
1.2.4.1.3 Olivine structure.....	10
1.2.4.2 Integration reaction cathodes.....	11
1.2.4.2.1 Sulfur electrode .....	11
1.2.4.2.2 Oxygen electrode.....	14
1.2.5 Anodes in Li (ion) batteries .....	14
1.2.5.1 Li metal .....	14
1.2.5.2 Carbonaceous materials .....	15
1.2.5.3 Alloy anode.....	16
1.2.5.4 Nanomaterials .....	16
1.2.6 Electrolyte.....	17
1.3 Fuel cells .....	17
1.3.1 Basic concepts .....	17

1.3.2 Classification of fuel cells .....	18
1.3.3 Polymer electrolyte membrane fuel cells (PEMFC).....	19
1.3.3.1 Membrane electrode assembly.....	19
1.3.3.2 Electrocatalysts in direct formic acid fuel cells (DFAFC).....	20
1.3.4 Electrocatalyst preparation techniques .....	22
1.3.4.1 Impregnation method .....	22
1.3.4.2 Colloidal method.....	23
1.3.4.3 Microemulsion method .....	23
1.3.5 Comparison between batteries and fuel cells .....	23
1.4 Mesoporous materials .....	24
1.4.1 Mesoporous silica.....	25
1.4.1.1 M41S.....	25
1.4.1.2 SBA-15 .....	26
1.4.1.2.1 Mechanism of SBA-15 formation.....	27
1.4.1.2.2 Mesopore-micropore network .....	27
1.4.1.2.3 Morphology control of SBA-15 .....	28
1.4.1.3 KIT-6 – “cubic SAB-15” .....	29
1.4.2 Non-siliceous mesoporous materials .....	30
1.4.2.1 Synthesis strategies .....	30
1.4.2.1.1 Soft template method .....	30
1.4.2.1.2 Hard template (nanocasting) method .....	32
1.4.2.2 Ordered mesoporous carbons (OMC).....	34
1.4.2.2.1 CMK family .....	34
1.4.2.2.2 Regarding precursors.....	35
1.4.2.2.3 Graphitic mesoporous carbons.....	35
1.4.2.3 Applications of mesoporous materials in energy storage/conversion systems	36
1.4.2.3.1 In Li (ion) batteries.....	36
1.4.2.3.2 As catalyst supports in fuel cells.....	37

1.5 Thesis scope .....	37
Chapter 2 Characterization Techniques .....	39
2.1 Powder X-ray diffraction (PXRD) .....	39
2.2 Scanning electron microscopy (SEM) and energy dispersive X-ray analysis (EDX)...	41
2.3 Transmission electron microscopy (TEM).....	42
2.4 Thermal analysis .....	44
2.5 Surface area and pore size distribution measurement .....	44
2.6 Raman measurements.....	45
2.7 X-ray photoelectron spectroscopy.....	46
2.8 Electrochemical techniques.....	47
2.8.1 Galvanostatic cycling technique.....	47
2.8.2 Potentiostatic technique (Cyclic Voltammetry) .....	48
2.9 Electrochemical test set up for batteries.....	48
2.10 Electrochemical test set up for PEM fuel cell catalysts .....	49
Chapter 3 Nanorods of SBA-15 and CMK-3.....	51
3.1 SBA-15 nanorods .....	51
3.1.1 Introduction .....	51
3.1.2 Experimental.....	52
3.1.3 Results and discussion.....	53
3.1.3.1 Microscopy studies .....	53
3.1.3.2 Low angle XRD and surface area measurements .....	55
3.1.3.3 Formation mechanisms .....	57
3.1.3.4 Influence of P123/ TEOS ratio on morphology .....	59
3.2 CMK-3 nanorods.....	60
3.2.1 Experimental.....	60
3.2.2 Results and discussion.....	61

3.3 Conclusions .....	63
Chapter 4 Carbon/MoO <sub>2</sub> Composite Based on Graphitic Mesoporous Carbon Prepared from In Situ Carbonization of Tri-Block Copolymers .....	65
4.1 Introduction .....	65
4.2 Experimental .....	68
4.2.1 Synthesis of SBA-15, DGMC and DMC.....	68
4.2.2 Synthesis of composite DGMC/MoO <sub>2</sub> .....	69
4.2.3 Electrochemistry and conductivity measurements .....	69
4.3 Results and discussion.....	70
4.3.1 DGMC .....	70
4.3.1.1 About the synthetic strategy.....	70
4.3.1.2 Characterizations of DGMC .....	71
4.3.1.2.1 Ordered structure.....	71
4.3.1.2.2 Graphitic structure.....	78
4.3.1.3 About preparation temperature .....	81
4.3.2 DGMC/MoO <sub>2</sub> composite as an electrode in a Lithium ion battery .....	84
4.3.2.1 Composite structure with MoO <sub>2</sub> .....	84
4.3.2.2 Galvanostatic cycling of DGMC/MoO <sub>2</sub> .....	86
4.4 Conclusions .....	92
Chapter 5 A Highly Ordered Nanostructured Carbon-Sulfur Cathode for Li-S Batteries.....	93
5.1 Introduction .....	93
5.2 Experimental .....	94
5.2.1 Preparation of ordered mesoporous carbons (OMC).....	94
5.2.1.1 Preparation of CMK-3 .....	94
5.2.1.2 Preparation of CMK-8 .....	95

5.2.1.3 Preparation of graphitized CMK-3 (GCMK-3) by chemical vapor deposition (CVD) method .....	95
5.2.2 Preparation of OMC/S composites .....	96
5.2.3 Preparation of PEG coated CMK-3/S.....	97
5.2.4 Electrochemistry .....	97
5.3 Results and discussion.....	98
5.3.1 Physical characterizations of OMC materials .....	98
5.3.2 OMC/S composites.....	101
5.3.2.1 Physical characterizations of CMK-3/S composite .....	101
5.3.2.2 Electrochemical studies of CMK-3/S .....	108
5.3.2.2.1 Electrochemical reduction mechanism of sulfur electrode .....	108
5.3.2.2.2 Impact of encapsulation degree.....	109
5.3.2.2.3 Rate capability of CMK-3/S-155 cell.....	111
5.3.2.2.4 Cycling life of Li-S cells .....	113
5.3.2.3 Electrochemical studies of C/S composites based on other OMC's.....	116
5.3.3 Polymer coating strategy for stabilizing capacity of Li-S cells.....	119
5.3.3.1 Brief introduction.....	119
5.3.3.2 Physical characterizations of PEG coated composites.....	120
5.3.3.3 Electrochemical studies of CMK-3/S-PEG600 .....	123
5.3.3.4 Electrochemical studies of CMK-3/S-PEG4600 and CMK-3/S-PEG200.....	124
5.3.3.5 Passivating mechanism of PEG on CMK-3/S .....	127
5.3.3.6 Optimization of capacity in the PEG-modified material .....	129
5.3.3.7 Analysis of sulfur retention on cycling.....	130
5.3.3.8 Investigation of self-discharge.....	132
5.3.3.9 Summary of the polymer coating strategy .....	133
5.4 Conclusions .....	133

Chapter 6 Nucleated Growth of Nanocrystalline Metal and Intermetallics in Ordered Mesoporous Carbon: Direct Formic Acid Fuel Cell Anodes.....	135
6.1 Introduction .....	135
6.2 Experimental .....	136
6.2.1 Preparation of carbon-S and carbon-metal composites .....	136
6.2.2 Electrochemical measurement.....	137
6.3 Results and discussion.....	138
6.3.1 Structure studies of OMC-S .....	138
6.3.2 Sulfur as a metal trap.....	141
6.3.3 Physical characterizations of OMC-Pt catalysts.....	146
6.3.4 Incorporation of Pd, Ru, Rh into OMC-S.....	148
6.3.5 Incorporation of Ni, Co, and Cu into OMC-S .....	151
6.3.6 Sulfur functionalized disordered carbons .....	153
6.3.7 Physical characterizations of intermetallic PtBi nanoparticles supported on OMC .....	157
6.3.8 Electrochemical studies of catalyzed formic acid oxidation reactions.....	163
6.4 Conclusion.....	167
 Chapter 7 Agitation Induced Loading of Sulfur into Carbon CMK-3 Nanotubes: Scavenging of Pt Ions from Aqueous Solution .....	169
7.1 Introduction .....	169
7.2 Experimental .....	170
7.3 Results and discussio.....	171
7.3.1 Characterizations of sulfur filtration.....	171
7.3.2 Infiltration mechanisms .....	174
7.3.3 Nano-CMK-3/S's uptake of aqueous Pt ions .....	177
7.4 Conclusions .....	182

References.....	183
References for Chapter 1.....	183
References for Chapter 2.....	192
References for Chapter 3.....	193
References for Chapter 4.....	194
References for Chapter 5.....	196
References for Chapter 6.....	198
References for Chapter 7.....	200

## List of Figures

Figure 1.1 Schematic of an electrochemical cell [3].....	4
Figure 1.2 Schematic diagram of charge and discharge in a lithium ion battery with Li insertion compound used as both electrodes. ....	8
Figure 1.3 Schematic of a H <sub>2</sub> polymer electrolyte membrane fuel cell.....	17
Figure 1.4 Dual-path reaction mechanism of formic acid oxidation on Pt.....	20
Figure 1.5 Illustration of catalytic reactions of formic acid oxidation on Pt intermetallic compound and pure Pt. ....	21
Figure 1.6 Schematic diagram for formation of mesoporous silicate.....	25
Figure 1.7 Self-assembly of copolymer into supramolecular hexagonal architecture [99]. ...	28
Figure 1.8 Morphologies of SBA-15: a) fiber-like; b) short-rod-like.....	29
Figure 1.9 An example of the nanocasting route, in which SBA-15 is employed as a hard template. ....	32
Figure 1.10 Schematic model for the structure of CMK-5. ....	35
Figure 2.1 X-ray diffracted from the lattice.....	40
Figure 2.2 Simplified diagram for the concept given below. ....	45
Figure 2.3 A coin cell assembly of rechargeable Li batteries.....	49
Figure 2.4 Set up of a three electrode electrochemical cell. ....	49
Figure 3.1 SEM images of SBA-15 materials: a) SBA1/1; b) SBA2/5; c) SBA1/5; d) SBA1/10.....	53
Figure 3.2 TEM images of mesoporous SBA1/5 nanorods. ....	54
Figure 3.3 XRD of SBA-15 materials: a) SBA1/1; b) SBA2/5; c) SBA1/5; d) SBA1/10; e) SBA1/5-2/5; f) SBA2/5-1/5. ....	55
Figure 3.4 N <sub>2</sub> adsorption-desorption isotherm of SBA1/5. The sample was degassed at 150 °C for over 12 hrs on a vacuum line. (Inset) Pore size distribution of SBA1/5.....	56
Figure 3.5 Schematic diagrams depicting the influence of dilution of reaction solution on particle growth. A) conventional synthesis, B) highly dilute case. ....	58
Figure 3.6 TEM image of SBA1/5 with two inset parts magnified.....	58

Figure 3.7 SEM image of SBA1/5-2/5. ....	59
Figure 3.8 SEM images of a) SBA1/5; b) nano-CMK-3; c) TEM image of nano-CMK-3....	61
Figure 3.9 Low angle XRD patterns of a) SBA1/5; b) Nano-CMK-3; c) CMK-3.....	62
Figure 3.10 N <sub>2</sub> adsorption-desorption isotherms of a) CMK-3; b) nano-CMK-3. ....	62
Figure 4.1 Schematic diagram showing the synthesis of DGMC materials: (A) as-synthesized SBA-15; (B) partially carbonized as-synthesized SBA-15; (C) after catalyst loading; (D) after graphitization and complete carbonization; (E) removal of the silica by HF etching showing the carbon fibers that connect the carbon nanorods as dash lines; (F) graphitized carbon nanorod replica.....	70
Figure 4.2 Small angle XRD patterns of graphitic nanoporous carbon materials (a) Fe-DGMC, (b) Co-DGMC, and (c) Ni-DGMC. ....	72
Figure 4.3 SEM images of (a) DMC; (b) Fe-DGMC; (c) Co-DGMC; (d, e) Ni-DGMC. ....	73
Figure 4.4 TEM images of Ni-DGMC a, b) (001) plane; c) (110) plane. The tubular structure of the rods is indicated by the outlined red squares (inset) in part c.....	75
Figure 4.5 N <sub>2</sub> adsorption-desorption isotherm for (a) Co-DGMC; (b) Ni-DGMC shifted up by 50 for clarity; and (c) Fe-DGMC shifted up by 200 for clarity. (Inset) PSDs: red, Co-DGMC; black, Ni-DGMC; green, Fe- DGMC. ....	76
Figure 4.6 Wide-angle XRD patterns of (a) DMC; (b) Co-DGMC; (c) Ni-DGMC; (d) Fe-DGMC. The peak at $2\theta = 18^\circ$ is due to the XRD holder.....	79
Figure 4.7 Raman spectra of (a) DMC; (b) Ni-DGMC; (c) Co-DGMC; and (d) Fe-DGMC. ....	80
Figure 4.8 TGA curves showing slightly improved thermal stability in air for the graphitized carbon materials: green, DMC; blue, Ni-DGMC; black, Co-DGMC; and red, Fe-DGMC. ..	81
Figure 4.9 XRD patterns of DGMC materials obtained at 1000 °C: (a) Ni-DGMC, (b) Co-DGMC, and (c) Fe-DGMC.....	82
Figure 4.10 XRD patterns of (a) Ni-DGMC at 900 °C and (b) Ni-DGMC at 1000 °C. ....	83
Figure 4.11 SEM images of materials obtained at 1000 °C: (a) Ni-DGMC and (b) Co-DGMC. ....	83
Figure 4.12 Wide-angle XRD pattern of the nanocomposite DGMC/MoO <sub>2</sub> .....	84

Figure 4.13 TEM images of (a) the nanocomposite DGMC/MoO <sub>2</sub> at low magnification showing the stuffed channel structure and presence of a minor amount of MoO <sub>2</sub> crystallites external to the DGMC channels; (b) high magnification showing the MoO <sub>2</sub> within the channels; (c) “empty” DGMC reproduced from the Figure 4.4, for easy comparison with part b.....	85
Figure 4.14 TGA-DSC curves of the DGMC/MoO <sub>2</sub> nanocomposite to determine carbon percentage. ....	86
Figure 4.15 Galvanostatic discharge and charge profiles of the first two cycles of DGMC/MoO <sub>2</sub> .....	87
Figure 4.16 Discharge and charge cycle performance of DGMC/MoO <sub>2</sub> at a constant rate of C/10; the first seven cycles were recorded in the window 3.0-0.05 V; the lower cutoff voltage was then raised to 0.3 V during the subsequent seven cycles; and the cutoff voltage was then reset to 0.05 V to show the regain in capacity. The contributions of the partially graphitized carbon and MoO <sub>2</sub> are estimated as described in the text. ....	88
Figure 4.17 Galvanostatic discharge and charge profiles of the first two cycles of DGMC. .	90
Figure 5.1 Schematic diagram showing chemical vapor deposition for preparation of GCMK-3. ....	95
Figure 5.2 Schematic showing the process of composite preparation. ....	96
Figure 5.3 TEM images of a) CMK-3; b) CMK-8 and SEM images of c) CMK-3; d) CMK-8. ....	98
Figure 5.4 Low angle XRD patterns of mesoporous materials I: a) CMK-3; b) GCMK-3; II: a) KIT-6; b) CMK-8. ....	99
Figure 5.5 Wide angle XRD patterns of a) DGMC at 900 °C; b) DGMC at 1000 °C; c) GCMK-3.....	101
Figure 5.6 SEM images of a) a mixture of CMK-3 and sulfur before heating; b) CMK-3/S prepared at 145 °C; c) the CMK-3/S prepared at 155 °C. Sulfur outside of structure of CMK-3 is indicated by the outlined red square (inset) in part a, b.....	102

Figure 5.7 a) TEM image of a CMK-3/S-155 composite particle; b) image expansion corresponding to the area outlined by the red square; inset shows the TEM image for pristine CMK-3 at the same magnification; c) corresponding carbon elemental map; d) corresponding sulfur elemental map; e) schematic showing sulfur (yellow) confined in the interconnected pore structure of OMC, CMK-3. The carbon nano-fibers are propped apart by carbon micro-fibers.....	103
Figure 5.8 a) Low angle X-ray diffraction patterns of a mixture of CMK-3 and sulfur (i) before heating (ii) after heating at 155°C; b) wide angle X-ray diffraction patterns of a mixture of CMK-3 and sulfur (i) before heating (ii) after heating at 155°C. ....	105
Figure 5.9 Thermogravimetric analysis of a typical CMK-3/S composite in a N <sub>2</sub> atmosphere with a heating rate of 20 °C/min, showing the sulfur content of 69.3wt%.....	107
Figure 5.10 Schematic diagram for an electrochemical reduction mechanism of a sulfur electrode with a depth of discharge of Li-S cells. ....	108
Figure 5.11 Galvanostatic discharge and charge profiles of the first cycles of the carbon-sulfur composites at a current rate of 168 mA·h/g <sub>s</sub> (C/10).....	109
Figure 5.12 Galvanostatic discharge/charge profiles of the first cycle of CMK-3/S-155 recorded at 55°C at 168 mA/g <sub>s</sub> on discharge to 1.0 V followed by quasi-equilibrium discharge at 16.8 mA/g <sub>s</sub> .....	111
Figure 5.13 The galvanostatic discharge and charge profiles of the first cycle of CMK-3/S-155 at 336 mA/g <sub>s</sub> (C/5) compared to 168 mA/g <sub>s</sub> (C/10). ....	112
Figure 5.14 Cycling life of CMK-3/S-155 at 168 mA/g <sub>s</sub> (C/10) at 300K. ....	113
Figure 5.15 Coulombic efficiency of CMK-3/S-155 on cycling. ....	114
Figure 5.16 Cycling life of CMK-3/S-155 at 336 mA/g <sub>s</sub> (C/5) at 300K. ....	115
Figure 5.17 The galvanostatic discharge and charge profiles of the first cycle of various composites a) CMK-3/S; b) CMK-8/S; c) GCMK-3/S at a current rate of 168 mA/g <sub>s</sub> (C/10).....	116
Figure 5.18 Cycling life of a) CMK-8/S; b) GCMK-3/S at 168 mA/g <sub>s</sub> (C/10) at 300K. ....	117

Figure 5.19 Cycling life (discharge capacity only) of a) CMK-3/S (black); b) GCMK-8/S (blue); c) GCMK-3 (red) at 168 mA/g <sub>s</sub> (C/10) at 300K. ....	118
Figure 5.20 Thermogravimetric analysis of the PEG4600 modified CMK-3 in air with a heating rate of 20 °C/min, compared with PEG4600 itself. The PEG4600 TGA and DSC curves are shown as dashed lines, and PEG-CMK-3 as solid lines.....	120
Figure 5.21 Schematic showing PEG coated CMK-3/S composites which comprise: a) PEG200; b) PEG4600; c) PEG600.....	121
Figure 5.22 SEM images of a) CMK-3/S and PEG coated CMK-3/S materials b) PEG200 coated; c) PEG600 coated; d) PEG4600 coated. ....	122
Figure 5.23 Cycling life of CMK-3/S-PEG600 at 168 mA/g <sub>s</sub> (C/10) at 300K.....	123
Figure 5.24 Schematic showing detachments of PEG chains from composite surface. ....	124
Figure 5.25 Cycling life of a) CMK-3/S-PEG4600; b) CMK-3/S-PEG200 at 168 mA/g <sub>s</sub> (C/10) at 300K.....	125
Figure 5.26 Cycling life of a) CMK-3/S, (blue); b) CMK-3/S-PEG200 (Black); c) CMK-3/S-PEG4600 (Red); d) CMK-3/S-PEG600 (Olive).....	126
Figure 5.27 SEM images of surface morphology of composites before cycling and after 15 <sup>th</sup> charge a), b) CMK-3/S; c), d) CMK-3/S-PEG200; e), f) CMK-3/S-PEG4600.....	127
Figure 5.28 The galvanostatic discharge and charge profiles of the first cycle of a) PEG200 modified CMK-3/S (45:55 in weight); b) PEG200 modified CMK-3/S (30:70 in weight). ....	129
Figure 5.29 Cycling life of PEG200 modified CMK-3/S (C/S 45:55 in weight) at 168 mA/g <sub>s</sub> (C/10) at 300K.....	129
Figure 5.30 Percentage of sulfur dissolution into electrolyte from a) CMK-3/S-PEG200 composite cathode; b) CMK-3/S composite cathode; c) a cathode made of a mixture of acetylene black carbon and sulfur with the exact same C/S ratio. ....	130
Figure 5.31 Galvanostatic discharge profile for PEG200 modified CMK-3/S (C/S 45:55 in weight) at 168 mA/g <sub>s</sub> (C/10) at 300K until a voltage of 2.25 V was reached, followed by a rest for 9 days at open circuit voltage.....	132

Figure 6.1 a) TEM image of OMC-S composite with 10wt% sulfur in the structure (dark field); b) image expansion corresponding to the area outlined by the red square in part a; c, d) corresponding carbon and sulfur elemental maps. ....	139
Figure 6.2 Schematic showing sulfur functional layers on carbon nanorods of CMK-3. ....	140
Figure 6.3 Low angle XRD patterns of a) OMC-S; b) CMK-3. ....	140
Figure 6.4 Thermogravimetric analyses in air of a) H <sub>2</sub> PtCl <sub>6</sub> impregnated OMC-S; b) OMC-Pt before evacuation; c) OMC-Pt after evacuation. ....	141
Figure 6.5 X-ray photoelectron spectra of a) S [2p] signal; b) Pt [4f] signal for OMC-Pt after evacuation. ....	142
Figure 6.6 Schematic diagram for A) conventional impregnation method to load noble metal nanoparticles into OMC; B) our new impregnation method with a support functionalized by sulfur. ....	143
Figure 6.7 a) Wide angle XRD pattern of conventionally prepared CMK-3/Pt; b) regeneration of (111) peak in a) by addition of the patterns of Pt (6 nm) and Pt (1.5 nm) materials. ....	144
Figure 6.8 TEM images of OMC-Pt a) Dark field; b) Bright field. ....	146
Figure 6.9 a) Low angle XRD pattern of OMC-Pt; b) Wide angle XRD pattern of OMC-Pt. ....	146
Figure 6.10 Representative TEM images of OMC-Pt treated at a) 600 °C (bright field); b) 800 °C (bright field). ....	147
Figure 6.11 TEM, SEM images and an elemental map of OMC-Pd. a) TEM image (dark field); b) SEM image; c) image expansion corresponding to the area outlined by the red square in b); d) corresponding Pd EDX map of part b; e) corresponding carbon EDX map of part b. ....	148
Figure 6.12 a) SEM image of OMC-Rh; b) image expansion corresponding to the area outlined by the red square in part a; c) corresponding Rh EDX elemental map of part a; d) TEM image (1100KX, dark field). ....	149

Figure 6.13 a) SEM image of OMC-Ru; b) image expansion corresponding to the area outlined by the red square in part a; c) corresponding Ru EDX elemental map of part a; d) TEM image (1100KX, dark field).....	150
Figure 6.14 Wide angle XRD patterns of a) OMC-Ni; b) OMC-Co, metal phases marked with * and metal sulfides ( $\text{Co}_4\text{S}_3$ , $\text{Ni}_3\text{S}_2$ ) marked with @. ....	151
Figure 6.15 TEM image of OMC-Ni (dark field). ....	152
Figure 6.16 Wide angle XRD patterns of OMC-Cu, Cu phase marked with * and $\text{Cu}_2\text{S}$ phase marked with @. ....	153
Figure 6.17 Wide angle XRD patterns of a) OMC-S; b) KB-S; c) Vulcan-S.....	154
Figure 6.18 a) TEM image (dark field) and b) SEM image of KB-Pt.....	155
Figure 6.19 Wide angle XRD patterns of a) KB-Pt; b) Vulcan-Pt; c) CMK-3/Pt composite where CMK-3 was not decorated by sulfur layer.....	156
Figure 6.20 Wide angle XRD pattern of OMC-Bi.....	157
Figure 6.21 a), b) TEM images of OMC-PtBi-1nm (dark field); c), d), corresponding Pt and Bi elemental maps to part b. ....	158
Figure 6.22 a) TEM image of OMC-PtBi-3nm (dark field); b) an ultra-high resolution TEM image of a representative PtBi particle in OMC-PtBi-3nm (bright field. ....	159
Figure 6.23, a, b) EDX spectra for individual PtBi nanoparticles in OMC-PtBi-3nm where the inset shows the corresponding TEM image with nanoparticles correspondingly labeled (dark field).....	160
Figure 6.24 Wide angle XRD patterns of a) OMC; b) OMC-PtBi-1nm; c) OMC-PtBi-3nm. Blue markers indicate Pt phase; red markers indicate PtBi phase [11]. ....	161
Figure 6.25 XPS of a) bulk PtBi Bi [4f] and b) OMC-PtBi-3nm Bi [4f]. ....	162
Figure 6.26 Steady state cyclic voltammograms obtained for formic acid oxidation on a) CMK-3/Pt (red) and OMC-Pt-2nm (black) b) OMC-PtBi-1nm (red) and OMC-PtBi-3nm (black) in $\text{N}_2$ saturated 0.5 M sulfuric acid plus 0.5 M formic acid solution. The scan rate is 10 mV/s. All catalysts were cleaned with faster scan at 50 mV/s for 3 cycles at a steady state.....	164

Figure 6.27 CA curve of the OMC-PtBi-3nm with working electrode rotated at 200 rpm at a given potential of 0.3 V vs. RHE. a) I-t curve shown for the first an hour; b) I-t curve shown for whole 20 hrs. ....	166
Figure 7.1 SEM images of nano-CMK-3/S prepared by a) melt-diffusion method; b) agitation-friction method; c) image expansion of the area outlined by the red square in part b. ....	171
Figure 7.2 SEM image of a) nano-CMK-3; b) nano-CMK-3/S prepared by agitation-friction method; c) corresponding EDX spectrum of inset area outlined by red square in part b; d) XRD patterns of (i) simple mixture of nano-CMK-3 and sulfur, (ii) nano-CMK-3/S prepared by agitation-friction. ....	173
Figure 7.3 Schematic diagram depicting the agitation-friction process a) initial mixture of nano-CMK-3 and sulfur; b) during infiltration; c) final stage with sulfur all infiltrated. ....	174
Figure 7.4 SEM images and sulfur map of bulk CMK-3/S composite prepared with agitation-friction method a) high resolution image; b) corresponding EDX sulfur map to part a; c) enlarged image corresponding to the area outlined by the red square in part a; d) low resolution image. ....	176
Figure 7.5 Pore size distribution curves of a) nano-CMK-3; b) nano-CMK-3/S before sulfur melting; c) nano-CMK-3/S after sulfur melting. ....	178
Figure 7.6 Plots of $\ln(C/C_0)$ vs. t, on Pt sorption kinetics, nano-CMK-3/S (solid black dots) and bulk CMK-3/S (hollow circle), inset: pseudo-second-order model fitting on sorption kinetics. ....	179

## List of Tables

Table 1.1 Classification of fuel cells.....	18
Table 1.2 Summary of the CMK family .....	34
Table 3.1 Physical characteristics of ordered mesoporous silicate samples.....	56
Table 3.2 Physical characteristics of mesoporous carbon samples.....	62
Table 4.1 Characteristics of nanoporous carbons .....	77
Table 5.1 Physical characteristics of OMCs.....	100
Table 5.2 Characteristics of CMK-3, and the CMK-3/S composite.....	106
Table 6.1 BET and BJH results of various carbons.....	154
Table 7.1 Parameters calculated from the pseudo-second-order model and obtained from experiments.....	180

## Glossary

BET	Brunauer-Emmett-Teller
BJH	Barrett-Joyner-Halenda
CA	Chronoamperometry
CV	Cyclic voltammetry
CVD	Chemical vapor deposition
DFAFC	Direct formic acid fuel cells
DGMC	Direct graphitic mesoporous carbon
DMC	Direct mesoporous carbon
DSC	Differential scanning calorimetry
EDX	Energy dispersive X-ray analysis
EV	Electric vehicles
GCMK-3	Graphitic CMK-3
GITT	Galvanostatic intermittent titration technique
HRTEM	High resolution transmission electron microscopy
LIB	Lithium (ion) batteries
LTMO	Lithium transition metal oxide

MEA	Membrane electrode assembly
OMC	Ordered mesoporous carbon
P123	(ethylene oxide) <sub>20</sub> (propylene oxide) <sub>70</sub> (ethylene oxide) <sub>20</sub>
PEG	Polyethylene glycol
PEMFC	Polymer electrolyte membrane fuel cells
PGM	Platinum group metals
PITT	Potential intermittent titration technique
PVDF	Poly(vinylidene fluoride)
RHE	Reversible hydrogen electrode
SEI	Solid electrolyte interface
SEM	Scanning electron microscopy
SIAC	Sulfur impregnated activated carbon
TEGDME	Tetra(ethylene glycol) dimethyl ether
TEOS	Tetraethylorthosilicate
TGA	Thermal gravimetric analysis
XPS	X-ray photoelectron spectroscopy
XRD	X-ray diffraction

# Chapter 1

## Introduction

### 1.1 Brief overview of energy problems

Modern lifestyles and population growth demand steady and reliable supplies of energy. Energy sources can be categorized into three broad types [1]. The first is derived from the chemical energy stored in some reductants, for example, hydrocarbons. By oxidizing these substances, heat or electricity can be generated. Fossil energy typically belongs to this category. The second type relies on the reactions of nuclei. Nuclear energy, something that plays a very important role in today's energy pattern, can be released either by splitting heavy nuclei (nuclear fission) or by fusing light nuclei (nuclear fusion). The third type combines solar energy and thermomechanical types of energy in the form of wind, water, or geological sources of steam or hot water. Today's world is basically fueled by fossil energy. In 2008, fossil fuels accounted for 83.4% of the entire energy consumption of the United States [2]. With the dramatically increasing global demand for energy and the depletion of fossil energy, identifying alternative clean energy sources is becoming a global focus. The alternative energy sources are preferably renewable and of low environmental impact.

Renewable means of producing and storing electrical energy, the most important form of energy, is critically important. Technologies based on fuel cells and solar cells to convert renewable energy sources to electricity more efficiently are under intensive development. To conveniently store energy from sustainable sources, rechargeable batteries represent a very

viable solution. From portable electronic devices to electric vehicles, rechargeable batteries, which are environmentally benign, of high energy density and low cost, are much needed to meet a booming demand.

Vehicles powered by internal combustion engines (ICE) are the major consumers of fossil fuels. To control global warming and, more importantly, relieve our heavy reliance on fossil fuels, green transportation is of great importance. Hybrid electric vehicles (HEV), plug in hybrid electric vehicles (PHEV), and fuel-cell powered vehicles are considered green choices. HEVs, with their excellent fuel economy, are penetrating the auto market. Toyota Prius, one of the first mass-produced HEVs, has already achieved a huge success. The Chevrolet Volt, a plug-in HEV of General Motors, is expected to be launched soon. Further developments of rechargeable batteries, especially Li (ion) batteries, will determine the future of electric vehicles and establish a new worldwide auto market pattern. Vehicles powered by fuel cells are very promising as well. Fuel cell powered buses have been commercialized by Ballard. However, the debut of the publicly affordable fuel cell powered cars is still awaited. Batteries and fuel cells as candidates to replace the ICE are both coveting the privilege of powering future vehicles. Nevertheless, the efficient combination of batteries and fuel cells may compensate each other's drawbacks and render a great power system.

## 1.2 Rechargeable batteries

### 1.2.1 Basic concepts

Electrical energy is fundamentally significant in our everyday life. How to store electrical energy for various applications is of great importance. Capacitors can hold electrical energy directly; however, their capacity is very limited. A battery is a cell or a group of cells containing chemical energy which can be converted into electrical energy in a controlled manner. There are two types of batteries: primary batteries (one-time use) and secondary batteries (rechargeable). A secondary battery can be charged by running a current in the opposite direction of the discharge current through the battery. Rechargeable batteries offer economical and environmental benefits for obvious reasons, and they strongly influence the quality of a portable device or an electric vehicle by determining its weight, size and operating time.

In a cell,  $S(N)_{\text{red}}$  and  $S(P)_{\text{ox}}$  are active materials in the negative electrode and the positive electrode, respectively. Herein, S, N, and P represent the phrases “substance”, “negative electrode”, and “positive electrode”, respectively. The cathode is the electrode that absorbs electrons, and the anode is the electrode that provides electrons. During discharge, the positive electrode of a cell is the cathode and the negative electrode is the anode. Discharge half and overall reactions are shown in equations (1-1) to (1-3). When supplying electricity to a cell during charge, the reactions are reversed, and the negative electrode of the cell is the cathode and the positive electrode is the anode.





The Gibbs free energy change ( $\Delta G$ ) of the reaction (1-3) is the maximum chemical energy which can be converted into electrical energy. The equilibrium voltage of the cell is given by

$$\Delta U_0 = -\Delta G/n \cdot F \quad (1-4)$$

where  $n$  is the number of electrons transferred in the reaction,  $F$  is the Faraday constant (equivalent to 96485 A·s/eq), and  $\Delta U_0$  is the equilibrium voltage of the cell. **Figure 1.1** schematically shows an electrochemical cell.

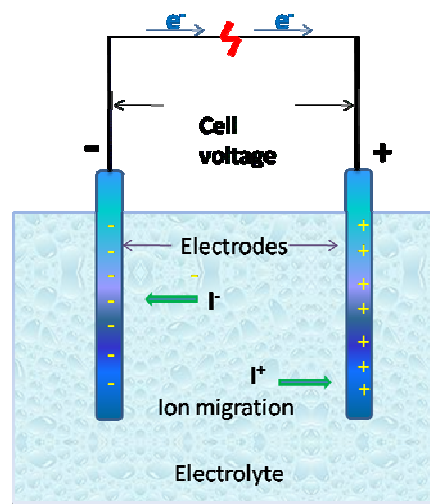


**Figure 1.1 Schematic of an electrochemical cell [3].**

### 1.2.2 History of rechargeable batteries

Based on the chemistry employed, rechargeable batteries can be categorized into several types, including lead-acid, nickel-cadmium (NiCd), nickel metal hydride (NiMH),

sodium-sulfur (Na-S), and lithium (ion) batteries (LIB). The practical energy densities of these batteries are illustrated in **Figure 1.2**.

Invented in the 1860s by Planté [3], the lead-acid battery is the most technologically mature rechargeable battery, used extensively in automobiles as the SLI (starter, lighter, and ignition) battery because of its capacity for delivering high current. Despite its short cycle life (300 to 500 cycles), lead-acid battery is probably the most recycled product in the world, partially leading to its low cost. However, its low energy density (40 W·h/kg, 80 W·h/l) rules out its possibility to power future electric vehicles.

The NiCd battery, first proposed by Jungner in 1899, contains nickel oxyhydroxide (NiOOH) as the cathode and cadmium metal as the anode. The NiCd battery has a higher energy density (60 W·h/kg, 130 W·h/l) and a better cycle life than lead-acid battery. It is widely used in relatively cheap devices which cannot tolerate the higher price of NiMH and Li-ion batteries. The NiMH battery employs NiOOH as the cathode as well and a hydrogen-absorbing alloy as the anode. It has a much higher energy density (75 W·h/kg and 200 W·h/l) than the NiCd battery. High energy paste electrode technology was first developed for the NiMH battery, which allowed it to power the first mass-produced HEVs.

The Na-S battery has attracted some interest for its low cost, good cycle life and high energy and power densities [4]. Molten sulfur and sodium as the cathode and anode, respectively, are separated by a solid ceramic electrolyte (beta-alumina). It operates at temperatures above 300°C. The high operating temperatures present some difficulty for transportation applications of the Na-S battery.

The LIB exhibits the highest energy density among rechargeable batteries. Pioneering work on the primary lithium battery was carried out by G. N. Lewis in 1912, and it became commercially available in the 1970s [5]. However, the rechargeable LIB did not enter the market until the graphite anode was employed. Li ion polymer battery comprising laminated electrode and separator sheets has become a dominant force by addressing the need for thin and light batteries with customizable shapes and sizes [6]. Since the LIB can be made compact and light-weight with a satisfactory cycle life while offering high energy densities, it has been widely used in portable electronics such as cellular phones, MP3s and laptop computers. The LIB is widely believed to power the next generation electric vehicles. The new Chevrolet Volt will be equipped with LIB supplied by LG Chem.

### **1.2.3 How to evaluate a Li (ion) battery electrode**

To evaluate an electrode, some characteristics are very important. They are electrode potential, discharge/charge profiles, capacity, energy density, rate capability, and cycle life.

Within the thermodynamically stable potential window of the electrolyte with respect to the redox potentials of both the cathode and anode, a high potential difference between cathode and anode is preferred because the output power of a battery is the product of current and voltage. In terms of characteristic discharge/charge profiles, the voltage difference between discharge and charge curves, a measure of the degree of polarization, should be very small. When a cell is discharged or charged at a sufficiently slow rate, the discharge and charge curves should completely overlap, due to the reversibility of the reaction. The specific capacity ( $\text{mA}\cdot\text{h/g}$ ) and volumetric capacity ( $\text{mA}\cdot\text{h/cm}^3$ ) denote the amount of charge stored per unit mass and per unit volume, respectively. In terms of a whole cell, the specific energy

density and (volumetric) energy density represent the energy output per unit mass ( $\text{W}\cdot\text{h}/\text{kg}$ ) and per unit volume ( $\text{W}\cdot\text{h}/\text{l}$ ), respectively. Correspondingly, power density is given in units of  $\text{W}/\text{kg}$  or  $\text{W}/\text{l}$ . C-rate signifies a charge or discharge current equal to the capacity of a battery divided by 1 hour. Normally, higher C-rate leads to lower capacity and larger polarization of a cell. Rate capability is the ability of a cell to maintain its capacity at higher current rates. The cycle life is the total number of discharge/charge cycles the cell can sustain before the capacity is significantly reduced.

#### **1.2.4 Cathodes in Li (ion) batteries**

Li (ion) batteries should not be confused with Li batteries which employ lithium metal as the anode. There are two major types of electrodes in Li (ion) batteries categorized from a mechanistic point of view. Insertion electrodes operate on the basis of topotactic intercalation reactions: reversible uptake of Li ions and electrons in a solid with minimal change to the structure. Conversion reactions define “integration” electrodes which Li reversibly reacts with, rather than intercalates into [7]. Insertion cathode materials include layered oxides, spinels, olivines, and others. Sulfur and  $\text{O}_2$  are examples of integration cathodes.

##### **1.2.4.1 Insertion cathodes**

###### **1.2.4.1.1 Layered structures**

Ever since Whittingham *et al.* demonstrated that Li ions could be de/intercalated into layered  $\text{TiS}_2$  in 1976 [5], tremendous attention has been devoted to find efficient Li-insertion compounds. Layered lithium transition metal oxides represent the most successful category

of insertion compounds in the last 20 years. Compounds with formula  $\text{LiMO}_2$  (M: V, Cr, Fe, Co and Ni) crystallize in a layered structure [8]. The structure comprises a cubic close-packed (ccp) oxygen atom array with  $\text{Li}^+$  and  $\text{M}^{3+}$  ions occupying the octahedral interstitial sites, and this layered structure offers excellent ion diffusion pathways.

#### 1.2.4.1.1.1 Lithium cobalt oxide, $\text{LiCoO}_2$

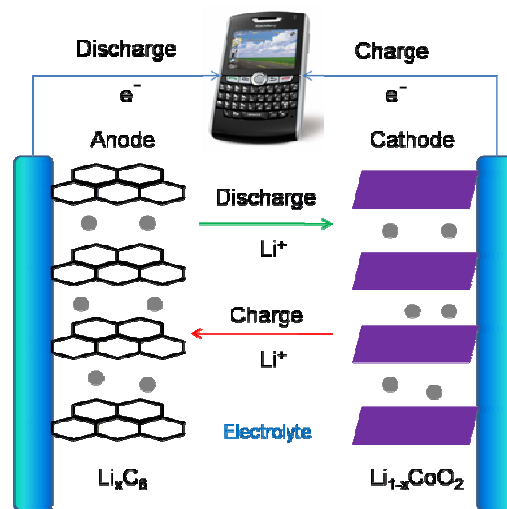


**Figure 1.2** Schematic diagram of charge and discharge in a lithium ion battery with Li insertion compound used as both electrodes.

In 1980, Goodenough *et al.* first identified  $\text{LiCoO}_2$  as a viable cathode material from which all the Li can be electrochemically removed [9]. With Li complete removed, ccp oxygen layers rearrange into a hexagonal close-packed (hcp) structure [10]. Between the composition limits ( $\text{LiCoO}_2 \leftrightarrow \text{CoO}_2$ ), several phases are formed with different degrees of distortion of the ccp oxygen lattice. The phase transition can cause capacity loss, low rate capability and poor stability of the electrodes. In the lithium ion battery market, the combination of  $\text{LiCoO}_2$  and carbon anode (see **Figure 1.2**), first commercialized by the

SONY Corporation, is still the dominant technology. Although  $\text{LiCoO}_2/\text{C}$  batteries have achieved great success in the portable electronics market, they can not meet the demand to power electric vehicles (EV) due to the toxicity and high price of cobalt metal. Consequently, alternative electrodes are highly necessary for large-scale applications.

#### 1.2.4.1.1.2 Lithium nickel oxide, $\text{LiNiO}_2$

$\text{LiNiO}_2$  is isostructural to  $\text{LiCoO}_2$ . Although nickel is more available and less toxic than cobalt,  $\text{LiNiO}_2$  is not recognized as a promising cathode material for Li ion batteries for a variety of reasons. It is very difficult to synthesize stoichiometric  $\text{LiNiO}_2$  [11]. The  $\text{Li}_{1-y}\text{Ni}_{1+y}\text{O}_2$  phase is usually formed because the instability of the  $\text{Ni}^{3+}$  oxide favors conversion to  $2y \text{Ni}^{2+}$  and  $(1-y) \text{Ni}^{3+}$  with concomitant loss of  $y\text{Li}$  [12]. Consequently, the degree of cation order is very low (nickel is always found in the lithium layer which pins neighboring  $\text{NiO}_2$  layers together, thus reducing Li ion diffusion rate and rate capability) [13]. Most importantly, irreversible phase changes occur during the charge-discharge processes, and the resultant phases are unstable in contact with organic solvents, which results in a serious safety problem [14]. To keep nickel in the nickel layer, one or two other elements can be introduced into the structure [15,16,17]. Particularly,  $\text{LiNi}_{0.5}\text{Mn}_{0.5}\text{O}_2$  [18] and  $\text{LiNi}_{1/3}\text{Mn}_{1/3}\text{Co}_{1/3}\text{O}_2$  [19] have attracted much attention due to their better thermal stability and cycling characteristics.

#### 1.2.4.1.2 Spinel structure

Spinel  $\text{LiMn}_2\text{O}_4$  as an alternative to  $\text{LiCoO}_2$  first proposed by Thackeray *et al.* has attracted attention due to the fact that Mn is less expensive and toxic than either Co or Ni [20]. The spinel structure also contains a cubic close-packed oxygen array.  $\text{Li}^+$  and  $\text{M}^{4+/3+}$

occupy 1/8 tetrahedral and 1/2 octahedral interstitial sites, respectively. Its discharge curve shows two plateaus: one around 4 V and the other around 3 V. During the latter plateau, a phase transition from cubic to tetragonal occurs due to the Jahn-Teller distortion associated with  $\text{Mn}^{3+}$  ions, resulting in rapid capacity fade. Therefore, only the discharge process at 4 V is practical, corresponding to a capacity of 130 mA·h/g.

#### 1.2.4.1.3 Olivine structure

Recently, much attention of materials electrochemists has been focused on  $\text{LiFePO}_4$ . Padhi *et al.* first discovered the electrochemical properties of  $\text{LiFePO}_4$  and suggested its application as a cathode material in Li ion batteries in 1997 [21].  $\text{LiFePO}_4$  has many desirable characteristics including low cost, environmental friendliness and good thermal stability. It can approach a capacity of 170 mA·h/g, higher than  $\text{LiCoO}_2$ . The lithium de/insertion potential in  $\text{Li}_{1-x}\text{FePO}_4$  is around 3.5 V versus  $\text{Li}^+/\text{Li}^\circ$ , and there is almost no capacity fading after several hundreds of cycles.  $\text{LiFePO}_4$  has an orthorhombic (*Pnma*) olivine structure where  $\text{Li}^+$  and  $\text{Fe}^{2+}$  occupy two unique octahedral sites, respectively, with no mixing. Compared to  $\text{LiFeO}_2$ , the phosphate groups in  $\text{LiFePO}_4$  raise the potential of the  $\text{Fe}^{3+}/\text{Fe}^{2+}$  redox couple from ~2 to 3.5 V due to the “inductive effect” [22], but on the other hand, they dramatically decrease the electrical conductivity. The low electrical conductivity ( $10^{-9}$  S/cm) was considered the major hurdle for its utilization. Our group has made significant contributions to solving this problem. By introducing low loading of carbon *via* a carbon gel in the synthesis step, the theoretical capacity was almost obtained [23]. Our group also proposed that the conductivity can be substantially increased by the formation of metallic iron phosphides,  $\text{FeP}/\text{Fe}_2\text{P}$ , a surface film, at high temperatures in the presence of a

reductant [24]. Other olivine structures based on Mn, Co, Ni suffer various serious problems, impeding their application as electrodes.

#### 1.2.4.2 Integration reaction cathodes

##### 1.2.4.2.1 Sulfur electrode

Currently, lithium ion batteries are based on topotactic intercalation compounds. After 2 decades of optimization, these batteries have virtually reached their theoretical energy density limit (500-700 W·h/kg); however, this energy density cannot offer an electric vehicle the comparable drive range provided by the ICE. New systems with substantially higher energy density are being sought for the next-generation batteries, and one of the new systems is the lithium-sulfur battery. The low equivalent weight, low cost, and nontoxicity of sulfur render it a promising electrode material. Compared to the insertion electrode, a sulfur electrode operates quite differently. The redox couple, described by the reaction  $S_8 + 16Li \leftrightarrow 8Li_2S$  lies near 2.2 V with respect to  $Li^+/Li^\circ$ , a potential about 2/3 of that exhibited by conventional positive electrodes. However, this is offset by the very high theoretical capacity afforded by the non-topotactic “assimilation” process, of 1675 mA·h/g. Thus compared to the conventional batteries, Li-S batteries have the opportunity to provide specific energy 5 times higher. Theoretical values can approach 2500 W·h/kg or 2800 W·h/l on a weight or volume basis [25], respectively, assuming complete reaction to  $Li_2S$  and no Li excess required.

Despite its considerable advantages, the Li-S cell is plagued with problems that have prevented its practical realization. Early configurations of the sulfur electrode consisted of simple mixtures of sulfur and carbon powder [26,27]. These cells suffered poor discharge

and cycle efficiency. Without intimate contact between the sulfur and carbon particles, the poor conductivity is a major problem since both sulfur and its ultimate discharge product  $\text{Li}_2\text{S}$  are both electrical and ionic insulators. Much attention has been paid to increase the conductivity of the sulfur electrode. Composites with sulfur embedded within a conducting polymer have shown some promising results [28]. However, the large polarization reduces the energy density of cells. The low surface area of the conducting polymer also limits the loading of sulfur active mass. The conductivity of the sulfur electrode can be greatly enhanced by carbons with “honeycomb” nanostructures that molten sulfur can be absorbed into. These carbons with good conductivity, high surface area, and large specific pore volume not only increase the conductivity but also exhibit some absorbing effect for soluble sulfur species [29,30].

Another major problem arises from soluble polysulfide ions ( $\text{S}_n^{2-}$ ) formed during cycling [31]. These polysulfide ions can diffuse from the sulfur electrode into the electrolyte, and are then self-discharged onto the Li anode, forming a solid electrolyte interface. On completing each discharge, polysulfide ions are reduced to solid  $\text{Li}_2\text{S}_2$  and/or  $\text{Li}_2\text{S}$  which gradually form a thick layer on the cathode surface over cycles [32]. Much of  $\text{Li}_2\text{S}/\text{Li}_2\text{S}_2$  in the thick layer becomes electrochemically irreversible after prolonged cycles, which causes active mass loss and capacity fading. The thick layer also blocks the ionic paths into the inner parts of the sulfur electrode, impeding further electrochemical reactions. Another problem caused by polysulfide ions is the “polysulfide shuttle phenomenon”. During the latter stages of the charge process, higher order polysulfides (*e.g.*,  $\text{Li}_2\text{S}_8$ ), which are generated at the sulfur electrode, diffuse to the lithium negative electrode where they react directly with

lithium in a parasitic reaction to create lower order polysulfides. These species diffuse back to the positive electrode and are re-oxidized into the original higher order polysulfides. The above process takes place repeatedly, thus creating a shuttle phenomenon. This reduces the coulombic efficiency.

Extensive work has been done to prevent the polysulfide dissolution. Visco *et al.* proposed to coat the cathode with a mixed ionic electronic conductor (MIEC) [33]. They claimed that the MIEC layer allows rapid removal of discharge product precipitates on the cathode. Ahn *et al.* reported that  $\text{Mg}_{0.6}\text{Ni}_{0.4}\text{O}$  particles (~50 nm) as a cathode additive exhibit a certain degree of an adsorption effect on polysulfide ions [34]. Gorkovenko *et al.* described that porous carbon materials can retard polysulfide dissolution [35]. However, these solutions still fall short of the mark for practical electrochemical performance.

Attention on Li-S batteries was paid to soluble polysulfide electrodes [36]. Although the ionic conductivity of these “catholytes” is very high, capacity fading typically occurs due to the reactions with the Li electrode. This caused a rapid abandonment of this “all liquid” system. In 1997, Chu described an “all solid” cell system employing a gel-like polymer electrolyte [37]. However, this cell achieves practical discharge efficiency only at high temperatures (above 80°C), and it also suffers capacity fading during cycling [38].

There is still a vast potential to improve the Li-S batteries. Polysulfide dissolution is the major hurdle to be cleared for the sulfur electrode, and even for Li-S batteries. In *Chapter 5*, a highly ordered carbon/sulfur nanocomposite as the cathode will be discussed.

#### 1.2.4.2.2 Oxygen electrode

Recently, Li-air batteries emerged as a promising alternative and have drawn some attention. Employing O<sub>2</sub> in air as the cathode active “mass” is not a new concept. O<sub>2</sub> has been extensively used in fuel cells and zinc-air batteries. However, both systems rely on the aqueous nature of the electrolyte which does not have a large electrochemical “window”. To utilize Li as an anode, a non-aqueous electrolyte is a necessity. The first Li-air battery was successfully assembled by Abraham *et al.* in 1996 [39]. Rechargeability was proven only recently by Bruce *et al.* [40]. Li<sub>2</sub>O<sub>2</sub> was determined to be the principle product after discharge, and O<sub>2</sub> was indeed detected as a charging product, confirming the reversibility of the reaction. In a Li-air battery, O<sub>2</sub> reduction typically proceeds in porous carbon as a current collector with help from electrochemical catalysts. The discharge reaction leads to filling the voids of the porous carbon current collector and automatically terminates when the carbon voids are completely filled. Active electrolytic manganese dioxide is suggested as the catalyst for the splitting of O<sub>2</sub>; however, high overpotentials were still observed. A huge effort is needed to bring the Li-air rechargeable battery up to a commercializable level.

### 1.2.5 Anodes in Li (ion) batteries

#### 1.2.5.1 Li metal

Lithium metal is an attractive anode material due to its low potential (-3.045 V versus the reversible hydrogen electrode, RHE) and high theoretical specific capacity (3860 mA·h/g) [41]. Lithium metal has been utilized as a primary battery anode for decades. However, lithium metal rechargeable batteries have not been massively commercialized for public customers yet. The reactivity of lithium towards electrolytes is problematic since its

potential is much lower than the safe “window” of electrolytes which is typically between 1 to 5 V versus  $\text{Li}^+/\text{Li}^{\circ}$  [42]. A passivating layer can be formed on the Li anode after reactions with electrolytes; however, this layer is not sturdy enough to prevent further reactions with electrolytes, especially at high temperatures. Lithium dendrite growth on cycling causes safety concerns [43]. To stabilize Li anode, protective layers which can separate Li anode from the electrolyte are highly desirable [44]. Recently, lithium phosphorus oxynitride (LiPON) [45] has attracted attention as a protective layer for Li anode in Li-air batteries [46].

#### 1.2.5.2 Carbonaceous materials

Carbonaceous materials still dominate the LIB anode market. Graphite exhibits a theoretical specific capacity of 372 mA·h/g based on the formation of  $\text{LiC}_6$ . Practically, about 350 mA·h/g can be reached [47]. Graphite has a layered structure which consists of hexagonal graphene sheets of  $\text{sp}^2$  carbon atoms. Van der Waals forces hold the graphene sheets together [48]. Li ions can be de/inserted between these graphene sheets. Graphite has a potential of 0.01-0.1 V versus lithium metal, below the stable “window” of electrolytes [49]. Extensive reactions between graphite and electrolytes form a solid electrolyte interface (SEI) [50], which is instrumental to the successful operation of a cell. The SEI is widely believed to be conductive for Li ions but insulating for electrons. To form a proper SEI, electrolytes need to be carefully selected [e.g.,  $\text{LiPF}_6$  in ethylene carbonate (EC) and dimethyl carbonate (DMC) is commonly used]. Non-graphitic carbon carbonized at low temperatures (500 to 1000 °C) can exhibit higher specific capacity than graphite [51,52,53]. However, these carbons suffer enormous irreversible capacity in the first cycle. These carbons also exhibit a large degree of polarization during discharge/charge processes.

### 1.2.5.3 Alloy anode

Li can form alloys with a number of metals and semiconductors [54,55]. Normally, a large number of Li atoms can be incorporated into an alloy (e.g.  $\text{Li}_{4.4}\text{Si}$  can be formed, corresponding to a theoretical specific capacity of 4200 mA·h/g). However, the high capacities are inevitably associated with a large volume change. During cycles of alloying and unalloying, volume change leads to loss of contact between particles. Rapid capacity fading can be observed. It has been reported by Li *et al.* that the above problems can be partially relieved by employing some special binders [56].

### 1.2.5.4 Nanomaterials

Conversion reactions involving nanomaterials changed electrochemists' definition of electrode materials. It is no longer a necessity for an electrode material to have an open structure with interstitial voids [57]. Tarascon *et al.* first identified nano-scale binary oxides (MO, M = Co, Ni, Cu, Fe and others) as promising electrode materials which can be reversibly converted into metal nanoparticles embedded in a polymer-like  $\text{Li}_2\text{O}$  matrix for hundreds of cycles at room temperature, providing large capacities [58]. The pioneering work in oxides initiated a new round of searching for new electrode materials with high performance. Conversion reactions in nano-scale nitrides, fluorides, phosphides, sulphites and borates have been reported [59,60,61]. With anions of varying electro-negativity, one can tune the potential of the conversion reactions.

### 1.2.6 Electrolyte

Electrolyte provides for the separation of ionic transport and electronic transport. It normally comprises a lithium salt solution in a mixture of organic solvents. The details of the electrolyte are beyond the scope of the thesis.

## 1.3 Fuel cells

### 1.3.1 Basic concepts

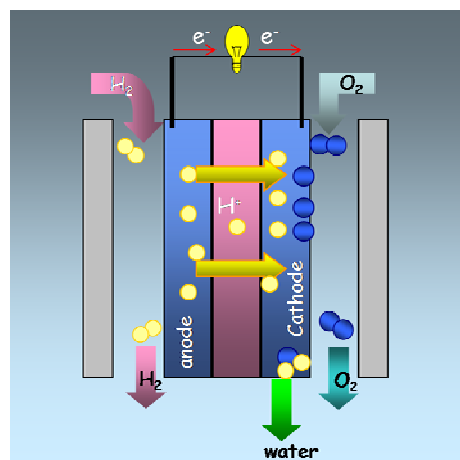
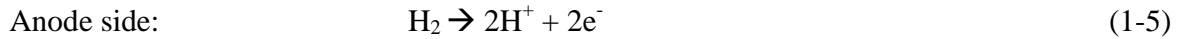


**Figure 1.3 Schematic of a H<sub>2</sub> polymer electrolyte membrane fuel cell.**

The principle of fuel cells was first conceived by Sir William Grove in the 1840s [62], but they did not find their first application until the space exploration in the 1960s. For the last two decades, intensive world-wide efforts have been devoted to develop fuel cell materials and fuel cell systems. The driving forces include the need for more efficient energy conversion system for transportation and the demand to prevent global warming.

Unlike a battery, a fuel cell can continuously supply electricity as long as a fuel, such as H<sub>2</sub>, is provided. This concept is schematically shown in **Figure 1.3**.

The chemical reactions in a H<sub>2</sub> fuel cell are given in equations (1-5) to (1-7)



like a battery, the Gibbs free energy change in a fuel cell is also associated with the cell voltage shown in equation (1-4). At standard conditions, a  $\text{H}_2$  fuel cell has an equilibrium voltage of 1.23V [63].

### 1.3.2 Classification of fuel cells

**Table 1.1 Classification of fuel cells [64].**

Type	Electrolytes	Charge carriers	Operating temperature (°C)	Fuels	Efficiency (System)
AFC	Aqueous KOH	$\text{OH}^-$	60-90	Pure $\text{H}_2$	35-65%
PEMFC	Polymer membrane	$\text{H}^+$	60-90	$\text{H}_2$ , $\text{CH}_3\text{OH}$ , $\text{HCOOH}$	35-45%
PAFC	$\text{H}_3\text{PO}_4$	$\text{H}^+$	180-220	Pure $\text{H}_2$ tolerate 1% CO	40-45%
SOFC	Solid oxide electrolyte	$\text{O}^{2-}$	800-1000	$\text{H}_2$ , CO, $\text{CH}_4$ , hydrocarbons	50-60%
MCFC	$\text{Li}_2\text{CO}_3 / \text{K}_2\text{CO}_3$	$\text{CO}_3^{2-}$	550-650	$\text{H}_2$ , CO, $\text{CH}_4$ , hydrocarbons	50-60%

Fuel cells are generally classified by the types of electrolytes employed, corresponding to different chemistry and operating temperatures. Five major types of fuel cells have been commercially developed. They are Alkaline Fuel Cells (AFC), Polymer Electrolyte Membrane Fuel Cells (PEMFC), Phosphoric Acid Fuel Cells (PAFC), Solid

Oxide Fuel Cells (SOFC), and Molten Carbonate Fuel Cells (MCFC). Their characteristics are listed in **Table 1.1**.

### **1.3.3 Polymer electrolyte membrane fuel cells (PEMFC)**

The PEMFC has most desirable features for transportation and portable power [65]. However, there are still many hurdles to be cleared before the mass commercialization of PEMFCs can be realized, such as the high price of the electrocatalysts (normally noble metals), electrocatalyst dissolution, slow oxygen reduction reaction (ORR) kinetics, and water management.

#### **1.3.3.1 Membrane electrode assembly**

The electrochemical processes occur within a PEMFC's inner three layers – the membrane electrode assembly (MEA) - which consists of a cathode layer, an electrolyte membrane, and an anode layer. Typically, the electrolyte membrane, as a proton conductor/electron insulator, is a plastic material with sulfonic-acid side chains and a fluorocarbon or hydrocarbon backbone. Each electrode layer is composed of a polymer binder and certain electrocatalysts which are often noble metal nanoparticles supported on carbon materials. The electrode layers in fuel cells serve the following three functions: (i) to present a stable interface between reactant (gas or liquid) and the electrolyte, (ii) to catalyze the fuel oxidization or the oxygen reduction reactions, and (iii) to conduct electrons to or from the reaction sites.

### 1.3.3.2 Electrocatalysts in direct formic acid fuel cells (DFAFC)

Compared to  $H_2$  gas, liquid fuels with much higher volumetric energy density are much more convenient for storage and shipping. PEMFCs fueled with small organic molecules in liquid form such as methanol and formic acid have attracted much attention [66].

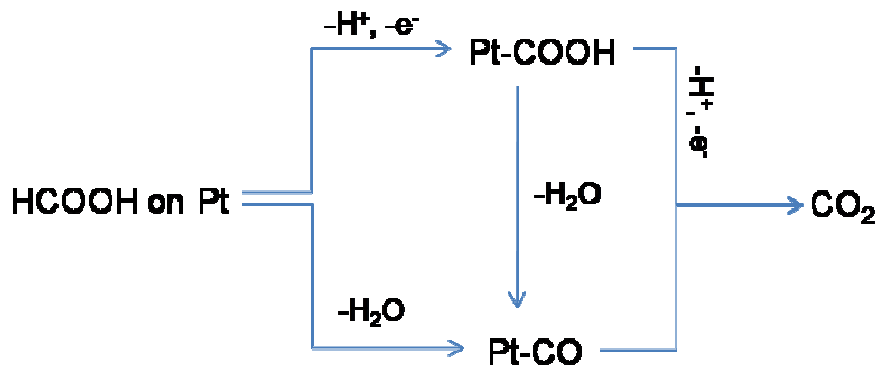


**Figure 1.4 Dual-path reaction mechanism of formic acid oxidation on Pt.**

Recently, increasing attention has been paid to direct formic acid fuel cells (DFAFC) [67,68] because formic acid exhibits a two orders lower crossover flux through Nafion<sup>®</sup> membranes compared to methanol [69]. Initially, Pt was intensively investigated as a catalyst for formic acid oxidation [70,71]. It is well known that Pt in its pure form suffers serious self-poisoning when catalyzing formic acid oxidation [72,73] which arises from the dual-path reaction mechanism as shown in **Figure 1.4** [74].

In one path, sequential dehydrogenation steps lead to the direct formation of  $CO_2$  (path 1). In the other path,  $CO$ , as a reaction intermediate, formed via dehydration (path 2), readily adsorbs onto the Pt surface, impeding further fuel oxidation. It has been widely believed that the dehydration path requires the presence of Pt atom ensembles - continuous

neighbouring atomic sites - while the dehydrogenation path does not [75]. Therefore, the CO poisoning effect can be inhibited by the breach of Pt ensembles, as shown in **Figure 1.5**.

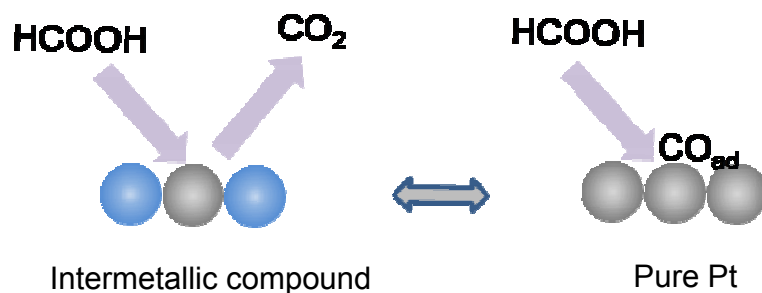


**Figure 1.5 Illustration of catalytic reactions of formic acid oxidation on Pt intermetallic compound and pure Pt.**

By employing bulk Pt with ad-atoms on surface [76,77,78,79] or bulk PtM (M: Bi or Pb) intermetallic catalysts [80,81], CO poisoning resistance of catalyzed formic acid oxidation was improved. Furthermore, intermetallic crystallites are highly desirable to achieve high-mass activity and complete CO poisoning resistance. Some progress has been achieved. By employing the polyol process [82] or co-reduction method by sodium borohydride [83,84], DiSalvo, Abruña *et al.* generated unsupported intermetallic PtBi and PtPb nanoparticles (~20 nm or larger). Although the mass activity of these catalysts was not effectively maximized due to particle agglomeration, nearly complete elimination of CO poisoning was observed. To avoid agglomeration of the alloy nanoparticles normally formed at high temperature, special care is required. Most recently, a few advances have been reported in terms of particle size control of supported intermetallic nanoparticles. Schaak *et al.* introduced the preparation of supported intermetallic nanocrystals including PtBi by employing pre-formed supported single metal nanoparticles as nucleation sites [85].

However, the particle size of their material was still larger than a desired value owing to the higher temperature needed to nucleate intermetallic phases. Up to date, major efforts have been devoted to particle size control of intermetallic nanoparticles with only limited success. This requires a good catalyst support which can be efficient in charge and mass transfer, and capable of inhibiting sintering and loss of the catalysts during operation. Further development of supported catalysts, especially intermetallics, requires a reliable methodology which facilitates not only the particle size control but the fine dispersion of these nanoparticles on an ideal support such as ordered mesoporous carbons (OMC) [86]. The preparation of OMC supported catalysts and their catalytic performances on formic acid oxidation will be presented in detail in *Chapter 6*.

#### **1.3.4 Electrocatalyst preparation techniques**

It is well known that the performance of a catalyst layer in a fuel cell is influenced not only by the properties of nanoparticles, but also by where and how those particles are supported [87]. Ideally, nanoparticles with a uniform size are homogeneously dispersed on a high surface area support. To achieve this, generally, there are three major methods: impregnation method, colloidal method, and microemulsion method.

##### **1.3.4.1 Impregnation method**

In this method, particle growth can be restricted by the presence of high surface area supports. A precursor solution is formed first, followed by the addition of a support. The transition from precursors to metal particles is realized by introducing a reductant. Particle size and dispersion of nanoparticles are strongly influenced by the porosity and surface area

of the supports. The major drawback of this method is the lack of accurate control on particle size and dispersion.

#### 1.3.4.2 Colloidal method

The first step is to suspend nanoparticles in a solvent with the suspension being stabilized. Generally, there are three methods to stabilize a suspension: electrostatic stabilization, steric stabilization, and ligand stabilization [88]. Later on, the formed colloid will be deposited onto a support, followed by chemical reduction. Although nanoparticles can be prepared with a uniform size by this method, the drawback is the presence of protective agents on the nanoparticles which may undermine the catalysis. These agents need to be removed completely.

#### 1.3.4.3 Microemulsion method

In a microemulsion, droplets which accommodate precursors are immiscibly and uniformly dispersed in a medium. A co-surfactant is often added to adjust the size of the microemulsion droplets. The precursor reduction is carried out in the droplets which serve as micro- or nano-reactors. The size and distribution of the nanoparticles can be strictly controlled by this method; however, it is not yet applicable to large-scale syntheses due to the use of expensive surfactants.

### **1.3.5 Comparison between batteries and fuel cells**

Both batteries and fuel cells can convert chemical energy into electrical energy, following the fundamentals of electrochemical thermodynamics and kinetics. They both consist of a cathode, an anode, and an electrolyte. They differ in their way of carrying

chemical energy. A battery is not only an energy conversion device but also an energy storage device. A battery, primary or secondary, is a sealed system (except Li-air or zinc-air batteries) with a certain amount of chemical energy stored on board, and the power output of a battery terminates on depletion of the stored chemical energy. A fuel cell, as an open system, can endlessly run as long as a fuel is constantly supplied. Fuel cells, especially low temperature ones (e.g. PEMFCs), employ aqueous electrolyte systems, but secondary Li (ion) batteries employ organic solvent electrolytes.

#### **1.4 Mesoporous materials**

Mesoporous materials have pore sizes between microporous ( $< 2$  nm) and macroporous ( $> 50$  nm) regimes according to the Union of Pure and Applied Chemistry (IUPAC) classification. Mesoporous materials with controllable porous structures are in high demand for various fields, such as catalysis, electrodes, adsorption (absorption), and drug delivery. The first synthetic mesoporous silicates were reported separately by Japanese scientists and Mobil Corporation scientists [89,90,91]. Up to now, long range ordered mesoporous structures have been developed in many inorganic materials, such as carbon, oxides, sulphides, and composites. With their high surface area and strictly ordered structure with large pore size and volume, mesoporous materials, especially non-siliceous structures, have potential applications in rechargeable batteries and fuel cells.

## 1.4.1 Mesoporous silica

### 1.4.1.1 M41S

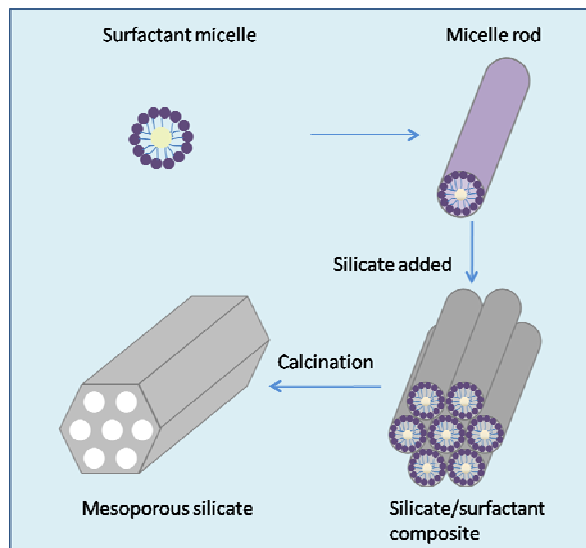


**Figure 1.6 Schematic diagram for formation of mesoporous silicate.**

Prepared by following the procedures shown in **Figure 1.6**, MCM-41 typically exhibits a  $d(100)$  spacing of about 4 nm, a channel size 2 to 3 nm and a wall thickness of 1 to 2 nm. Typically, it has surface area around  $700 \text{ m}^2/\text{g}$  and a pore volume of about  $0.7 \text{ cm}^3/\text{g}$ . Cetyltrimethylammonium bromide [ $\text{C}_{16}\text{H}_{33}\text{N}(\text{CH}_3)_3\text{Br}$ , CTAB], a cationic surfactant, was employed as a structure directing agent in the synthesis. The structure and pore dimensions of MCM-41 are determined by the properties of the surfactant, including surfactant chain length and solution chemistry. The Mobil Corporation scientists suggested that the structure is defined by the organization of the surfactant molecules into micellar liquid crystals which serve as templates for the formation of the MCM-41 structure, rather than the condensation of silicate precursor. For this reason, the types of materials which can be formed this way are certainly not limited to silicates. Their theory accurately predicted the feasibility of

synthesizing non-siliceous mesoporous materials [90]. The applications of MCM-41 are restricted by its limited pore size. A truly two dimensional structure limits its ability to replicate non-siliceous materials.

By changing the ratio between the structure directing agent and the silicate source to a certain point, MCM-48 with a three dimensionally cubic structure (*Ia3d*) can be obtained [92]. The surface area of MCM-48 normally varies from 660 to 1010 m<sup>2</sup>/g, with a pore size from 0.5 to 0.8 cm<sup>3</sup>/g and a wall thickness between 0.3 and 1.3 nm [93]. Thin walls and poor reproducibility of the synthesis limit the applications of MCM-48.

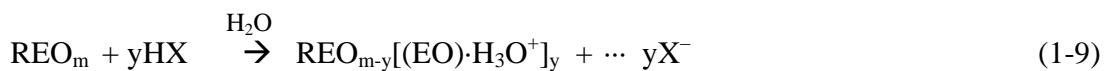
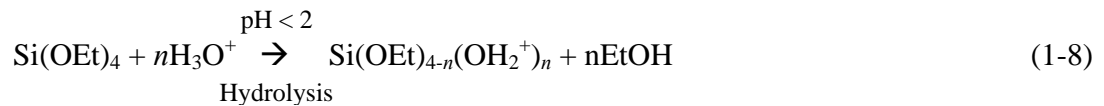
M41S was the first group of materials to display a long range ordered mesoporous structure. The development of these frameworks opened the door to controlling the mesostructure of materials. Extensive research has been focused on them in the past 15 years. However, the materials' inherent problems limit their applications. Their pore sizes are not large enough for most bio molecules and their relatively thin walls lead to poor thermal stability. Better mesoporous materials were then sought after in the following years as described below.

#### 1.4.1.2 SBA-15

SBA-15, with a two dimensionally hexagonal structure (*p6mm*), was first prepared by Zhao *et al.* in 1998 [94]. It is obtained by employing a tri-block copolymer HO(CH<sub>2</sub>CH<sub>2</sub>O)<sub>20</sub>(CH<sub>2</sub>CH(CH<sub>3</sub>)O)<sub>70</sub>(CH<sub>2</sub>CH<sub>2</sub>O)<sub>20</sub>H (P123), a nonionic polymer, as the template. The pore size of SBA-15 varies from 4.6 to 30 nm and the wall thickness is between 3.1 and 6.4 nm giving it obvious advantages over the M41S family.

#### 1.4.1.2.1 Mechanism of SBA-15 formation

The cooperative assembly of mesostructured polymer-silica composite (as-synthesized SBA-15) occurs *via* an  $(S^{\circ}H^+)(X^{-}I^+)$  pathway in acidic medium [95] ( $S^{\circ}$ : surfactant,  $X^{-}$ : a mediator ion,  $I^+$ : inorganic species). First, alkoxy silane species are hydrolyzed, followed by partial oligomerization. More hydrophilic ethylene oxide moieties of the surfactant in a strong acidic medium will associate with hydronium ions as shown in equation (1-9). More hydrophobic propylene oxide moieties will be engulfed as a core in the surfactant micelles.



where R: alkyl or poly (propylene oxide) and  $X^{-}$  :  $\text{Cl}^{-}$ ,  $\text{Br}^{-}$ . It is proposed that charge-associated EO units and the cationic silica species are assembled together by electrostatic, hydrogen bonding, and van der Waals interaction. The  $\text{REO}_{m-y}[(\text{EO})\cdot\text{H}_3\text{O}^+]_y \dots y\text{X}^{-} \dots I^{-}$  interaction is usually designated as  $(S^{\circ}H^+)(X^{-}I^+)$ . The mechanism for SBA-15 particle growth has not been completely understood, although SBA-15 is 10 years old. In **Chapter 3**, some insight and corresponding evidence on SBA-15 particle growth will be introduced.

#### 1.4.1.2.2 Mesopore-micropore network

Stucky *et al.* found that the surface area of SBA-15 is far too large for a material with approximately cylindrical pores with that size and volume, which in turn indicated that the mesopores are accompanied by another pore system in this material. Various reports prove

the existence of microporosity by nitrogen adsorption data for surfactant free SBA-15 samples on the basis of the plot analysis, and pore size distributions [96,97,98]. The formation of micropores is corroborated by supramolecular studies illustrated in **Figure 1.7**.

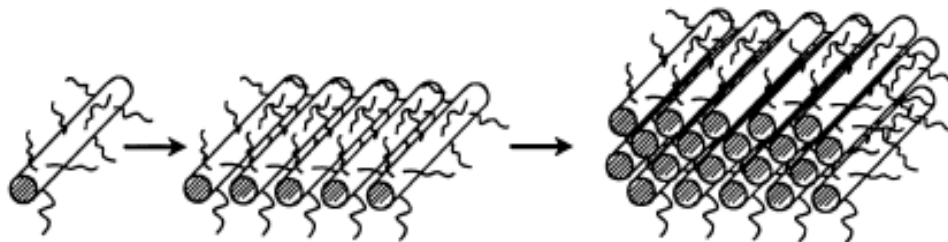


**Figure 1.7 Self-assembly of copolymer into supramolecular hexagonal architecture [99].**

The complementary pore system is suggested to form as a result of penetration of poly (ethylene oxide) chains of the tri-block copolymer template within the silica walls of as-synthesized SBA-15. These significantly smaller pores are disordered and located in the walls providing the connection between paralleling mesoporous channels. This is a substantial difference between SBA-15 and MCM-41.

The microporosity of SBA-15 plays a very important role in the preparation of SBA-15's negative replicas which are formed by a "nanocasting" method (explained later). Many replicas have been successfully prepared from SBA-15, including carbon, metal and oxides. However, long range ordered replicas based on MCM-41 are rare [110].

#### 1.4.1.2.3 Morphology control of SBA-15

The synthesis of mesoporous materials with controllable morphology has been one of the focuses in this field. Mesoporous materials in the form of films [101,102], monoliths [103,104], spheres [105,106], fibers [107], rod-like powders [108,109,110] and crystals [111] have been obtained by employing block copolymers as structure directing agents (**Figure**

1.8). It is important to design the morphology of mesoporous materials as well as the mesostructure itself for the desired applications. In comparison with conventional fiber-like morphology of SBA-15, short-rod-like morphology, with a uniform particle size that can supply more access points for the guest molecules, has attracted much interest. Different morphologies of SBA-15 can be obtained by adjusting reaction conditions, such as stirring time and rate, temperature, and reactant ratios [112]. **Chapter 3** will present the preparation of SBA-15 nanorods by a dilution strategy.

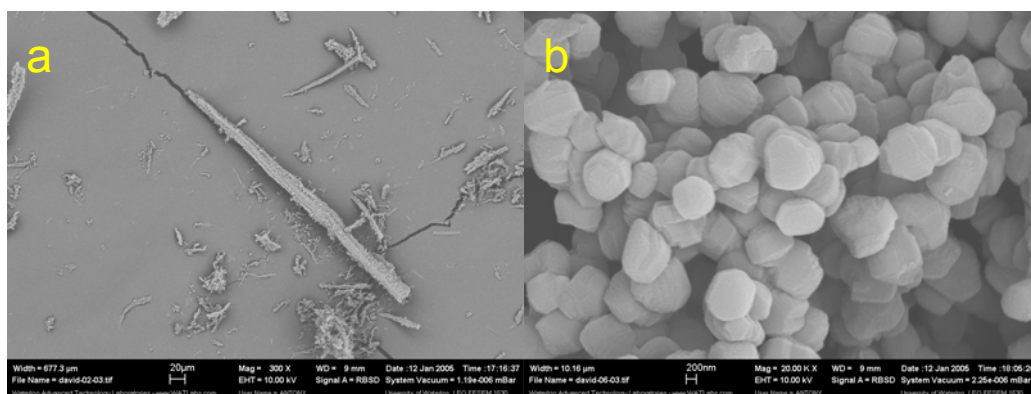


**Figure 1.8 Morphologies of SBA-15: a) fiber-like; b) short-rod-like.**

#### 1.4.1.3 KIT-6 — “cubic SBA-15”

KIT-6 was first reported by Ryoo *et al.* in 2003 [113]. Similar to SBA-15, KIT-6 enjoys large surface area, large pore size (up to 12 nm), and thick walls (>3 nm). Different from SBA-15, KIT-6 exhibits a cubic ( $Ia3d$ ) symmetry structure. In the synthesis of KIT-6, butanol as a co-surfactant leads to the swelling of hydrophobic blocks of P123 micelles, resulting in decreased curvature of micelle aggregates. Consequently, a meta-stable lamellar mesophase forms at 35 to 38 °C, which evolves into a highly ordered cubic structure through

silicate condensation at hydrothermal conditions. Recently, KIT-6 with unique properties has been frequently utilized as a hard template to prepare other mesoporous materials [114].

#### **1.4.2 Non-siliceous mesoporous materials**

With mesoporous silicates successfully prepared, non-siliceous mesoporous materials, with a lot potential applications, became the next research focus [115]. The possibility to synthesize non-siliceous mesoporous materials was first discussed mechanistically in 1993 [116]. The first examples were reported in 1994 [117]. However, the templates could not be removed from the as-synthesized materials without disturbing their structures and thus only mesostructured composites were obtained. The first non-siliceous mesoporous solids were reported in 1995/1996 [118,119]. Since then a wide variety of non-siliceous mesoporous materials have been developed with different strategies. There are two major strategies: “soft template” method and “hard template” method. The latter is also called “nanocasting” method. The “soft template” method has been successfully adopted in the preparation of mesoporous silicates.

##### **1.4.2.1 Synthesis strategies**

###### **1.4.2.1.1 Soft template method**

In this method, the interaction between surfactant and precursors as well as the interaction among different precursors are important. Interactions including electrostatic and/or charge attraction, Lewis acid-base interaction and hydrogen bonding, are necessary to achieve cross-linkage of precursors and precursor-surfactant cooperative assembly.

Block copolymers were identified as surfactants highly adaptable to prepare non-siliceous mesoporous materials. Wiesner *et al.* used an amphiphilic block copolymer, where hydrophilic component was infiltrated with an inorganic oxide precursor [120]. These composites can be tuned to form any structure guided by the phase diagram of block polymers, *via* adjustment of the fraction of hydrophilic and hydrophobic blocks. By employing an evaporation-induced self assemble (EISA) strategy, originally utilized for fabrication of mesoporous silica thin films [121], various mesoporous metal oxides were successfully prepared [122,123]. The key factor in EISA strategy is the use of alcohol as a solvent, which leads to essentially non-hydrolytic conditions. It is suggested that the propylene oxide part of the template binds the metal ions in an essentially crown-ether-like fashion, which, together with the mesophase formation driven by the different polarities of the EO and PO blocks, leads to mesostructuring of an inorganic-organic composite. However, the compositions of materials which can be prepared by the EISA strategy are limited.

The chemistry between surfactants and precursors was believed the most important factor to form the cooperative assembly. Zhao *et al.* found that the interactions among different precursors were equally important. They reported that the cross-linking and gelation of an inorganic precursor can be tuned by addition of a second precursor as a pH adjustor and hydrolysis-condensation controller [124]. The combination of two precursors is often in the form of “acid-base pair”. In this cooperative assembly, inorganic precursor No.1 ( $I_1$ ), inorganic precursor No.2 ( $I_2$ ) and organic template (O) are involved. As a general principle, the order of interaction strength between reactants is as following:  $I_1I_2 \gg I_1I_1, I_2I_2$  and  $O(I_1I_2) \gg OI_1, OI_2$ . Guided by this principle, various highly ordered mesoporous metal

oxides, mixed metal oxides, metal phosphates and metal borates materials have been successfully synthesized [124].

Recently, stable mesoporous organic frameworks have been obtained employing the soft template strategy [125,126,127]. Inspired by the interaction between inorganic precursors and organic surfactants, one can employ the organic-organic interaction to construct self-assemblies. For example, a cooperative assembly is formed with P123 and a polymer from polymerization of phenol and formaldehyde. The interaction between P123 and plenty of hydroxyl groups on the polymer is instrumental to the successful assembly.

#### 1.4.2.1.2 Hard template (nanocasting) method

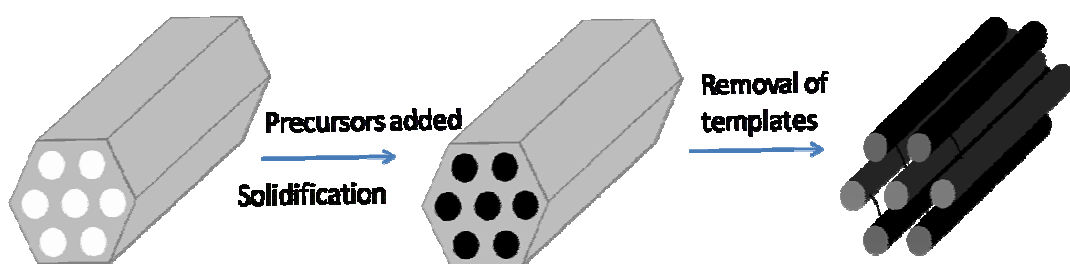


**Figure 1.9** An example of the nanocasting route, in which SBA-15 is employed as a hard template.

The nanocasting method is an extension of the templating concept. Instead of employing an organic template, mesoporous materials with ordered interconnected voids are utilized as molds to prepare inverse replicas. By sorption, ion exchange, complex and covalent grafting, precursors are incorporated into the voids of mesoporous silicates. After thermal treatment or other solidification methods, the precursors decompose and mechanically stable fillers can be created. If the voids of the mesoporous hard template are

sufficiently filled, after solidification, the fillers inside the voids will form an interlinked framework. After removal of the molds, inverse mesoporous structures can be preserved. By this hard template route schematically illustrated in **Figure 1.9**, various replicas of mesoporous materials can be easily prepared.

The possibility of using ordered mesoporous silica as a mold for other materials, especially polymers, has already been realized [128]. Later, ordered mesoporous carbons (OMC) [129] and metals were synthesized by the nanocasting method as well. Because an interconnected structure of a mold is key to prepare a stable replica, only experiments with MCM-48, MSU-1, SBA-15 and KIT-6 as hard templates were successful. SBA-15, in principle, has a one-dimensional channel system. However, micropores connect the linear hexagonally packed channels, thus ensuring an interconnected porous system for obtaining a stable replica. As the negative replica of mesoporous silicates, OMC materials may also be employed as hard templates for other materials. SBA-15 can be regenerated from its replica CMK-3 as the template [130,131]. MCM-41, on the other hand without cross-linked micropores, is less suitable as a template.

In order to obtain highly ordered mesostructures by this hard template route, the following four requirements should be considered [132]. (i) The mesoporous templates should possess high order thermal stability. (ii) A full impregnation of the desired precursors within the voids of templates is necessary and such precursors should be easily converted to the desired solid structures with as little volume shrinkage as possible. For this requirement, the famous “like dissolves like” principle may be used for reference considering the physicochemical properties of both the templates and the precursors. (iii) The templates

should be easily and completely removed in order to achieve a faithful replica. (iv) To control the morphology of a replica, the morphology of a template should be controllable.

#### 1.4.2.2 Ordered mesoporous carbons (OMC)

##### 1.4.2.2.1 CMK family

**Table 1.2 Summary of the CMK family**

OMC	Silicate Template	Carbon Precursor	Space Group	Reference
CMK-1	MCM-48	Sucrose	$I4_132$ or lower	127
CMK-2	SBA-1	Sucrose	Unknown	133
CMK-3	SBA-15	Sucrose	$P6mm$	134
CMK-4	MCM-48	Acetylene	$Ia\bar{3}d$	135
CMK-5	SBA-15	Furfuryl alcohol	$P6mm$	136,137
CMK-8	KIT-6	Sucrose	$Ia3d$	113

The preparation of OMC by the nanocasting method has been very successful. The CMK family listed in **Table 1.2** is the earliest and most famous group of non-siliceous mesoporous materials. The first OMC reported by Ryoo *et al.* in 1999 was replicated from MCM-48 [129]. Later on, they reported a series of OMC materials including CMK-1 and CMK-4 replicated from MCM-48, CMK-3 and CMK-5 replicated from SBA-15, and CMK-8 replicated from KIT-6. Sucrose and other carbon sources are incorporated into the voids of mesoporous silicates which are etched by HF or NaOH solution after carbonization of carbon sources.

#### 1.4.2.2.2 Regarding precursors

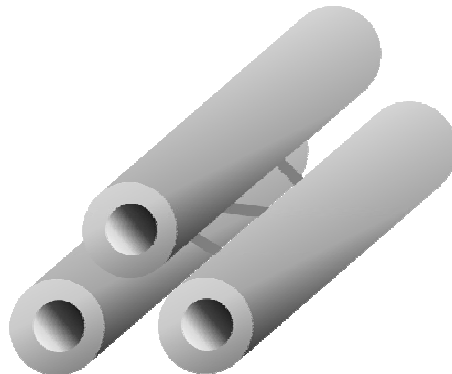


**Figure 1.10 Schematic model for the structure of CMK-5.**

Block copolymer surfactants within the channels of as-synthesized mesoporous silicates also can be pyrolyzed. OMC prepared directly from the block copolymer P123 ( $\text{EO}_{20}\text{PO}_{70}\text{EO}_{20}$ ) inside as-synthesized SBA-15 were reported by Hyeon *et al.* and our group [138,139]. Compared to the impregnation method, this strategy has some advantages. Firstly, 100% carbon precursor homogeneously occupies the channels of the silicate templates, which guarantees a faithful structure of the carbon replica. Secondly, from an economical point of view, this route makes use of the otherwise wasted surfactant.

#### 1.4.2.2.3 Graphitic mesoporous carbons

OMC are normally amorphous carbon with no graphitic lattice order. However, the electrical properties of carbon materials are closely related to their graphitization degree. The temperature for graphitization has to be as high as 2400 °C according to traditional methods, which is too severe for the long range order of OMC's to survive. Recently, interest increased in OMC with a graphitic structure. In 2003, Ryoo *et al.* reported a way to

synthesize graphitic OMC, by using aluminum containing SBA-15 as the template and acenaphthene as a carbon source. However their synthetic route was complicated and dangerous to operate. In 2004, Zhao *et al.* reported a one-step impregnation method to prepare graphitic OMC by employing mesophase pitches (MPs) as the precursor. The graphitized materials have been proven anisotropic by electrochemical measurements and present low surface areas ( $\sim 350 \text{ m}^2/\text{g}$ ) and pore volumes ( $\sim 0.4 \text{ cm}^3/\text{g}$ ) possibly due to the higher density of graphitized frameworks compared with amorphous OMC. The OMC introduced above only have low degrees of structural graphitization. Very recently, highly graphitized OMC have been prepared by a chemical vapor deposition (CVD) method at the relatively low temperature of  $900 \text{ }^\circ\text{C}$  with SBA-15 as a template [140,141].

#### 1.4.2.3 Applications of mesoporous materials in energy storage/conversion systems

##### 1.4.2.3.1 In Li (ion) batteries

Recently, much attention of electrochemists has been attracted to mesostructured electrode materials. Compared to their bulk counterparts, these materials normally exhibit higher rate capability. Their nanosized walls provide very short electronic and ionic paths in an electrode. Most importantly, their micron-sized particles do not expand or contract to a destructible degree on electrochemical cycling due to their built-in empty space; therefore, the mesoporous material electrodes do not have the disconnection problems as nanoparticles or nanofibers normally do [142,143,144]. Their disadvantages include undesirable electrode/electrolyte reactions and lower volumetric energy density.

#### 1.4.2.3.2 As catalyst supports in fuel cells

With many desirable characteristics, OMC have attracted much attention as catalyst supports for fuel cells [145,146,147,148,149]. To maximize the catalysis mass activity and take advantage of the unique architectures of OMC, it is critical, however, that the catalyst nanoparticles be completely loaded *within* the mesoporous voids. This has proven very challenging. The so-called “wet” process - the only route explored to date - is limited by poor compatibility between the hydrophobic carbon and the hydrophilic solvents necessary to dissolve the catalyst precursors [150]. This results in heterogeneous particle size distribution both within and on the outer surface of OMC’s. To solve this problem, one approach is to transform the OMC into a more hydrophilic material [151,152]. However, successful modification of OMC which facilitates metal nanoparticle loading has not been reported [153]. As an alternative approach, OMC nanofiber wrapped Pt and PtRu nanoparticles were recently reported [154,155,156]. They show improved methanol tolerance as cathode catalysts for the direct methanol fuel cell, but suffer from very poor accessibility of the catalysts for liquid fuels such as formic acid. A new methodology to solve the above problem will be given in detail in *Chapter 6*.

### 1.5 Thesis scope

This thesis will probe the possibility of improving the performance of energy storage and conversion systems with nanostructured materials as electrodes. The principle is to try to fabricate nanostructured materials for higher energy density, faster kinetics, and better stability. By investigating these nanostructured electrode materials, there are chances to closely observe and better understand their unique electrochemical behaviors, which can help

find future energy materials to serve the demands for cheaper and greener energy. **Chapter 2** describes the main characterization techniques employed in this thesis. **Chapter 3** introduces a dilution synthetic strategy to prepare mesoporous silica or carbon nanorods. **Chapter 4** discusses a highly ordered graphitic mesoporous carbon prepared from the *in situ* polymer surfactant. Furthermore, in this chapter, a nanostructured MoO<sub>2</sub>/C composite employing the above carbon as a template will be introduced. Employed as the Li ion battery anode, its electrochemical properties will be discussed. **Chapter 5** presents the preparation and investigation of a highly ordered nanostructured carbon/sulfur cathode for lithium-sulfur batteries. **Chapter 6** presents a simple and robust synthetic scheme to load electrocatalyst nanocrystals into ordered mesoporous carbon and their applications as direct formic acid fuel cell anode catalysts. **Chapter 7** describes the efficient “agitation-friction” preparation for the nano-CMK-3/S composite and its application as a sorbent to capture low concentrated aqueous Pt ions.

## Chapter 2

### Characterization Techniques

To understand the nature of electrode materials at the level required to alter them controllably and predictably requires comprehensive information of their physical and electrochemical properties. Powder X-ray diffraction (PXRD) is a powerful tool for structural characterizations of materials. Scanning electron microscopy (SEM) can be utilized to collect topographical and composition information. Transmission electron microscopy (TEM) can provide invaluable localized structural information. Thermal properties and composition information can be obtained by thermal gravimetric analysis (TGA) and differential scanning calorimetry (DSC). Physical characteristics including surface area, pore size, and pore volume are measured by N<sub>2</sub> adsorption and desorption measurements. Vibrational information of chemical bonds in materials can be collected by Raman spectroscopy. X-ray photoelectron spectroscopy (XPS) can be used to identify the chemical composition of a sample. The electrochemical properties are investigated by galvanostatic and potentiostatic techniques. This chapter outlines the basic principles of these characterization techniques used in this study.

#### 2.1 Powder X-ray diffraction (PXRD)

X-rays were discovered by Röntgen in 1895 [1]. In 1912, Laue *et al.* found out that X-ray beams could be diffracted by crystals [2]. In 1913, the well known Bragg law (**equation 2.1**) [3] was introduced, precisely explaining the appearance of a diffraction pattern arising from the X-ray reflections on crystal planes.

$$n \cdot \lambda = 2d \cdot \sin\theta \quad (2.1)$$

where  $\theta$  represents the angle between incident X-ray beam and crystallographic planes under probe, as shown in **Figure 2.1**. With two parallel X-ray beams diffracted on parallel atomic planes a distance of  $d$  apart, the deeper beam travels an extra distance of  $2d \cdot \sin\theta$ , which is a multiple of the X-ray wavelength ( $\lambda$ ) and an integer ( $n$ ), if the two beams are in phase. Various  $d$  spacings of crystallographic planes can be obtained by scanning  $\theta$ .

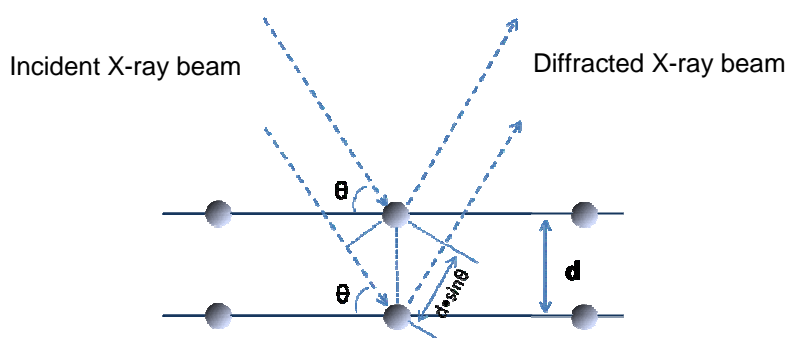


**Figure 2.1** X-ray diffracted from the lattice.

Bragg's law is applicable to PXRD. When a beam of X-ray hits a finely ground sample (particle size  $< 10 \mu\text{m}$ ), there must be a fraction of crystals with crystallographic planes orientated with a Bragg angle  $\theta$ , at which Bragg diffraction can take place. With sample stage rotating with respect to the incident X-ray beam, a pattern containing characteristic diffractions can be recorded by a detector. As a structure analysis method, the PXRD pattern cannot give direct information on chemical composition of a compound. Instead, it shows characteristic crystalline phases which are unique to each different

compound. Therefore, a PXRD pattern can be employed as a fingerprint for identification purposes with the help of a comprehensive database [4].

To characterize nanomaterials with PXRD, one should know the Scherrer Equation [5] which explains the relationship between the broadening of diffraction lines in a pattern and crystal domain sizes.

$$L = \alpha \cdot \lambda / [B \cdot \cos\theta] \quad (2.2)$$

where  $L$  represents the coherence length of a crystal domain and  $B$  is the full width in radians at the half maximum intensity (FWHM) measured at angle  $\theta$ . The numerical constant  $\alpha$  is close to unity [6]. The wavelength  $\lambda$  of X-ray is 1.5406 Å if Cu K $\alpha$ 1 radiation is employed as the X-ray source.

All the XRD patterns (low angle or wide angle) in this study were collected on a D8-ADVANCE powder X-ray diffractometer operating at 40 kV and 30 mA and employing Cu-K $\alpha$  radiation ( $\lambda = 1.5406$  Å).

## **2.2 Scanning electron microscopy (SEM) and energy dispersive X-ray analysis (EDX)**

By directing electrons with high energy (up to 40 keV) onto the surface of a specimen, secondary electrons (SE), backscattered electrons (BSE), and characteristic X-rays can be generated. These scattered species contain information on the topography and composition of a specimen's surface. Some signals can be processed and translated into high resolution images of specimen surface. When secondary electrons are emitted, empty or partially empty shells are created in the atomic structure of a specimen. With electrons

dropping from outer shells into the holes in inner shells, characteristic X-rays are radiated, which can be used to identify the elements in a specimen, especially from the surface. This technique is known as energy dispersive X-ray analysis (EDX). As a quasi-quantitative analysis, EDX is helpful to learn the stoichiometry of a sample. Furthermore, elemental mapping based on the combination of SEM imaging and EDX can provide spatial elemental distribution in a specimen.

Most of the SEM images in this thesis were taken on a LEO 1530 field emission SEM instrument equipped with an EDX system attachment. The backscattering detection mode was usually employed to obtain images. To avoid surface charging, specimens under LEO 1530 were first sputtered with a thin layer of gold (thickness:  $\sim 3\text{nm}$ ). In *Chapter 5*, a Hitachi S-5200 SEM instrument was used to investigate the surface morphology of the polyethylene glycol (PEG) modified sulfur/CMK-3 nanocomposites before and after galvanostatic cycling. The specimens under Hitachi S-5200 were not coated with any conductive layer; therefore, faithful surface morphology was provided.

### **2.3 Transmission electron microscopy (TEM)**

In a TEM, emitted electrons are accelerated under a very high voltage of 200 kV to achieve a small wavelength ( $\lambda = 0.025\text{\AA}$ ) for high resolution. The stream of electrons is confined by a set of magnetic lenses and apertures before it is diffracted through a specimen which is normally a thin slice. Most of TEM images in this thesis were obtained with a Hitachi HD-2000 scanning transmission electron microscope (STEM). In an STEM, an image is generated simply by moving the focused beam step by step over a specimen. Hence a STEM image may be considered as a collection of individual TEM experiments. Various

types of signals discriminated in scattering angle and/or energy loss yield different structural and chemical information and may be captured simultaneously in different channels. This simultaneous and controlled acquisition of information lends itself to quantitative analyses. In addition, as there is no limitation to the solid angle and the energy loss interval over which the scattered electrons may be collected, 60-100% of them contribute to the image.

In *Chapter 6*, selected high resolution work was carried out on a FEI Titan™ 80-300 equipped with an imaging lens aberration corrector and monochromator and also a FEI Titan™ 80-300 Cubed equipped with a high-brightness electron source, aberration correctors of the probe-forming lens and of the imaging lens as well as a monochromator. High-resolution imaging on the Titan 80-300 was carried out at 300 KeV after tuning the aberration corrector to achieve 0.08nm resolution in standard Young's fringes experiments. EDX measurements on the Titan 80-300 Cubed were obtained at 80 KeV so as to minimize electron beam irradiation occurring due to the use of the high-brightness electron source. Spectra of individual particles were collected for 300 seconds each while the electron beam was kept rastering on the selected individual particle so as to minimize effect of sample drift during the long acquisition time. Compared to the conventional TEM systems, in which light or electron beams are deflected strongly near the edge of lenses, resulting in blurred images, FEI Titan™ systems have specially shaped magnetic lenses which enable the researchers to correct the previously unavoidable aberration with greatly improved mechanical, thermal and electronic stability.

## **2.4 Thermal analysis**

Thermal gravimetric analysis (TGA) and differential scanning calorimetry (DSC) measurements were performed under a controlled atmosphere on a SDT Q600 analyzer.

DSC is a thermal analytical technique in which differences in the amount of heat required to increase the temperature of a sample and the reference are measured as a function of temperature. Both the sample and the reference are maintained at nearly the same temperature throughout the experiment. Generally, the temperature program for a DSC analysis is designed such that the sample holder temperature increases linearly as a function of time. The reference sample should have a well-defined heat capacity over the range of temperatures to be scanned. The main application of DSC is in studying phase transitions, such as melting, glass transitions, or exothermic decompositions. These transitions involve energy changes or heat capacity changes that can be detected by DSC with great sensitivity.

## **2.5 Surface area and pore size distribution measurement**

The measurements were carried out with a GEMINI III 2375 Surface Area Analyzer. Samples were normally degassed at 150°C overnight on a vacuum line before the measurements. The N<sub>2</sub> sorption-desorption isotherms were measured at -196 °C. In the GEMINI system, there are a sample tube and a balance tube. Both tubes are maintained at identical liquid nitrogen bath conditions. A differential pressure transducer measures the pressure imbalance between the sample and balance tubes. The imbalance is caused by the adsorption or desorption of the adsorbate (normally nitrogen gas) into or out of the sample tube. The Brunauer-Emmett-Teller (BET) [7] method was utilized to calculate the surface

area. The pore size distribution (PSD) was calculated by the Barrett-Joyner-Halenda (BJH) [8] method which is applied to the desorption branch.

## 2.6 Raman measurements

Raman spectra were recorded with a Renishaw 1000 spectrometer using a He-Ne laser with an excitation wavelength of 632.8 nm as the radiation source and 25% of the total power (40 mW) was employed for the Raman scattering measurements. The Raman emitted radiation is of three types: Stokes scattering, anti-Stokes scattering, and Rayleigh scattering. The last is a process during which photons are elastically scattered. Its wavelength is exactly the same as the source.

Raman Spectroscopy is based on the Raman Effect, which is the inelastic scattering

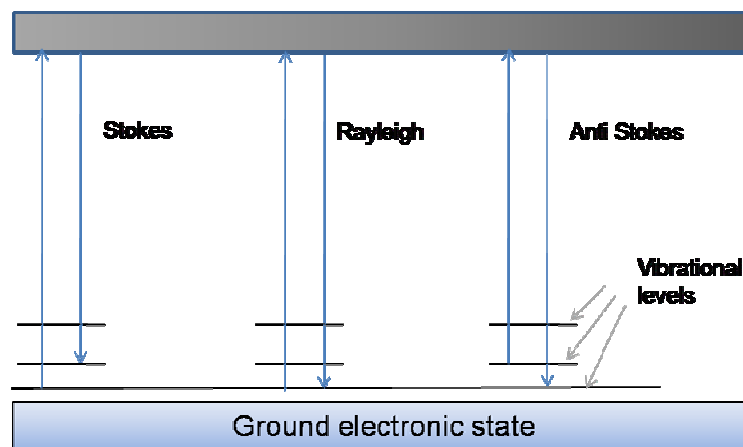


**Figure 2.2** Simplified diagram for the concept given below.

of photons by molecules [9]. The Raman Effect comprises a very small fraction, about 1 in  $10^7$ , of the incident photons. In Raman scattering, the energies of the incident and scattered photons are different, as shown in **Figure 2.2**. The energy of the scattered radiation is less

than the incident radiation for the Stokes line and the energy of the scattered radiation is more than the incident radiation for the anti-Stokes line. The energy increase or decrease from the excitation is related to the vibrational energy spacing in the ground electronic state of the molecule and therefore the wave number of the Stokes and anti-Stokes lines is a direct measure of the vibrational energies of the molecule. In the example spectrum, notice that the Stokes and anti-Stokes lines are equally displaced from the Rayleigh line. This occurs because in either case one vibrational quantum of energy is lost or gained. Also, note that the anti-Stokes line is much less intense than the Stokes line. This occurs because only molecules that are vibrationally excited prior to irradiation can give rise to the anti-Stokes line. Hence, in Raman spectroscopy, only the more intense Stokes line is normally measured.

## **2.7 X-ray photoelectron spectroscopy**

X-ray photoelectron spectroscopy (XPS), also known as electron spectroscopy for chemical analysis (ESCA), was developed in the mid-1960's by Siegbahn and his research group at the University of Uppsala, Sweden [10]. This technique is based on the photoelectric effect described by Einstein in 1905 where the concept of the photon was employed to explain the ejection of electrons from a surface when photon irradiates it. Due to the very short range of the photoelectrons that can be excited from a solid, XPS is only a surface specific technique. The information is collected only from the outer layers (<10 nm) of a material. The kinetic energy of ejected photoelectrons can be measured with an electron energy analyzer, which gives rise to a set of photoelectron peaks. Each element exhibits characteristic binding energies of the peaks. XPS can not detect hydrogen and helium, but is sensitive to all other elements. XPS must be carried out in ultra-high-vacuum conditions to

make sure the emitted photoelectrons can be analyzed without interference from gas phase collisions. As an elemental analysis technique, XPS is unique to provide chemical state information of a sample. Binding energies of the emitting atom can be slightly shifted due to a change of the chemical state. Therefore, XPS can be used to provide a quantitative measure of covalency.

The samples in this study were run on the Thermo Scientific K-Alpha XPS spectrometer. The samples were run at a take-off angle (relative to the surface) of  $90^\circ$ . A monochromatic Al  $K_\alpha$  X-ray source (1486.6 eV) was used, with a spot area (on a  $90^\circ$  sample) of 400  $\mu\text{m}$ . The main C 1s feature (C-C) at 284.6 eV was collected to provide an internal reference. Samples were etched by  $\text{Ar}^+$  sputtering to obtain XPS signals from clean regions within the samples.

## **2.8 Electrochemical techniques**

### **2.8.1 Galvanostatic cycling technique**

In the galvanostatic mode, a constant current is applied to a cell. Voltage is recorded as a function of the number of lithium atoms de/inserted. The current direction is inverted at the cut-off potentials. Electrode characteristics, such as capacity, rate capability and cycle life can be revealed by this technique. To investigate the equilibrium voltage of a cell, galvanostatic intermittent titration technique (GITT) is often carried out. In the GITT mode, during galvanostatic cycling, a cell is typically charged or discharge at a constant current for a short preset time. The cell is allowed to relax under open circuit conditions until a preset time or until a potential varying decay limit is reached to approach the thermodynamic quasi-equilibrium conditions. In the GITT mode, the shape of an open circuit potential (OCP) curve

can be used to identify whether an electrochemical reaction is a one-phase process or a two-phase process. The OCP curve of a two-phase process exhibits a distinct voltage plateau, but a one-phase process shows a continuously changing voltage.

### **2.8.2 Potentiodynamic technique (Cyclic Voltammetry)**

In a potentiodynamic experiment, the potential is ramped linearly versus time, and the current is recorded as a function of the applied potential. Current maxima occur at potentials where redox reactions take place. In the potentiostatic intermittent titration technique (PITT) mode, cell voltage does not change until after a preset time or until the current decay limit is reached to approach the equilibrium state of a cell.

When evaluating formic acid oxidation on Pt based catalysts with cyclic voltammetry (CV), a three electrode cell was used. The potential was measured between the working electrode and the reference electrode, and the current was measured between the working electrode and the counter electrode.

Potentiodynamic techniques are very helpful to study fuel cell reactions including fuel oxidation reactions and oxygen reduction reaction (ORR). To study kinetically controlled reactions, such as ORR, the diffusion rate of reactants needs to be defined by employing a rotating disc (working) electrode (RDE).

## **2.9 Electrochemical test set up for batteries**

Electrochemical evaluations of Li (ion) batteries were mainly carried out in 2325 coin cells (see **Figure 2.3**) using a commercial (MacPile) multichannel system operating in galvanostatic cycling mode. To prepare a working electrode, a slurry was formed by mixing

an electrode material, a polymer binder, and a conductive additive in an organic solvent. The slurry was spread onto a carbon coated current collector and dried overnight. Typical loading of the active mass was between 3 and 6 mg/cm<sup>2</sup>. The cells were assembled in an argon-filled glove box with oxygen and moisture levels lower than 5 ppm. The electrolytes are composed of a 1 to 1.2 M LiPF<sub>6</sub> solution in polar organic solvents, i.g., carbonates, sulfones. Lithium metal foil was used as a counter electrode.

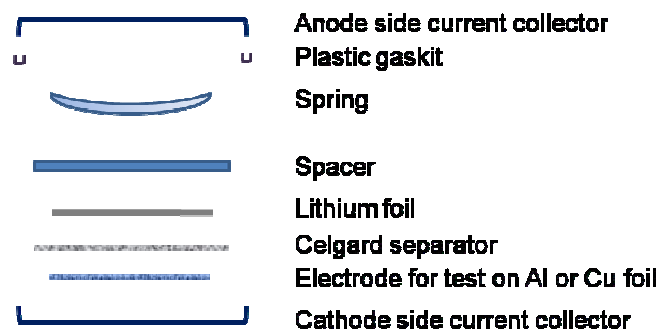


Figure 2.3 A coin cell assembly of rechargeable Li batteries.

## 2.10 Electrochemical test set up for PEM fuel cell catalysts

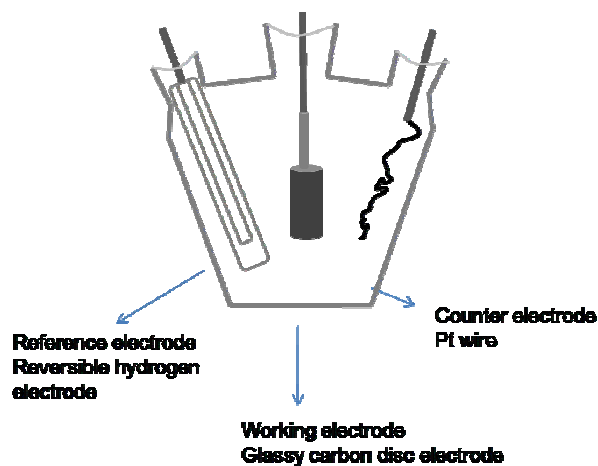


Figure 2.4 Set up of a three electrode electrochemical cell.

To prepare a working electrode, 10.0 mg metal/mesoporous carbon composites (24 wt% metal) were suspended in 5.0 ml of 2-propanol, and then ultrasonically blended for 30 minutes to form catalyst inks. Next, 10  $\mu$ l of this catalyst ink was pipetted onto the surface of the glassy carbon disk electrode (geometric area of 0.196 cm<sup>2</sup>). The catalyst coated electrode surface was then dried under atmospheric conditions, followed by the addition of 5  $\mu$ l of 2-propanol solution containing 1 wt% Nafion, on the top of the catalyst layer. The loadings of metals were all controlled to 24  $\mu$ g/cm<sup>2</sup>.

The cell used was a conventional three electrode electrochemical cell containing a glassy carbon (GC) disk coated with a catalyst as the working electrode, Pt wire as the counter electrode and a reversible hydrogen electrode (RHE) as reference electrode (**Figure 2.4**). The electrolyte was N<sub>2</sub> saturated 0.5 M H<sub>2</sub>SO<sub>4</sub> solution containing 0.5 M HCOOH. The electrode potential was scanned in the range of 0.05-1.2 V versus RHE for formic acid oxidation reaction. All electrochemical experiments were carried out at room temperature and ambient pressure.

## Chapter 3

### Nanorods of SBA-15 and CMK-3

#### 3.1 SBA-15 nanorods

##### 3.1.1 Introduction

Periodic mesoporous materials have sparked great research interest since the discovery of the M41S family and extensive efforts have been devoted to their morphological control [1]. Recently, increasing attention has been focused on the morphology control of mesoporous silicates prepared with block copolymer directing agents. SBA-15, introduced by Zhao *et al.* in 1998, has many highly desirable characteristics such as an adjustable large pore size, sturdy walls and an interconnected quasi-2D hexagonal mesostructure ( $p6mm$ ) [2]. Many forms of mesoporous silicates closely related to SBA-15 have been obtained by utilizing block copolymers as structure directing agents, including fibers [3], spheres [4], crystals [5] and monoliths [6]. To render the pores of SBA-15 more accessible for guest molecules in various applications, it is crucial to decrease its particle size to shorten the diffusion path length. Discrete rod-like particles of SBA-15 (ca.  $1.5 \times 1\mu\text{m}$ ) have been obtained in the presence of KCl by Zhao *et al.* [7]. Sayari *et al.* have introduced a synthesis of monodispersed SBA-15 rods with uniform size (ca.  $1.5 \times 0.4\mu\text{m}$ ) under static conditions without any additives [8], although the mechanism of particle size control was not detailed. The particle growth process has been examined by several *in-situ* techniques that probe the mechanism. According to these studies, wormlike nano-domains are proposed to form first, which then pack into larger particles (more than  $1\mu\text{m}$ ) after a period of time (60 to 100 min)

[9,10,11]. Nonetheless, almost all syntheses of SBA-15 in the past decade were carried out with P123 (EO<sub>20</sub>PPO<sub>70</sub>EO<sub>20</sub>) and TEOS (Tetraethylorthosilicate) concentrations in the reaction mixture of respectively 2.5 - 3 wt% and 5 - 6 wt%.

In this chapter, a synthetic strategy for SBA-15 nanodimensioned rods (ca. 0.5 × 0.1 μm) is presented. The synthesis employs a dilute solution of P123 and TEOS in an acidic aqueous medium under static conditions without any additives. The dilution helps halt the synthesis at the initial stage in the nucleation and growth mechanism, and thus trap nanorods with particle sizes many orders of magnitude smaller than previously reported. The studies moreover lend strong support to the proposed microstructure evolution theories based on sophisticated cryo-TEM, and SAXS/XRD studies [9,10,11].

### **3.1.2 Experimental**

In a typical synthesis, 2 g of Pluronic P123 (EO<sub>20</sub>PPO<sub>70</sub>EO<sub>20</sub>) was dissolved in 360 ml of 2 M HCl at 38 °C. Tetraethylorthosilicate (TEOS, 4.2 g) was added into the above solution with vigorous stirring. The concentrations of P123 and TEOS in the solution are 0.53 wt% and 1.1 wt% respectively, ~ 1/5 of those in conventional syntheses of SBA-15 reported in the literatures [8,9,10,11]. The mixture was stirred for 6 min and remained quiescent for 24 hrs at 38 °C. It was subsequently heated at 100 °C for another 24 hrs in an autoclave. The as-synthesized SBA-15 was collected by centrifugation, dried and calcined at 550 °C in air. A series of concentrations of P123 and TEOS in 2 M HCl were prepared, with the ratio between P123 and TEOS kept the same as above. These were 1/1, 2/5, 1/5, and 1/10 of the concentrations of P123 and TEOS employed in a conventional synthesis of SBA-15. These SBA-15 materials are referred as SBA1/1, SBA1/2.5, SBA1/5, and SBA1/10.

Compared to SBA1/5, in the preparation of SBA2/5-1/5, the concentration of P123 was doubled, and for SBA1/5-2/5, the concentration of TEOS is doubled.

### 3.1.3 Results and discussion

#### 3.1.3.1 Microscopy studies

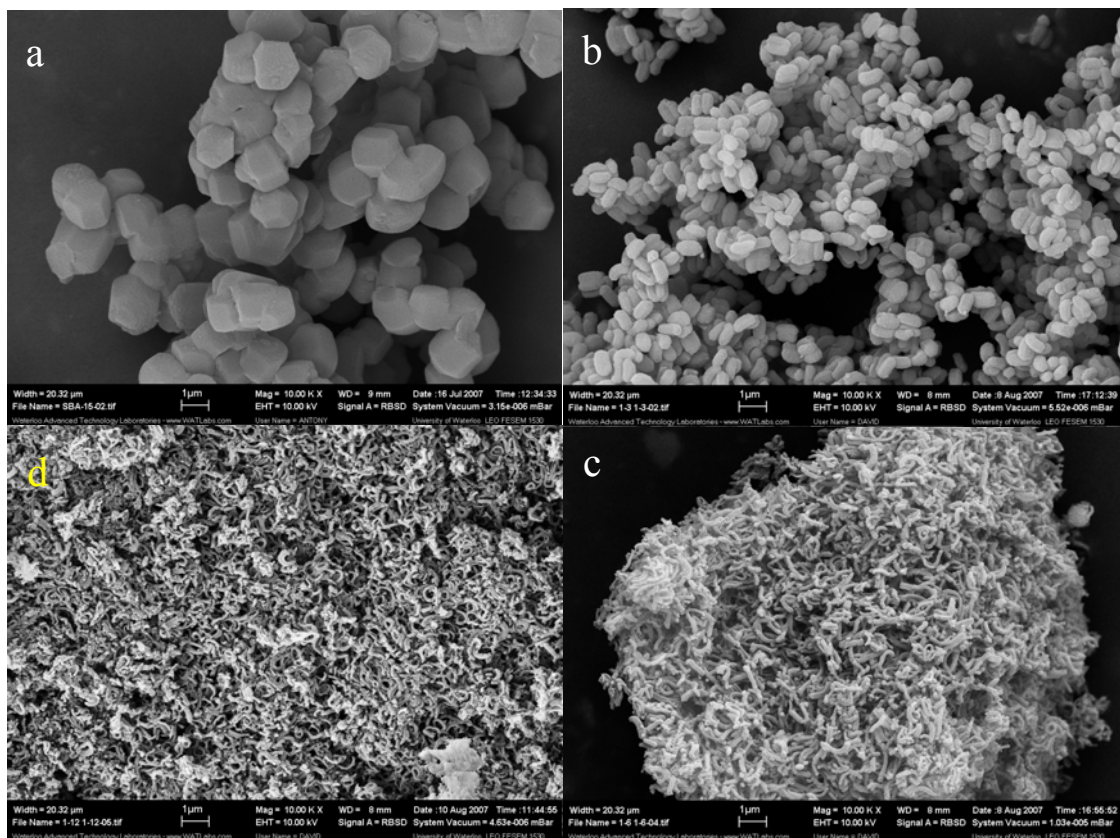


**Figure 3.1 SEM images of SBA-15 materials: a) SBA1/1; b) SBA2/5; c) SBA1/5; d) SBA1/10.**

The trend in declining particle size along the series from SBA1/1 to SBA1/10 is evident in the scanning electron microscopy (SEM) images shown in **Figure 3.1**. SBA1/5 and SBA1/10 exhibit the smallest particle size along with a similar morphology (**Figure 3.1c, d**). A survey of the entire sample of SBA1/5 revealed a remarkably homogeneous particle

size distribution that was confirmed by particle size analysis. The diameters of the rods of SBA1/5 and SBA-1/10 are less than 100 nm,  $\sim 1/15$  of SBA1/1 (**Figure 3.1a**). The length of the rods of SBA1/5 and SBA1/10 ranges from 300 nm to 600 nm.

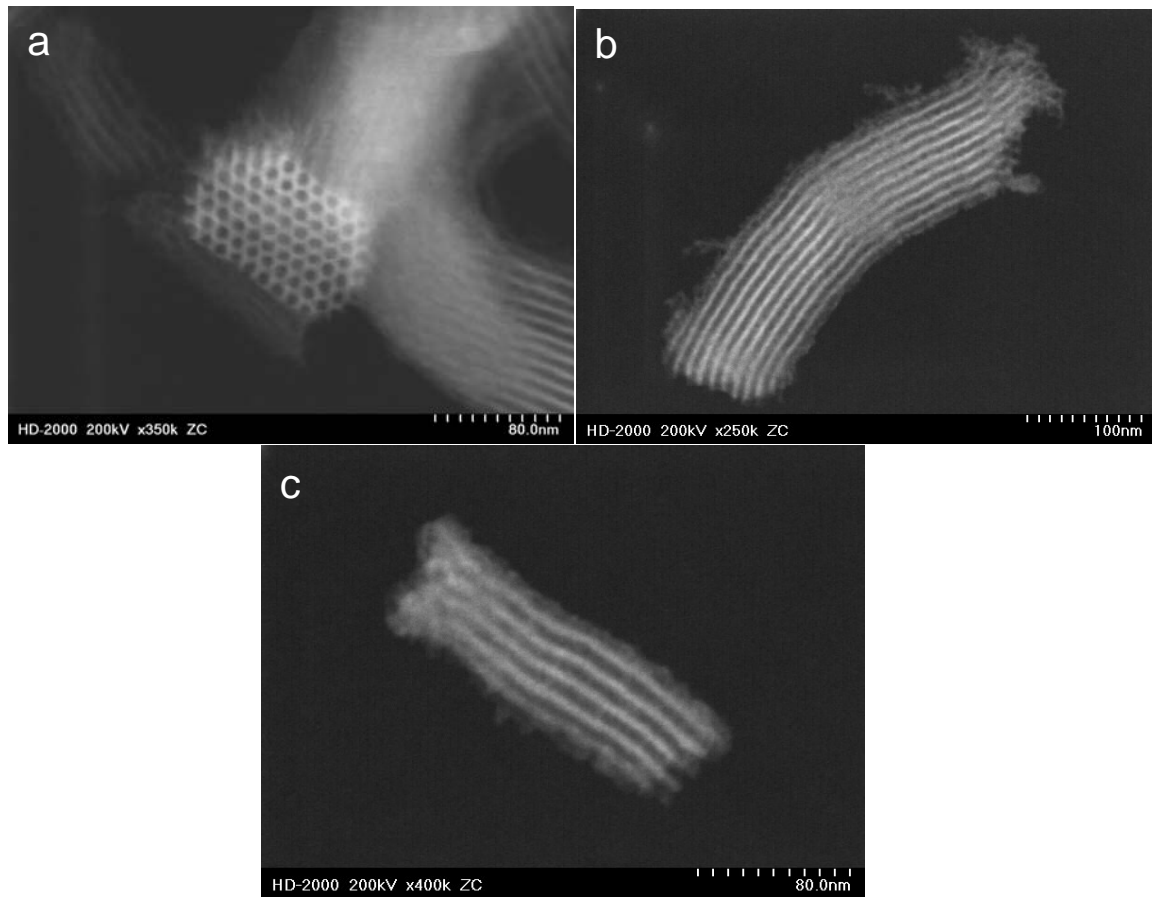


**Figure 3.2 TEM images of mesoporous SBA1/5 nanorods.**

SBA1/5 as a representative of this family of materials was studied under transmission electron microscopy (TEM). As shown in **Figure 3.2a, b**, nanorods of SBA1/5 span only  $\sim 10$  mesoporous silica channels in diameter. Some nanorods only span 3 or 4 channels in diameter, as shown in **Figure 3.2c**. The ordered channels are oriented along the longest axis

of the rods. Although the particle size is strictly controlled due to the minimized degree of the cooperative assembly, SBA1/5 still exhibits well maintained long range order.

### 3.1.3.2 Low angle XRD and surface area measurements

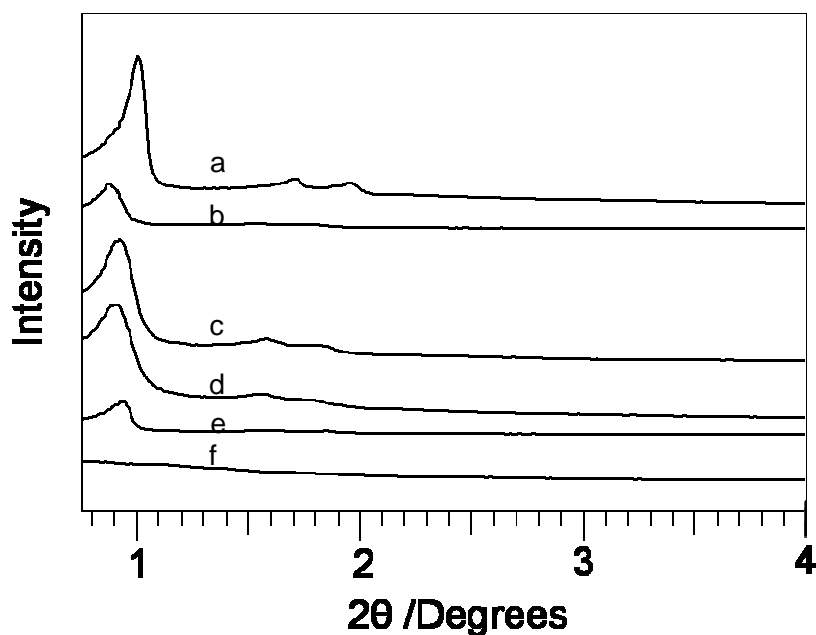


**Figure 3.3** XRD of SBA-15 materials: a) SBA1/1; b) SBA2/5; c) SBA1/5; d) SBA1/10; e) SBA1/5-2/5; f) SBA2/5-1/5.

The low angle powder X-ray diffraction (PXRD) patterns of SBA-15 materials are presented in **Figure 3.3**. All the diluted versions of SBA-15 exhibit slightly less resolved peaks than SBA1/1. Similar to nanoparticles with ordered crystalline lattices, smaller mesoporous particles with the long range order of nano-sized  $d$  spacing will also result in less well defined X-ray diffraction peaks since the effective coherence length is reduced [12]. Prepared with extremely low concentrations of P123 and TEOS, SBA1/10 still displays well maintained long range order, as shown by its XRD pattern (**Figure 3.3d**). This is in contrast

to previous reports that claimed when the concentration of copolymer is lower than 0.5 wt%, only amorphous silica is formed [2].

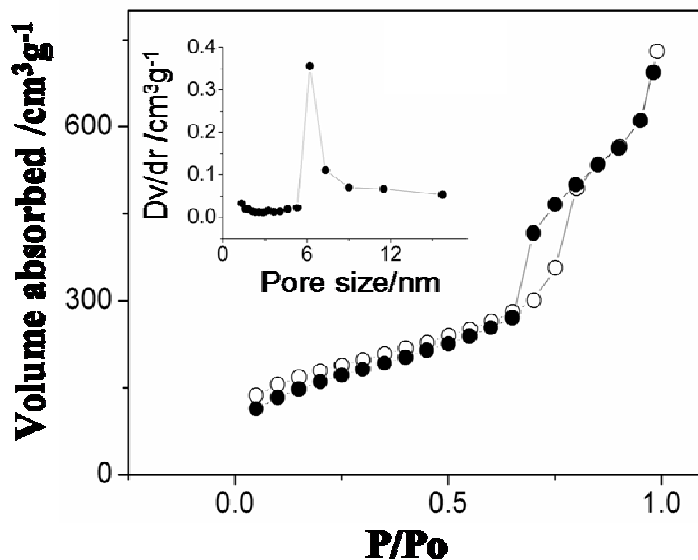


**Figure 3.4** N<sub>2</sub> adsorption-desorption isotherm of SBA1/5. The sample was degassed at 150 °C for over 12 hrs on a vacuum line. (Inset) Pore size distribution of SBA1/5.

**Table 3.1** Physical characteristics of ordered mesoporous silicate samples.

Samples	Dimensions ( $\mu\text{m}$ )	$S_{\text{BET}}$ ( $\text{m}^2 \text{g}^{-1}$ )	$V_p$ ( $\text{cm}^3 \text{g}^{-1}$ )	Pore sized (nm)	$d_{100}$ spacing (nm)	Wall thickness (nm)
SBA1/1	ca. 1.5×1.2	601	0.83	5.4	8.6	4.5
SBA2/5	ca. 0.8×0.5	769	1.06	6.3	10.2	5.4
SBA1/5	ca. 0.5×0.1	619	1.13	6.2	10.5	5.9
SBA1/10	ca. 0.5×0.08	479	0.73	6.5	10.8	6.0
Calcined SBA1/5 at 900°C	ca. 0.5×0.1	217	0.39	4.3	9.6	6.7
Calcined SBA1/1 at 900°C	ca. 1.5×1.2	35	0.15	N/A	N/A	N/A

Nitrogen adsorption and desorption isotherms were performed for surfactant free samples, and a typical type IV curve is shown in **Figure 3.4** for SBA1/5. The pore size was determined from the desorption branch, and the resultant physical characteristics of the samples are presented in **Table 3.1**. The pore dimensions of all of the series (5.4 – 6.2 nm) are typical of SBA-15 [2]. However, compared with SBA1/1, all SBA2/5, SBA1/5 and SBA1/10 have a larger d-spacing and pore size, and thicker walls (size difference between d-spacing and pore size), the latter being presumably a result of the slower rate process during nucleation. It can be noted that the calculated wall thickness of SBA1/5 is consistent with estimation from the TEM images. As a consequence, SBA1/5 exhibited better thermal stability compared to SBA1/1. After calcination at 900 °C for 2 hours, SBA1/5 still maintained appreciable surface area, pore volume and long range order. In contrast, SBA1/1 suffered pore collapse. The characteristics of the high temperature calcined samples are shown in **Table 3.1**.

### 3.1.3.3 Formation mechanisms

The slower rate of nucleation and growth in dilute solutions has a strong effect on the physical characteristics of the materials. The key to control the particle size of mesoporous silicates is to minimize the chances of collision of the nano-domains formed at an early stage of cooperative assembly/condensation. **Figure 3.5** depicts the difference between conventional case and a highly dilute case in terms of the degree of particle growth. In a highly dilute reaction condition, the newly formed wormlike nano-domains are kinetically inhibited from forming larger agglomerates. This is evident in **Figure 3.6**, where only a few

particles are partially connected end to end (inset  $\alpha$ ) and side to side (inset  $\beta$ ), indicating that the

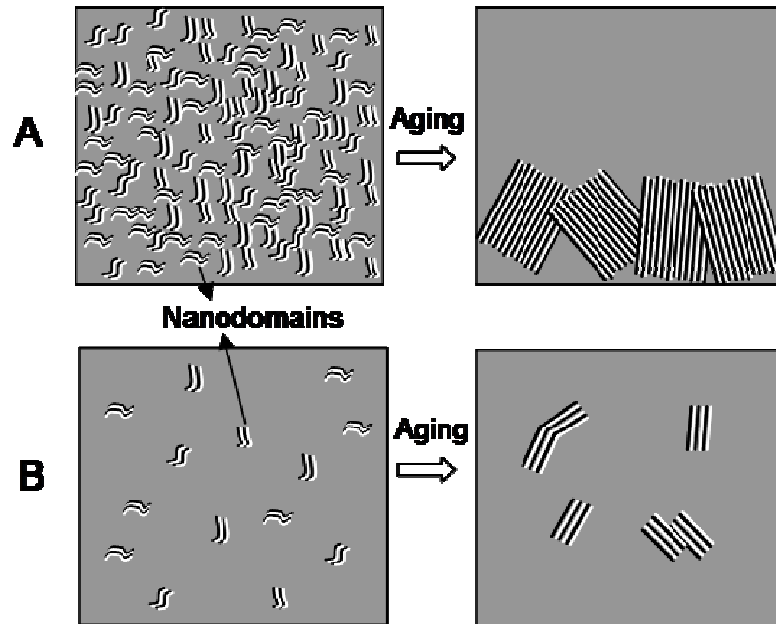


**Figure 3.5** Schematic diagrams depicting the influence of dilution of reaction solution on particle growth. A) conventional synthesis; B) highly dilute case.

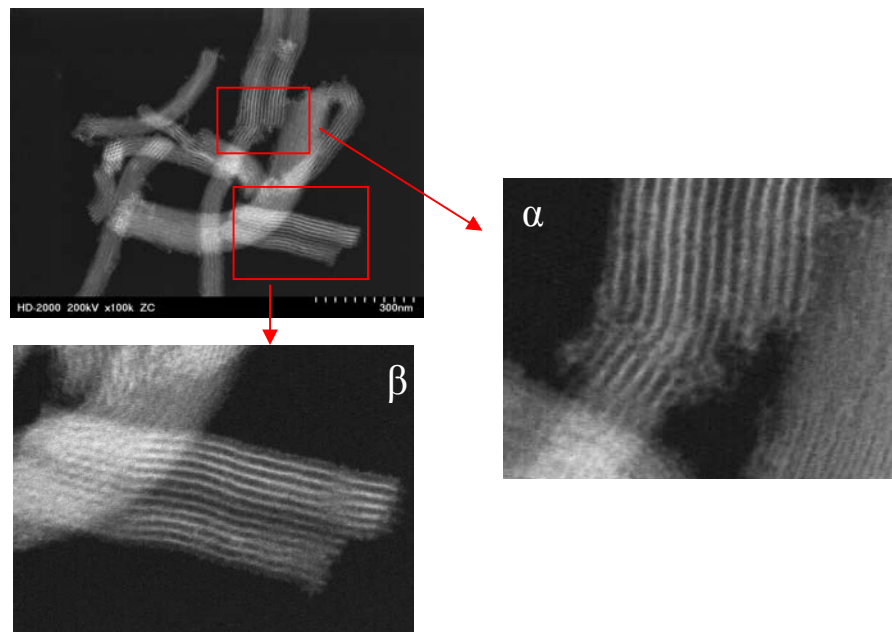


**Figure 3.6** TEM image of SBA1/5 with two inset parts magnified.

merging of these nanorods is not complete even under hydrothermal conditions owing to the slower rate of nucleation and growth. The very small particle size gives rise to formation of a stable, completely non-settling milky suspension  $\frac{1}{2}$  hr after the TEOS was added, necessitating material recovery by centrifugation. Under conventional conditions, the nano-domains are closely distributed and rapidly agglomerate into large particles owing to driving forces that minimize surface free energy. In accord, for SBA1/1 and SBA2/5, the cloudy suspension appeared in half the time after the addition of TEOS, followed by rapid precipitation.

#### 3.1.3.4 Influence of P123/ TEOS ratio on morphology

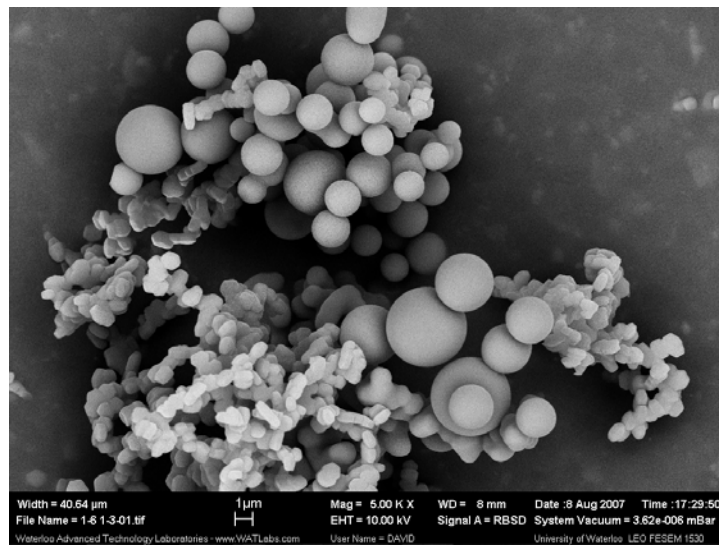


**Figure 3.7 SEM image of SBA1/5-2/5.**

The ratio between P123 and TEOS was halved and doubled in the preparation of SBA1/5-2/5 and SBA2/5-1/5, respectively. As shown in **Figure 3.7**, SBA1/5-2/5 is composed of two different silica phases: the often observed rod-like particles and the spheres.

This sphere morphology resembles Stöber silica spheres which are formed directly from soluble silicates without the presence of any surfactant at basic conditions [13,14]. In the synthesis of SBA1/5-2/5, TEOS is present in excess compared to P123 surfactant. Therefore, the spare TEOS self-condensed into large “Stöber silica spheres”. On the other hand, in the preparation of SBA2/5-1/5, P123 is present in excess compared to TEOS. Without enough TEOS as feed stock, a stable cooperative assembly/condensation could not be formed, as shown by its XRD pattern with no long range order features (**Figure 3.3f**). Our results here indicate that the surfactant/precursor ratio is a vital factor for the cooperative assembly.

### **3.2 CMK-3 nanorods**

Ordered mesoporous carbons (OMC) are quite useful in adsorption, catalysis, energy storage, and other practical applications, as introduced in **section 1.4.2.2**. Fabrication of desirable morphologies is important as well as the control in composition, porosity, and structure. The morphology control of OMC highly depends on the development of their silica templates, defined by the nature of the nanocasting method. Herein, by employing SBA1/5 as a hard template, CMK-3 nanorods (referred as nano-CMK-3) were prepared and characterized.

#### **3.2.1 Experimental**

Firstly, 1.25 g of sucrose was dissolved in 5.0 ml aqueous solution containing 0.14 g of H<sub>2</sub>SO<sub>4</sub>. Next, 1.0 g of surfactant free SBA1/5 was dispersed into the above solution and the mixture was sonicated for 1 hr. Then, it was heated at 100°C for 12 hrs and 160°C for another 12 hrs. The above impregnation process was repeated once with another 5.0 ml

aqueous solution containing 0.8 g sucrose and 0.09 g H<sub>2</sub>SO<sub>4</sub>. The composite was completely carbonized at 900°C for 5 hrs in argon atmosphere. To remove the SBA1/5 template, the composite was stirred in a 5% HF solution at room temperature for 4 hrs. Nano-CMK-3 was obtained after filtration.

### 3.2.2 Results and discussion

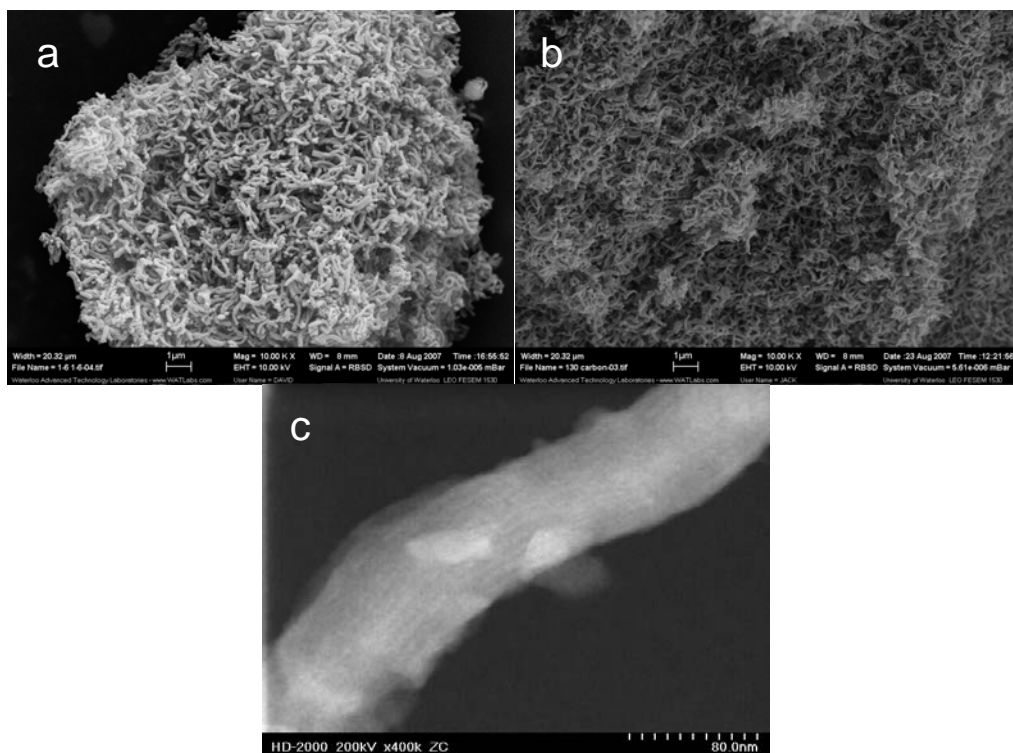


Figure 3.8 SEM images of a) SBA1/5; b) nano-CMK-3; c) TEM image of nano-CMK-3.

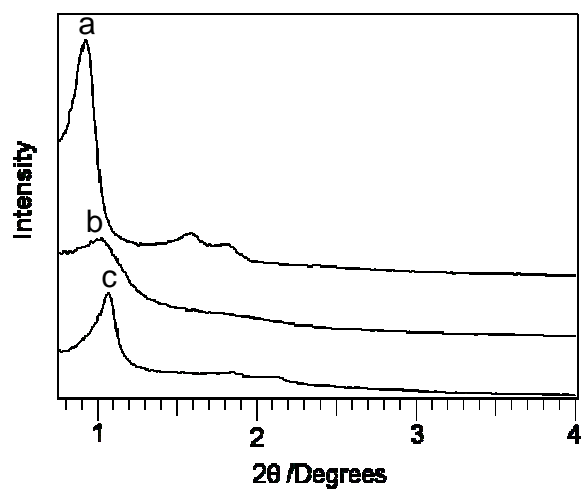


Figure 3.9 Low angle XRD patterns of a) SBA1/5; b) Nano-CMK-3; c) CMK-3.

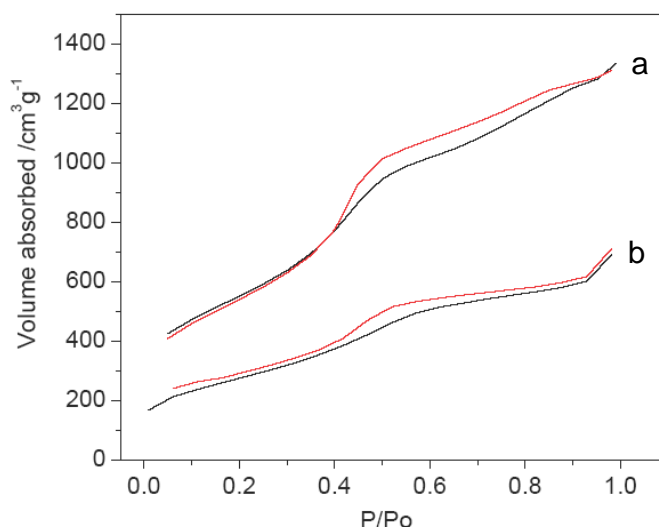


Figure 3.10 N<sub>2</sub> adsorption-desorption isotherms of a) CMK-3; b) nano-CMK-3.

Table 3.2 Physical characteristics of mesoporous carbon samples.

Samples	Dimensions (μm)	S <sub>BET</sub> (m <sup>2</sup> g <sup>-1</sup> )	V <sub>p</sub> (cm <sup>3</sup> g <sup>-1</sup> )	Pore size (nm)
CMK-3	ca. 1.3×1.0	1976	2.06	3.3
Nano-CMK-3	ca. 0.5×0.1	1014	0.89	3.5

As shown in **Figure 3.8a, b**, the nano-rod morphology is retained in nano-CMK-3. TEM studies reveal that nano-CMK-3 still maintains an ordered structure (**Figure 3.8c**), confirmed by its low angle XRD pattern (**Figure 3.9b**). Nano-CMK-3 exhibits much less intense XRD peaks than its bulk counterpart, which probably due to the much smaller coherence length (**Figure 3.9a, b**). **Figure 3.10** shows the N<sub>2</sub> adsorption and desorption isotherms of CMK-3 and nano-CMK-3. In contrast to CMK-3, with little hysteresis loop, the isotherm exhibited by nano-CMK-3 is not a typical type IV curve for mesoporous solids. Namely, in the carbon nano-scaffolds, the adsorption and desorption almost reversibly take place at the same pressure, which has been rarely observed for other mesoporous materials. This is most likely due to the small particle size and the open structure. The physical data of nano-CMK-3 and CMK-3 are listed in **Table 2**. The surface area and specific pore volume of nano-CMK-3 are much less than CMK-3. As known, SBA1/5 exhibits larger pore volume and larger pore size than SBA1/1; therefore, it's normal that the comparison of their replicas is opposite. The pore size of nano-CMK-3 exceeds CMK-3 by 0.2 nm, as a result of thicker walls of SBA1/5 compared to SBA1/1. With small particle size and a built-in nanostructure, nano-CMK-3 may provide better kinetics properties and find potential applications in Li (ion) batteries, fuel cells, or adsorption.

### **3.3 Conclusions**

Mesoporous silica with novel nano-rod morphology has been prepared and characterized. This is the first example of such a confined organization of silica channels, whose formation under the controlled conditions supports previously proposed mechanisms of growth and nucleation. This dilution strategy potentially can be applied to other syntheses

of mesostructured materials by employing amphiphilic molecules and/or copolymers as structure directing agents. By employing SBA1/5 as a hard template, mesoporous carbon CMK-3 nanorods have been prepared and characterized as well.

## Chapter 4

### Carbon/MoO<sub>2</sub> Composite Based on Graphitic Mesoporous Carbon Prepared from In Situ Carbonization of Tri-Block Copolymers

#### 4.1 Introduction

Mesoporous carbon materials with high surface area and ordered porous structures have rapidly attracted growing attention for their potential applications in catalysis, hydrogen storage, and electrodes of electrochemical devices. Following the report of Ryoo *et al.* of CMK-1 in 1999 [1], a series of mesoporous carbon materials have been synthesized as the inverse replicas of mesoporous silicates. Typically, carbon precursors impregnated within the hollow cavity of mesoporous silicates serve as the sources for carbon replica mesostructures formed after removal of silica scaffolds [2,3]. However, the framework of the carbon replica materials prepared by the above method is inevitably amorphous (of no short range order), which limits their applications in electrochemistry due to their relatively low electrical conductivity. Developing graphitic mesoporous carbons with higher conductivity is one of the major challenges in this field. In general, high-temperature routes are the conventional way to obtain highly graphitized carbon materials, but such heat treatment inevitably leads to very poorly ordered mesoporous structures [4]. Employing graphitizable carbon precursors and using catalyzed syntheses at low temperatures are two alternatives to high-temperature methods. Some initial work along these lines has very recently appeared [5,6,7,8]. The methods in the literature have the important limitation of needing to post-impregnate the silica with carbon precursors, thus adding an additional and intensive process step. Very recently, and simultaneous with ongoing work in our laboratory, Hyeon *et al.* reported that

the polymer structure directing agents used for silica formation can be utilized to synthesize amorphous carbon mesostructures [9].

Here, I present a convenient in situ synthetic route to obtain graphitized mesoporous carbon directly from the copolymer surfactant P123 (EO<sub>20</sub>PPO<sub>70</sub>EO<sub>20</sub>), by employing transition metals as catalysts. As P123 polymer is the structure directing agent for SBA-15, it need not be removed from the silica pores once the replica is formed. Furthermore, its transformation to a graphitic phase is initiated by an impregnated catalyst. This graphitic carbon material is referred as DGMC (directly from a surfactant to graphitic mesoporous carbon). Mesoporous carbon with an amorphous framework directly synthesized in situ from P123 without a catalyst is referred to as DMC. The transition metals (Fe, Co, Ni) were utilized as a catalyst in a 7% H<sub>2</sub>/N<sub>2</sub> mixture atmosphere [10]. A feature of highly ordered graphitized porous carbon is that it can serve as a conductive scaffold to encapsulate other materials. This leads to design of structured composites where both components play a role in controlling the characteristics. Only a handful of such carbon-based composite negative materials have been reported including carbon coated silicon nanoparticles [11] and an amorphous carbon/tin/cobalt composite utilized by Sony in their new Nexelion cell. However, these have a very different microstructure than the composites reported here based on a core-shell design. A seminal report on tin-filled mesoporous carbon as a negative electrode was given recently, but their carbon framework was electrochemically inactive, perhaps as a result of its nongraphitized nature [12]. DGMC is chosen as a framework to host nanowires of a metallic metal oxide. Along with the interesting properties that such confined systems may exhibit, low valent metal oxides such as CoO, Co<sub>3</sub>O<sub>4</sub>, CuO, and MoO<sub>3-δ</sub> have been

shown to be promising negative electrode materials in lithium-ion batteries. These electrodes uptake lithium ions (and electrons) by “conversion reactions” that lead to materials consisting of nanometer-scale metallic clusters dispersed in an amorphous  $\text{Li}_2\text{O}$  matrix. The reverse reaction reforms the metal oxide and lithium. Very high capacities are achievable, although an unacceptably high degree of hysteresis is usually seen between oxidation and reduction. A key issue is to restrict crystallite size to nanodimensions to ensure a high degree of reversibility of the reaction. With 20 nm hematite particles, for example, reversible insertion of 0.6 Li per  $\text{Fe}_2\text{O}_3$  is possible, whereas large hematite particles (1 to 2  $\mu\text{m}$ ) undergo an irreversible phase transformation on reaction of only  $\sim 0.05$  Li. Equally important is inhibiting growth and agglomeration of the metal nanoparticles that are extruded and also ensuring electronic and ionic access of the electrode material. Since graphitic carbon itself is an excellent negative electrode, the carbon framework can be used as both an active lithium insertion host and as a restrictive containment system for a complementary negative electrode material,  $\text{MoO}_2$ . This pure metallic oxide shows good capacity for lithium uptake but poor reversibility on cycling [13]. Conversely, the electrochemical properties of the composite material described herein show very good cycling stability. This mesostructured carbon/metallic oxide composite, the first to be reported, takes advantage of the Li uptake properties of both composite components. The graphitic carbon framework serves to constrain the dimensions of the oxide and sustain reversibility of the Li uptake. The  $\text{MoO}_2$  adds gravimetric and volumetric capacity to that of the active carbon, and its metallic properties enhance the conductivity. The resultant composite displays promising electrochemical properties including a stable reversible gravimetric capacity of 760  $\text{mA}\cdot\text{h/g}$ .

## 4.2 Experimental

### 4.2.1 Synthesis of SBA-15, DGMC and DMC

SBA-15 with rod-like morphology was synthesized following a well established method in a literature [14]. Briefly, 2 g of Pluronic P123 was completely dissolved in 60 ml of 2 M HCl solution at 38 °C. TEOS, the silicate precursor, 4.2 g was added into the above solution under vigorous stirring. The mixture was stirred for 8 min and remained quiescent for 24 hrs at 38 °C. It was subsequently hydrothermally heated at 100 °C for another 24 hrs in an autoclave. The as-synthesized SBA-15 was collected by centrifugation, dried.

As-prepared SBA-15 (1.0 g) was dispersed into 5 mL of an aqueous solution containing 0.08 g of H<sub>2</sub>SO<sub>4</sub>, and the mixture was heated at 100 °C for 12 hrs and 160 °C for another 12 hrs. The composite was partially carbonized at 550 °C for 6 hrs in N<sub>2</sub>. The carbonized nanocomposite was then placed into 8 mL of an aqueous solution of a catalyst precursor based on FeSO<sub>4</sub>, CoCl<sub>2</sub>, or NiSO<sub>4</sub> (carbon/metal salt = 100:1.5 by molar ratio). The mixture was stirred for 3 hrs and heated at 100 °C for 12 hrs, prior to graphitization which was carried out at 900 °C in a 7% H<sub>2</sub>/N<sub>2</sub> mixture atmosphere for 6 hrs. To remove the silica in the composite, the sample was stirred in a 10% HF solution. The graphitized mesoporous carbon replica DGMC was obtained by centrifugation and then dried.

After dehydration by sulfuric acid, the silica/copolymer nanocomposite was completely carbonized at 900 °C in argon for 6 hrs. The product, DMC, was obtained by dissolution of the silica with a 10% HF solution.

#### 4.2.2 Synthesis of composite DGMC/MoO<sub>2</sub>

MoO<sub>3</sub> 0.288 g was completely dissolved in 1.5 mL of concentrated ammonium hydroxide solution, and 0.144 g of DGMC (0.012 mol) was added to this transparent solution (C/Mo molar ratio of 6:1). The mixture was sonicated for 1 hr until a fine slurry of DGMC/(NH<sub>4</sub>)<sub>2</sub>MoO<sub>4</sub> was obtained. The slurry was heated at 80 °C for 12 hrs and then under an atmosphere of 7% H<sub>2</sub>/N<sub>2</sub> mixture at 400 °C for 5 hrs to obtain the composite material DGMC/MoO<sub>2</sub>. The percentage (weight) of MoO<sub>2</sub> determined by thermogravimetric analysis (TGA) is 63.7%.

#### 4.2.3 Electrochemistry and conductivity measurements

A slurry containing 90 wt% composite [DGMC/MoO<sub>2</sub> (weight) = 36.3/63.7] and 10 wt% poly(vinylidene fluoride) (PVDF) in cyclopentanone was spread onto a carbon coated copper foil and dried under vacuum overnight at 80 °C prior to punching the electrodes from the current collector. Typical loading of the active mass was between 3 and 6 mg/cm<sup>2</sup>. Electrolyte is composed of a 1 M LiPF<sub>6</sub> solution in 1:1 ethylene carbonate (EC)/dimethyl carbonate (DMC). Lithium metal is employed as the counter electrode.

Conductivity measurements were performed at room-temperature using the four-point method. Sample bars for measurements were cut from the pellets and then cold pressed using a force of 5 kN.

## 4.3 Results and discussion

### 4.3.1 DGMC

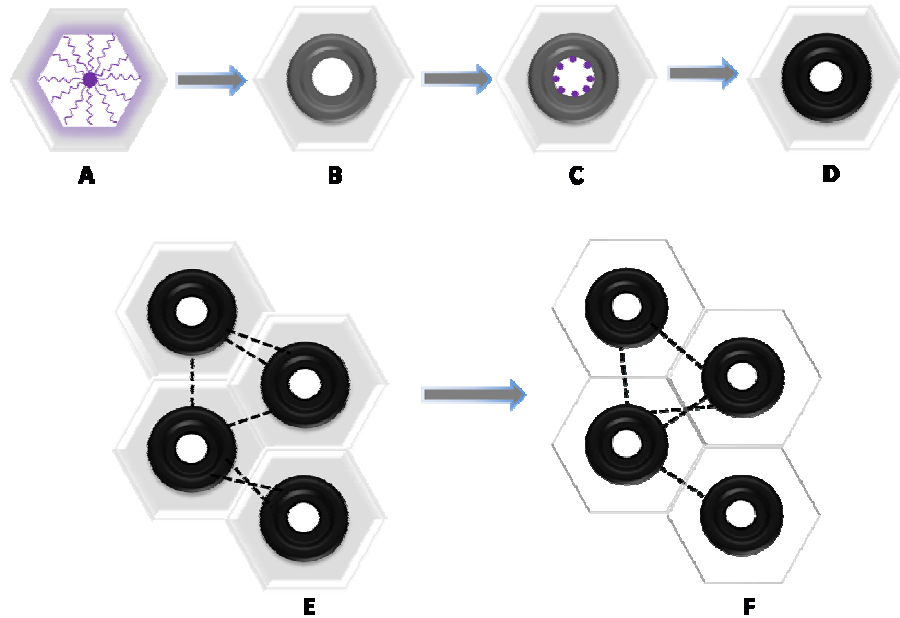


**Figure 4.1** Schematic diagram showing the synthesis of DGMC materials: A) as-synthesized SBA-15; B) partially carbonized as-synthesized SBA-15; C) after catalyst loading; D) after graphitization and complete carbonization; E) removal of the silica by HF etching showing the carbon fibers that connect the carbon nanorods as dash lines; F) graphitized carbon nanorod replica.

#### 4.3.1.1 About the synthetic strategy

**Figure 4.1** shows a schematic diagram outlining the synthesis route employed to create the porous partially graphitized carbon nanorods (DGMCs). SBA-15 with a tubular morphology (rods 1–2  $\mu\text{m}$  long) served as the template for the DGMC materials. The structure-directing tri-block copolymer P123, cross-linked in the channels of as-synthesized SBA-15, was dehydrated with sulfuric acid and partially carbonized at 550  $^{\circ}\text{C}$  in  $\text{N}_2$  for 6 hrs. The channels of the SBA-15 become partially hollow and coated with hydrophilic amorphous

carbon [15]. A transition metal  $M^{II}$  salt ( $M = Ni, Fe, \text{ or } Co$ ) was then impregnated into the carbon-coated channels and reduced to its metallic state in a  $H_2/N_2$  atmosphere. These nanoparticles are responsible for catalyzing the graphitization that was activated by a second heat treatment at  $900\text{ }^\circ C$  (**Figure 4.1A-D**). Because the density of the carbon produced is higher than that of the starting surfactant, the carbon rods have a tubular structure (**Figure 4.1C, D**). The silica scaffold is then removed from the structure by dissolution with HF, to yield the partially graphitized carbon replica.

#### 4.3.1.2 Characterizations of DGMC

##### 4.3.1.2.1 Ordered structure

The highly ordered structure of the resultant mesostructured carbon materials Ni-DGMC and Co-DGMC displays well-resolved XRD patterns shown in **Figure 4.2a, b**. The reflections are assigned to (100), (110), and (200) reflections of the two-dimensional hexagonal space group ( $P6mm$ ), similar to the case of SBA-15. No silica residue could be detected by EDX mapping after etching by HF, indicating the long range order is exclusively from the mesoporous carbon replica. There is only a single broad peak in the low angle XRD pattern of the Fe-DGMC sample, which shows that a structure with limited mesostructured order was generated after catalysis with iron nanoparticles (**Figure 4.2c**). The carbon materials obtained are not a collection of carbon fibers but bundles of nanoporous carbon rods with a cylindrical hole that runs down their length, whose formation is illustrated in the bottom half of **Figure 4.1**. Evidence will be provided for this in the following discussion.

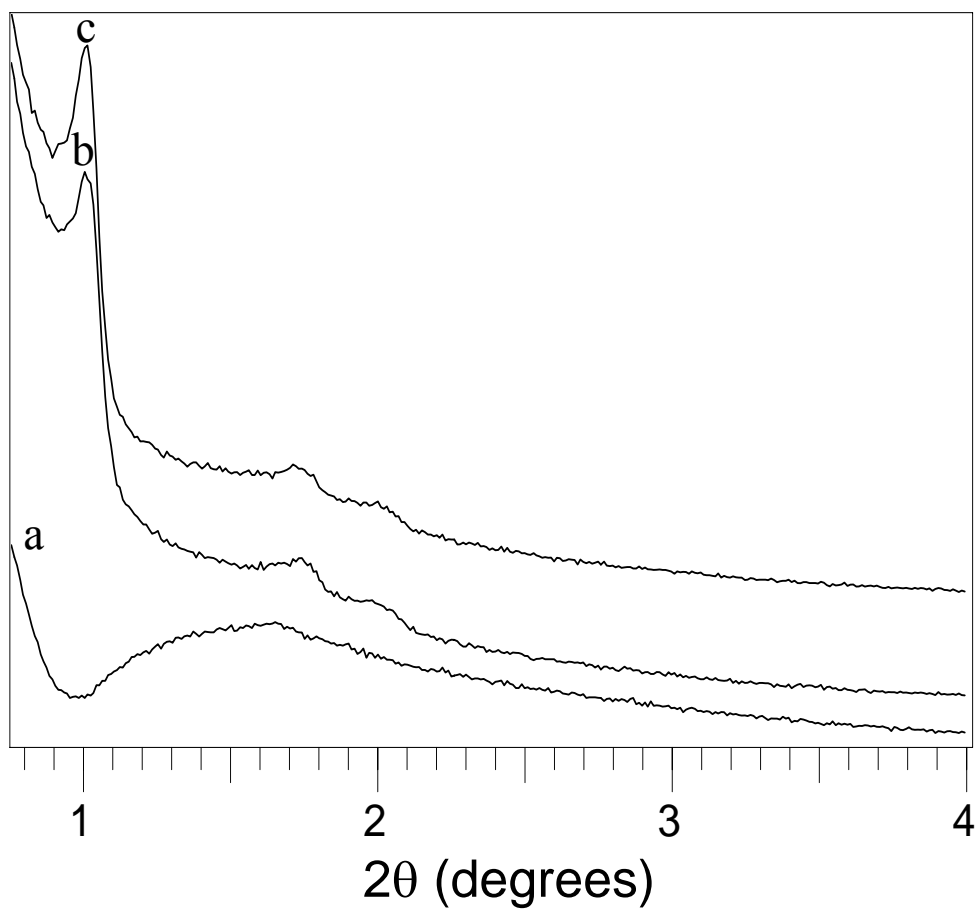


**Figure 4.2** Small angle XRD patterns of graphitic nanoporous carbon materials a) Fe-DGMC; b) Co-DGMC; c) Ni-DGMC.

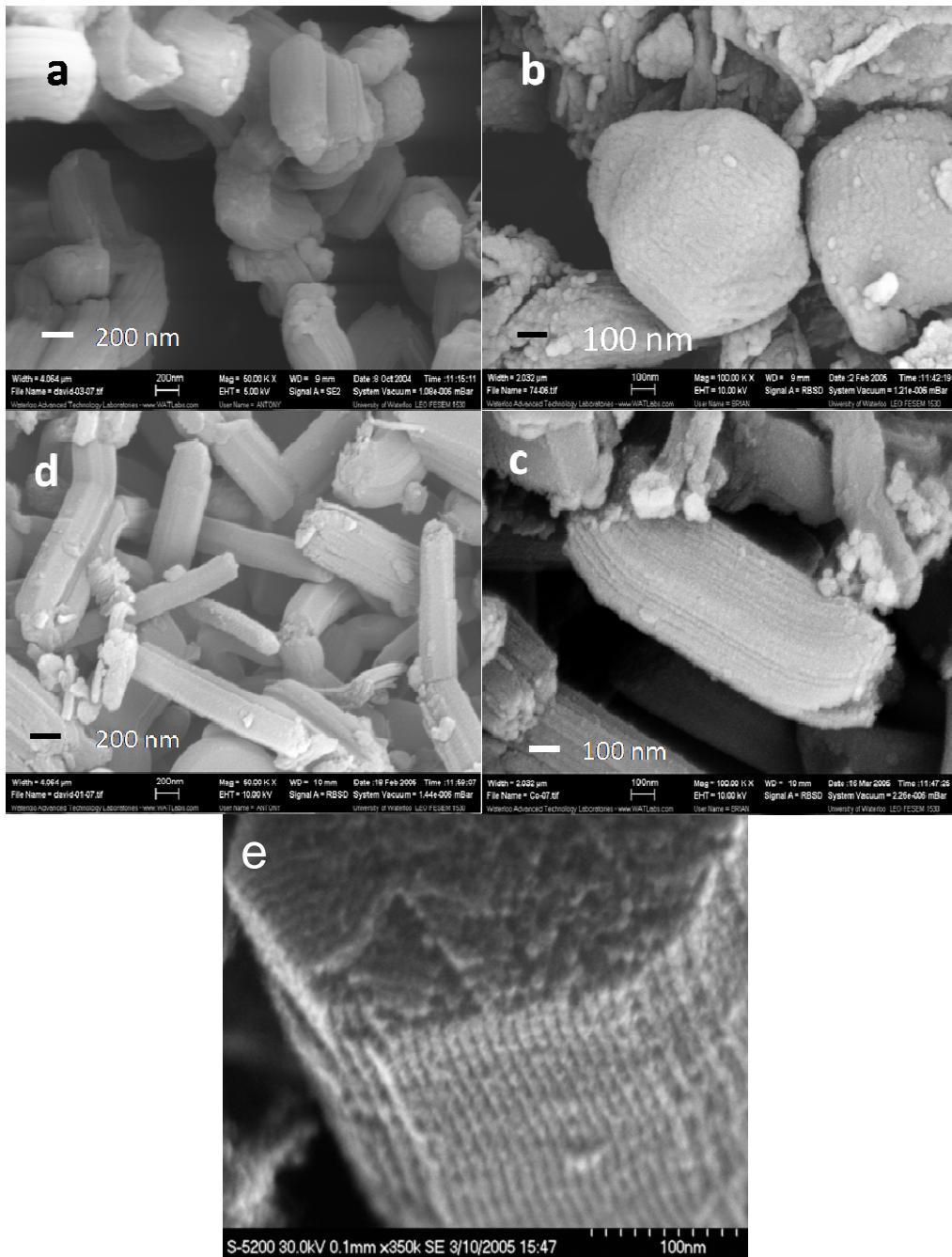


**Figure 4.3 SEM images of a) DMC; b) Fe-DGMC; c) Co-DGMC; d, e) Ni-DGMC.**

SEM was employed to investigate the morphology and structure of the DGMC materials obtained. The SEM image of DMC (**Figure 4.3a**) revealed a rod-like morphology, as did the Co-DGMC and Ni-DGMC materials (**Figure 4.3c, d**). This was in contrast to Fe-DGMC, which has an irregular spherical morphology (**Figure 4.3b**) and which also displayed the lowest degree of order in the low angle XRD pattern (**Figure 4.2a**). A very small fraction of nanoparticles were also apparent on the surface (**Figure 4.3b-d**), identified as pure carbon by EDX. They arise from cross-linked polymer, either partially graphitized or amorphous, formed external to the SBA-15 framework. These did not form in DMC itself, which indicates that they are probably produced by catalysis via a minor amount of metal nanoparticles distributed on the surface of the silica-carbon rods. As Ni-DGMC, Co-DGMC, and DMC are all synthesized from the same SBA-15 starting material with the same morphology, the catalyst must control the nature of the final graphitic mesostructure to some degree. For Ni-DGMC and Co-DGMC, it is believed that the one-dimensional growth of carbon nanofibers occurs in the channels of SBA-15. This explains why the rods of Ni-DGMC and Co-DGMC are much thinner compared with the amorphous mesoporous carbon DMC rods (**Figure 4.3a**). It can be assumed that three dimensional nucleation and growth processes occur in Fe-DGMC, however, resulting in a lack of well-ordered carbon rod bundles in the SEM image of Fe-DGMC (**Figure 4.3b**). The different catalysis mechanisms are related to the different properties of metal catalyst particle surfaces and the intrinsic properties of the metal itself. It is well-known that the orientation of graphite layers of catalytically produced graphite nanofibers (GNFs) can be controlled by the choice of catalyst [16].

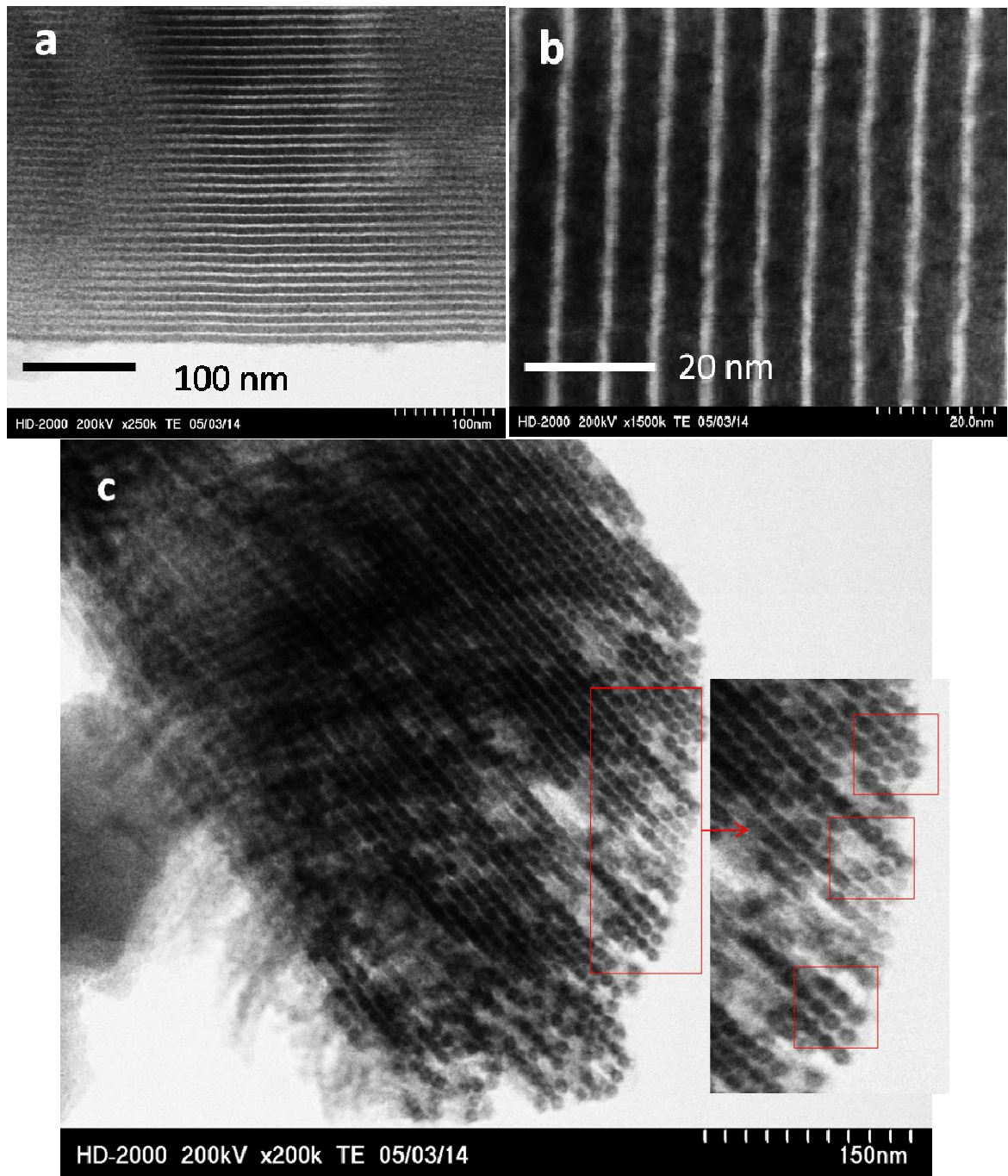


**Figure 4.4** TEM images of Ni-DGMC a, b) (001) plane; c) (110) plane. The tubular structure of the rods is indicated by the outlined red squares (inset) in part c.

TEM images of Ni-DGMC along two different zone axes, [110] and [001] (**Figure 4.4a–c**), clearly show the highly ordered hexagonal mesostructure of the carbon replica, in good agreement with the low angle XRD results. The hollow structure of the rods (i.e., “tubes”) can be faintly seen at the edges of the high-resolution image (**Figure 4.3c**, indicated by red outlines). The empty channels between adjacent nanoporous tubes are formed by extraction of the SBA-15 silica framework, which has an estimated wall thickness of 3 nm (**Figure 4.3a, b**).

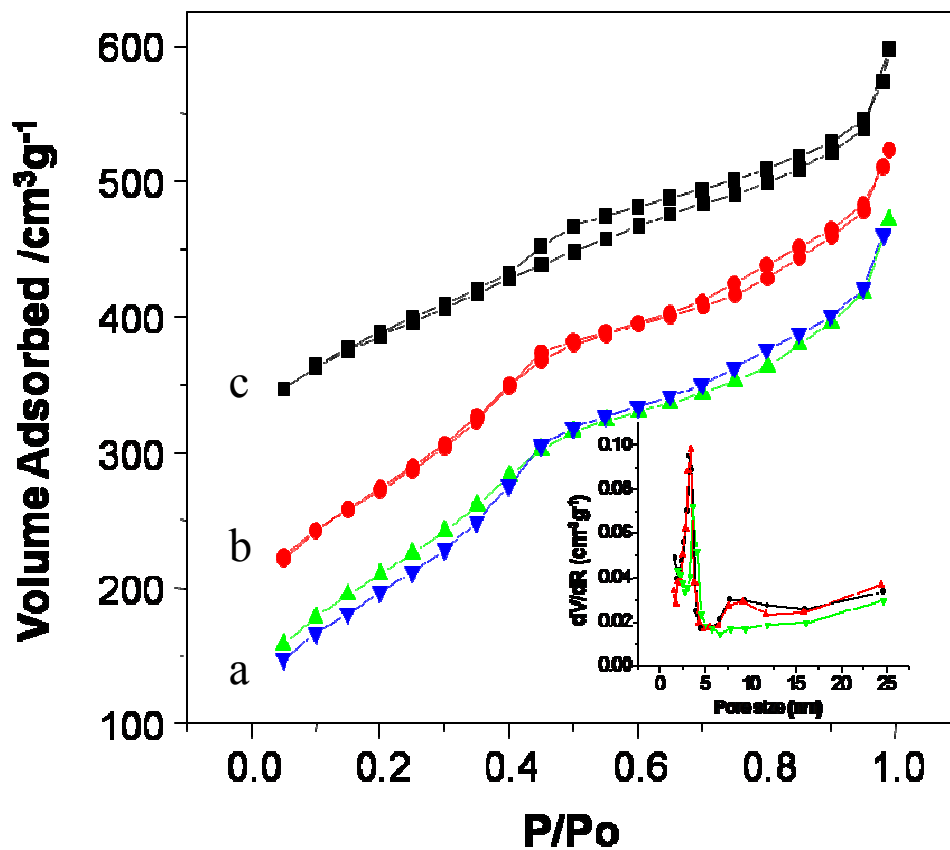


**Figure 4.5** N<sub>2</sub> adsorption-desorption isotherm for a) Co-DGMC; b) Ni-DGMC shifted up by 50 for clarity; and c) Fe-DGMC shifted up by 200 for clarity. (Inset) PSDs: red, Co-DGMC; black, Ni-DGMC; green, Fe- DGMC.

**Table 4.1 Characteristics of nanoporous carbons.**

Samples	$S_{\text{BET}}$ ( $\text{m}^2\text{g}^{-1}$ )	Micropore surface area ( $\text{m}^2\text{g}^{-1}$ )	$V_p$ ( $\text{cm}^3\text{g}^{-1}$ )	Pore size (nm)	d(002) (angstrom)	Electrical conductivity ( $\text{Scm}^{-1}$ )
SBA-15(calcined)	600	72	0.83	7.5	N./A.	N./A.
DMC	1800	260	2.1	3.44	4.05	0.003
Fe-DGMC	642	132	0.62	3.65	3.56	1.12
Ni-DGMC	799	69	0.73	3.23, 7.2	3.62	1.08
Co-DGMC	756	41	0.73	3.41, 7.2	3.62	1.63

BET measurements were carried out on all of the materials. **Figure 4.5** depicts the  $\text{N}_2$  sorption isotherms of the DGMC materials, and **Table 4.1** summarizes the physical characteristics. All the isotherms show hysteresis at high relative pressures up to  $0.95 P/P_0$ , which is not observed in CMK-3 synthesized by completely filling the channels. The capillary condensation of  $\text{N}_2$  molecules at high relative pressures indicates the existence of another pore system with smaller size and/or structural defects in the carbon walls [17]. The surface areas and pore volumes of DGMC are almost half of their amorphous counterpart, whereas the pore sizes are about the same. The lower surface area of DGMC affirms a well stacked partially graphitized structure which has a higher density than the amorphous carbon materials. The graphitized structure will not support the large fraction of micropores that contribute to high surface areas in amorphous carbon. Fe-DGMC exhibits a high ratio of

micropore surface area to the total surface area, indicating the largest amount of structural defects. The primary pore size distribution is bimodal (pore sizes: 3.4 and 7 nm) for the Ni and Co catalyzed DGMCs but is essentially unimodal for the Fe catalyzed sample. It is obvious that the majority of the pore volume with a pore dimension of 3.4 nm is generated from the removal of the silica that forms the original SBA-15 templated structure. These correspond to the channels evident in the TEM image of Ni-DGMC, for example (**Figure 4.4a, b**). Pores with a larger diameter are often observed in mesoporous carbon when the carbon filling is not completed by the nanocasting method. The channels are undoubtedly randomly cross-linked with carbon induced by nucleation and growth (**Figure 4.1D, E**), as proposed for other mesostructured carbons formed by replica template growth [18]. Such cross-linking would form an ill-defined porous carbon net that is responsible for preventing collapse of the carbon nanowires to a close-packed bundle.

#### 4.3.1.2.2 Graphitic structure

The wide-angle XRD patterns of all of the DGMC materials (**Figure 4.6b-d**) exhibit two intense peaks which can be indexed as the (002) and (10) reflections, characteristic of graphitic carbon. The reflections for the DMC carbon are less intense and well defined (**Figure 4.6a**), in accord with its much lesser graphitized content. The *d*-spacing of the (002) peak, 0.35 nm, is a little larger than that for graphitized carbon treated at 2800 °C, indicating that the degree of graphitization is very limited [19]. The XRD peaks are also not nearly as sharp as graphitic carbon obtained at high temperatures.

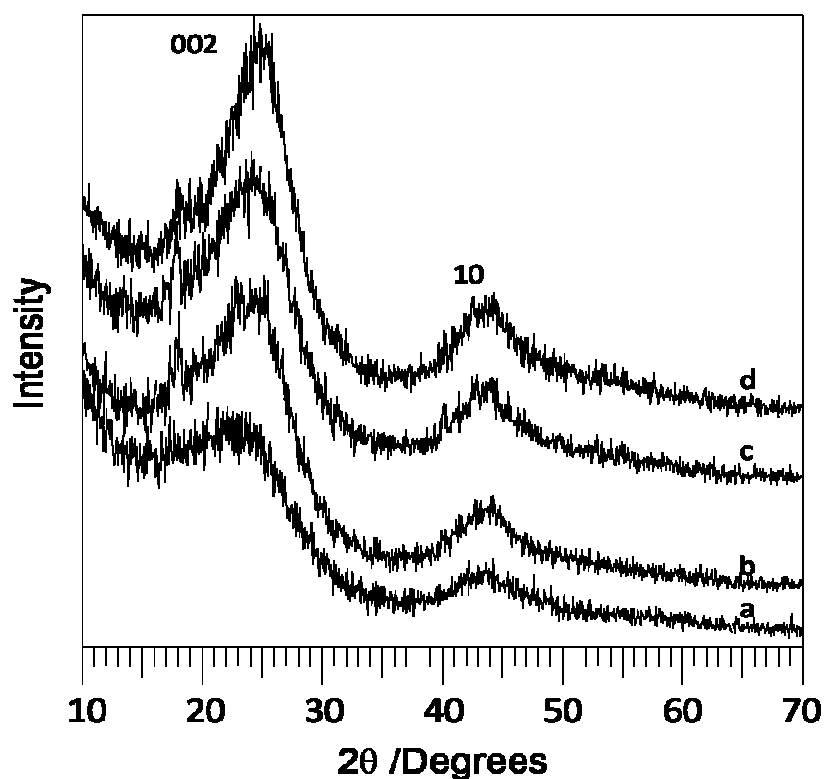


**Figure 4.6** Wide-angle XRD patterns of a) DMC; b) Co-DGMC; c) Ni-DGMC; d) Fe-DGMC. The peak at  $2\theta = 18^\circ$  is due to the XRD holder.

The semi-graphitic nature of the carbon rods is also very evident in the Raman spectra shown in **Figure 4.7**. The G band at  $1580\text{ cm}^{-1}$  due to in-plane stretching is noticeably sharper compared with that of non-graphitic DMC (**Figure 6b-d**). The shoulder at  $1150\text{ cm}^{-1}$  is attributed to  $sp^2$ -bonded configurations in the graphite structure, as proposed in recent work that elucidates the origin of this feature[20]. Among three treated mesoporous carbons, Ni-DGMC has the largest G/D ratio, indicating its higher degree of graphitization.

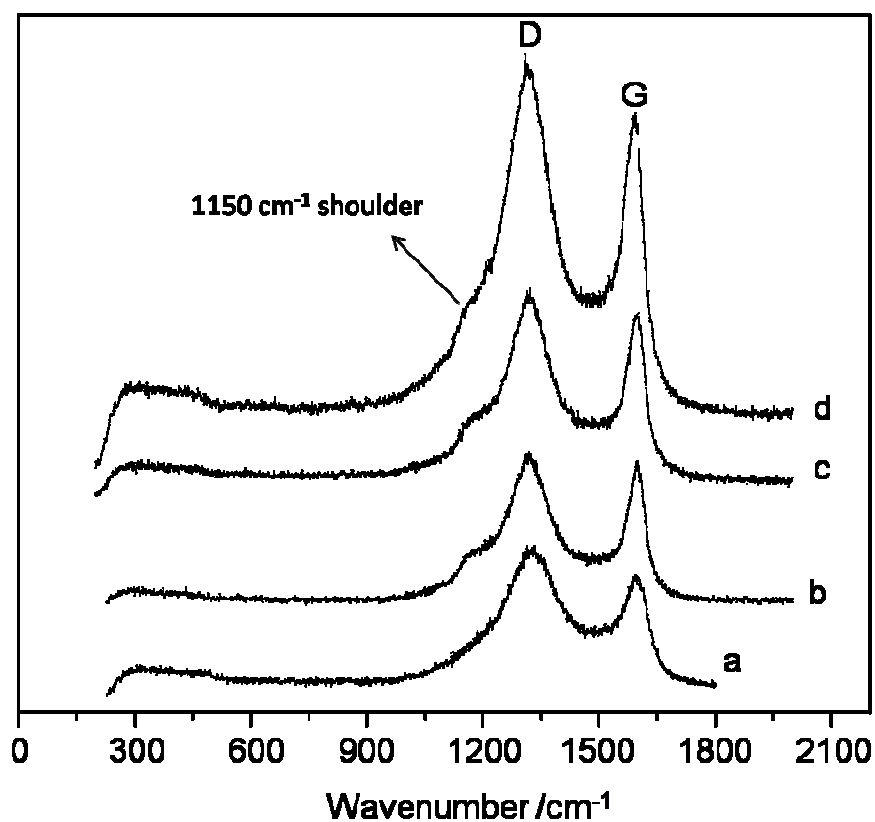


**Figure 4.7** Raman spectra of a) DMC; b) Ni-DGMC; c) Co-DGMC; and d) Fe-DGMC.

DGMC exhibits better thermal stability in air than DMC (**Figure 4.8**). Mass loss in DMC due to oxidation commenced at 350 °C, while DGMC materials all began to oxidize at 470 °C. The conductivity of DGMC materials was in accord with the thermal stability, which is an indirect measure of the graphitic content. The Fe and Co-DGMC exhibited both a slightly higher oxidation temperature and higher conductivity than the Ni-DGMC. Compared with non-graphitic mesoporous carbon, all of the DGMC materials exhibit higher conductivity by almost 3 orders of magnitude (**Table 4.1**). The better thermal stability and

electrical conductivity confirms the graphitic structure of the DGMC materials and has ramifications for materials properties that rely on a more graphitic ordering.

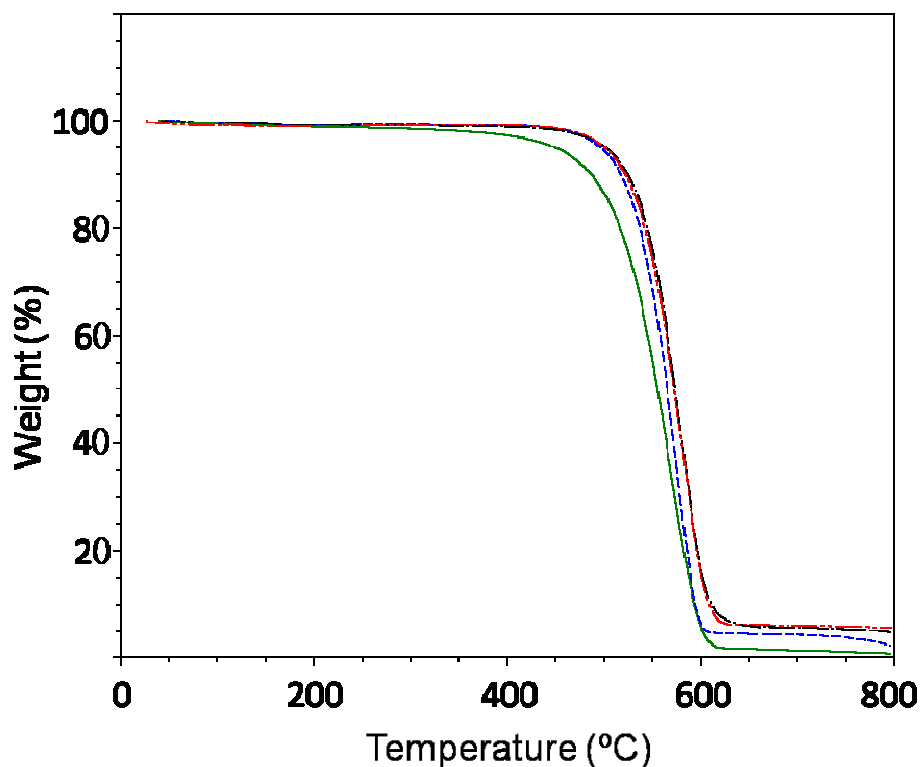


**Figure 4.8** TGA curves showing slightly improved thermal stability in air for the graphitized carbon materials: green, DMC; blue, Ni-DGMC; black, Co-DGMC; and red, Fe-DGMC.

#### 4.3.1.3 About preparation temperature

DGMC materials were also synthesized at the higher temperature of 1000 °C. The Ni and Co-DGMC materials give rise to a structure with limited order, indicated by their low angle XRD pattern (**Figure 4.9a, b**) and the SEM images (**Figure 4.11**). The Ni and Co-DGMC materials obtained at 1000 °C have a much more disordered morphology than the

DGMC materials obtained at 900 °C. Interestingly, a broad peak is still present in the XRD pattern of Fe-DGMC (**Figure 4.9c**), suggesting that higher temperature treatment does not have such a large influence on Fe-DGMC. On the other hand, the degree of graphitization in the DGMC materials was improved at 1000 °C, illustrated by the increase in the (002) peak and decreased  $d$  value (0.345 nm) in the XRD pattern of the Ni-DGMC material obtained at 1000 °C compared to the material fired at 900 °C (**Figure 4.10**). However, the higher degree of graphitization comes at the expense of partial loss of mesoporous order, as discussed earlier. Therefore 900 °C is chosen to synthesize DGMC materials for their applications.

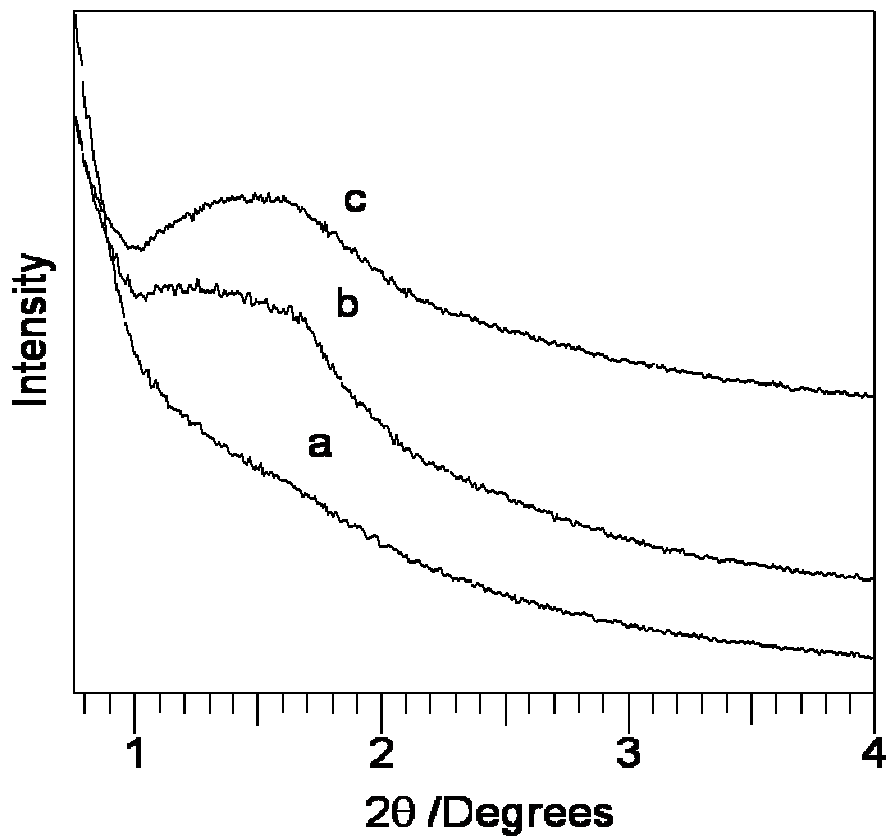


**Figure 4.9** XRD patterns of DGMC materials obtained at 1000 °C: a) Ni-DGMC; b) Co-DGMC; c) Fe-DGMC.

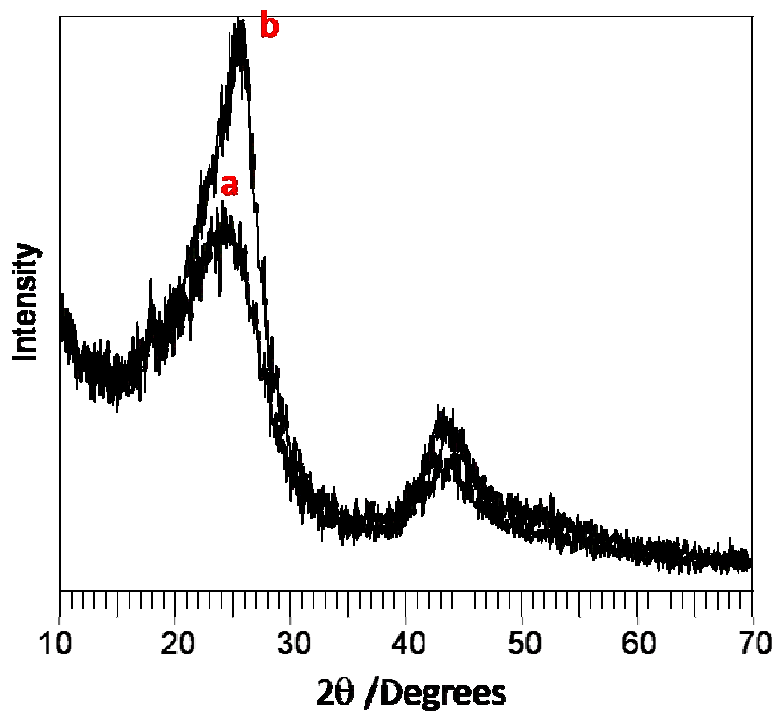


Figure 4.10 XRD patterns of a) Ni-DGMC at 900 °C and b) Ni-DGMC at 1000 °C.

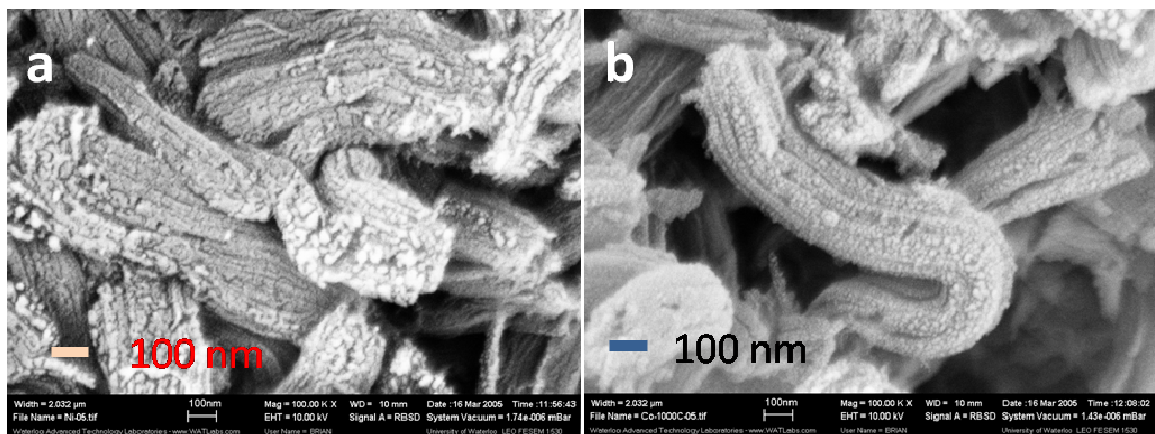
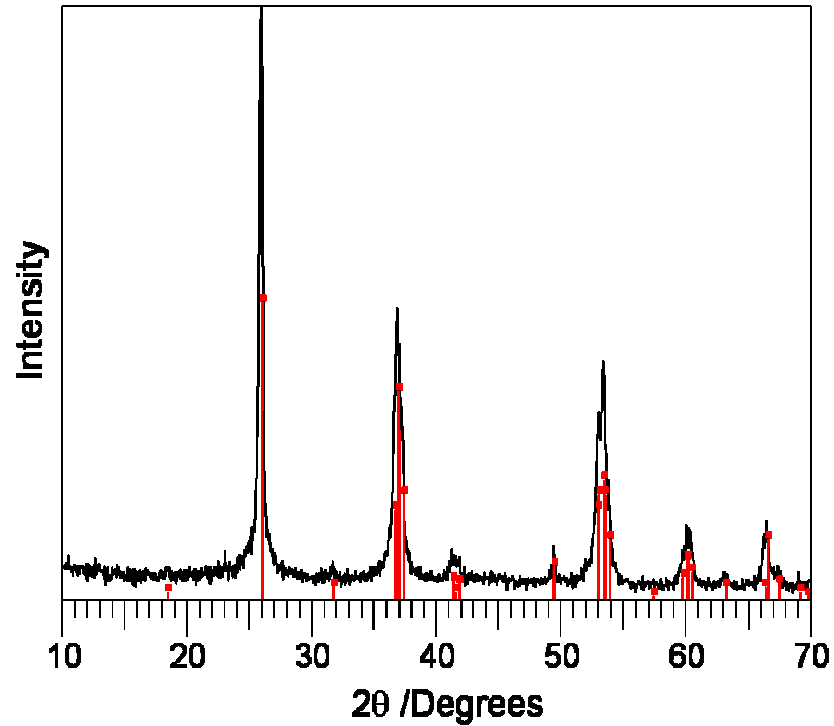


Figure 4.11 SEM images of materials obtained at 1000 °C: a) Ni-DGMC and b) Co-DGMC.

### 4.3.2 DGMC/MoO<sub>2</sub> composite as an electrode in a Lithium ion battery

#### 4.3.2.1 Composite structure with MoO<sub>2</sub>



**Figure 4.12** Wide-angle XRD pattern of the nanocomposite DGMC/MoO<sub>2</sub>.

The composite material was prepared via impregnation of the DGMC catalyzed by Ni with soluble ammonium molybdate, followed by heat treatment in H<sub>2</sub>/N<sub>2</sub> to reduce the salt to MoO<sub>2</sub>. The composite composition was confirmed by XRD measurements (**Figure 4.12**) showing reflections of single phase monoclinic MoO<sub>2</sub>. The line shapes can be deconvoluted at least into two components: one, highly broadened, that is attributed to the MoO<sub>2</sub> confined within the channels, and another which is relatively sharp, suggestive of some MoO<sub>2</sub>

crystallites >50 nm in diameter that are external to the nanorod surface. These findings were corroborated by TEM studies.

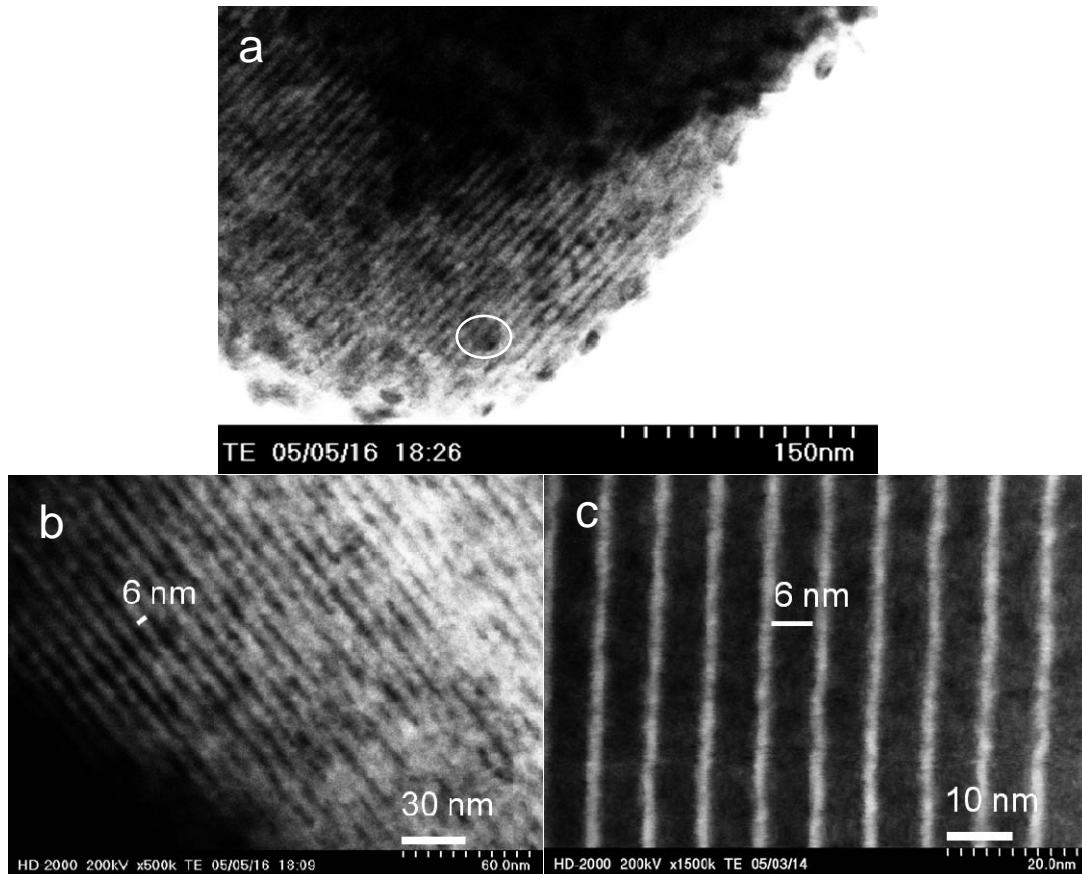


**Figure 4.13** TEM images of a) the nanocomposite DGMC/MoO<sub>2</sub> at low magnification showing the stuffed channel structure and presence of a minor amount of MoO<sub>2</sub> crystallites external to the DGMC channels; b) high magnification showing the MoO<sub>2</sub> within the channels; c) “empty” DGMC reproduced from the Figure 4.4, for easy comparison with part b.

The channels of DGMC-MoO<sub>2</sub> (Figure 4.13 a, b) show substantial expansion compared with the nanorods themselves (Figure 4.13c), indicative of filling of the channels. Note that the carbon rods, which appear dark in Figure 4.13 c due to the contrast between the carbon and the empty tunnel, appear white in Figure 4.13 b in contrast to the higher density

MoO<sub>2</sub> (dark) that now fills the channels. The metal oxide is relatively continuous along the channel dimension although some disorder of the structure is apparent, vis a vis the DGMC. Some small MoO<sub>2</sub> crystallites 30-50 nm in diameter are also evident on the surface of the DGMC rods in **Figure 4.13a**, shown by the dark features (indicated by a circled area on the figure) superimposed upon the lattice image. TGA-DSC analysis showed that the composites were 63.7 wt% MoO<sub>2</sub>/ carbon (**Figure 4.14**).

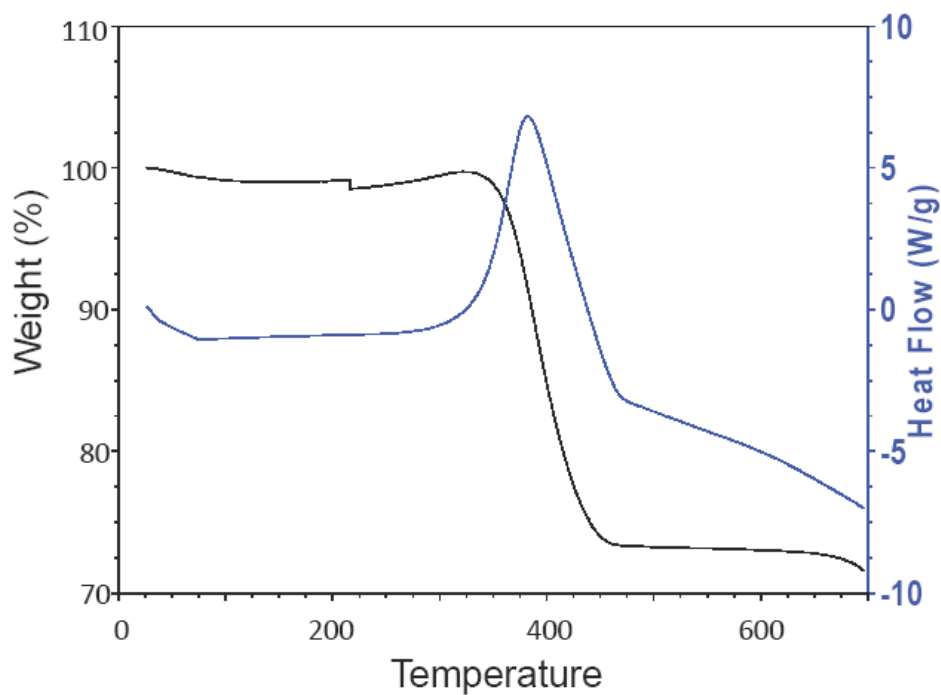


**Figure 4.14** TGA-DSC curves of the DGMC/MoO<sub>2</sub> nanocomposite to determine carbon percentage.

#### 4.3.2.2 Galvanostatic cycling of DGMC/MoO<sub>2</sub>

The galvanostatic charge-discharge profiles of the DGMC/MoO<sub>2</sub> composite recorded at a current rate of  $C/10$  (see **section 1.2.3**) in the 3.0-0.0 V voltage window are shown in **Figure 4.15**.

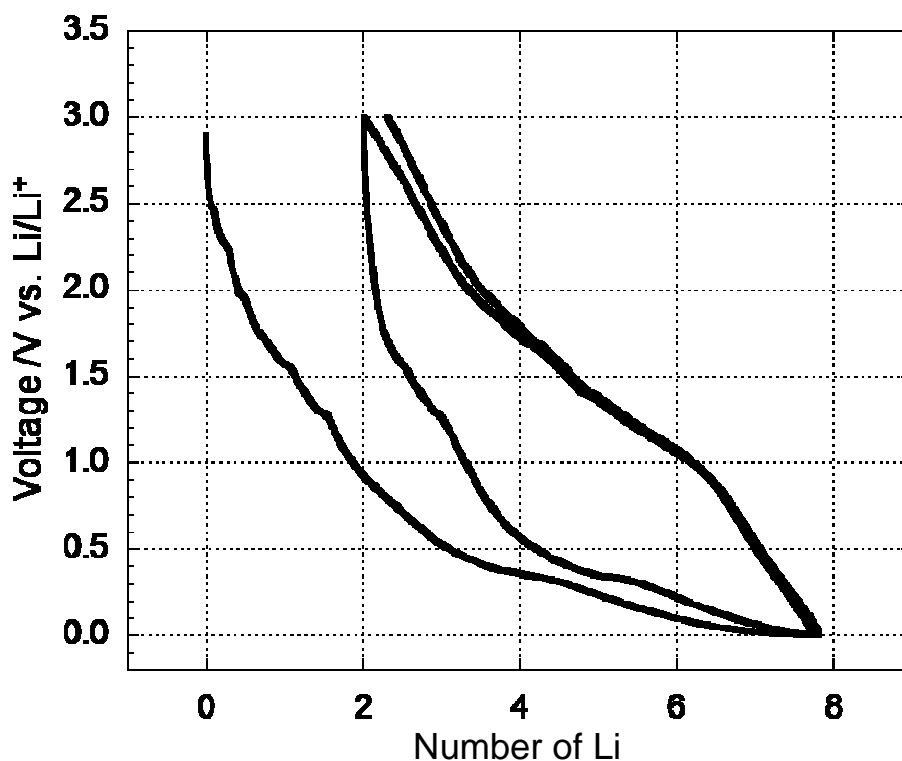


**Figure 4.15 Galvanostatic discharge and charge profiles of the first two cycles of DGMC/MoO<sub>2</sub>.**

The characteristic plateaus [13], representative of crystalline bulk MoO<sub>2</sub> are barely visible, confirming the presence of very small nanocrystallites and/or a quasi-amorphous structure [21]. Resembling the situations of FePO<sub>4</sub>/LiFePO<sub>4</sub>, there will be a voltage plateau when two phases are involved in discharge/charge profiles. Bulk MoO<sub>2</sub> exhibits a voltage plateau at 1.3 V versus Li/Li<sup>+</sup>, where an irreversible phase transition occurs. The phase transition leads to considerable capacity fade in following cycles. Distinct from bulk MoO<sub>2</sub> with large dimensions, conversion reactions can easily occur to nano-dimensioned MoO<sub>2</sub>.

The first discharge sweep yielded a very large specific capacity of 1040 mA·h/g, with an irreversible capacity of 250 mA·h/g (24%) on the first cycle.

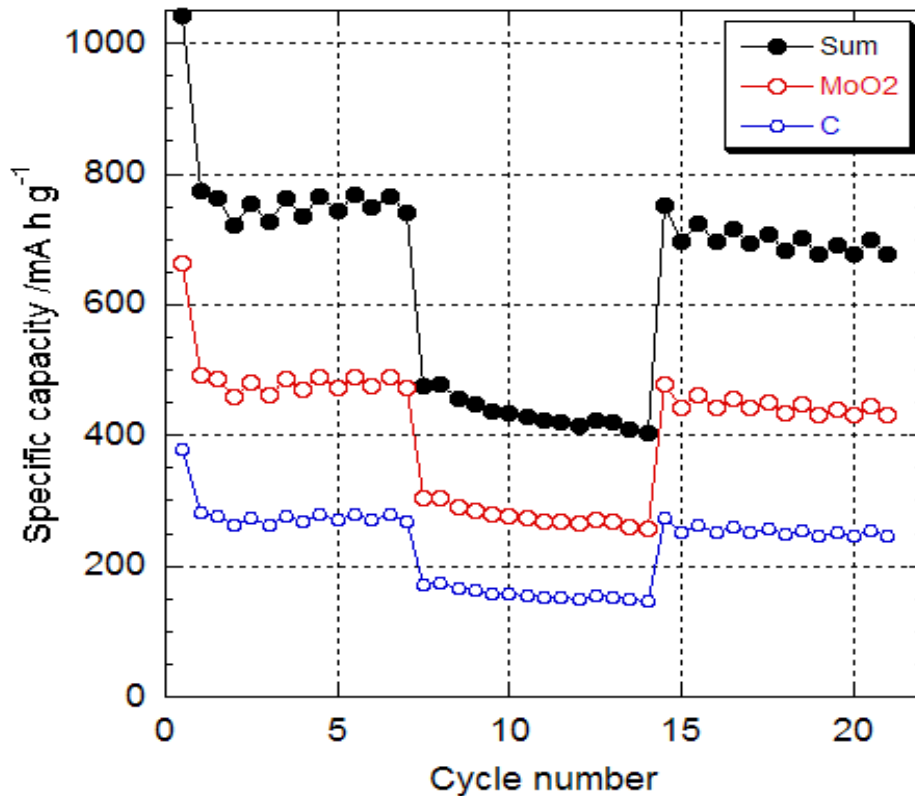


**Figure 4.16** Discharge and charge cycle performance of DGMC/MoO<sub>2</sub> at a constant rate of C/10; the first seven cycles were recorded in the window 3.0-0.05 V; the lower cutoff voltage was then raised to 0.3 V during the subsequent seven cycles; and the cutoff voltage was then reset to 0.05 V to show the regain in capacity. The contributions of the partially graphitized carbon and MoO<sub>2</sub> are estimated as described in the text.

**Figure 4.16** displays the capacity evolution with cycle number in different voltage windows for the same cell. A reversible, stable charge capacity of 760 mA·h/g was obtained during the first seven cycles in the window 3.0-0.05 V. Raising the lower cutoff voltage to

0.3 V during the subsequent seven cycles decreased the capacity to about 450 mA·h/g, but the initial value of 760 mA·h/g was immediately regained on resetting the cutoff voltage to 0.05 V. The cycling performance was promising, stabilizing at 700 mA·h/g on the 20th cycle. Even better stability was observed when the lower cutoff voltage was maintained at 0.05 V throughout the experiment with very little loss in capacity being observed after 20 cycles.

The very good electrochemical performance arises from two factors. First, both the carbon and the MoO<sub>2</sub> contribute to the capacity of the composite electrode material, according to the proposed reactions:



Here, it can be assumed that full and reversible reduction of MoO<sub>2</sub> to Mo metal (+Li<sub>2</sub>O) occurs within this voltage window, based on previous work reported for metal oxides such as MoO<sub>3</sub> [22], CoO [23,24], and many others. The DGMC also plays an important role as an active lithium insertion host in the composite electrode. Typical graphitic carbon displays a reversible capacity  $Q_r$  of about 370 mA·h/g according to the reaction  $6\text{C} + \text{Li} \rightarrow \text{LiC}_6$ . The capacity of mesoporous carbon well exceeds this, with values reported as high as 850-1100 mA·h/g for CMK-3 [25]. Our DGMC shows a lesser uptake of about 580 to 650 mA·h/g as shown by the first two charge-discharge profiles in **Figure 4.17** and also a correspondingly lower irreversible capacity ( $Q_{\text{irr}}$ ) on the first charge sweep. The fraction of reversible capacity (about 30% with respect to the total on first discharge) is the same as CMK-3 [25], however. It is highly characteristic of mesoporous and/or high specific capacity carbons prepared at temperatures no higher than 700 °C. It is thought to arise from

reaction of lithium with the active surface groups on the carbon, including dangling C-H and C-OH bonds, as well as via formation of the solid electrolyte interface (SEI). As the graphitic character of such carbons increases, either by heat treatment (or by catalysis in our case) both the irreversible and the reversible capacity, and hysteresis in the curve undergoes a dramatic decrease [25]. Accordingly those parameters for DGMC are almost exactly midway between amorphous mesoporous carbon CMK-3 and graphite.

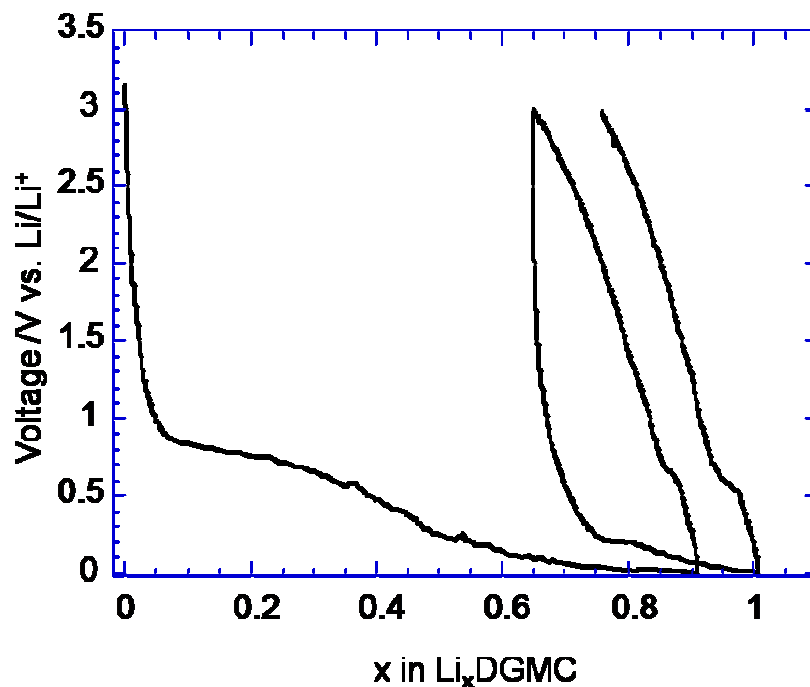


**Figure 4.17 Galvanostatic discharge and charge profiles of the first two cycles of DGMC.**

It is assumed that the capacity of DGMC is the same when it coexists with MoO<sub>2</sub> nanoparticles. It can be noted that this is contrary to a report of the electrode properties of metallic Sn/mesoporous carbon composites. Those authors did not observe any

electrochemical contribution from the carbon even at low potential, possibly due to the amorphous nature of the carbon [12]. Taking into account the 36.3 wt% fraction of mesoporous carbon in our material, the contribution of DGMC in the composite electrode to the overall capacity is about 276 mA·h/g. By this same estimation, the contribution from MoO<sub>2</sub> to the overall total capacity of 760 mA·h/g is about 484 mA·h/g, about 58% of the theoretical value (830 mA·h/g) when Mo(IV) is reduced to its metallic state. The breakdown of the components is illustrated in **Figure 4.16**. In the composite, in principle, complete Li-driven decomposition of MoO<sub>2</sub> is possible because of the small dimensions of the metal oxide nanoparticles, and the intimate contact with the conductive carbon host. That the full reduction is not achieved under the conditions may be due to an overestimate of the carbon contribution and/or hindered transport of Li within the composite structure. It is important to note that the composite system described here still presents considerable advantages over the bulk material. Crystalline MoO<sub>2</sub>, which exhibits an average redox potential vs Li/Li<sup>+</sup> of 1.3 V, exhibits a monoclinic-orthorhombic phase transition at 1.6 V that leads to very rapid capacity fading if the cell is discharged below this voltage [20]. This is not the case for the composite material, due to the confined, nanosized dimensions of the MoO<sub>2</sub>. Therefore, not only is more redox capacity accessed, but also the overall voltage is lowered. The pronounced improvement of capacity fading of MoO<sub>2</sub> in the DGMC/MoO<sub>2</sub> composite is attributable to the controlled particle size of the MoO<sub>2</sub>. The electrochemical properties of DGMC/MoO<sub>2</sub> indicate that the graphitized mesoporous carbon and transition metal oxide composite materials may be promising candidates to replace graphite anodes in lithium ion batteries.

#### 4.4 Conclusions

Highly ordered mesostructured carbon wires with a graphitic structure directly from an as synthesized SBA-15 silica/triblock nanocomposite was synthesized, by employing transition metals as catalysts. The graphitic structure can be generated directly from the copolymer in the presence of metallic catalysts based on Fe, Co, or Ni. The catalysts played a major role in determining the morphology of the materials. Enhanced electrical conductivity and thermal stability were exhibited by the graphitic nanoporous carbon materials compared with those prepared in the absence of catalyst. A graphitic mesoporous carbon/MoO<sub>2</sub> nanocomposite was prepared by a simple impregnation method. Its properties as a negative electrode in a lithium cell, wherein both composite components are active and operate in concert, were evaluated. The graphitic carbon framework serves to constrain the dimensions of the oxide and sustains reversibility of Li uptake. The MoO<sub>2</sub> adds substantial gravimetric capacity to that of the carbon which is limited to about 370 mA·h/g (at best), and its metallic properties enhance the conductivity. Thus, forming a nanocomposite with MoO<sub>2</sub> gives a synergistic effect: the MoO<sub>2</sub> contributes to the two- to threefold increase in capacity of the composite material as a whole, while the carbon still functions as an active material but also constrains the conversion reaction of the MoO<sub>2</sub>. This results in a much more stable and reversible capacity of 760 mA·h/g, showing the advantages of this approach in developing nanocomposite electrode materials.

## Chapter 5

### A Highly Ordered Nanostructured Carbon-Sulfur Cathode for Li-S Batteries

#### 5.1 Introduction

As described in **section 1.2.4.2.1**, the lithium-sulfur (Li-S) cell, as one of the most promising energy storage devices, consists of sulfur as the positive electrode, and lithium as the negative electrode in its simplest configuration [1,2]. Sulfur or sulfur-containing organic compounds are highly electrically and ionically insulating [3]. To enable a reversible electrochemical reaction at high current rates, the sulfur must maintain intimate contact with an electrically conductive additive. Various carbon-sulfur composites were employed for this purpose, but they have limitations due to the scale of the contact area. Typical reported capacities are between 300 - 550 mA·h/g at moderate rates [4]. To make a sulfur containing cathode ionically conductive, liquid electrolytes are employed which act as an ion transport medium not only between electrodes but within the sulfur containing cathode [5]. This presents difficulties of electrolyte access. Another major problem of Li-S batteries is the capacity degradation on repeated discharge-charge of the cell. In part, this is due to the solubility of the polysulfide anions formed on reduction of  $S_8$  on discharge, in the polar organic solvents used in electrolytes [6]. During cycling, these polysulfide anions can be irreversibly converted to solid precipitates ( $Li_2S_2$  and/or  $Li_2S$ ) on both electrodes causing capacity fading [7].

In response to these considerable challenges, some novel advances in materials design, such as new electrolytes [8,9,10,11], and protective films for the lithium anode have

been proposed [12,13,14]. For cathode materials where most of the difficulty remains, there have been few developments although some interesting approaches have been recently reported [15,16,17,18]. However, they still fall well short of the mark for practical electrochemical performance.

In this project, it has been demonstrated that cathodes based on nanostructured interwoven sulfur-OMC composites can overcome the challenges of Li-S cells to a large degree, and exhibit stable, high reversible capacities with good rate properties. All the benefits exhibited by sulfur-OMC composites in the electrochemistry of Li-S cells are presented. In addition, thin films composed of polyethylene glycol (PEG) of various chain lengths tethered on surface of nanocomposite particles can further improve the electrochemical performances of the sulfur electrode.

## **5.2 Experimental**

### **5.2.1 Preparation of ordered mesoporous carbons (OMC)**

#### **5.2.1.1 Preparation of CMK-3**

CMK-3 was synthesized with a nanocasting method that employs mesoporous silicate SBA-15 with a homogeneous rod-like morphology (the preparation of SBA-15 rods was introduced in **section 4.2.1**) as a hard template. The rod-like morphology of SBA-15 and CMK-3 can facilitate easy access to the mesoporous channels and the sorption properties [19]. Please find preparation procedure for nanorods of CMK-3 in **section 3.2.1**.

### 5.2.1.2 Preparation of CMK-8

CMK-8 is an OMC with a 3D bi-continuous porous structure (*la3d*), fabricated from mesoporous silicate KIT-6 as a template [20]. In a typical synthesis of KIT-6, 6 g of P123 was dissolved in a 230 ml HCl (1.7wt%) aqueous solution. To this, 6 g of butanol was added under vigorous stirring at 38 °C. After 1 hr stirring, 12.9 g of TEOS was added at 38 °C. The mixture was left to stir for 24 hrs at 38 °C, and subsequently hydrothermally heated for 24 hrs at 100 °C under static conditions. The solid product was filtered and dried at 80 °C. The surfactants were removed by calcination at 550°C. CMK-8 was synthesized by pyrolysis of sucrose in KIT-6, following the nanocasting procedure described for nanorods of CMK-3 in **section 3.2.1**.

### 5.2.1.3 Preparation of graphitized CMK-3 (GCMK-3) by chemical vapor deposition (CVD) method

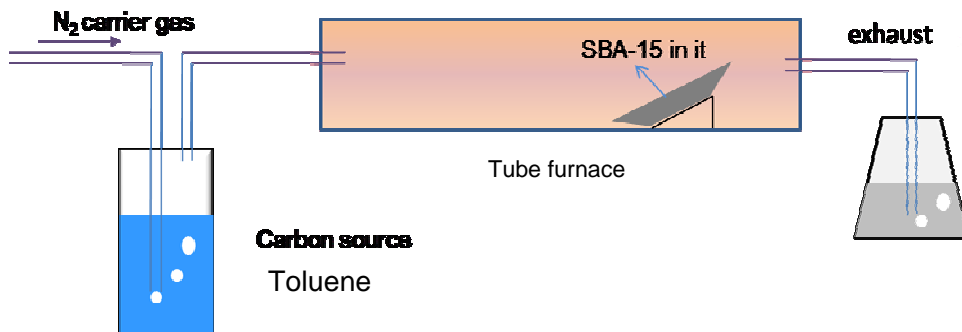


**Figure 5.1** Schematic diagram showing chemical vapor deposition for preparation of GCMK-3.

The apparatus set up for CVD process is shown in **Figure 5.1**. Toluene was employed as a carbon precursor. The tube furnace was heated to 900 °C under  $N_2$ .  $N_2$  gas then carried toluene vapor (@60 °C) into a tube furnace and passed it over a crucible containing the

CMK-3 for 30 min at a flow rate of 30 cm<sup>3</sup>/min for 30 min. The temperature of the tube furnace was lowered down to room temperature at a rate of 10 °C/min under N<sub>2</sub>. After removal of the silica template with HF etching, the GCMK-3 was collected by filtration and dried.

### 5.2.2 Preparation of OMC/S composites

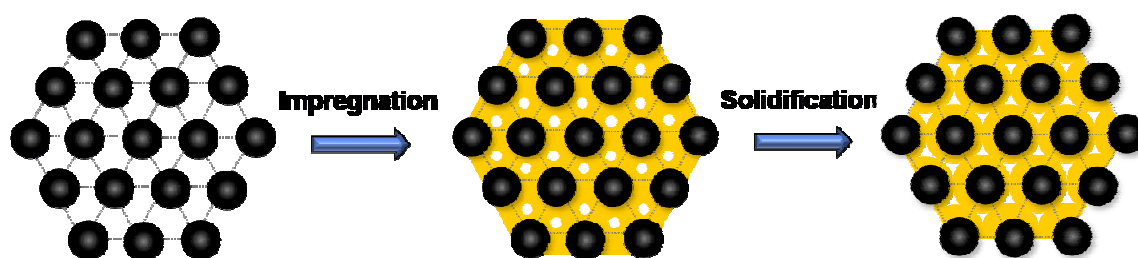


**Figure 5.2 Schematic showing the process of composite preparation.**

**Figure 5.2** schematically displays the preparation of OMC/S composite by a melt-diffusion strategy. A well ground mixture of OMC and elemental sulfur was heated at 155 °C where the viscosity of molten sulfur is the lowest [21]. Molten sulfur can thus be imbibed into the channels by capillary forces, whereupon it solidifies and shrinks to form sulfur nanofillers in intimate contact with the conductive carbon nanofibers. The employed ratio between sulfur and an OMC is calculated based on the assumption that the total pore volume of the OMC would be occupied by Li<sub>2</sub>S, the least dense compound and final discharge product in an electrochemical reaction of a Li-S cell. The physical characteristics, including pore volumes of OMC materials are summarized in **Table 5.1** in **section 5.3.1**. The employed weight ratios between OMC materials and sulfur are as following: 30/70 for CMK-3, 42/58 for CMK-8 and 41/59 for GCMK-3.

### 5.2.3 Preparation of PEG coated CMK-3/S

To prepare the CMK-3/S-PEG composite, CMK-3 was first functionalized with carboxylic groups by oxidization treatment in concentrated HNO<sub>3</sub> solution for 30 min at 80°C, prior to incorporation of the sulfur. To tether PEG chains to the surface of CMK-3/S composite, the composite was dispersed in an aqueous PEG solution and the solution was heated at 58 °C and stirred continuously overnight to ensure the complete reaction of the carboxylic group on the carbon particle with the hydroxyl group on PEG. The mixture was then sonicated for 20 min to completely remove physically absorbed PEG on the composite. CMK-3/S-PEG composite was collected by filtration and dried.

### 5.2.4 Electrochemistry

Positive electrodes were comprised of 84wt% CMK-3/S composite, 8wt% carbon black (trade name: Super S) and 8wt% poly(vinylidene fluoride) (PVDF) binder. The cathode materials were slurry-cast from cyclopentanone suspension onto a carbon coated aluminum current collector. The electrolyte is composed of a 1.0 M LiPF<sub>6</sub> solution in ethyl methyl sulfone (EMS) [22]. Coin cells utilizing a metallic Li anode were assembled to evaluate the materials.

To measure the degree of sulfur retention in the cathode, a 1.0 M LiPF<sub>6</sub> solution in tetra(ethylene glycol) dimethyl ether (TEGDME) was used as the electrolyte. Cathodes comprising CMK-3/S-PEG were compared with CMK-3/S and simple mixtures of sulfur and acetylene black at the exact same (55:45) S/C ratio. Swagelok™-type cells are employed, which accommodate a sufficient excess of the electrolyte to dissolve sulfur species. Swagelok™ cells were disassembled and immersed into TEGDME to completely extract

sulfur species from the electrolyte. Sulfur analysis was performed by Galbraith Laboratories using Inductively Couple Plasma - mass spectrometry.

### 5.3 Results and discussion

#### 5.3.1 Physical characterizations of OMC materials

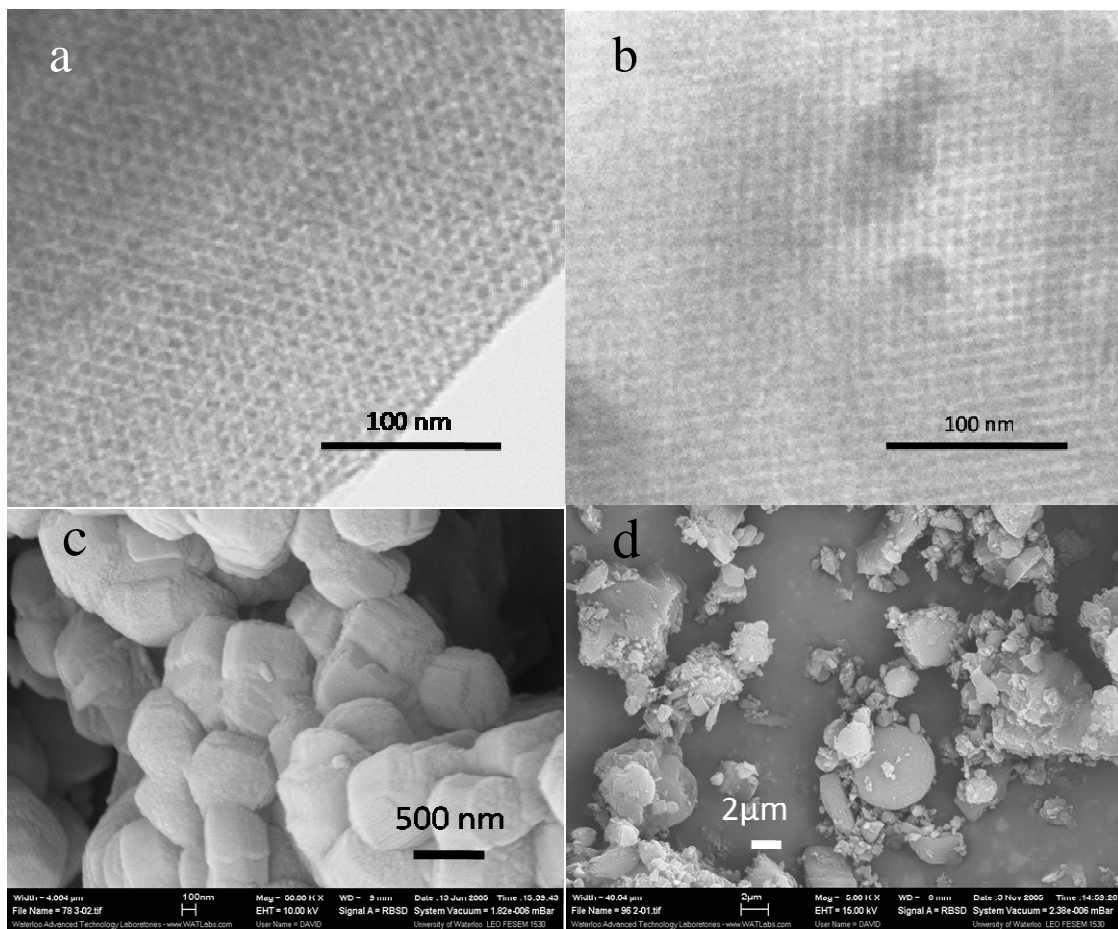


**Figure 5.3** TEM images of a) CMK-3; b) CMK-8 and SEM images of c) CMK-3; d) CMK-8.

The hexagonal pore arrangement of CMK-3 ( $P6mm$ ) and the cubic structure of CMK-8 ( $Ia3d$ ) are clearly shown in their TEM images, respectively (**Figure 5.3a, b**). Both TEM images are viewed along the direction of the pore structure. CMK-3 particles as shown in the SEM image (**Figure 5.3c**) are assemblies of carbon nanofibers which are spanned by randomly distributed micro-spacers. The centers of the adjacent nanofibers are 10 nm apart. CMK-8 does not exhibit a homogeneous morphology as shown in **Figure 5.3d**, similar to its template, KIT-6. However, cubic long-range order in CMK-8 particles is not compromised.

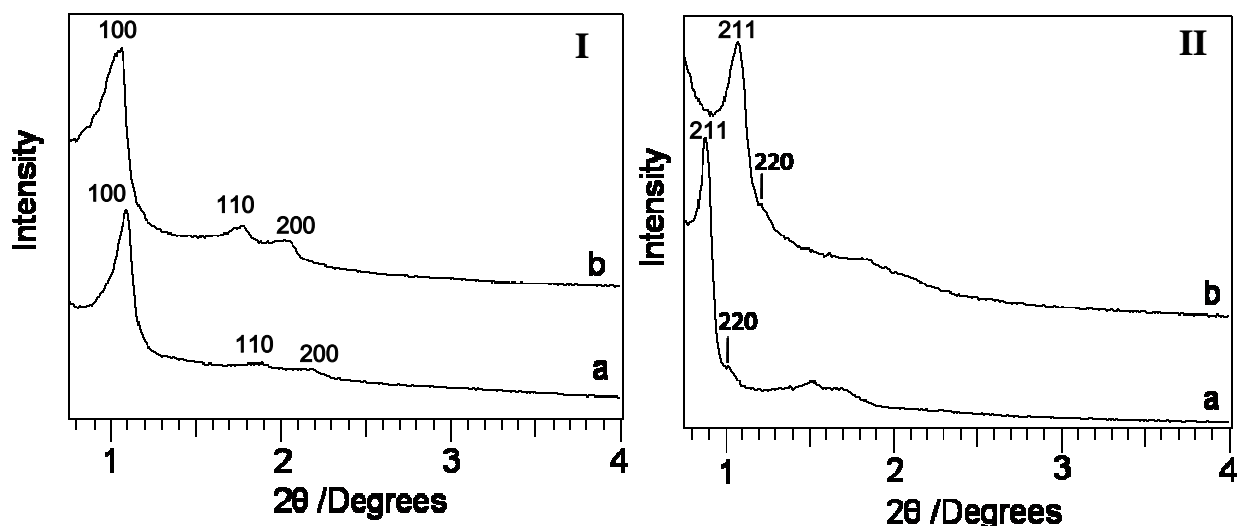


**Figure 5.4** Low angle XRD patterns of mesoporous materials I: a) CMK-3; b) GCMK-3; II: a) KIT-6; b) CMK-8.

The hexagonal symmetry in CMK-3 and GCMK-3 gives rise to the well resolved XRD peaks shown in **Figure 5.4I**, which can be assigned to (100), (110), and (200) reflections of space group ( $p6mm$ ), similar to their template, SBA-15. The high quality of cubic structure in KIT-6 and CMK-8 is demonstrated by their XRD patterns, presented in

**Figure 5.4II.** The first two peaks in these patterns can be assigned to (211) and (220) reflections.

**Table 5.1 Physical characteristics of OMCs**

Samples	$S_{\text{BET}}$ ( $\text{m}^2 \text{g}^{-1}$ )	$V_p$ ( $\text{cm}^3 \text{g}^{-1}$ )	Pore size (nm)
CMK-3	1976	2.06	3.3
GCMK-3	756	1.26	3.6 and 11.50
CMK-8	1060	1.17	3.8

**Table 5.1** summarizes BET surface area, pore volume and pore size of various OMC materials. The pore volume ( $V_p$ ) of an OMC reveals its capacity to accommodate active sulfur mass. CMK-3 is superior to the other OMCs in terms of its surface area and pore volume. A bimodal porous structure of GCMK-3 is evident. The larger pores (sized 11.50 nm) probably arise from the incomplete filling of SBA-15 voids during the CVD nanocasting process.

Introduced in **Chapter 4**, DGMC materials as semi-graphitic OMC were fabricated by catalysis with transition metals. As shown in **Figure 5.5**, the wide-angle pattern of the semi-graphitic ordered carbons shows two intense diffraction peaks which can be indexed as (002) and (100) diffractions for typical graphite carbons. The  $d$  spacing of the (002) plane for GCMK-3 and DGMC (prepared at 1000 °C) is 0.345 nm which is close to the value (0.335 nm) of graphitized carbons derived up to 2800 °C, suggestive of a high degree of graphitization in GCMK-3. Furthermore, GCMK-3 shows more intensive diffraction peaks than do DGMC materials. In this study, GCMK-3 is selected as a representative of highly

graphitized carbon materials in the preparation of a carbon-sulfur composite as a cathode for Li-S batteries.

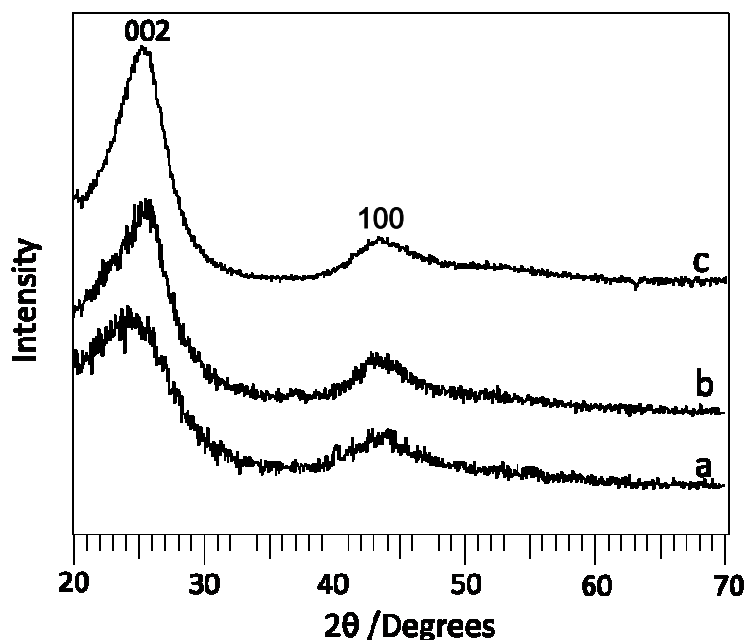


**Figure 5.5** Wide angle XRD patterns of a) DGMC at 900 °C; b) DGMC at 1000 °C; c) GCMK-3.

### 5.3.2 OMC/S composites

#### 5.3.2.1 Physical characterizations of CMK-3/S composite

Most proof-of-concept studies are based on CMK-3, the most well-known member of the OMC family [23,24], although they are not limited to this material. The SEM images in **Figure 5.6** reveal the changes in mixture of CMK-3 and sulfur before and after heating. The bulk sulfur evident in the SEM image of the composite on initial mixing (**Figure 5.6a**) largely disappears at 145 °C (**Figure 5.6b**), and completely disappears after heat treatment at 155 °C (**Figure 5.6c**). Full incorporation of sulfur into the channels of CMK-3 occurs at this

latter temperature. CMK-3 and sulfur are both hydrophobic materials, which accounts for the ready absorption of sulfur into the channel structure.

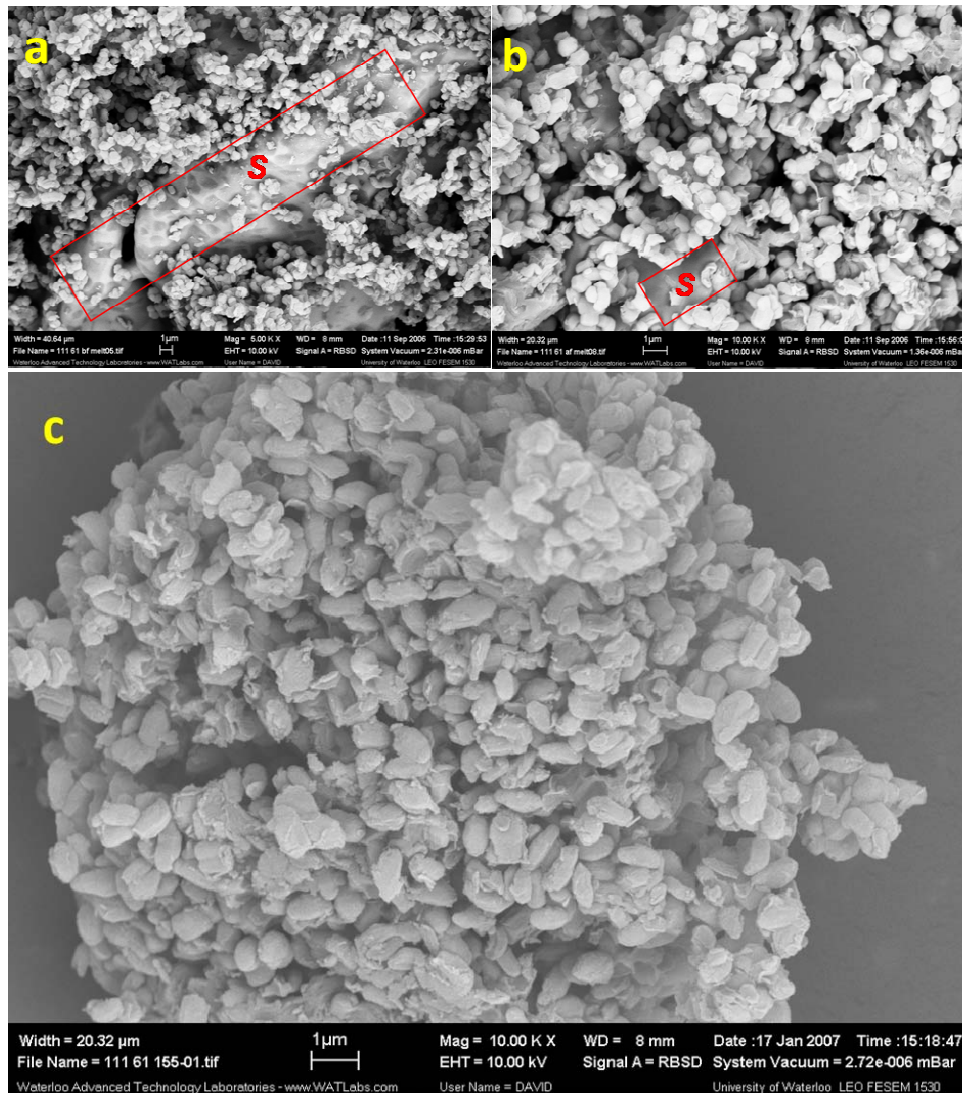


**Figure 5.6 SEM images of a) a mixture of CMK-3 and sulfur before heating; b) CMK-3/S prepared at 145 °C; c) the CMK-3/S prepared at 155 °C. Sulfur outside of structure of CMK-3 is indicated by the outlined red square (inset) in part a, b.**

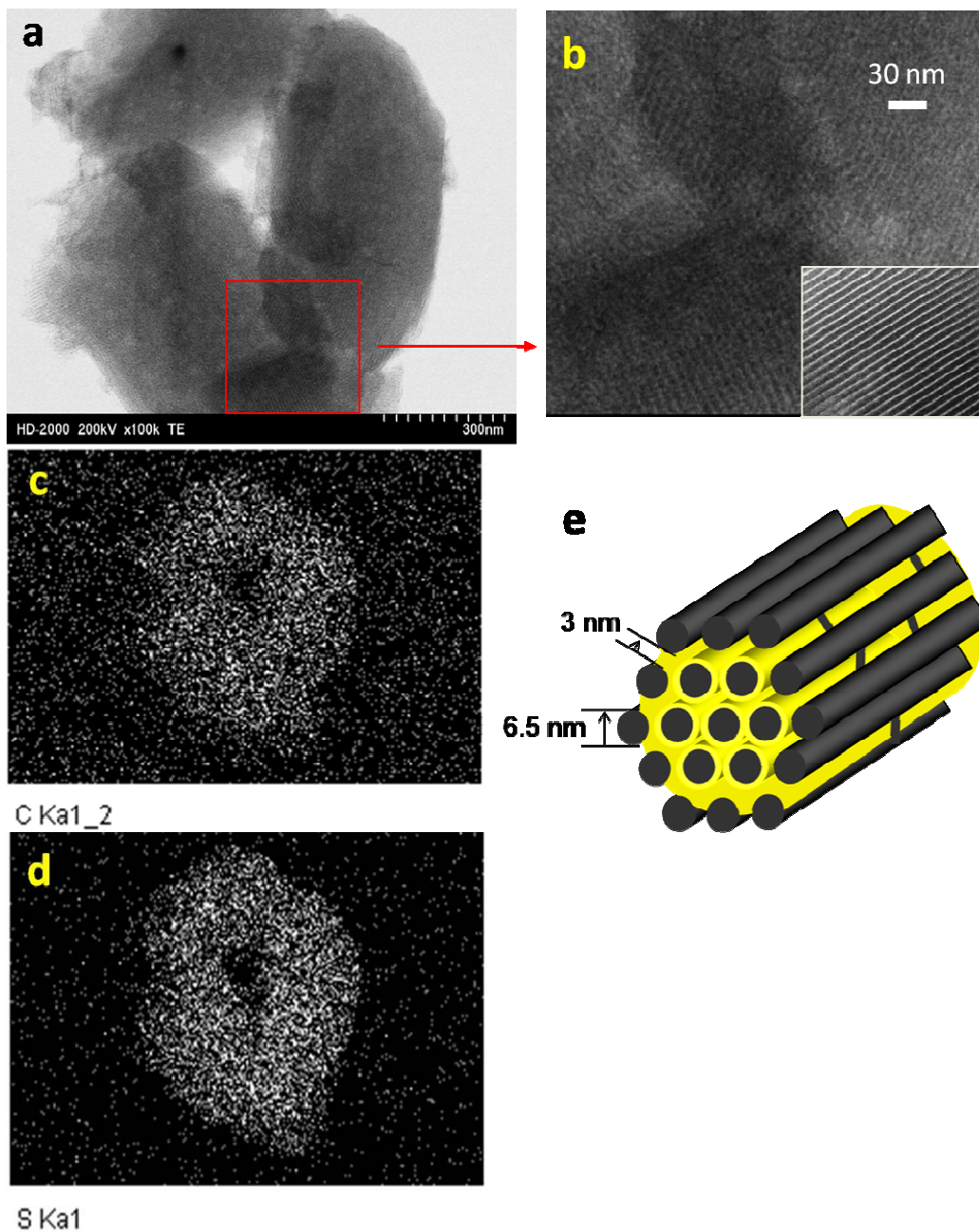


**Figure 5.7** a) TEM image of a CMK-3/S-155 composite particle; b) image expansion corresponding to the area outlined by the red square; inset shows the TEM image for pristine CMK-3 at the same magnification; c) corresponding carbon elemental map; d) corresponding sulfur elemental map; e) schematic showing sulfur (yellow) confined in the interconnected pore structure of OMC, CMK-3. The carbon nano-fibers are propped apart by carbon micro-fibers.

The filling of the carbon channels with sulfur is corroborated by the TEM image shown in **Figure 5.7a**, along with the magnified image shown in **Figure 5.7b**. The fillers have a similar diameter as that of the channels of the OMC (3.3 nm), and a comparable diameter to the carbon nanorods that enclose them (6-7 nm). The filling of the pores with sulfur, of similar density to carbon, is evident from the decrease in contrast *vis a vis* CMK-3 itself (shown in the inset in **Figure 5.7b**.) The sulfur and carbon elemental maps (**Figure 5.7c, d**) clearly demonstrate that sulfur is homogeneously distributed in the framework of OMC, with no significant fraction on the external surface. A schematic diagram illustrating the impregnation of the CMK-3 with sulfur is shown in **Figure 5.7e**, showing the alignment of the channels in comparison with the inset figure. Note that the vast majority of the sulfur is contained within the interior of the pore structure, as the particles span hundreds of carbon channels in width. The average CMK-3 particle is on the order of 1 $\mu$ m, as shown in **Figure 5.3c**.

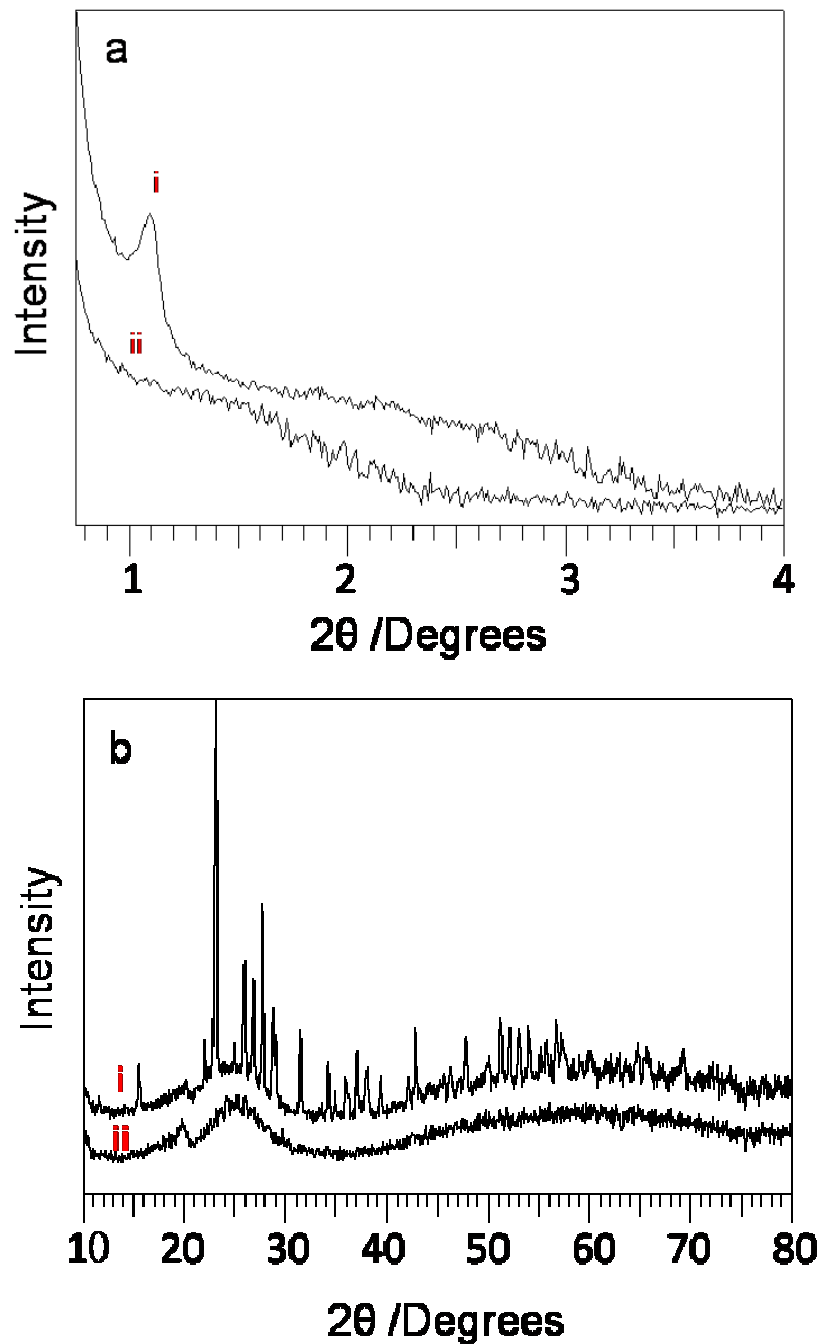


Figure 5.8 a) Low angle X-ray diffraction patterns of a mixture of CMK-3 and sulfur (i) before heating (ii) after heating at 155°C; b) wide angle X-ray diffraction patterns of a mixture of CMK-3 and sulfur (i) before heating (ii) after heating at 155°C.

The dramatic diminution of the low angle XRD peak due to long-range order in CMK-3 is further proof of pore-filling, which is also a result of the decrease in the scattering contrast (**Figure 5.8a, i and ii**) [25]. Comparing the wide angle XRD patterns in **Figure 5.8b, i and ii**, the well resolved peaks corresponding to highly crystalline sulfur disappear after sulfur impregnation. It is well known that when bulk molten sulfur cools down it solidifies into amorphous phase then eventually becomes crystallized [26]. The transition from amorphous phase to crystals takes time ranged from hours to days. Note that CMK-3/S composite displays exactly the same XRD pattern as the one shown in **Figure 5.8bii** 6 months after the preparation, indicative of the complete confinement of sulfur in OMC framework.

**Table 5.2 Characteristics of CMK-3, and the CMK-3/S composite**

Samples	BET total surface area (m <sup>2</sup> /g)	Pore volume (cm <sup>3</sup> /g)	Micropore surface area (m <sup>2</sup> /g)	BJH Pore size (nm)	Conductivity (S/cm) (± 0.02)
CMK-3	1976	2.1	152	3.3	0.20
CMK-3/S (S-70%)	*46	*0.028	*5.1	1.1	0.21

\* As it was not possible to follow the conventional protocol of evacuating the samples at 150°C prior to BET measurements due to the volatility of the sulfur, no pretreatment was used for CMK-3/S-70%. The possibility of water entrapment, and/or pore blockage in the predominantly micropore containing CMK-3/S means that the values represent lower estimates

**Table 5.2** summarizes the physical characteristics of CMK-3 and the CMK-3/S composite derived from BET and conductivity measurements. After imbibition of the sulfur into the channels, the pore size of CMK-3/S composite decreases dramatically, indicating that the channels of CMK-3 are partially filled. Along with the presence of residual

micropores in carbon nanofibers [27], this allows ingress of electrolyte within the structure. Empty volume within the pores is also necessary to accommodate the uptake of Li ions, *vis a vis*:  $S + 2Li \rightarrow Li_2S$ , because the lower density of  $Li_2S$  (1.66 g/cc) compared to molten sulfur corresponds to a volume expansion. Thus, composites ranging up to 70wt% sulfur/composite were prepared (as confirmed by thermogravimetric analysis (TGA); **Figure 5.9**). This is less than the theoretical limit of 79wt% sulfur based on the pore volume of CMK-3 (2.1 g/cc) and the density of molten sulfur (1.82 g/cc), and precisely tuned for the volume expansion. Employing even lower S/C ratios provides less “stuffed” structures and additional porosity, but at the expense of reduced active mass. Most importantly, the electrical conductivity of the composites (~0.2 S/cm for 70:30 S/C) is the same as its OMC counterpart. The insulating sulfur merely occupies the empty channels in the OMC and does not block the electrical current transporting paths. Three-dimensional, multi electronic contacts are provided by the numerous carbon interconnects that span the channels as illustrated schematically in **Figure 5.2** and **Figure 5.7e**

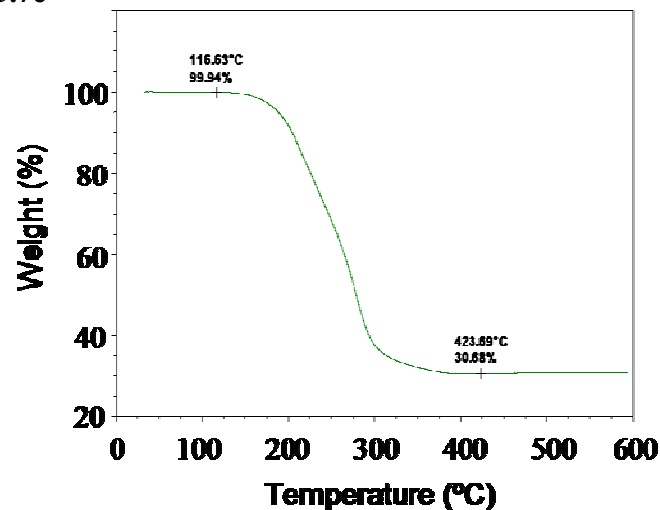


**Figure 5.9** Thermogravimetric analysis of a typical CMK-3/S composite in a  $N_2$  atmosphere with a heating rate of 20 °C/min, showing the sulfur content of 69.3wt%.

### 5.3.2.2 Electrochemical studies of CMK-3/S

#### 5.3.2.2.1 Electrochemical reduction mechanism of sulfur electrode

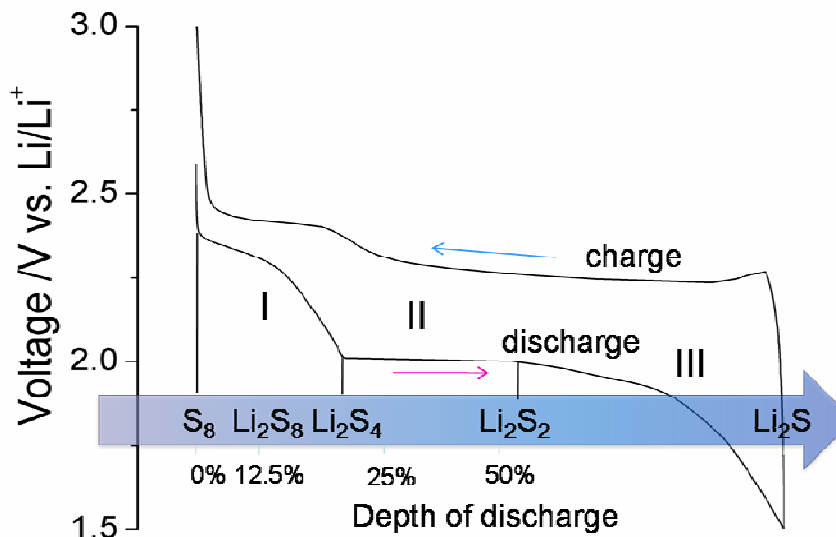


**Figure 5.10** Schematic diagram for an electrochemical reduction mechanism of a sulfur electrode with a depth of discharge of Li-S cells.

It is well known that an electrochemical reduction of sulfur is a very complicated process comprising a series of electron transfer reactions coupled with homogeneous chemical reactions [28]. The depth of discharge determines the electrode reactions and the corresponding coupled chemical reactions. As shown in **Figure 5.10**, a profile normalized to a 100% of utilization, there are three plateaus in the discharge. The first, which contributes a minor part to the overall capacity from 2.4 to 2.0 V, corresponds to the conversion from elemental sulfur ( $S_8$ ) to Li polysulfide anions ( $Li_2S_x$ ; where  $x$  is typically 4 to 5). The kinetics of this reaction are fast [29]. The second plateau at around 2.0 V, is due to the conversion of  $Li_2S_x$  ( $x$  is 4 or 5) to  $Li_2S_2$ . The last plateau, corresponding to the conversion from  $Li_2S_2$  to  $Li_2S$ , contributes to a half of the theoretical capacity. This solid-solid conversion process

occurs at a much slower rate [30].

### 5.3.2.2.2 Impact of encapsulation degree

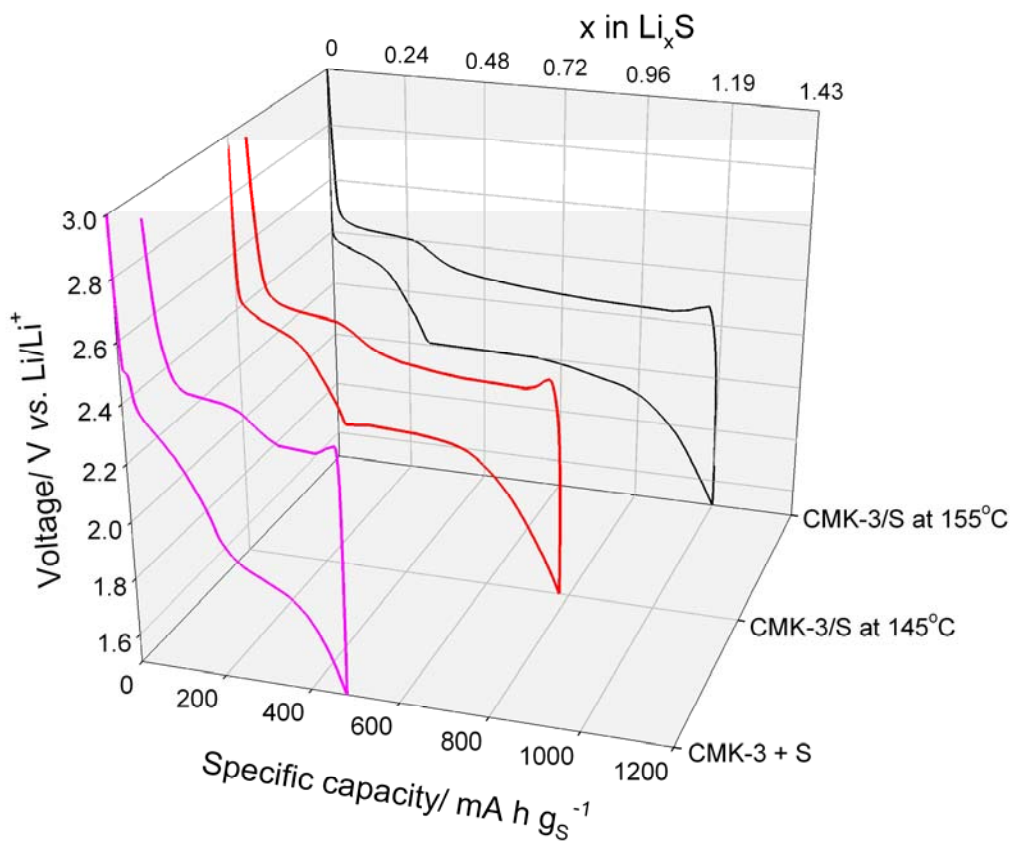


**Figure 5.11** Galvanostatic discharge and charge profiles of the first cycles of the carbon-sulfur composites at a current rate of 168 mA·h/g<sub>s</sub> (C/10).

The first discharge-charge curves for nanostructured CMK-3/S cathodes are shown in **Figure 5.11** and are compared with a simple physical (unheated) mixture of 7:3 weight ratio of sulfur and CMK-3. The nanostructured composite CMK-3/S-155, heated at 155 °C exhibits an impressive capacity of 1005 mA·h/g<sub>s</sub>. In contrast, the “macro-mixture” displayed

a typical reversible capacity of about 350 mA·h/g<sub>s</sub>, similar to that reported in literatures for C/S composites [15]. The capacity of CMK-3/S-155 was highly reproducible over many cells. The coulombic efficiency for CMK-3/S-155 in the first discharge-charge cycle is 99.94% without any overcharge, with virtually no irreversibility. This indicates that few lithium polysulfides dissolve into the electrolyte during the first redox cycle. The polarization was decreased by more than a factor of three, owing to the greatly enhanced electrical contact achieved in the nanostructure. Further unequivocal proof of the effectiveness of the contact arises from experiments in which the degree of S incorporation was varied. Nanostructured composites (CMK-3/S-145) with the same S/C ratio, but heated at 145 °C instead of 155°C result in less complete diffusion of sulfur into the channels because of the higher viscosity at the lower temperature. These composites showed less utilization of sulfur (capacity of 780 mA·h/g<sub>s</sub>) in the first discharge sweep (**Figure 5.11**), and an irreversible capacity of 50 mA·h/g<sub>s</sub> on charge.

Complete imbibition prevents sulfur agglomerates on the external surface of the mesoporous framework that would have poorer electrical wiring of the conductive carbon phase. These results are superior to those of sulfur in contact with multi-walled carbon nanotubes (MWNT), which exhibit lower capacities and a large electrochemical hysteresis [15]. Although sulfur is apparently confined in the carbon in that case, the contact is limited owing to the relatively large diameter (~50 nm) of the MWNT, and hence of the sulfur fibers within them. Thus, the efficiency of electron transfer to the sulfur mass, and accessibility to the Li<sup>+</sup> electrolyte plays an vitally important role in determining the electrochemical

behavior. As a nominal reversible capacity of  $\text{Li}_{1.2}\text{S}$  in the nanostructured composite CMK-3/S-155 is achieved, the limitations to full conversion will be the next to be explored.

### 5.3.2.2.3 Rate capability of CMK-3/S-155 cell

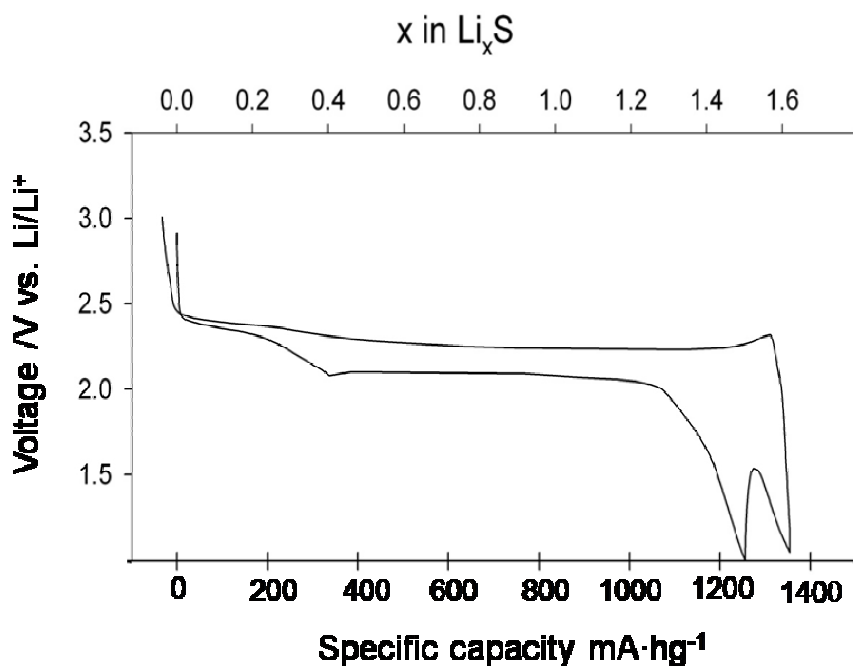


**Figure 5.12** Galvanostatic discharge/charge profiles of the first cycle of CMK-3/S-155 recorded at  $55^\circ\text{C}$  at  $168 \text{ mA/g}_s$  on discharge to 1.0 V followed by quasi-equilibrium discharge at  $16.8 \text{ mA/g}_s$ .

To gain a measure of the reversible capacity under conditions where the kinetics should be a minimal concern, discharge of the CMK-3/S cathode was carried out at  $55^\circ\text{C}$  at  $168 \text{ mA/g}_s$  to a cut-off voltage of 1.0 V, and allowed the voltage to relax to equilibrium. The discharge current was then switched to an equivalent  $16.8 \text{ mA/g}_s$  rate ( $C/100$ ) to the end of discharge, and completed charge at  $168 \text{ mA/g}_s$ . The electrochemical profiles are presented in **Figure 5.12**. Under these close-to-equilibrium conditions of full discharge, a reversible

capacity of  $1360 \text{ mA}\cdot\text{h/g}_s$  – 81% of the theoretical capacity ( $1672 \text{ mA}\cdot\text{h/g}_s$ ) was achieved. The slight overcharge is due to the dissolution of some polysulfide anions during the latter step. This also indicates that storage of the cell at partial or full discharge does not lead to significant capacity loss.

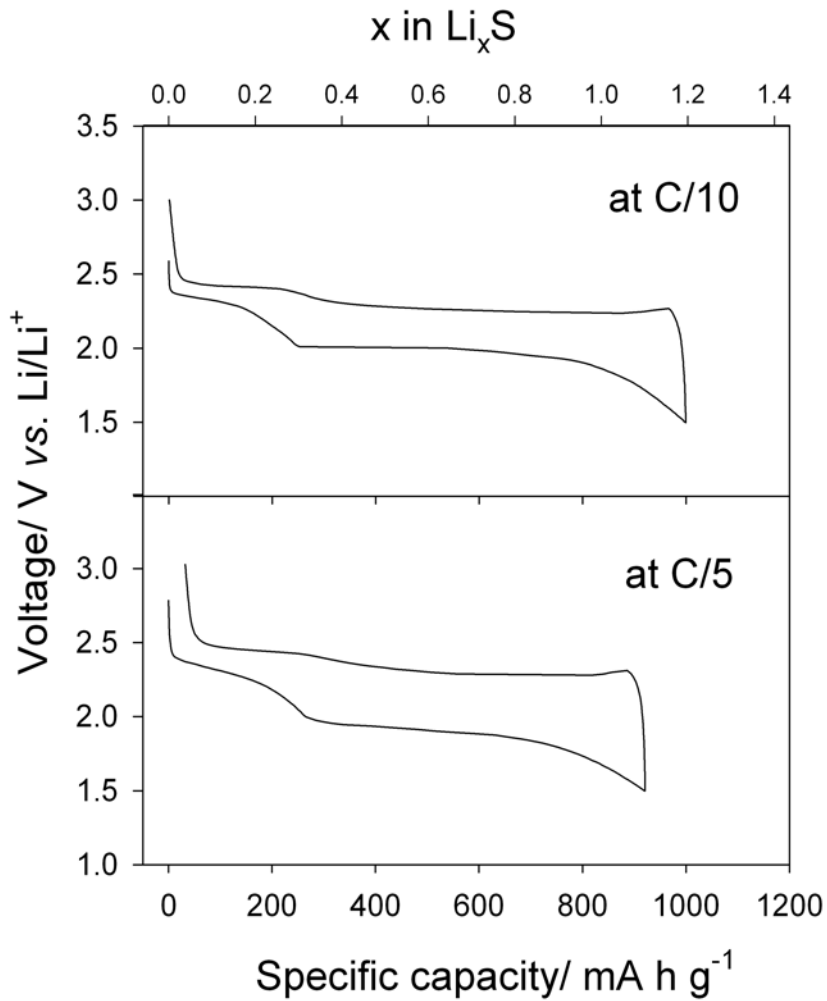


**Figure 5.13** The galvanostatic discharge and charge profiles of the first cycle of CMK-3/S-155 at  $336 \text{ mA/g}_s$  (C/5) compared to  $168 \text{ mA/g}_s$  (C/10).

The above results show that indeed, the kinetics of the last reaction step (from  $\text{Li}_2\text{S}_2$  to  $\text{Li}_2\text{S}$ ) in the discharge process plays a role in capacity limitation. A lower capacity was obtained at room temperature with equilibrium conditions, also indicating a transport problem of the Li-S cell. There is progressively more limited accessibility of  $\text{Li}^+$  ions and electrolyte to the sulfur mass towards the end of discharge since the pores become accommodated with insoluble  $\text{Li}_x\text{S}$  ( $x = 1-2$ ) - even though at 70wt% sulfur loading, there is sufficient space for the volume expansion based on the conversion of S to  $\text{Li}_2\text{S}$ . However, it was observed that in doubling the rate from 168  $\text{mA/g}_s$  to 336  $\text{mA/g}_s$ , the capacity is only reduced by a small amount to 930  $\text{mA}\cdot\text{h/g}_s$  (**Figure. 5.13**).

#### 5.3.2.2.4 Cycling life of Li-S cells

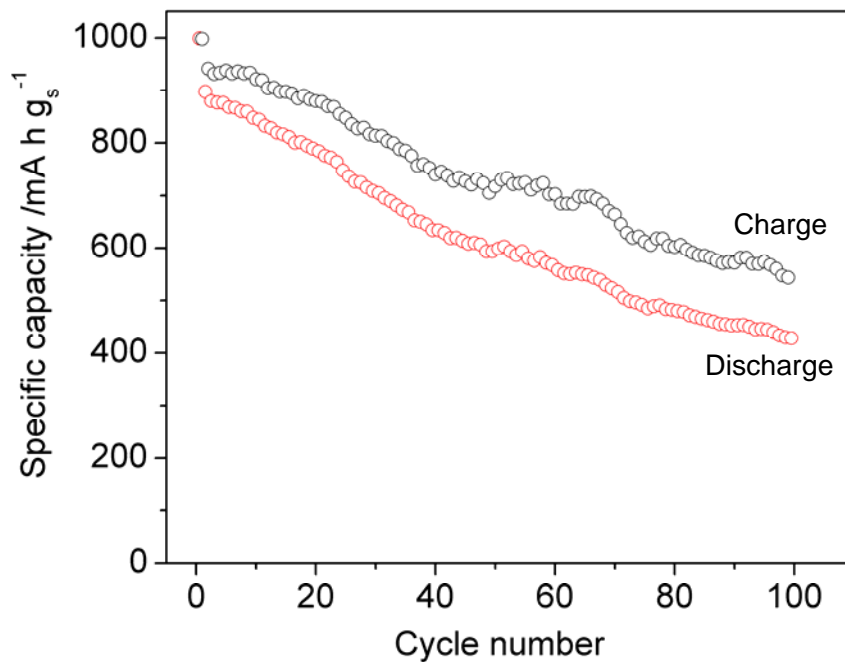


**Figure 5.14** Cycling life of CMK-3/S-155 at 168  $\text{mA/g}_s$  (C/10) at 300K.

The long-term cycling of a Li-S cell based on the CMK-3/S composite is shown in **Figure 5.14**. The cell suffers a certain degree of capacity degradation on repeated discharge-charge. Although the OMC clearly performs very well at the very beginning as a sulfur container, it still allows for some egress of dissolved sulfur species. The tortuous inner path retards the diffusion of the bulky polysulfide anions out from the channels into the electrolyte, but cannot entirely prevent it. The overcharge (difference between a charge capacity and the corresponding discharge capacity) indicates a weak shuttle mechanism. The ratio between a discharge capacity and the following charge capacity is defined as coulombic efficiency. The coulombic efficiency of this cell descends from 1 to 0.8 in 100 cycles, as shown in **Figure 5.15**. Note that excessive lithium is employed in all the galvanostatic cycling measurements; therefore, any decrease in discharge capacity in this study does not come from the depletion of a lithium anode.

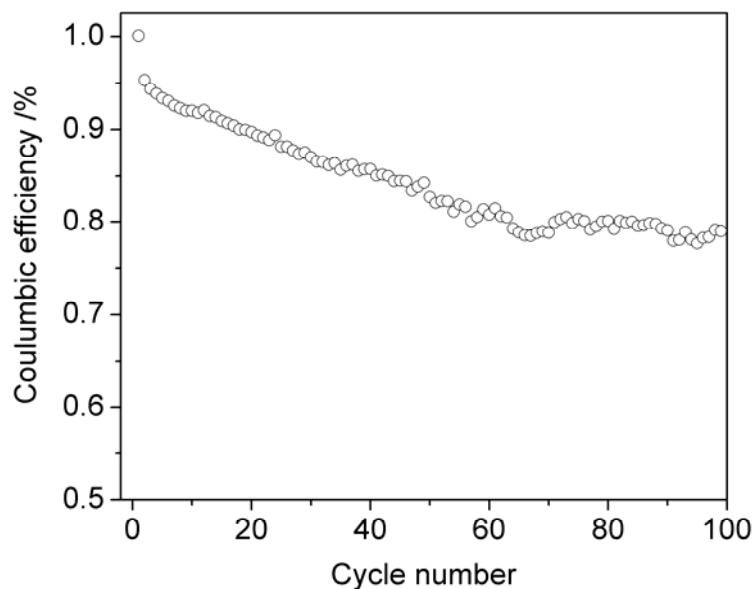


**Figure 5.15** Coulombic efficiency of CMK-3/S-155 on cycling.

The Li-S cell based on the CMK-3/S-155 composite maintained a discharge capacity of 400 mA·h/g<sub>s</sub> at 200<sup>th</sup> cycle with a current rate of 336 mA/g<sub>s</sub> (C/5), as shown in **Figure 5.16**. At 336 mA/g<sub>s</sub>, a charge or discharge process of the cell is completed in 3 hrs in the first cycle and 1.2 hrs in the 200<sup>th</sup> cycle. Actually, a C-rate cannot clearly define the current rate due to the capacity degradation of the cell. The real C-rate increases from C/3 (instead of C/5) in the first cycle to C/1.2 in the 200<sup>th</sup> cycle. Although the capacity fades on a long term cycling, 400 mA·h/g<sub>s</sub> at 200<sup>th</sup> cycle is still more than twice of the maximum specific capacity which conventional lithium metal oxides or phosphates can provide in their topotactic reactions. The average discharge voltage of a Li-S cell is 2.2 V, in comparison with 3.5 to 4.2 V of the conventional Li ion cells. The Li-S cell in this study at its 200<sup>th</sup> cycle still can generate an energy density of 880 W·h/kg, compared to 756 W·h/kg which a best conventional Li ion cell can provide.

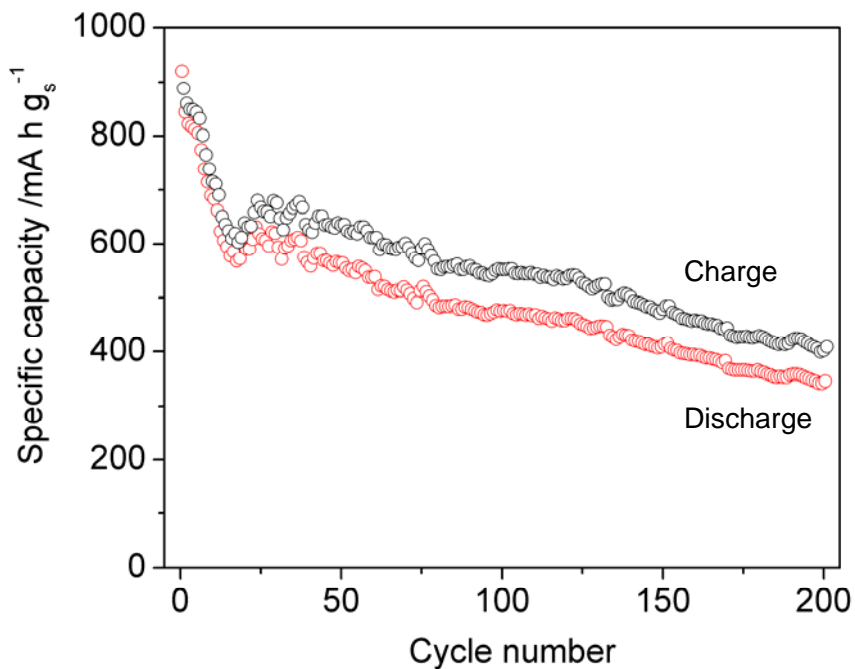


**Figure 5.16** Cycling life of CMK-3/S-155 at 336 mA/g<sub>s</sub> (C/5) at 300K.

### 5.3.2.3 Electrochemical studies of C/S composites based on other OMC's

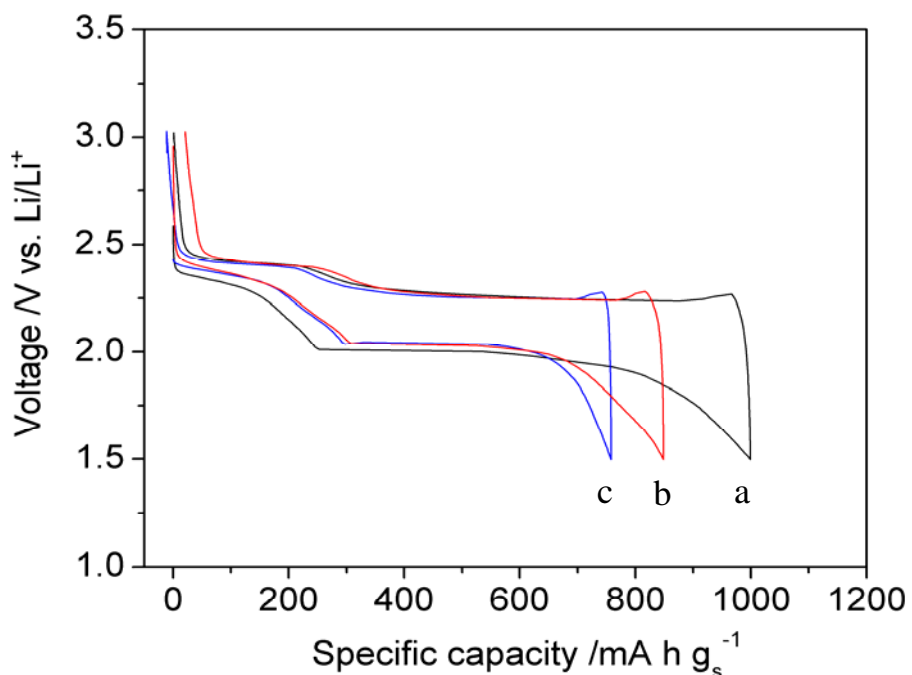


**Figure 5.17** The galvanostatic discharge and charge profiles of the first cycle of various composites a) CMK-3/S; b) CMK-8/S; c) GCMK-3/S at a current rate of 168 mA/g<sub>s</sub> (C/10).

As shown in **Figure 5.17**, both GCMK-3/S and CMK-8/S exhibit less specific capacity than does CMK-3/S. The lower capacity of GCMK-3/S is probably due to the limited electric contact between encapsulated sulfur in the larger voids (pore size: 11.5 nm) and carbon walls in the bimodal porous structure of GCMK-3 (**Table 5.1**). The irregular morphology of CMK-8 (**Figure 5.3d**) may negatively impact on its capacity. Nevertheless, it is evident that both GCMK-3/S and CMK-8/S exhibit slightly less polarization (the gap

between a discharge curve and the following charge curve) than does CMK-3/S, which is indicative of better mass and/or charge transportation in CMK-8/S and GCMK-3/S composites. This can be attributed to the 3D bi-continuous structure of CMK-8 and the higher electric conductivity of GCMK-3.

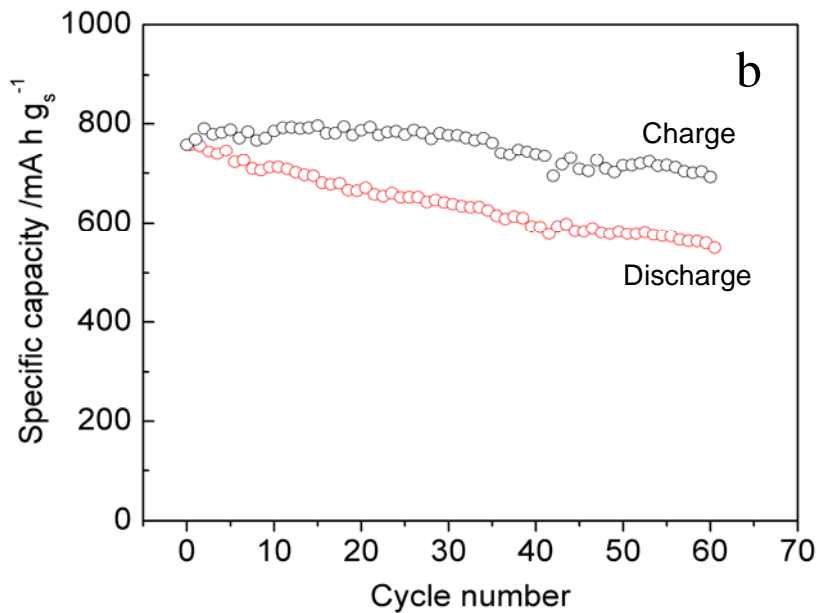
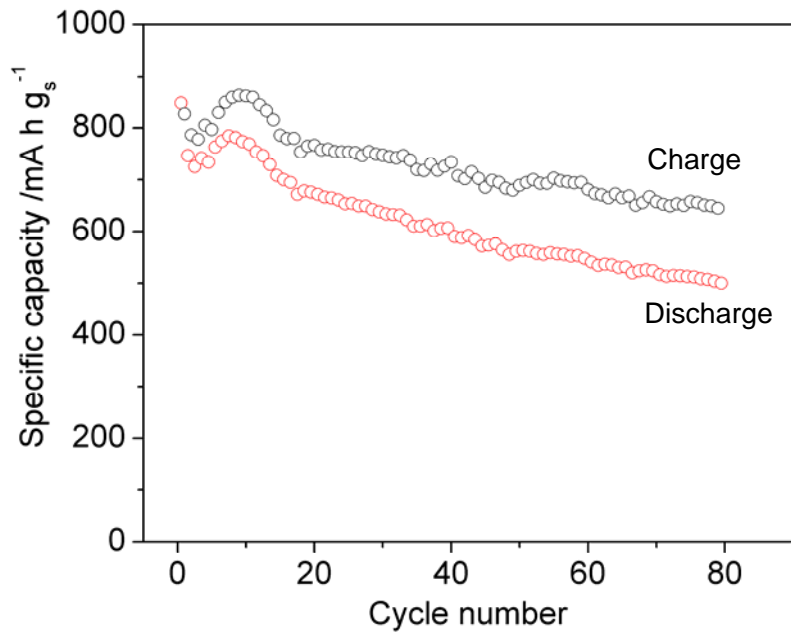


**Figure 5.18** Cycling life of a) CMK-8/S; b) GCMK-3/S at 168 mA/g<sub>s</sub> (C/10) at 300K.

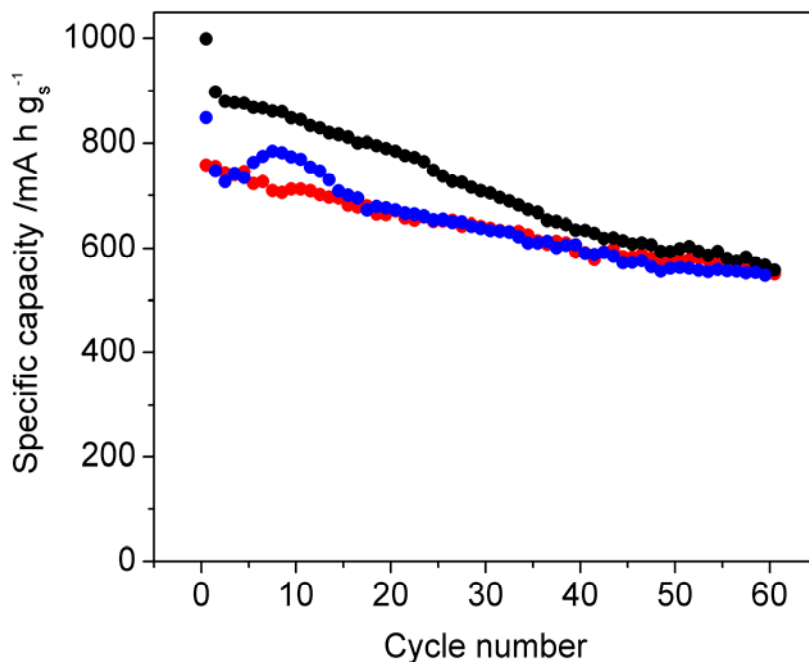


**Figure 5.19** Cycling life (discharge capacity only) of a) CMK-3/S (black); b) GCMK-8/S (blue); c) GCMK-3 (red) at 168 mA/g<sub>s</sub> (C/10) at 300K.

As shown in **Figure 5.18a, b**, both CMK-8/S and GCMK-3/S composites exhibit a certain degree of capacity degradation and the polysulfide shuttle phenomenon. **Figure 5.19** displays the comparison of all the different composites. Interestingly, they maintain a discharge capacity of ~560 mA·h/g<sub>s</sub> at the 60<sup>th</sup> cycle no matter what capacity these materials started with.

The results here suggest that physical characteristics of OMC, such as conductivity and pore symmetry, are not the key parameters which can be tuned to completely prevent polysulfide anions from diffusing into electrolyte. Physical and/or chemical barriers also

need to be introduced onto the external surface of OMC/S composite particles. In the following section, I describe polymer functionalized OMC/S materials, where the polymers are hydrophilic polyethylene glycols that play the role of not only a physical barrier, but possibly as a chemical trap.

### **5.3.3 Polymer coating strategy for stabilizing capacity of Li-S cells**

#### **5.3.3.1 Brief introduction**

Nanostructured organic/inorganic materials can exhibit beneficial chemical and physical properties that arise from the combination of components, which makes them indispensable for many advanced applications [31]. However, synthesis of such materials can be difficult. Polymer functionalized ordered mesoporous carbons (OMC), with surface properties from polymer and electrical, architectural properties from OMC are of great interest, particularly in energy related applications. To my best knowledge, polyethylene glycol (PEG), for the first time, is tethered onto the external surface of OMC/sulfur composite through the ester bonding. To prepare PEG coated composites (CMK-3/S-PEG), the entire surface of CMK-3 was functionalized with carboxylic group by concentrated nitric acid treatment at 80 °C for 30 min, prior to the impregnation of sulfur. Ester bonds are formed in the reaction between the hydroxyl group of PEG and the carboxylic group on the external surface of the CMK-3/S composite.

To further prevent polysulfide anions from diffusing into electrolyte, physical and/or chemical barriers are necessary to be introduced onto the external surface of OMC/S composite particles. The following three requirements should be considered for an efficient barrier. (i) A barrier should be firmly and homogeneously coated onto carbon surface, which

necessitates chemical bonding between it and carbon. (ii) As a chemical trap, it should attract polysulfides through effective interactions. (iii) It also needs to have low density to maintain high energy density of a cell. Under certain conditions, PEG chains potentially satisfy the above requirements. The CMK-3/S-PEG composite was investigated and employed as a cathode material in Li-S cells.

### 5.3.3.2 Physical characterizations of PEG coated composites

The chemical attachment of the PEG to CMK-3 is evident by TGA (**Figure 5.20**). The combustion of the PEG tethered to the CMK-3 occurs at 50°C higher than in PEG itself due to the ester bonds.

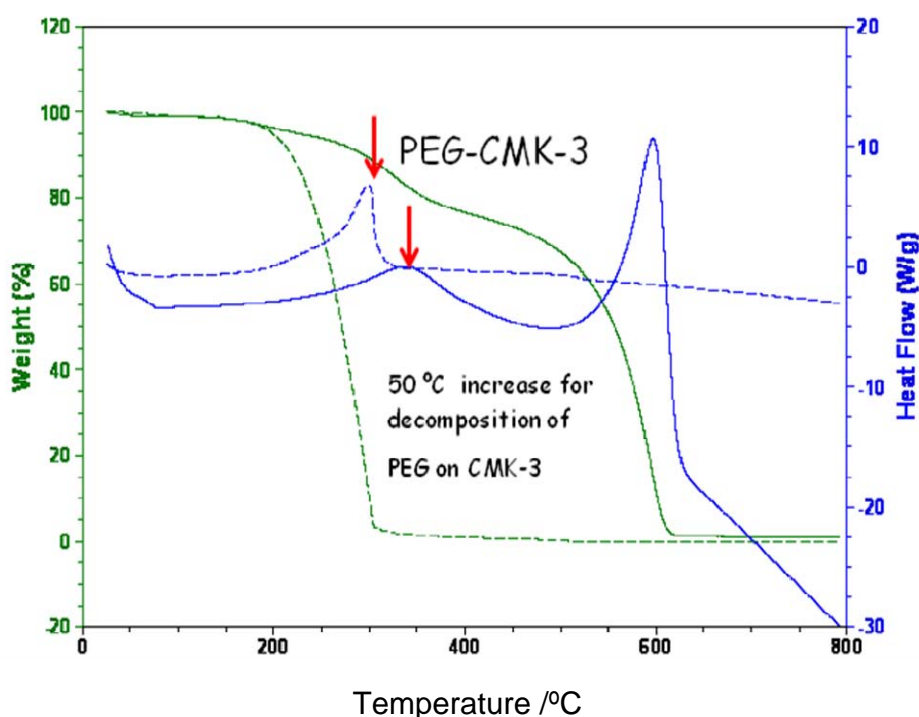


**Figure 5.20** Thermogravimetric analysis of the PEG4600 modified CMK-3 in air with a heating rate of 20 °C/min, compared with PEG4600 itself. The PEG4600 TGA and DSC curves are shown as dashed lines, and PEG-CMK-3 as solid lines.

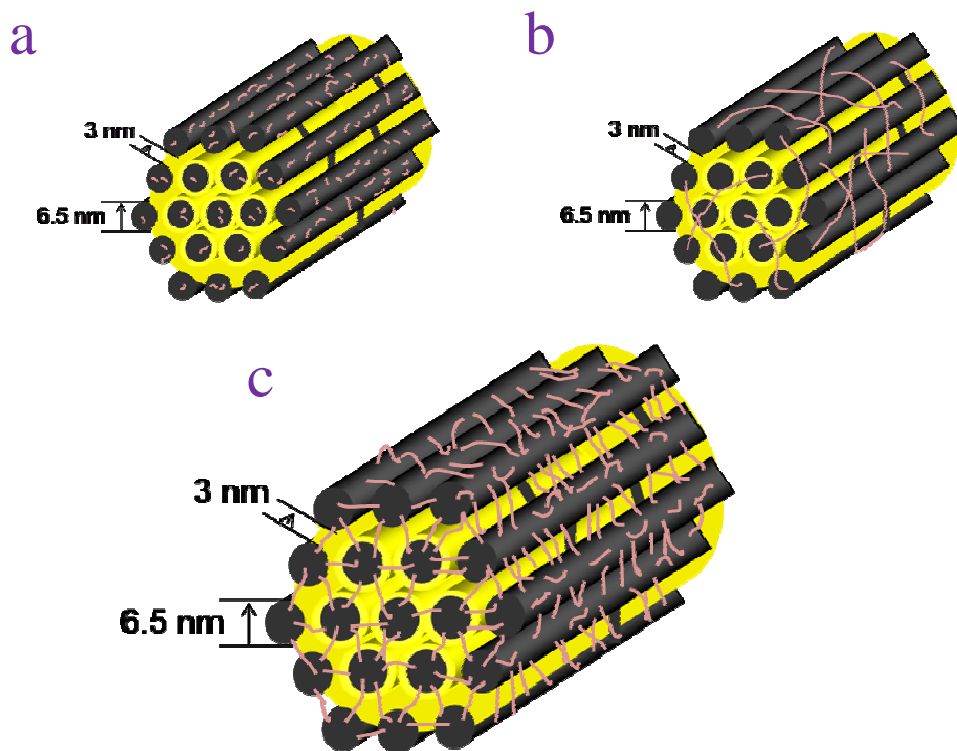


**Figure 5.21** Schematic showing PEG coated CMK-3/S composites which comprise: a) PEG200; b) PEG4600; c) PEG600.

PEG chains with molecular weight of 200, 600, and 4600 were employed to modify the CMK-3/S composite. Based on the distance between neighboring carbon nanofibers that form the arrays in CMK-3 [32,33] and our TEM results (**Figure 4.4** and **Figure 5.3**), PEG chains should be no shorter than 3 nm in order to bridge two neighbouring parallel carbon nanofibers in CMK-3 framework. Obviously, PEG200 (stretched chain length: ~1.2 nm) cannot span the carbon nanofibers and thus must not form a continuous coating on the

surface. On the other hand, PEG4600 chains (~26 nm) cannot tightly wrap the CMK-3 framework. Polysulfides can easily diffuse into electrolyte through this loosely packed coating. It is therefore postulated that an optimum chain length to provide both a chemical and physical barrier should range from 3 to 5 nm, *i.e.*, PEG600 (~ 4 nm). **Figure 5.21** shows a schematic of the arrangements that might be expected for the various glycol chains.

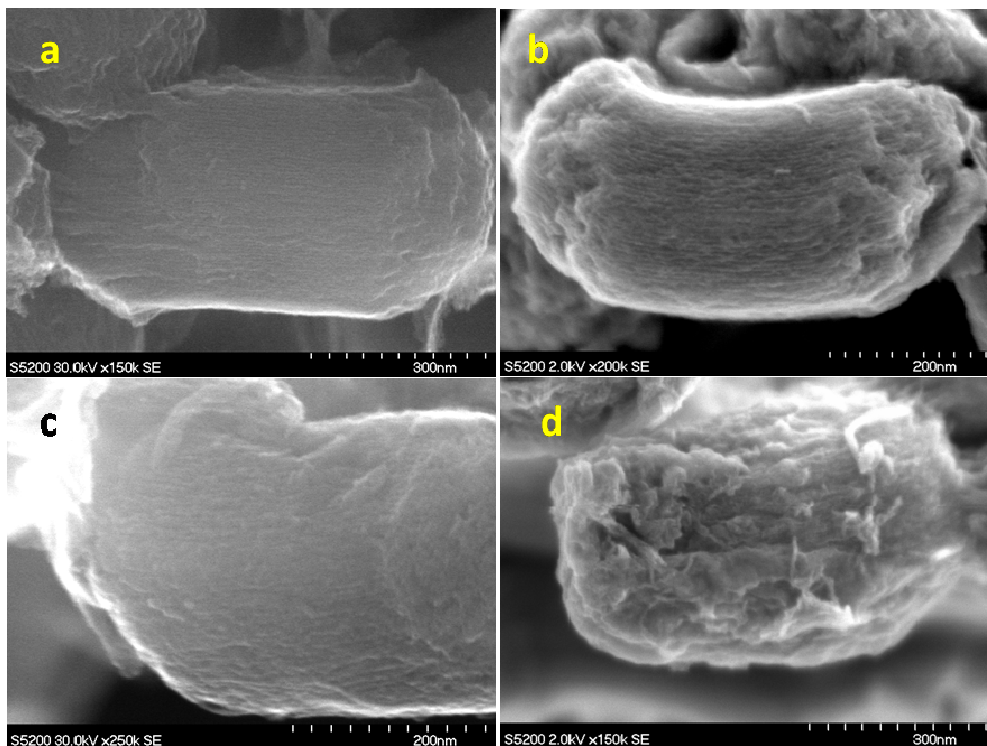


**Figure 5.22** SEM images of a) CMK-3/S and PEG coated CMK-3/S materials b) PEG200 coated; c) PEG600 coated; d) PEG4600 coated.

A PEG mass of about 4wt% in these composites was determined based on elemental analysis. The surface morphology, investigated with high resolution SEM, shows that CMK-3/S and CMK-3/S-PEG200 are essentially the same, presumably due to the short chain length

of PEG200 (**Figure 5.22a,b**). CMK-3/S-PEG600 exhibits a partially ordered surface, and CMK-3/S-PEG4600 displays disordered fibre-coated-like surface morphology (**Figure 5.22c, d**).

### 5.3.3.3 Electrochemical studies of CMK-3/S-PEG600

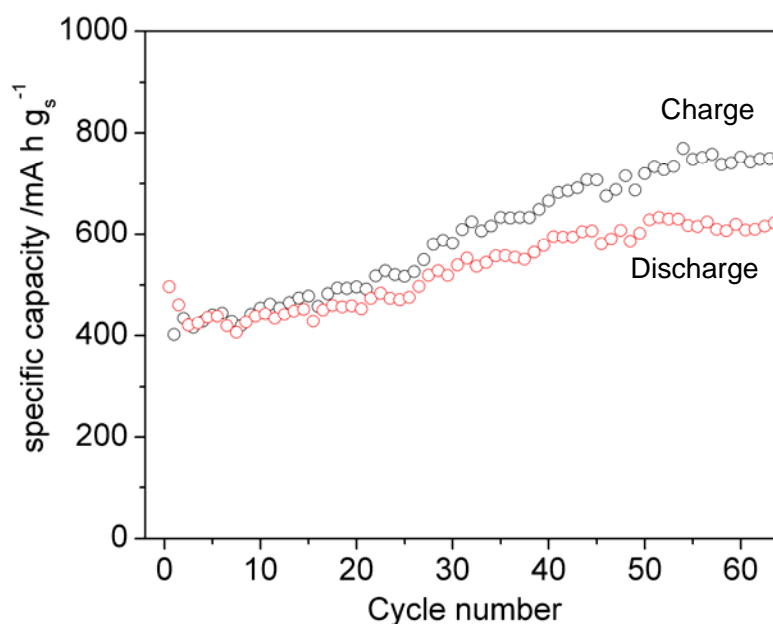


**Figure 5.23** Cycling life of CMK-3/S-PEG600 at 168 mA/g<sub>s</sub> (C/10) at 300K.

**Figure 5.23** shows the galvanostatic cycling of CMK-3/S-PEG600. The discharge capacity increases on cycling and stabilizes at 630 mA·h/g<sub>s</sub> after 65 cycles. The physical barrier imposed by PEG600 coating functions very well at the earlier stages of the cycling life. The absence of overcharge in the first 20-30 cycles indicates that the concentration of polysulfides in the electrolyte is very low. However, the overcharge becomes increasingly significant on cycling, indicative of polysulfide dissolution in the electrolyte. This is

probably due to the detachment of the PEG600 coating on the CMK-3/S composite through cleavage of the ester groups.

Note that only the bridging PEG chains are easily removed. Nevertheless, the non-bridging PEG600 should be firmly attached to carbon nanorods of a composite during cycling (see **Figure 5.24**).

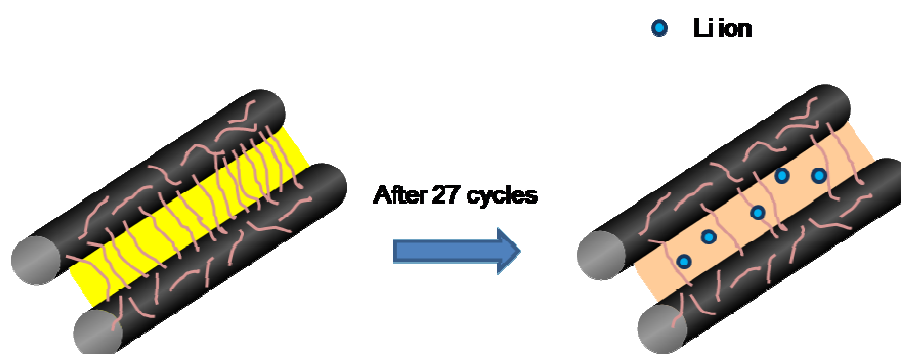


**Figure 5.24** Schematic showing detachments of PEG chains from composite surface.

#### 5.3.3.4 Electrochemical studies of CMK-3/S-PEG4600 and CMK-3/S-PEG200

The breach of the PEG600 coating does not result in capacity degradation. Recall that unmodified Li negative electrode is used in this study. It can be concluded that the stability of the cell is due to the positive electrode which has been improved by PEG, even when a physical barrier towards polysulfide anions does not exist. To simulate what happens in CMK-3/S-PEG600 after the PEG600 coating breaks, the electrochemistry of CMK-3/S composites coated by PEG4600 and PEG200 were investigated by galvanostatic cycling, as shown in **Figure 5.25**.

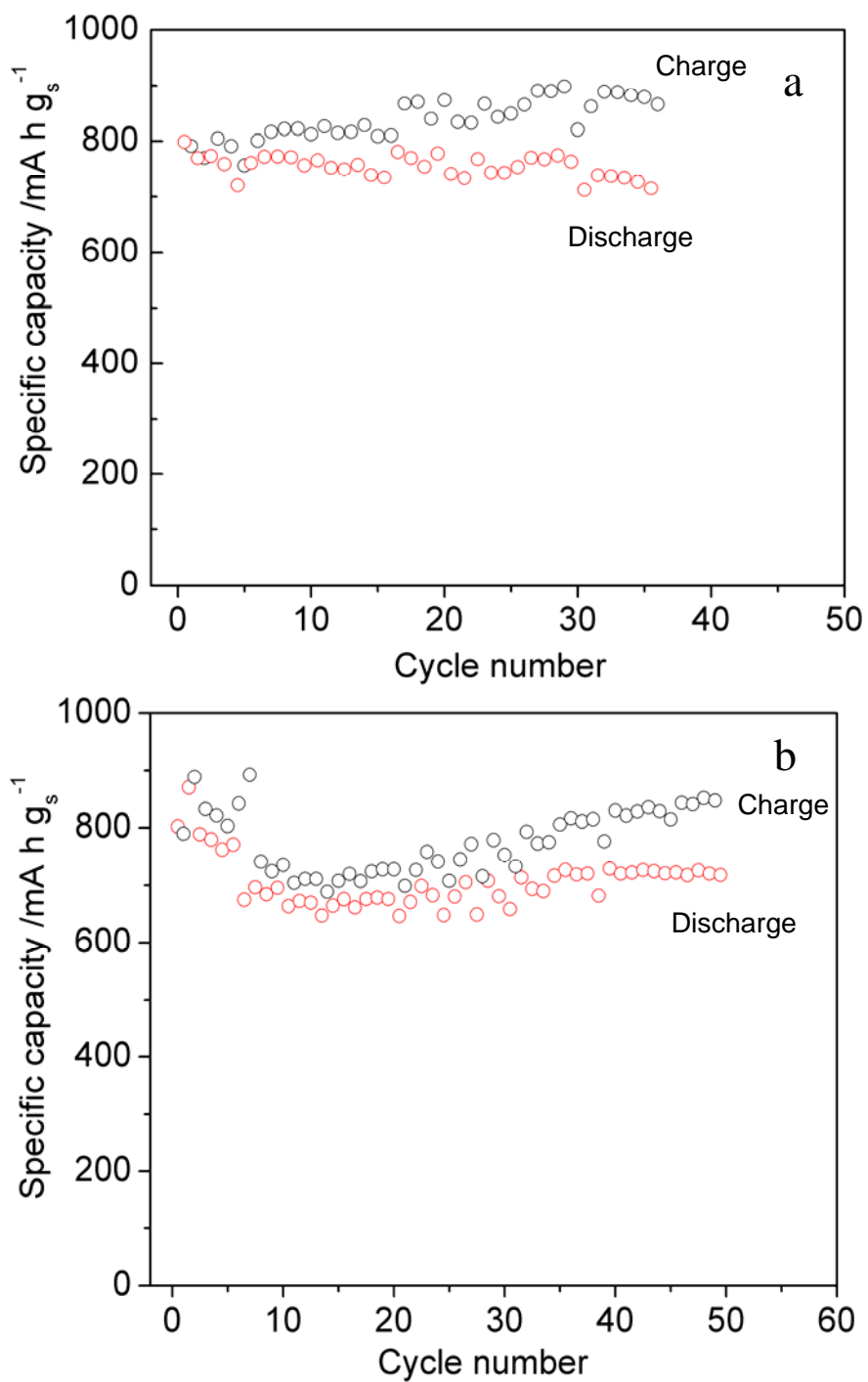


**Figure 5.25** Cycling life of a) CMK-3/S-PEG4600; b) CMK-3/S-PEG200 at 168 mA/g<sub>s</sub> (C/10) at 300K.

For CMK-3/S-PEG4600, the discharge capacity does not fade on cycling although overcharge appears after 4 cycles (Figure 5.25a). For CMK-3/S-PEG200, some overcharge appears on the 3<sup>rd</sup> cycle (Figure 5.25b). Nevertheless, both CMK-3/S-PEG200 and CMK-3/S-PEG4600 exhibit fairly stable cycling life.

The comparison of the discharge capacity of all the related composites is shown in Figure 5.26. As is clear, none of the PEG coatings can entrap the polysulfide anions for more than 30 cycles but they still stabilize the capacity in strong contrast to the CMK-3/S composite. The mechanism for this will be discussed in the next section.

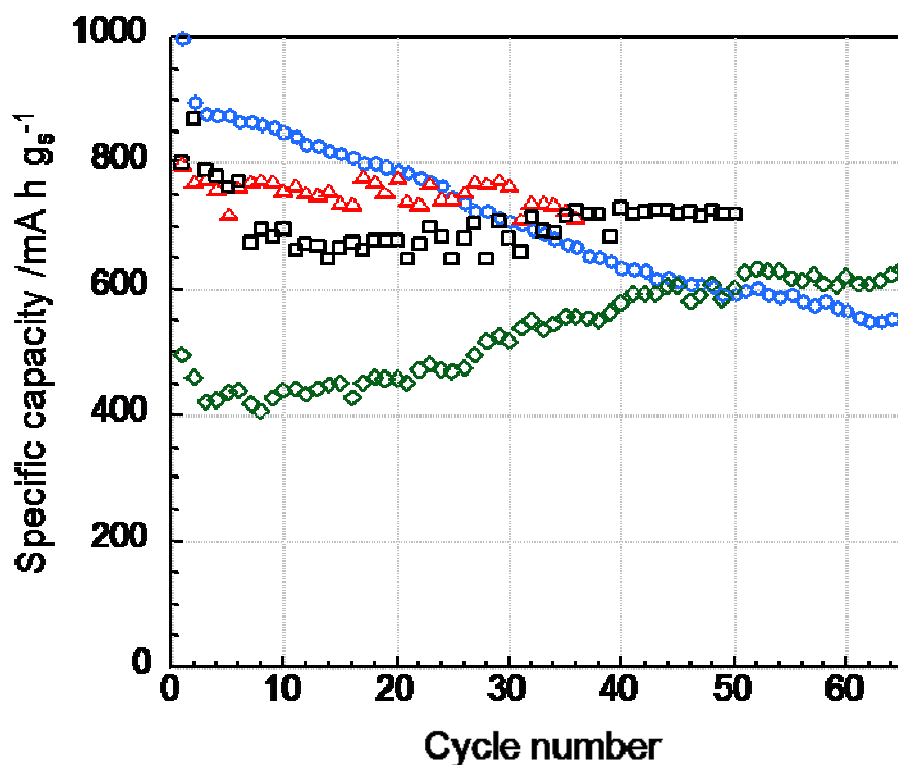
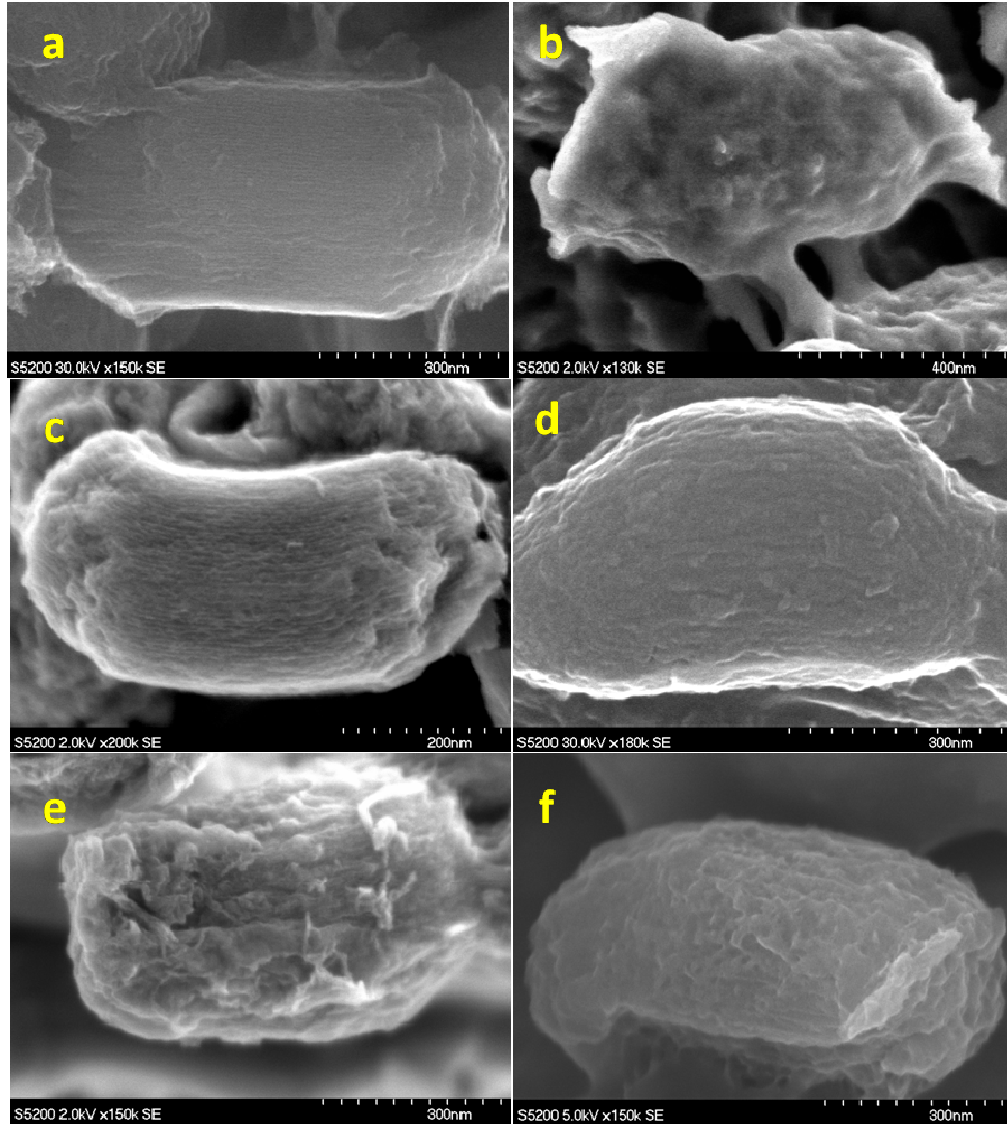


Figure 5.26 Cycling life of a) CMK-3/S, (blue); b) CMK-3/S-PEG200 (Black); c) CMK-3/S-PEG4600 (Red); d) CMK-3/S-PEG600 (Olive).

### 5.3.3.5 Passivating mechanism of PEG on CMK-3/S



**Figure 5.27** SEM images of surface morphology of composites before cycling and after 15<sup>th</sup> charge a), b) CMK-3/S; c), d) CMK-3/S-PEG200; e), f) CMK-3/S-PEG4600.

The loss of active mass due to the formation of irreversible sulfides on the positive electrode has been one of the most challenging problems for Li-S batteries [7]. This problem still occurs in the CMK-3/S cathode, exhibited by SEM images before and after cycling and results in extensive precipitation of insoluble products on the surface of the OMC particles as shown in **Figure 5.27a, b**. Such precipitation is not observed to the same degree in the PEG coated OMC particles which undergo a very low degree of surface morphology change on cycling, as shown in **Figure 5.27 c-f**.

The reason for the diminished precipitation of insoluble sulfides on the PEG-modified CMK-3/S is not completely clear, but may arise from two factors. One is that the polymer helps retain the polar polysulfide species ( $S_x^{2-}$ ) formed on initial reduction of the  $S_8$  molecules by providing a highly hydrophilic surface with a chemical gradient. This preferentially solubilizes them *vis a vis* the electrolyte. If the polysulfides diffuse into the electrolyte, they are partially reduced to solid precipitates ( $Li_2S_2$  and/or  $Li_2S$ ) on the anode, and/or redeposited on the cathode in the next cycle, resulting in high polarization and poor coulombic efficiency. By limiting the concentration of the polysulfide anions in the electrolyte, the deposition of insoluble sulfur species on the cathode is inhibited. In addition, the insulating polymer-coated surface may inhibit the reduction of any solubilized polysulfide anions. Therefore, the sulfide anions must gain access to the inner (unmodified) channels of OMC for electrochemical reduction to occur. This may effectively prevent precipitation on the external surface of OMC, which would further block access and further discharge of the cell. This could explain the coexistence of stabilized cycling life and a certain degree of overcharge.

### 5.3.3.6 Optimization of capacity in the PEG-modified material

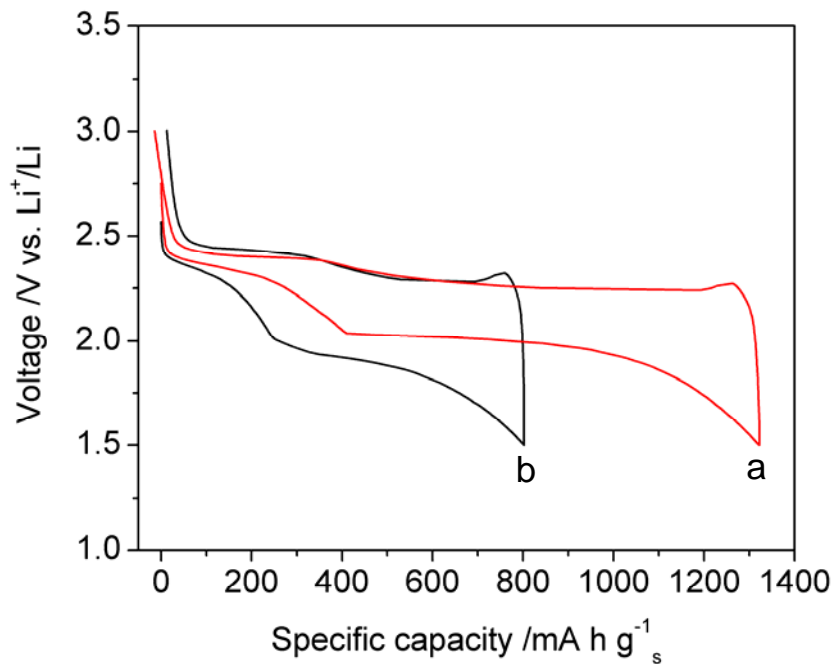


Figure 5.28 The galvanostatic discharge and charge profiles of the first cycle of a) PEG200 modified CMK-3/S (45:55 in weight); b) PEG200 modified CMK-3/S (30:70 in weight).

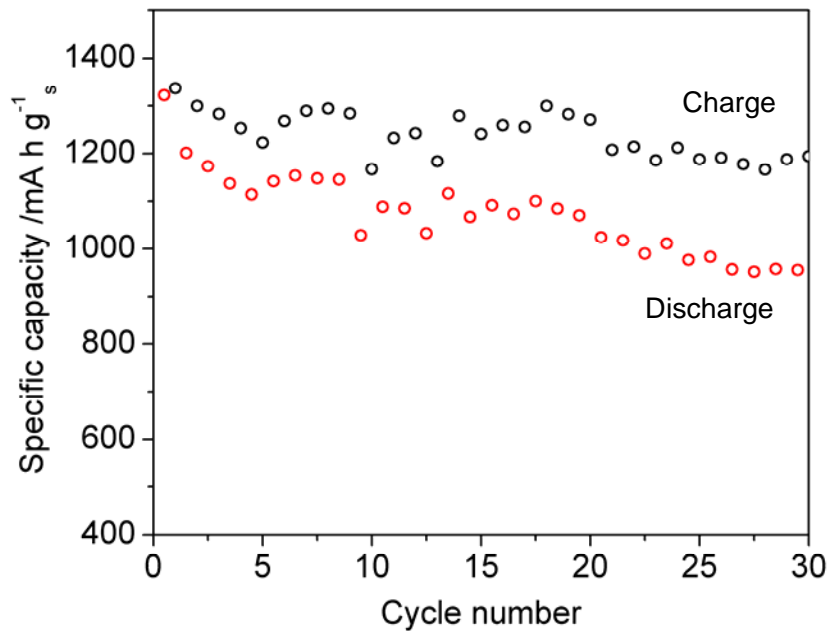
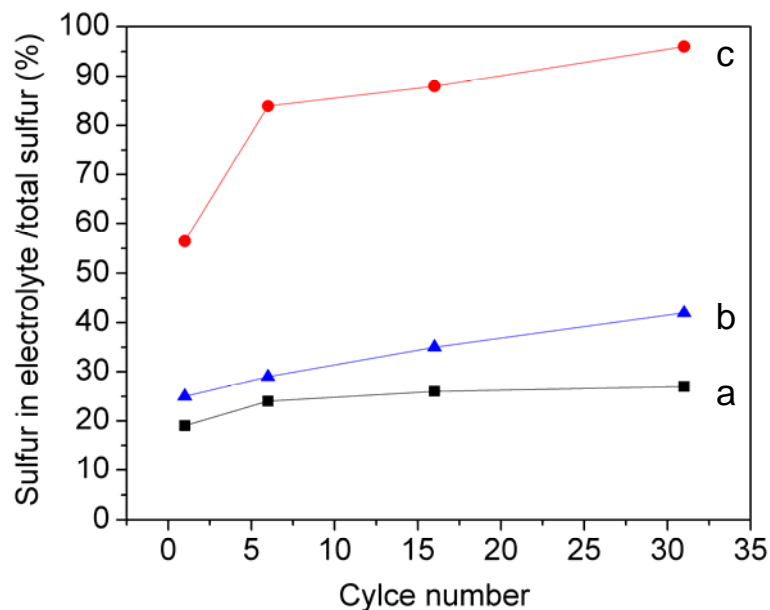


Figure 5.29 Cycling life of PEG200 modified CMK-3/S (C/S 45:55 in weight) at 168  $\text{mA/g}_s$  (C/10) at 300K.

In another PEG200 modified CMK-3/S composite, a lower S/C ratio (55:45, instead of 7:3 in weight) provides a less “stuffed” structure and additional porosity. The results that compare the two sulfur/carbon loadings are shown in **Figure 5.28**. The extra space can give rise to a better mass and/or charge transfer in the positive electrode. Thus, the accessibility of  $\text{Li}^+$  ions to the active mass is not limited even near the end of a discharge when the volume of the active mass is maximized due to the formation of  $\text{Li}_2\text{S}$ . Under these optimum conditions, the cell exhibits a capacity of  $1320 \text{ mA}\cdot\text{h/g}_s$ , about a factor of 1.6 greater than that of the more “stuffed” PEG modified composite. The cell also shows relatively stable cycling life, as shown in **Figure 5.29**. This same approach for the CMK-3/S materials has been attempted but without the same success.

### 5.3.3.7 Analysis of sulfur retention on cycling



**Figure 5.30** Percentage of sulfur dissolution into electrolyte from a) CMK-3/S-PEG200 composite cathode; b) CMK-3/S composite cathode; c) a cathode made of a mixture of acetylene black carbon and sulfur with the exact same C/S ratio.

The retention of sulfur active mass on cycling in the PEG modified CMK-3/S composite and unmodified CMK-3/S is demonstrated in **Figure 5.28a, b**. To measure the degree of sulfur retention in the cathode, a 1.0 M LiPF<sub>6</sub> solution in a sulfur-free solvent, tetra(ethylene glycol) dimethyl ether (TEGDME), was used as the electrolyte. Glyme solvents are known for their excellent ability to dissolve polysulfides, and hence represent an “aggressive” case. Compared to the cathode made of mixture of sulfur and acetylene black which loses 96% of the total active mass into the electrolyte after 30 cycles and the composite of CMK-3/S which loses 42% (**Figure 5.28c**), the PEG modified composite shows significant retention of sulfur. Only 27% of total active mass is solubilized in the electrolyte after 30 cycles. It is believed that the effect of the PEG functionalized surface is twofold. First, it serves to trap the polysulfide species by providing a highly hydrophilic surface chemical gradient that preferentially solubilizes them *vis a vis* the electrolyte. Second, by limiting the concentration of the polysulfide anions in the electrolyte, the redox shuttle mechanism is curtailed to a large degree and deposition of insoluble sulfur species on surface of Li electrode and formation of irreversible Li<sub>2</sub>S on cathode surface are strongly inhibited. The latter point is clearly demonstrated in SEM images of PEG-functionalized CMK-3/S cathode before and after cycling, which exhibit very little change in surface morphology (**Figure 5.27**), compared to CMK-3/S which clearly shows extensive precipitation of insoluble products on the surface of the OMC particles.

### 5.3.3.8 Investigation of self-discharge

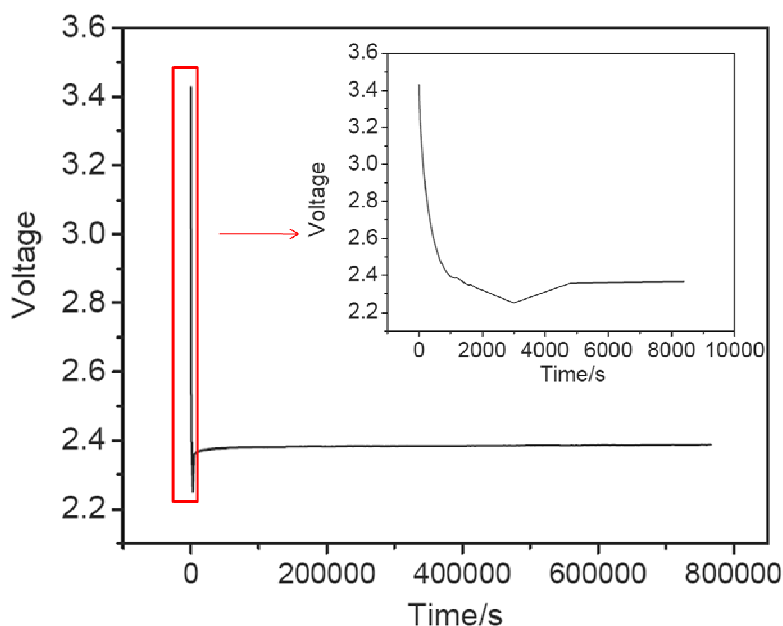


**Figure 5.31 Galvanostatic discharge profile for PEG200 modified CMK-3/S (C/S 45:55 in weight) at 168 mA/g<sub>s</sub> (C/10) at 300K until a voltage of 2.25 V was reached, followed by a rest for 9 days at open circuit voltage.**

According to the discharge profile normalized to a 100% of utilization (**Figure 5.10**), sulfur in the cathode is transformed into one or several types of soluble polysulfide ions ( $S_x$ ) at 2.25 V, and  $x$  is between six and eight. At this point, self-discharge occurs for Li-S cells where polysulfide ions can diffuse out of cathode and shuttle phenomenon takes place. The polysulfide ions ( $S_x$ ) would be reduced to ones with shorter chains which will be further reduced until an insoluble active mass forms. Consequently, open circuit voltage (OCV) of a cell would decrease gradually, which qualitative and quantitatively to some degree measures the self-discharge. To investigate the possible self-discharge on the polymer decorated sulfur electrode, the cell was switched into a rest mode after the voltage of 2.25 V was reached in a discharge process at a current rate of 168 mA/g<sub>s</sub>. As shown in the **Figure 5.31**, the open

circuit voltage remains the same after it stabilizes to a higher (equilibrium) value of 2.38 V on the mode switch, which illustrates the absence of the self-discharge of the polymer decorated composite cathode.

#### 5.3.3.9 Summary of the polymer coating strategy

CMK-3/S nanocomposite frameworks are shielded by a PEG600 layer. Dissolution of polysulfides is inhibited to a large degree in the first 25 cycles. Although polysulfide anions eventually made their way into the electrolyte, the PEG chains, apparently the non-bridging ones, still form a passivation layer on the external surface of CMK-3/S particles, preventing precipitation of irreversible sulfides on the composite surface, which stabilizes the cycling life. The PEG coating strategy for CMK-3/S composite represents a promising methodology to solve problems of Li-S cells by constructing multi-functional nanostructures.

### 5.4 Conclusions

In summary, the strategy illustrated here provides a versatile route to nanostructured PEG modified OMC-sulfur composites that display all the benefits of confinement effects at a small length scale. Intimate contact of the insulating sulfur and discharge product sulfides with the retaining conductive carbon framework at nanoscale dimensions affords excellent accessibility of the active material. The carbon framework not only acts as an electronic conduit to the active mass encapsulated within, but serves as a mini-electrochemical reaction chamber. The entrapment ensures more a complete redox process takes place, and results in fuller utilization of the active sulfur material. This is vital to the success of all conversion reactions to ensure full reversibility of the back-reaction. The PEG coating further helps to minimize the loss of the active mass in the cathode and improve the cycling stability. The

composite materials reported here can supply up to 80% of the theoretical capacity of sulfur (1320 mA·h/g<sub>s</sub>), representing about 3 times the energy density of lithium transition metal oxide (LTMO) cathodes, at reasonable rates with good cycling stability. Owing to the flexibility of the methodology, the high capacity of the carbon for active material incorporation and facile functionalization of the surface, I believe that a wide variety of nanostructured “imbibed” composites could find broad applications in many areas of materials science, not only as advanced electrode materials that rely on conversion reactions.

## Chapter 6

# Nucleated Growth of Nanocrystalline Metal and Intermetallics in Ordered Mesoporous Carbon: Direct Formic Acid Fuel Cell Anodes

### 6.1 Introduction

Direct formic acid fuel cells (DFAFC) show great prospects for micro power generation mainly because formic acid exhibits much lower crossover through Nafion<sup>®</sup> membranes compared to methanol. As described in **section 1.3.3.2**, it is well known that the self-poisoning on pure Pt, during catalytic formic acid oxidation, can be effectively inhibited by the breach of Pt ensembles [1,2]. Many methods have been employed to prepare PtM (M: Bi or Pb) intermetallic nanoparticles. Literature reports cite difficulty in synthesizing intermetallics in nanocrystalline form at low temperatures. Unsupported intermetallic PtBi and PtPb nanoparticles (~ 20 nm or larger) have been prepared [3,4,5]. Alternatively, alloy nanoparticles were also formed by employing pre-formed supported Pt nanoparticles as nucleation sites [6]. CO poisoning was prohibited [7,8]. However, the mass activity of these catalysts was not maximized due to their larger particle sizes than the ideal case. Further development of these catalysts requires not only the particle size control but also the fine dispersion of these nanoparticles on an ideal support such as ordered mesoporous carbon (OMC). As discussed in **section 1.4.2.3.2**, OMC have many desirable characteristics for their function as catalyst supports for fuel cells. However, it has been very challenging to load catalyst nanoparticles *into* the mesoporous voids.

Here, a simple and robust synthetic scheme is presented. The scheme enables, for the first time, single noble metal or intermetallic nanoparticles to be completely encapsulated within OMC voids. By using surface-modified OMC to trap the metal precursors, nanocrystallites are formed with monodisperse sizes as low as 1.5 nm, which can be tuned up to 2 and 3.5 nm (equivalent to the channel size of OMC) by thermal treatment. Ultra-fine dispersion and narrow particle size distribution result in excellent access to the catalyst centres. The encapsulated intermetallic PtBi exhibits excellent performance for catalyzing formic acid oxidation.

## **6.2 Experimental**

### **6.2.1 Preparation of carbon-S and carbon-metal composites**

Carbon-S nanocomposites were prepared by a melt-diffusion strategy. Typically, 0.1 g of sulfur and 0.9 g of a carbon material (CMK-3, Ketjen Black carbon or Vulcan-XC72R carbon) were ground together. The sulfur impregnation was carried out in air at 155 °C for 12 hrs. Carbon-S was impregnated with catalyst precursors by dispersing it in solutions containing the desired concentration of metal precursors. An aqueous solution was used for precursors including  $\text{H}_2\text{PtCl}_6 \cdot 6\text{H}_2\text{O}$ ,  $\text{Pd}(\text{NO}_3)_2 \cdot 2\text{H}_2\text{O}$ ,  $\text{Co}(\text{NO}_3)_2 \cdot 6\text{H}_2\text{O}$ ,  $\text{Ni}(\text{NO}_3)_2 \cdot 6\text{H}_2\text{O}$ , and  $\text{Cu}(\text{NO}_3)_2 \cdot 2.5\text{H}_2\text{O}$ . Ethylene glycol was employed to solvate precursors which easily hydrolyze in water, such as  $\text{Bi}(\text{NO}_3)_3 \cdot 5\text{H}_2\text{O}$ ,  $\text{RuCl}_3 \cdot \text{H}_2\text{O}$ , and  $\text{RhCl}_3 \cdot \text{H}_2\text{O}$ . The mixture of carbon-S and precursor solution was stirred for 6 hrs before solvents were evaporated. The reduction of metal precursors was completed under a flow of 7%  $\text{H}_2/\text{N}_2$  at 350 to 450 °C for 3 hrs. Finally, the samples were then evacuated at 300 °C for 12 hrs to completely remove

adsorbed H<sub>2</sub> and residual sulfur. Higher temperatures were also used for subsequent heat treatment, as indicated in the text.

### 6.2.2 Electrochemical measurement

For the preparation of working electrodes, 10.0 mg metal/mesoporous carbon composites (24wt% total metal) were suspended in 5.0 mL of 2-propanol, and then ultrasonically blended for 30 minutes to form the catalyst inks. Next, 10 µl of this catalyst ink was pipetted onto the surface of the glassy carbon disk electrode (geometric area of 0.196 cm<sup>2</sup>). The catalyst coated electrode surface was then dried under atmospheric conditions, followed by the addition of 5 µl of 2-propanol solution containing 1 wt% Nafion<sup>®</sup>, on the top of the catalyst layer. The loadings of total metals were all controlled to 24 µg/cm<sup>2</sup>.

The cell used was a conventional three-compartment electrochemical cell containing a glassy carbon (GC) disk coated with catalyst as working electrode, Pt wire as counter electrode and reversible hydrogen electrode (RHE) as reference electrode. The RHE contains an acid solution saturated with H<sub>2</sub> and a platinum wire electrode. The electrolyte was N<sub>2</sub> saturated 0.5 M H<sub>2</sub>SO<sub>4</sub> solution containing 0.5 M HCOOH. In a cyclic voltammetry (CV) measurement, the electrode potential was scanned in the range of 0.05-1.2 V versus RHE. Chronoamperometry (CA) was carried out with the working electrode rotating at a speed of 200 rpm with its potential held at 0.3 V vs. RHE, in an electrolyte solution containing 0.1 M H<sub>2</sub>SO<sub>4</sub>, and 0.5 M HCOOH. All the catalyst electrodes were cleaned with steady state CV scanned for three cycles in the range of 0.05-1.2 V versus RHE at 50 mV/s before data were collected. All electrochemical experiments were carried out at room temperature and ambient pressure.

## 6.3 Results and discussion

### 6.3.1 Structural studies of OMC-S

The proof-of-concept studies are based on CMK-3, a well investigated ordered mesoporous carbon (OMC) [9]. In a departure from any previously reported approaches, the carbon surface is functionalized with a thin layer of sulfur that functions as a metal trap (OMC-S). Normally considered as a potent catalyst poison, sulfur exhibits a strong affinity to noble metals owing to a soft acid-soft base interaction [10]. This acts to adsorb and bind the catalyst metal precursors from solution, and additionally restricts their particle growth on reduction to result in ultra-fine dispersions of metal nanocrystallites. The sulfur is readily imbibed by capillary forces into the OMC nanofibers from a sulfur melt as discussed in *Chapter 5*. Although S/composite fractions up to 79wt% S can be prepared which corresponds to complete filling of the empty channels, here, the S/C ratio is optimized at a much lower level (10 wt% S/composite) to provide a thin coating on the interior surfaces.

The TEM image (**Figure 6.1a**) along with energy-dispersive X-ray (EDX) carbon and sulfur maps of the same particle (**Figure 6.1c, d**) reveal a homogenous distribution of sulfur in OMC-S. We conclude that sulfur is homogeneously distributed within the interior, as no sulfur ‘halo’ is formed on the edges of the composite particle that would be indicative of an exterior coating. The image expansion (**Figure 6.1b**) on a sulfur populated area (**Figure 6.1d**) shows ordered channels with no contrast variation. This suggests that sulfur molecules form a thin layer on the surface of the carbon nanorods without forming aggregates that block the channels. This is in agreement with the previous studies that indicate that sulfur wets carbon very readily (**Chapter 5**). The successful loading and ultra-fine dispersion of

metal and intermetallic nanoparticles into the channels of the mesoporous carbon further supports the existence of the thin sulfur layer. The long-range order maintained in OMC-S is confirmed by the low angle X-ray diffraction (XRD) (**Figure 6.3a**). The XRD peaks exhibited by OMC-S are a little less intense than those of CMK-3 (**Figure 6.3b**), indicative of a certain degree of pore filling.

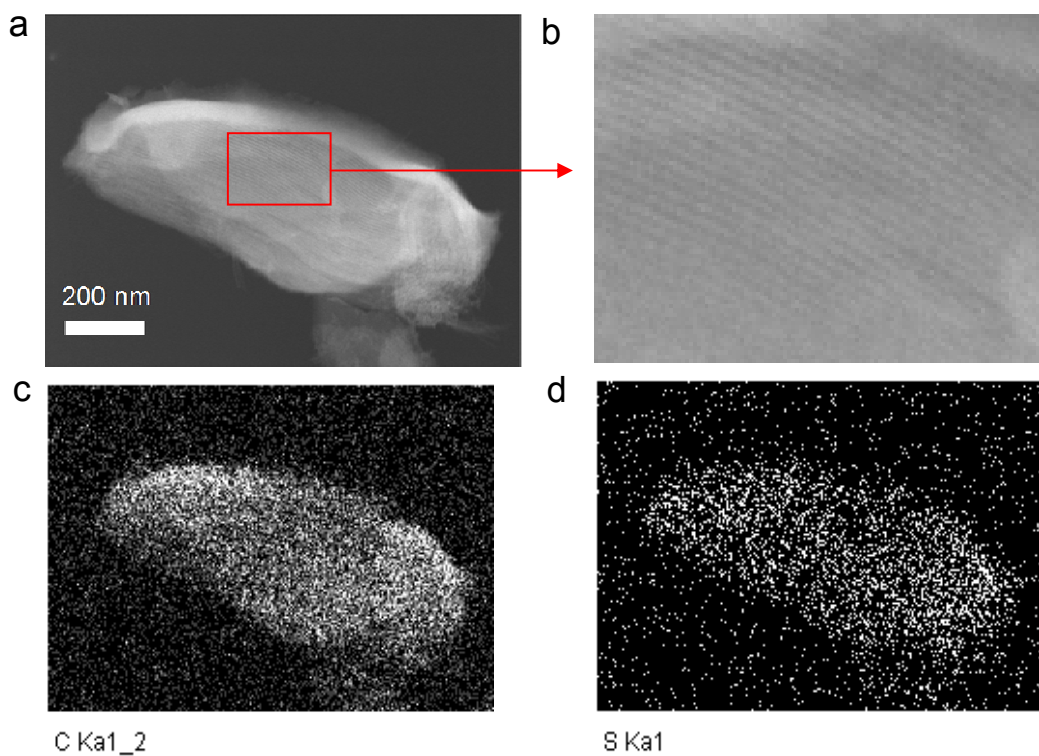


**Figure 6.1 a) TEM image of OMC-S composite with 10wt% sulfur in the structure (dark field); b) image expansion corresponding to the area outlined by the red square in part a; c, d) corresponding carbon and sulfur elemental maps.**

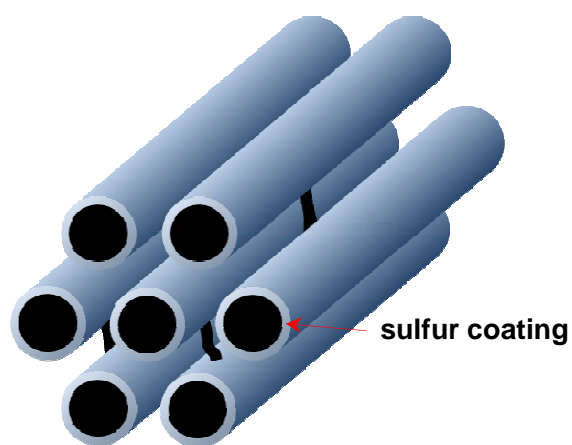


Figure 6.2 Schematic showing sulfur functional layers on carbon nanorods of CMK-3.

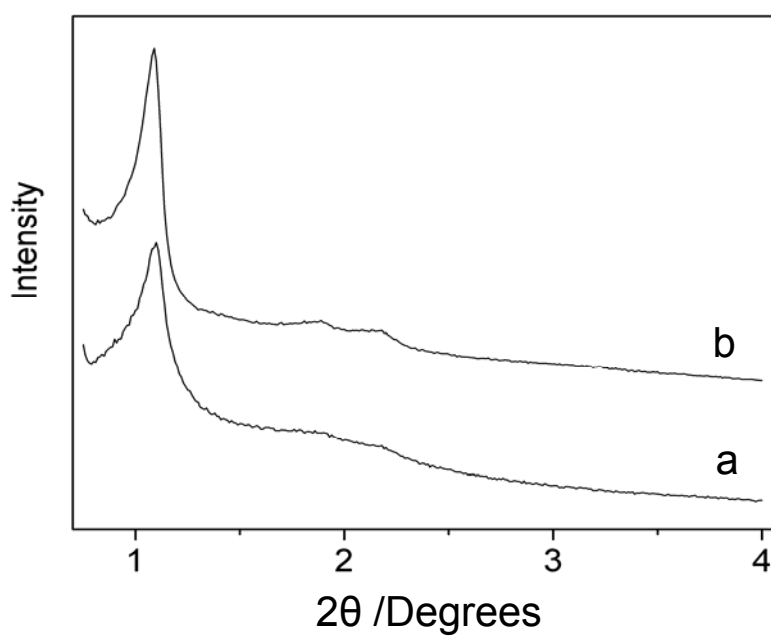


Figure 6.3 Low angle XRD patterns of a) OMC-S; b) CMK-3.

### 6.3.2 Sulfur as a metal trap

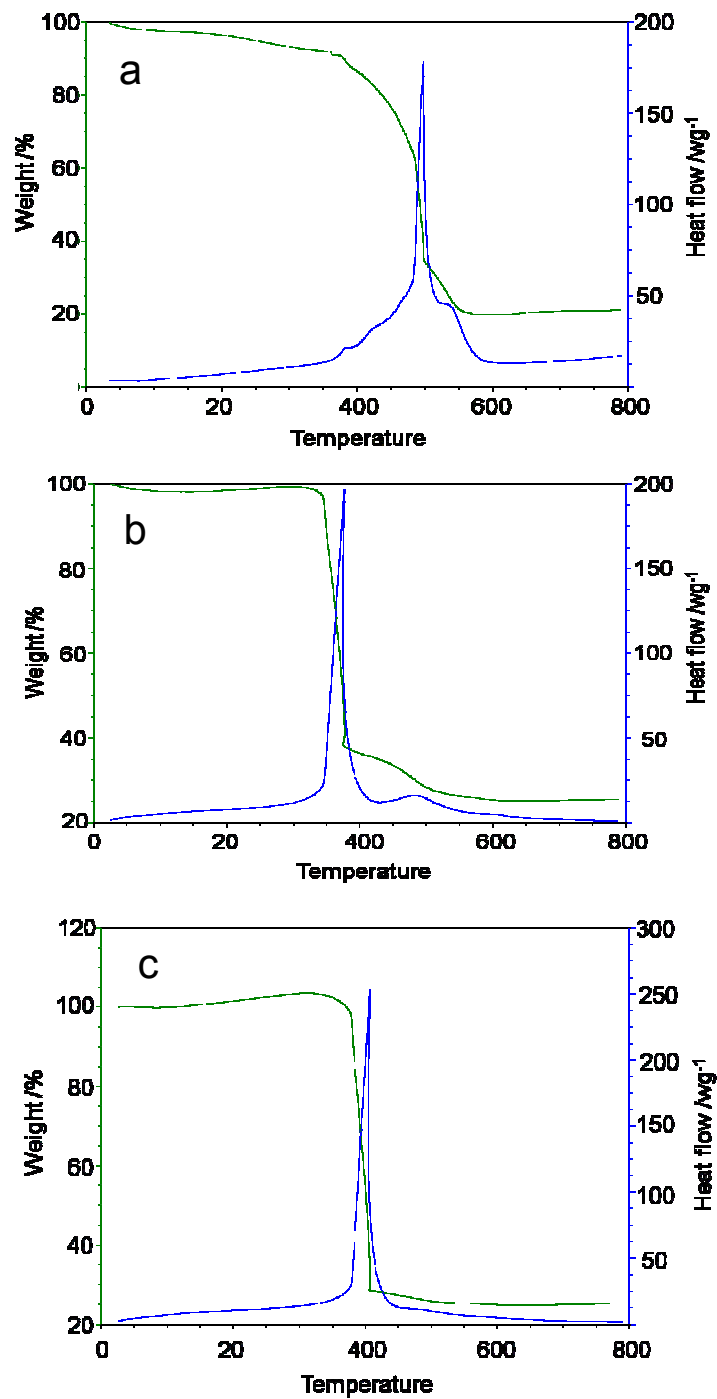
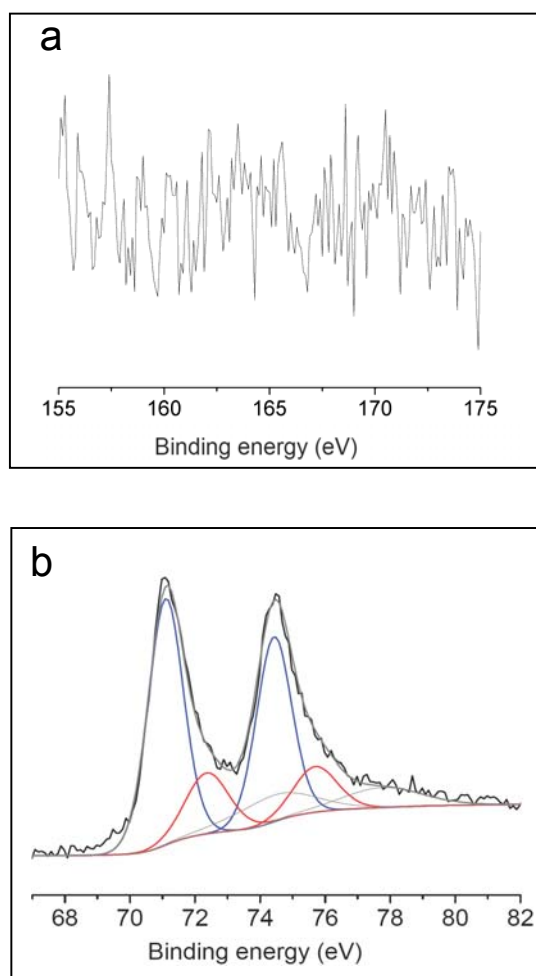


Figure 6.4 Thermogravimetric analyses in air of a)  $\text{H}_2\text{PtCl}_6$  impregnated OMC-S; b) OMC-Pt before evacuation; c) OMC-Pt after evacuation.



**Figure 6.5 X-ray photoelectron spectra of a) S [2p] signal; b) Pt [4f] signal for OMC-Pt after evacuation.**

OMC-Pt composite was first prepared to serve as proof of concept. The thermogravimetric analyses and differential scanning calorimetry (TGA-DSC) measurements (**Figure 6.4a, b**) show that certain amount of sulfur still remains in the composite after Pt formation on reduction at 350 °C. The residual sulfur (which would destroy catalytic activity) was then readily and completely removed by evacuation at 300 °C for 12 hrs. Its absence was

determined by the TGA-DSC wherein OMC-Pt only exhibits carbon weight loss (**Figure 6.4c**); and confirmed by the absence of any S [2p] signals in X-ray photoelectron spectra (XPS) of OMC-Pt (**Figure 6.5a**). Samples were etched by Ar<sup>+</sup> sputtering for 600 sec to obtain XPS signals from regions *within* the OMC-Pt composite. Further proof of complete sulfur removal was demonstrated by the high catalytic activity of the materials (*vide infra*). The metallic nature of the Pt is also demonstrated by the characteristic Pt [4f] signal in the XPS spectra (**Figure 6.5b**).

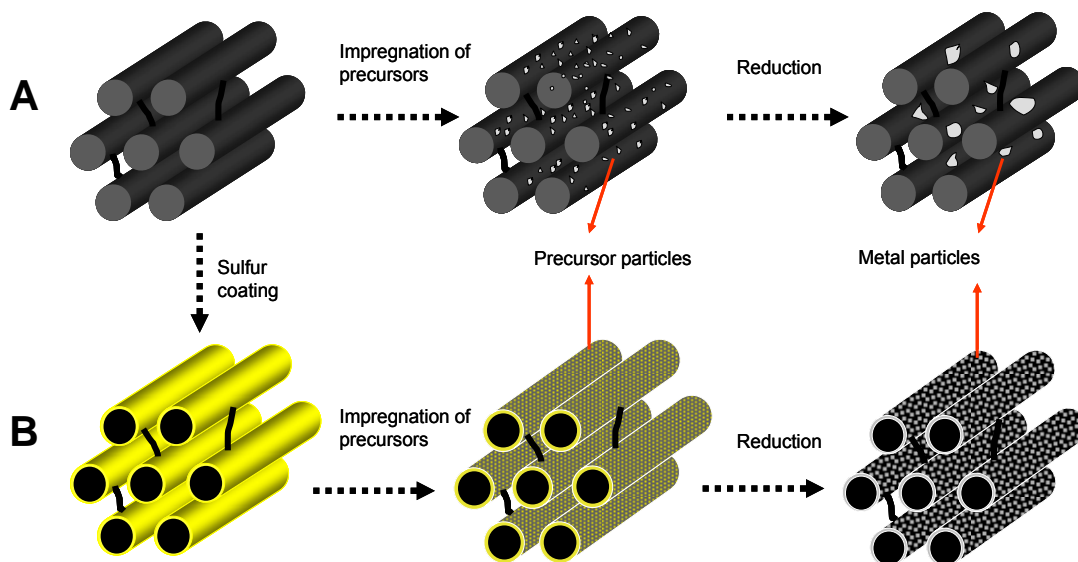


**Figure 6.6** Schematic diagram for A) conventional impregnation method to load noble metal nanoparticles into OMC; B) our new impregnation method with a support functionalized by sulfur.

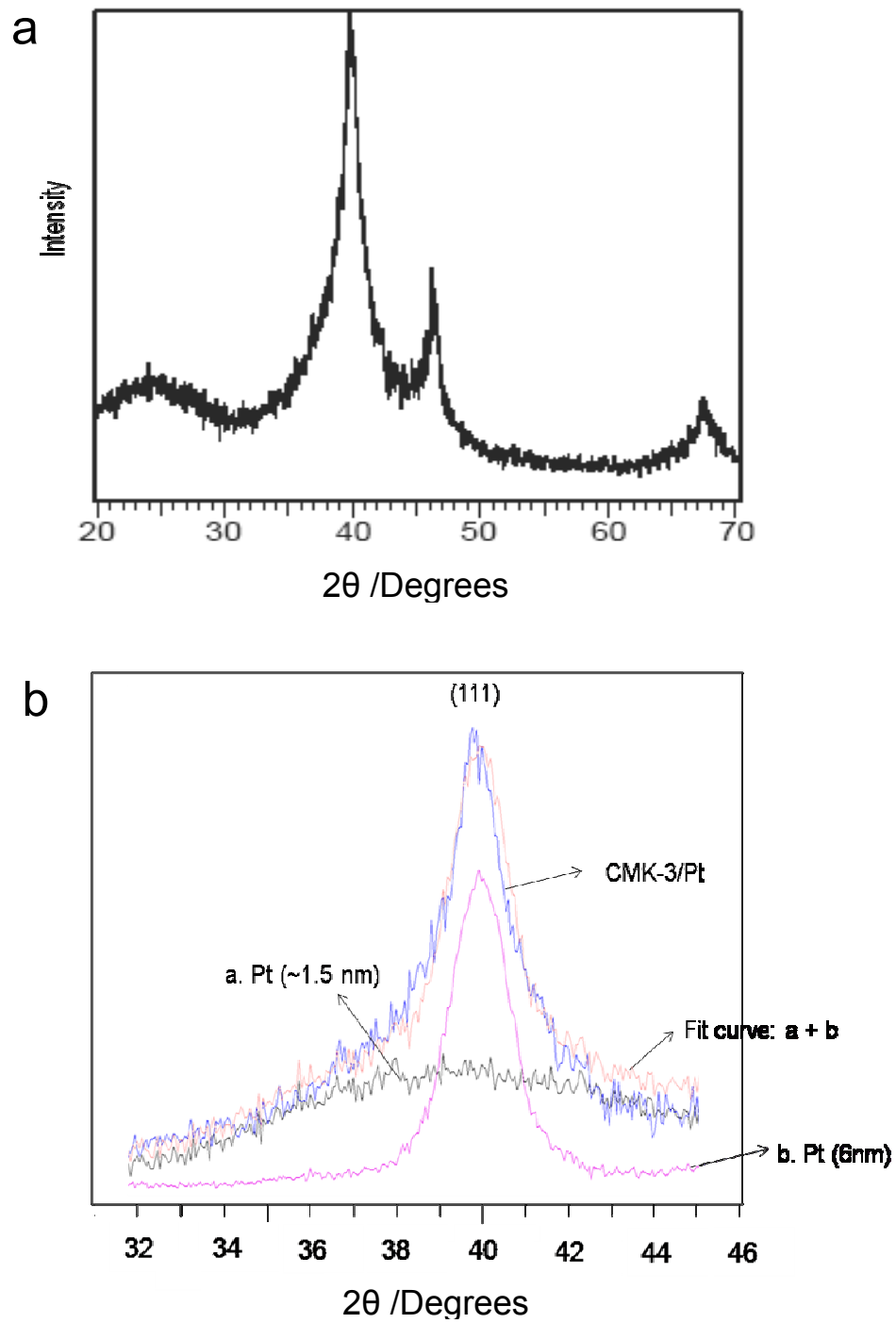


**Figure 6.7 a) Wide angle XRD pattern of conventionally prepared CMK-3/Pt; b) regeneration of (111) peak in a) by addition of the patterns of Pt (6 nm) and Pt (1.5 nm) materials.**

The schematic diagram (**Figure 6.6**) manifests how OMC-S differs from pure OMC in terms of the ability to incorporate catalyst nanoparticles into mesoporous voids during an impregnation process. Conventionally, acetone solutions of platinum precursors are contacted with CMK-3. **Figure 6.7a** shows the XRD pattern of conventionally prepared CMK-3/Pt composites (24wt% Pt). As **Figure 6.7b** shows, the (111) reflection of CMK/Pt can be regenerated by the addition of (111) reflections from two other Pt/C materials. One, highly broadened, is attributed to Pt nanoparticles of diameter less than 2 nm. The other sharp one arises from Pt domains with a coherence length of 6 nm as calculated by Scherrer line broadening. This larger domain size is almost double that of the CMK-3 channel size, indicating that either the particles are located on the external surface of CMK-3 or their particle growth causes structural damage in CMK-3. The poor compatibility between metal precursor solutions and carbon induces the inhomogeneity in the particle formation. In contrast, the OMC-Pt (24wt% Pt) derived from OMC-S exhibits a very narrow particle size distribution and ultra-fine dispersion, as shown in **Figure 6.8a**. A significantly higher degree of Pt dispersion within the channels of OMC prepared by the sulfur-entrapment route (vs. the conventional method) is achieved.

It can be concluded that thin layer of sulfur undoubtedly functions as a mediator which acts to adsorb and bind the catalyst metal precursors from solutions into OMC, and additionally restricts their particle growth during reduction to result in ultra-fine dispersions of metal nanocrystallites.

### 6.3.3 Physical characterizations of OMC-Pt catalysts

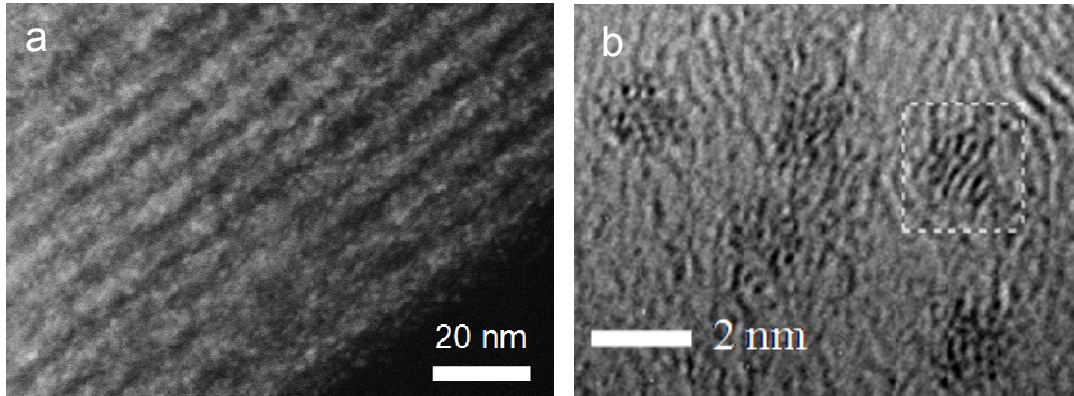


Figure 6.8 TEM images of OMC-Pt a) Dark field; b) Bright field.

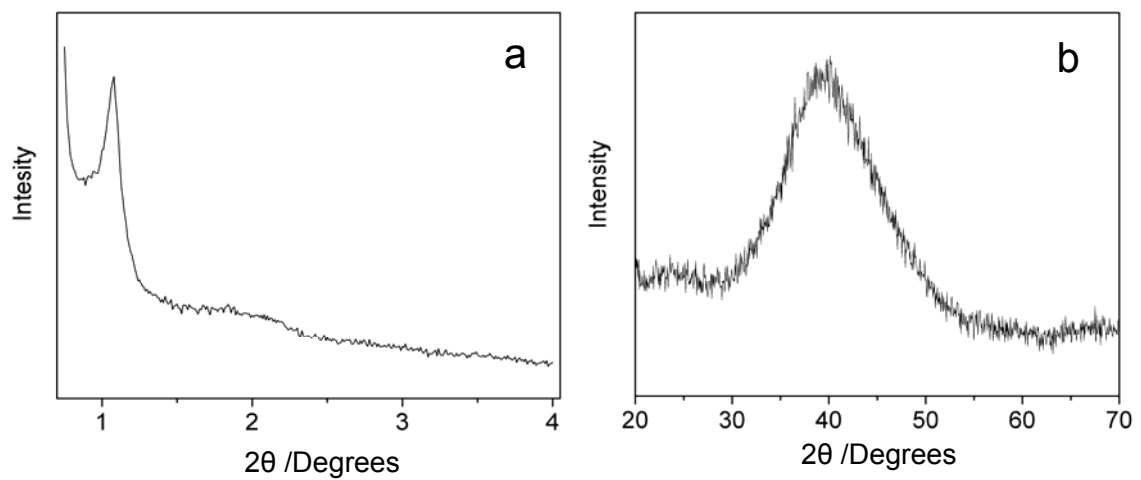
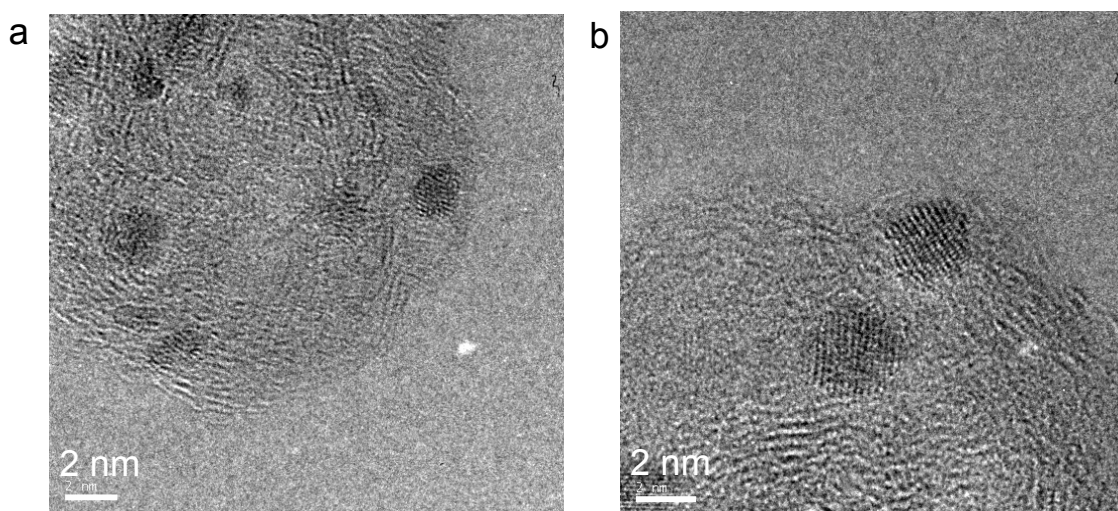


Figure 6.9 a) Low angle XRD pattern of OMC-Pt; b) Wide angle XRD pattern of OMC-Pt.

A representative HRTEM image of these nanocrystallites is shown in **Figure 6.8b**, revealing an average dimension of 1.5 nm in diameter with well-defined lattice planes. The lattice fringes of a highlighted particle can be clearly observed. These small particles do not

disrupt the internal carbon framework. The well-preserved long range order of the carbon walls in OMC-Pt (24wt% Pt) is evident in the TEM image (**Figure 6.8a**) and confirmed by the sharp peaks in the low angle XRD pattern (**Figure 6.9a**). The highly broadened XRD peaks exhibited by OMC-Pt can be attributed to the ultra-small particle size of Pt and/or the complete encapsulation of Pt nanodots in OMC particles (**Figure 6.9b**).



**Figure 6.10** Representative TEM images of OMC-Pt treated at a) 600 °C (bright field); b) 800 °C (bright field).

Furthermore, the size of the Pt particles can be precisely dialed up by heat treatment, up to the size of OMC channels, i.e., ~ 3.5 nm. For example, the Pt particles prepared at 350°C can be increased in size from less than 2 nm (OMC-Pt-1.5nm) to ~ 2 nm within 2 hours under argon at 600 °C (**Figure 6.10a**) and to ~ 3.5 nm within 30 min at 800 °C (**Figure 6.10b**), as shown by HRTEM. Well defined lattice fringes (scarcely detectable over the background intensity of the OMC for the smallest crystallites) are clearly evident in these larger crystallites.

### 6.3.4 Incorporation of Pd, Ru, Rh into OMC-S

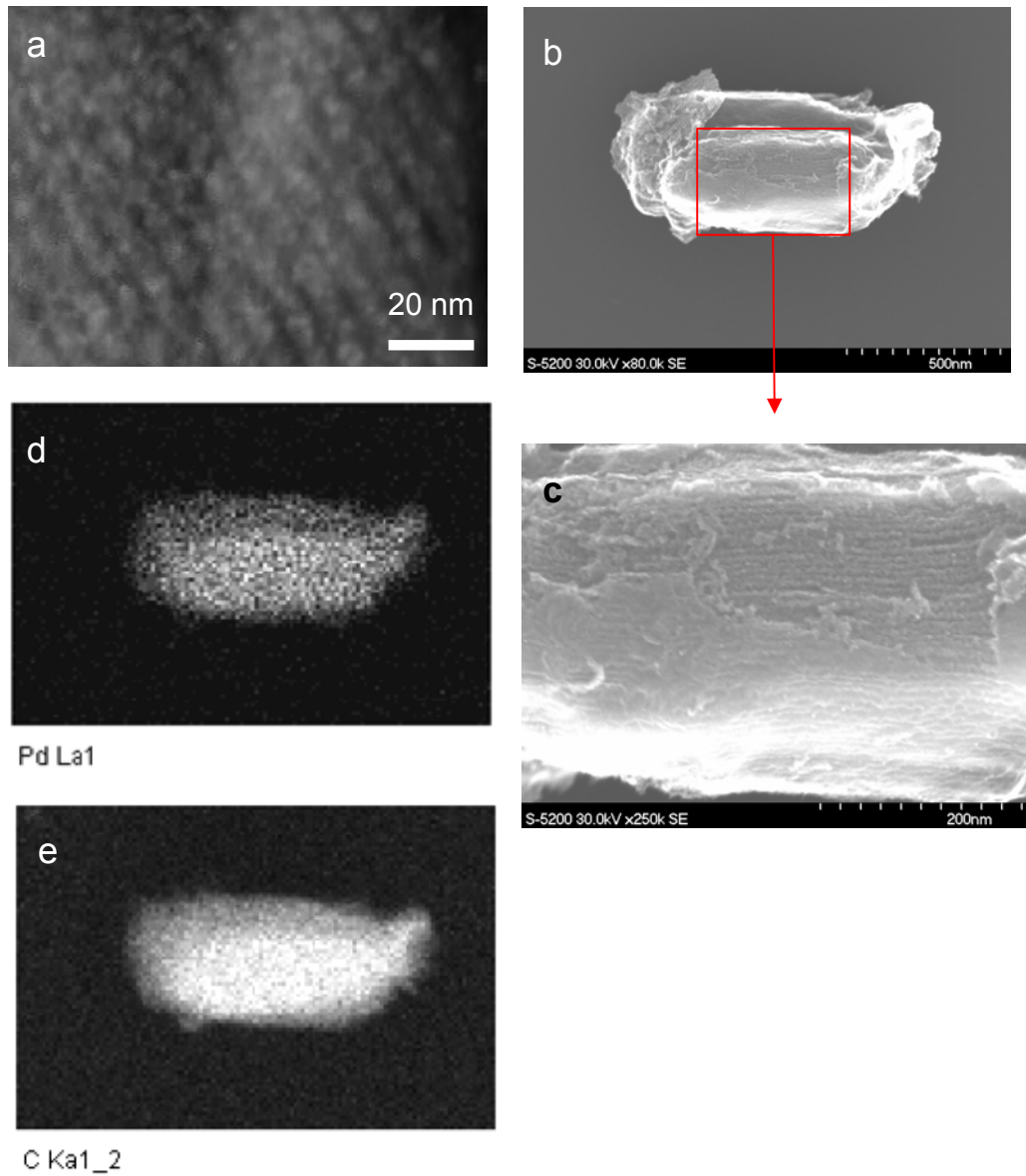


**Figure 6.11** TEM, SEM images and an elemental map of OMC-Pd. a) TEM image (dark field); b) SEM image; c) image expansion corresponding to the area outlined by the red square in b); d) corresponding Pd EDX map of part b; e) corresponding carbon EDX map of part b.

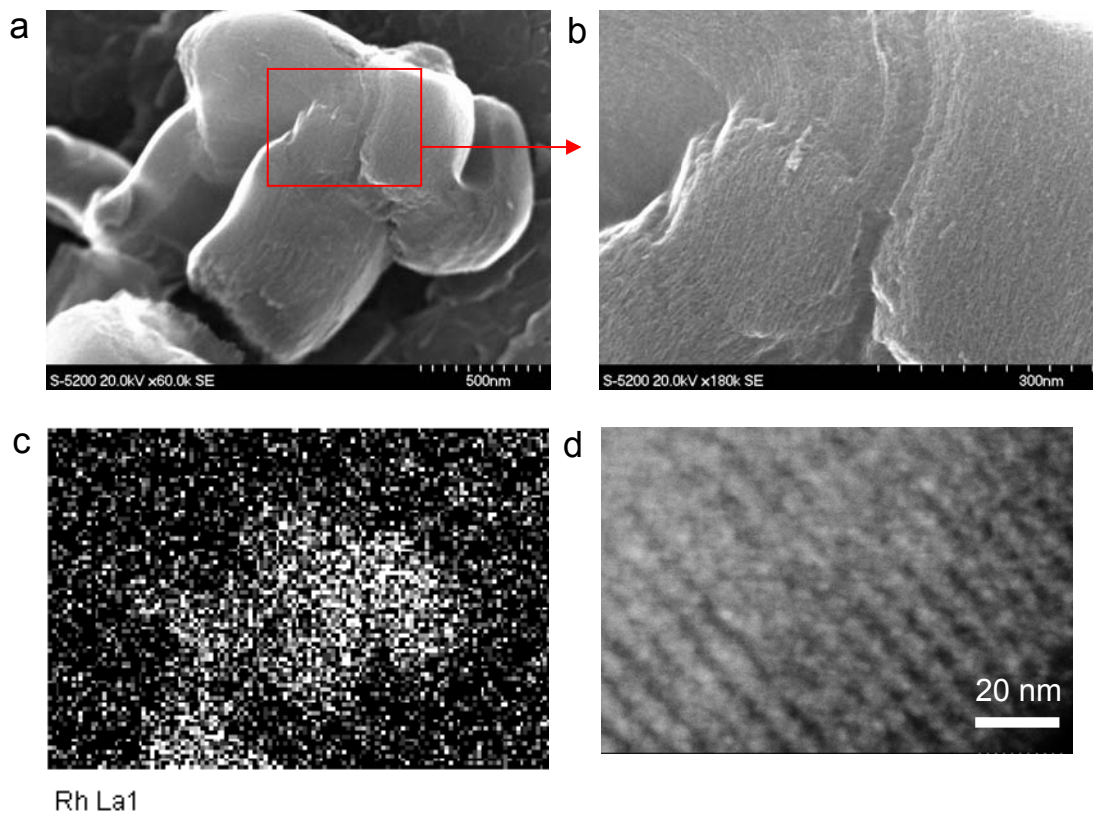


**Figure 6.12 a) SEM image of OMC-Rh; b) image expansion corresponding to the area outlined by the red square in part a; c) corresponding Rh EDX elemental map of part a; d) TEM image (1100KX, dark field).**

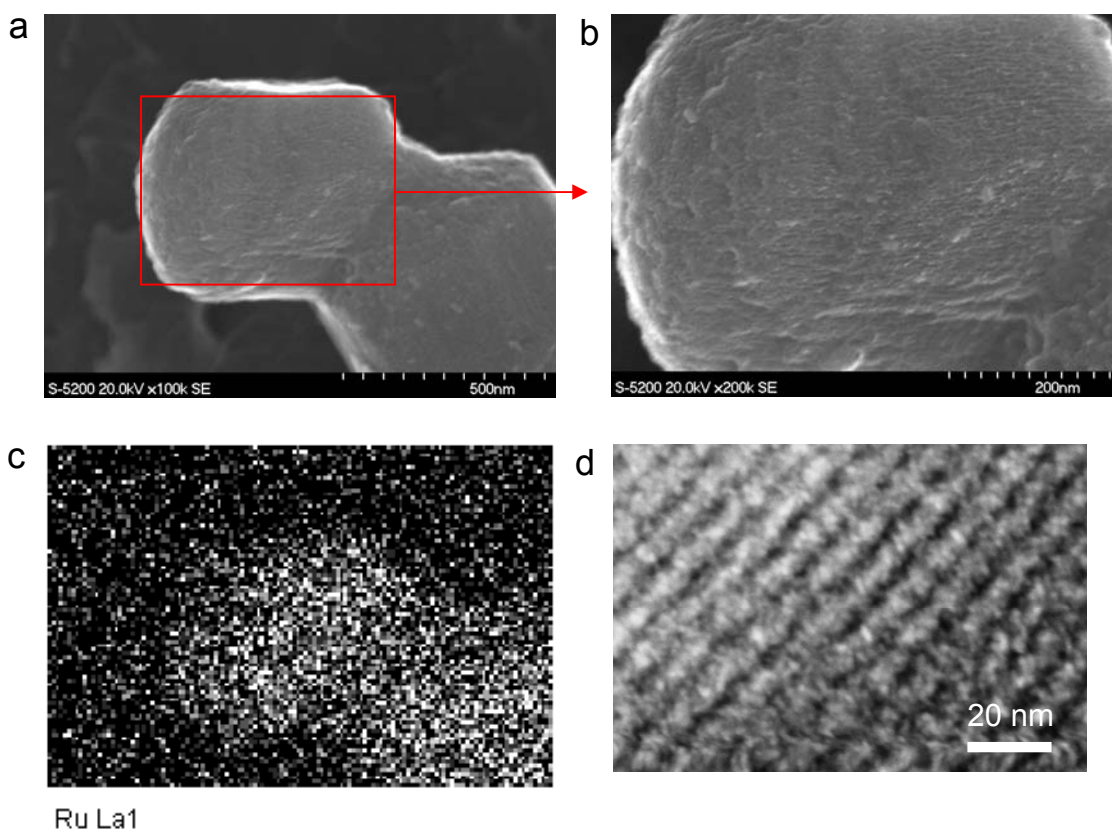


**Figure 6.13** a) SEM image of OMC-Ru; b) image expansion corresponding to the area outlined by the red square in part a; c) corresponding Ru EDX elemental map of part a; d) TEM image (1100KX, dark field).

This preparation methodology is also widely applicable to many noble metals. With OMC-S as a support, OMC-M (12wt% M/composite), (M = Pd, Rh, Ru,) were all successfully fabricated. These nanocrystalline composites also exhibit a narrow particle size distribution on the order of ~2 nm and a very fine dispersion, as shown in their TEM images (**Figure 6.11a**, **Figure 6.12d**, and **Figure 6.13d**). In SEM images, these composites exhibit very clean and ordered surface morphology indicating that these nanoparticles are well

confined (**Figure 6.11b, c, Figure 6.12a, b, and Figure 6.13a, b**). The corresponding elemental maps of these composites identify that these metal particles are homogeneously distributed in the framework of OMC (**Figure 6.11b, d, e, Figure 6.12a, c, and Figure 6.13a, c**). These materials are of interest as potential supercapacitor electrodes (Ru), methanol oxidation/formic acid fuel cell catalysts (Pd) or as heterogeneous catalysts for organic syntheses.

It is evident that sulfur layer is very effective in capturing platinum group noble metals. The power of this synthetic method on the other hand foreshows its applications in metal sorption which is presented in *Chapter 7*.

### 6.3.5 Incorporation of Ni, Co, and Cu into OMC-S

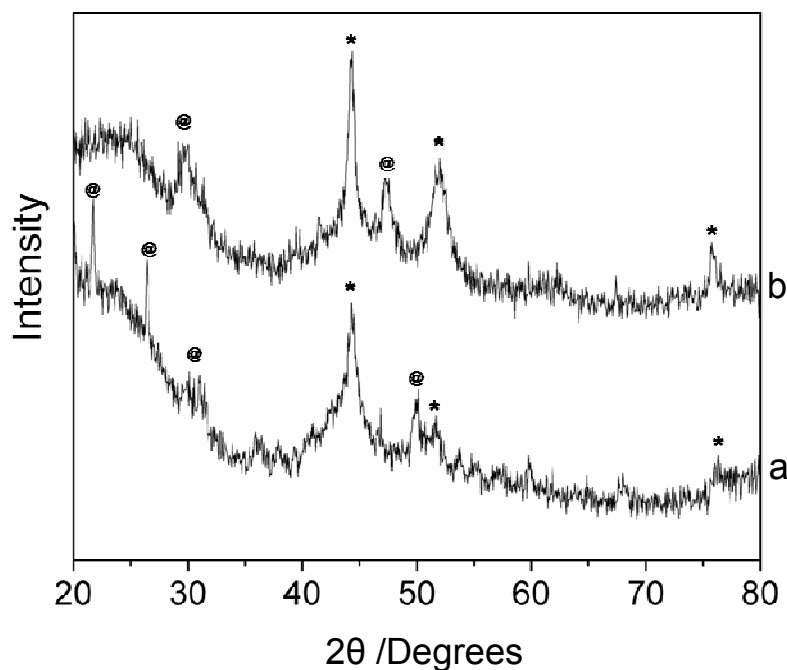


**Figure 6.14** Wide angle XRD patterns of a) OMC-Ni; b) OMC-Co, metal phases marked with \* and metal sulfides ( $\text{Co}_4\text{S}_3$ ,  $\text{Ni}_3\text{S}_2$ ) marked with @.

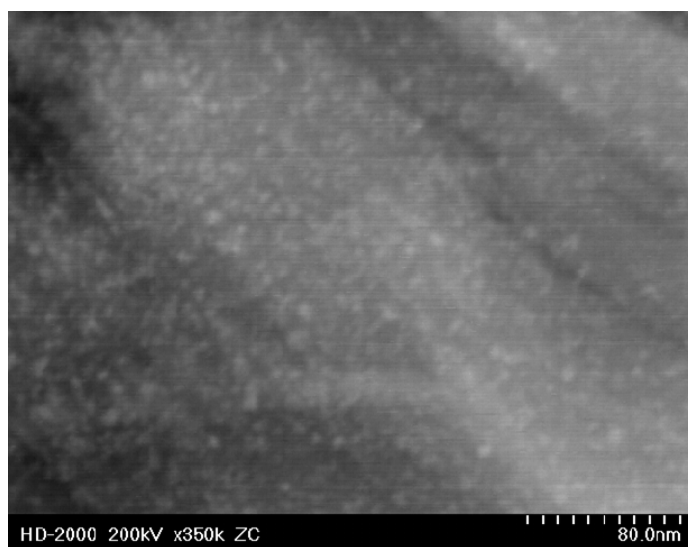


**Figure 6.15 TEM image of OMC-Ni (dark field).**

As just presented, platinum group noble metals, including Pt, Pd, Ru and Rh, can be readily captured and encapsulated by OMC-S. To better understand the mechanism of this sulfur metal trap, it is necessary to investigate whether it is applicable to non-noble transition metals. Aqueous solutions of transition metals including Co, Ni and Cu were contacted with OMC-S. After reduction, these materials were characterized. As shown in the XRD patterns of OMC-Ni (12wt% Ni) and OMC-Co (12wt% Co) (**Figure 6.14**), fairly well resolved peaks clearly reveal the larger size of Ni and Co particles than their noble metal counterparts. Metal sulfide peaks are identified in these patterns as well. It is evident that early transition metals can be oxidized by sulfur during a thermal reduction process. To further characterize these composites, OMC-Ni composite was studied under TEM (**Figure 6.15**). Ni/NiS<sub>x</sub> crystallites

exhibit an average particle size of ~ 6 nm in diameter, which indicates the breach of OMC framework in OMC-Ni.

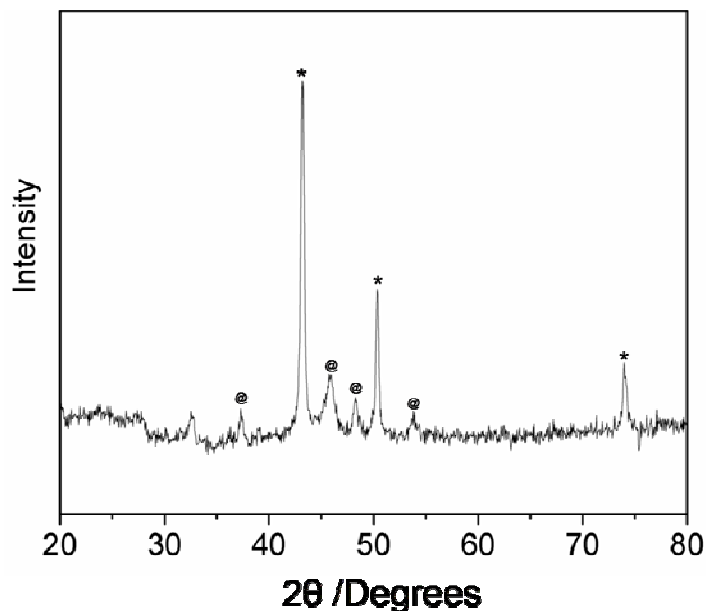


**Figure 6.16** Wide angle XRD patterns of OMC-Cu, Cu phase marked with \* and  $\text{Cu}_2\text{S}$  phase marked with @.

As shown in **Figure 6.16**, the XRD pattern of OMC-Cu displays highly crystalline features of metallic Cu, which suggests that the interaction between sulfur and copper is even weaker than that for nickel and cobalt. Note that  $\text{Cu}/\text{Cu}^{2+}$  with nearly completely filled d orbitals exhibits lower electron deficiency than Co and Ni.

In short, the interaction between sulfur and non-noble transition metals is weak, and the sulfides formed as side products may be problematic in potential applications.

### **6.3.6 Sulfur functionalized disordered carbons**

To determine whether conventional carbons can be functionalized with sulfur to trap metal nanoparticles, activated carbons including Ketjen Black (KB) carbon and Vulcan

XC72R carbon (Vulcan) are employed as supports to prepare sulfur functionalized carbon templates. The physical characteristics of these carbons are listed in **Table 6.1**, Ketjen Black exhibits a high surface area, large pore volume and disordered mesoporous structure which may facilitate its sulfur absorbance. Vulcan XC72R exhibits a much lower surface area and pore volume, in comparison with Ketjen Black and CMK-3.

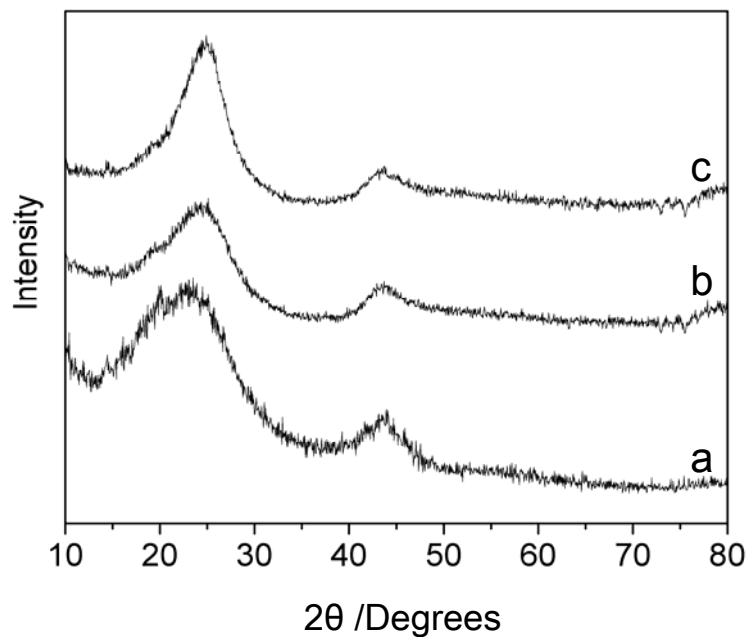


**Figure 6.17** Wide angle XRD patterns of a) OMC-S; b) KB-S; c) Vulcan-S.

**Table 6.1** BET and BJH results of various carbons.

Samples	BET total surface area (m <sup>2</sup> /g)	Pore volume (cm <sup>3</sup> /g)	BJH Pore size (nm)
CMK-3	1976	2.1	3.3
Ketjen Black	971	1.58	3.8
Vulcan XC72R	271	0.47	1.9

By employing the melting-diffusion method, sulfur functionalized Ketjen Black carbon and Vulcan XC72R carbon materials were fabricated, termed as KB-S and Vulcan-S (10wt% S/composite), respectively. **Figure 6.17** shows the wide angle XRD patterns of OMC-S, KB-S, and Vulcan-S, none of which exhibits any features of crystalline sulfur, indicating that amorphous thin sulfur layer has been formed even in Vulcan-S. This suggests that structural characteristics including high surface area and large pore volume are not the prerequisites for the formation of sulfur thin layer on carbon materials. Nevertheless, the affinity between non-polar S<sub>8</sub> molecules and non-polar carbon surface should be the key factor to enable the wetting of sulfur on carbon materials.

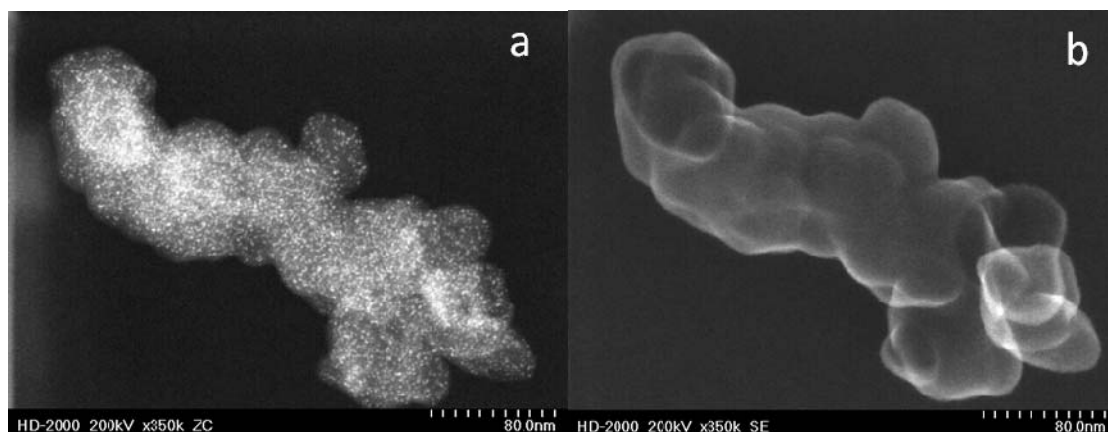


**Figure 6.18 a) TEM image (dark field) and b) SEM image of KB-Pt.**

By employing KB-S and Vulcan-S as supports, KB-Pt (24wt% Pt) and Vulcan-Pt (24wt% Pt) composites were prepared. In KB-Pt, Pt nanoparticles of ~1.5 nm in diameter are homogeneously dispersed on carbon nanoparticles, as shown in **Figure 6.18a**. The homogeneity of Pt nanoparticles in KB-Pt is further confirmed by the highly broadened Pt

XRD peaks (**Figure 6.19a**). Confined in the pores of Ketjen Black carbon, Pt particles glinting under TEM are completely invisible in the SEM mode (**Figure 6.18b**).

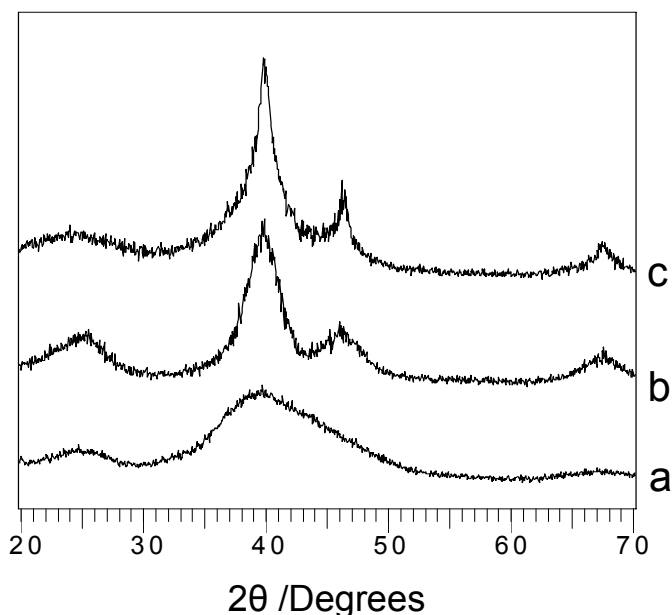


**Figure 6.19** Wide angle XRD patterns of a) KB-Pt; b) Vulcan-Pt; c) CMK-3/Pt composite where CMK-3 was not decorated by sulfur layer.

Calculated by Scherrer line broadening in the XRD patterns (**Figure 6.19**), the coherence length of Pt domains in Vulcan-Pt is determined to be 3.4 nm, in contrast to that (6.0 nm) of some Pt domains supported on pure CMK-3. Vulcan-S clearly exhibits superior Pt particle size control to pure CMK-3. Considering the much lower surface area and pore volume of Vulcan XC72R than CMK-3, it is evident that surface area and/or pore volume have less impact on particle size control than an effective “metal trap” agent. However, high surface area and/or large pore volume of a support do benefit the Pt particle size control. The combination of high surface area and “metal trap” in KB-S and OMC-S facilitates the

formation of even smaller Pt particles (1 to 1.5 nm), compared to the particles formed on Vulcan-S.

### 6.3.7 Physical characterizations of intermetallic PtBi nanoparticles supported on OMC

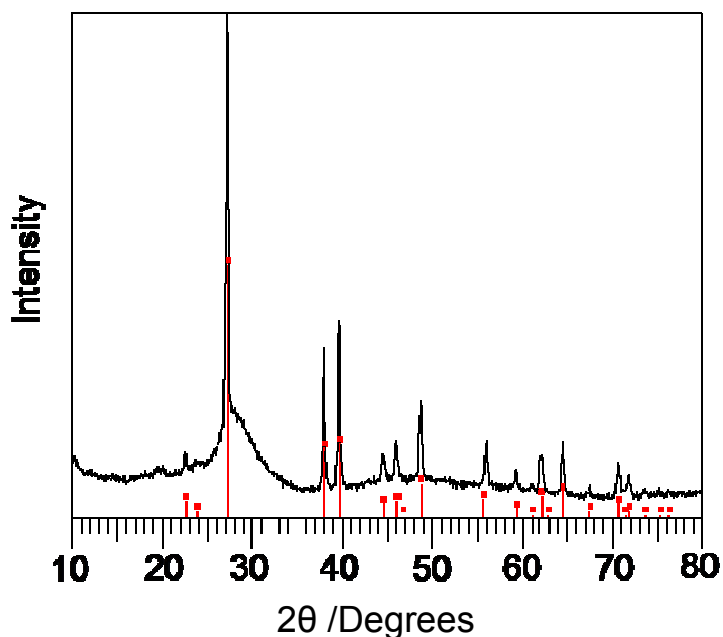
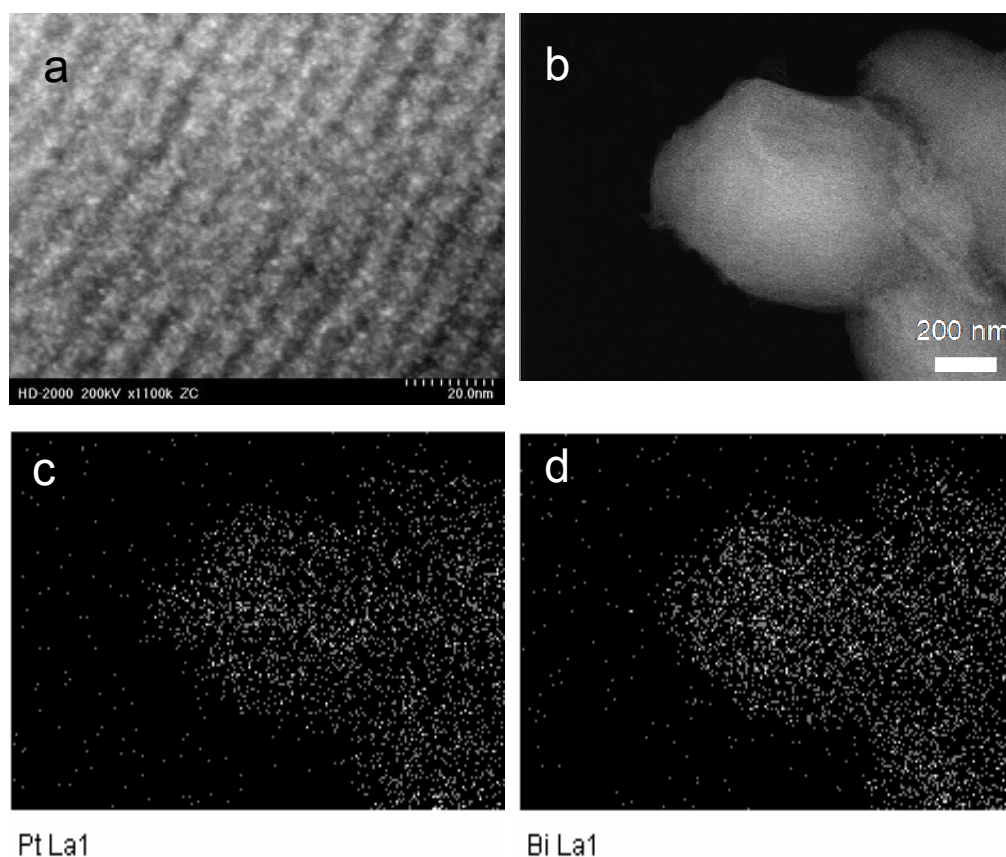


Figure 6.20 Wide angle XRD pattern of OMC-Bi.

While the synthesis of OMC-supported noble metal nanodots demonstrates the viability of the methodology, the ultimate goal lies in the preparation of intermetallic or bimetallic nanocatalysts in OMC channels that cannot be realized by other methods so far. For many applications including formic acid oxidation for fuel cell anodes, Pt or Pd based intermetallic nanomaterials based on main group metals such as Bi are of particular interest. The new route works unusually well, because it relies on the use of the OMC-S bonded Pt to act as a nucleation site for Bi. This is akin to reports that use Pt crystals deposited on carbon

to provide a growth centre for subsequent alloying with Bi. The difference in this case is that the Pt clusters generated *in-situ* within the carbon channels orchestrate the assembly of nearby Bi atoms produced during reduction into an ordered intermetallic phase.



**Figure 6.21 a), b) TEM images of OMC-PtBi-1nm (dark field); c), d), corresponding Pt and Bi elemental maps to part b.**

In the absence of Pt, reduction of OMC-Bi(NO<sub>3</sub>)<sub>3</sub> under H<sub>2</sub>/N<sub>2</sub> at 350 °C produces bulk Bi metal external to the OMC-S (not nano-Bi) due to its low melting temperature (271.5 °C), as shown by its XRD pattern (**Figure 6.20**). Newly formed Bi clusters agglomerate into large droplets to decrease their surface tension, unless they can immediately form a solid

phase with nearby incipient Pt clusters. A TEM image of the material OMC-PtBi heated at 350 °C under 7% H<sub>2</sub>/N<sub>2</sub> for 3hrs shown in **Figure 6.21a**, along with the corresponding EDX elemental maps (**Figure 6.21b, c, d**) indicate that both Pt and Bi are homogeneously distributed in the ordered mesoporous framework and are intimately mixed. The crystallite size was roughly estimated as 1-2 nm from an expanded section of **Figure 6.21a** (“OMC-PtBi-1nm”).

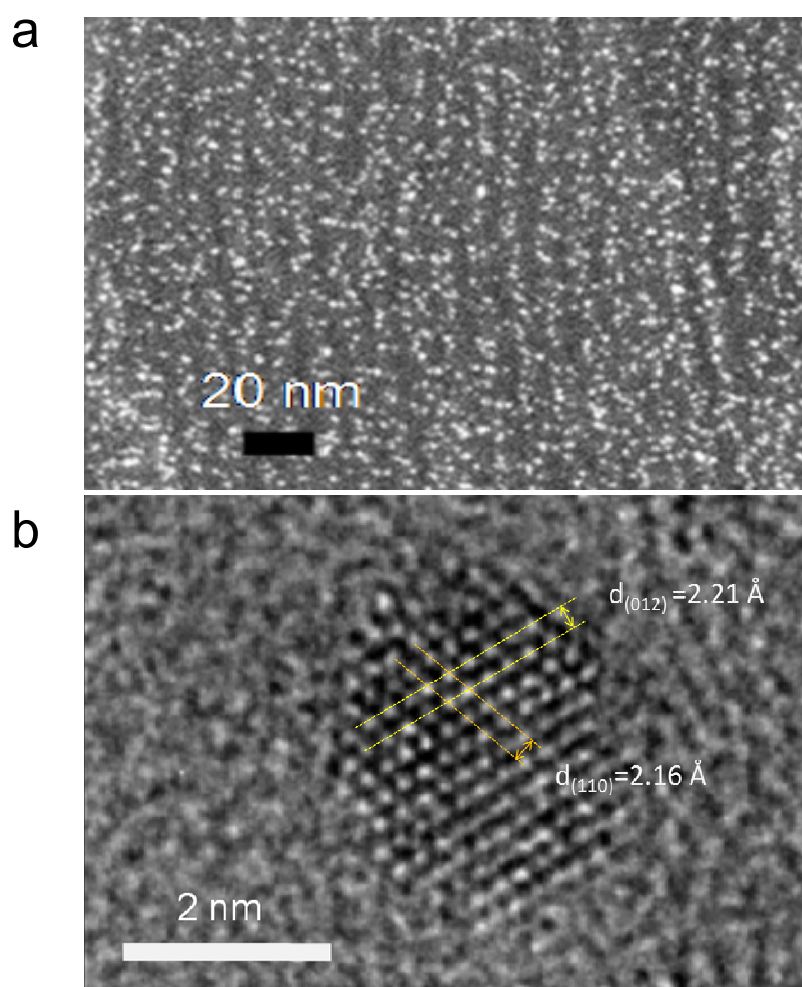


**Figure 6.22 a) TEM image of OMC-PtBi-3nm (dark field); b) an ultra-high resolution TEM image of a representative PtBi particle in OMC-PtBi-3nm (bright field).**

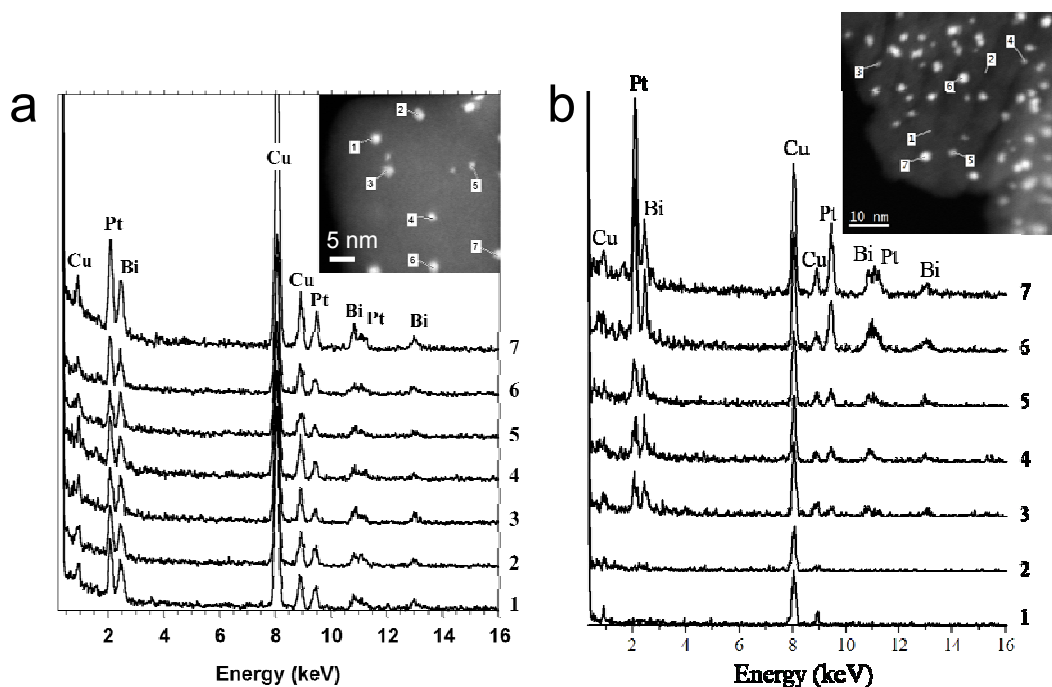


**Figure 6.23, a, b) EDX spectra for individual PtBi nanoparticles in OMC-PtBi-3nm where the inset shows the corresponding TEM image with nanoparticles correspondingly labeled (dark field).**

To further crystallize the intermetallic structure (24wt% total metal/composite), the material was heated in argon at 600 °C for 2 hrs. This resulted in uniform growth of the PtBi to form slightly larger, well dispersed crystallites (**Figure 6.22a**). An average dimension of about 2 - 3 nm was estimated from the Annular Dark-Field STEM images, and also from the Dark-Field TEM data shown in **Figure 6.23 (inset)**. This annealed material is termed as OMC-PtBi-3nm. A HRTEM image shows a representative PtBi particle along the [112] zone axis (**Figure 6.22b**). The spacing and angle ( $\sim 60^\circ$ ) of the two visible set of fringes correspond to the (012) and (110) planes of PtBi: [(012) - 2.21 Å expected, 2.21 Å obs; (110) - 2.15 Å expected, 2.16 Å obs]. These planes are unique for PtBi. EDX measurements

were conducted on single particles from different areas of the sample using a scanning transmission electron microscope equipped with an aberration-corrector of the electron probe and a high-brightness electron source (FEI Titan 80-300 Cubed). The EDX spectra (**Figure 6.23**) from two different regions unequivocally demonstrated the existence of both Pt and Bi *in each crystallite*, as did simultaneous sampling of many particles over a larger area. As the spectra (**Figure 6.23b,1,2**) show, Pt/Bi EDX is absent in the background area, which indicates the reliability of the EDX data due to its high resolution.

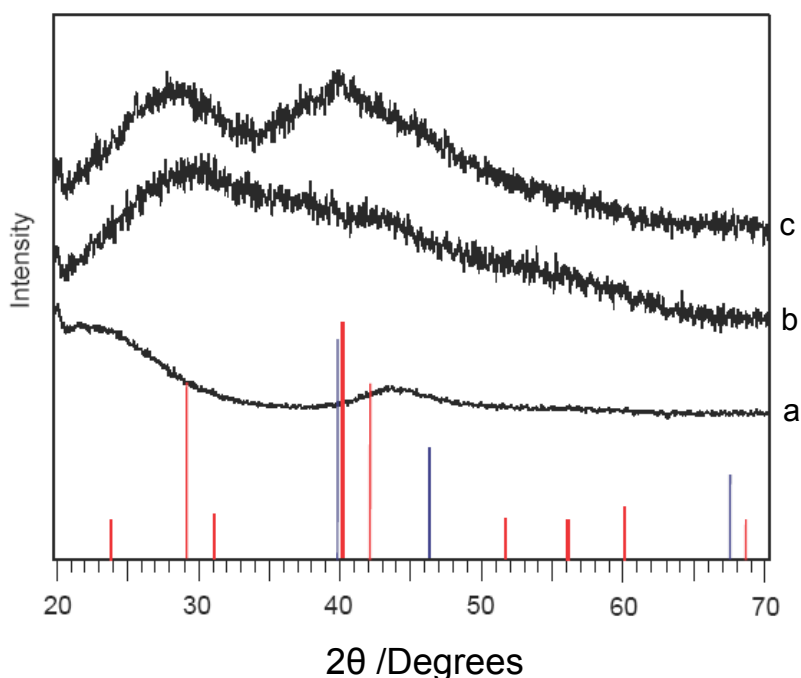


**Figure 6.24** Wide angle XRD patterns of a) OMC; b) OMC-PtBi-1nm; c) OMC-PtBi-3nm. Blue markers indicate Pt phase; red markers indicate PtBi phase [11].

A transition from PtBi-1nm to larger, more ordered 3 nm nanocrystallites upon heat treatment is also evident by XRD (**Figure 6.24b, c**). The growth from OMC-PtBi-1nm to OMC-PtBi-3nm results in sharpened reflections. Although there is a considerable degree of

peak broadening owing to the very small crystallite size, the reflections exhibited by OMC-PtBi-3nm are in good accord with that of bulk PtBi [11], and do not match that of either end member phase (Pt or Bi) or any of their oxides. Note that the broad carbon contribution from the OMC (**Figure 6.24a**) does not interfere with the PtBi pattern.

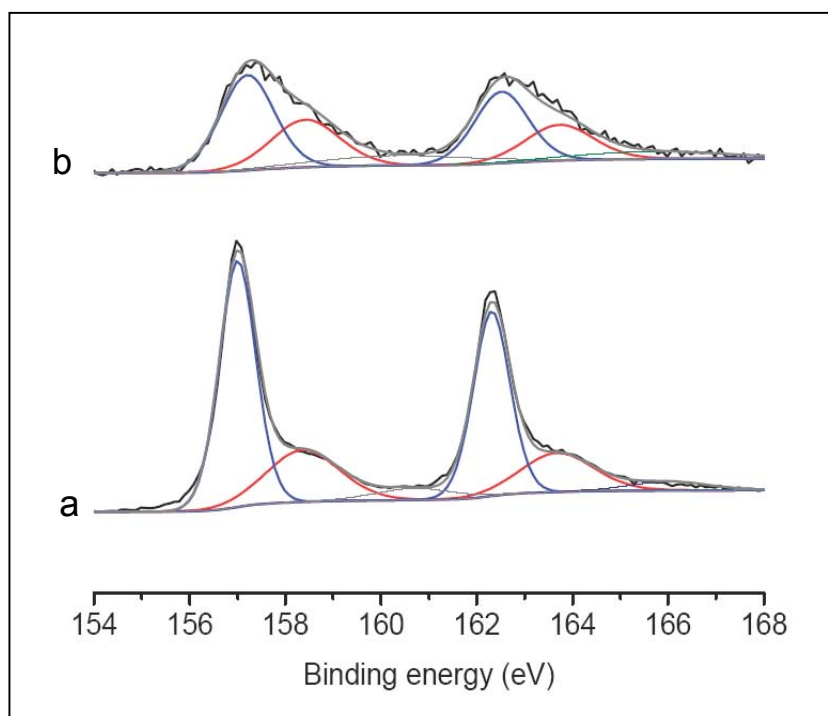


**Figure 6.25 XPS of a) bulk PtBi Bi [4f] and b) OMC-PtBi-3nm Bi [4f].**

XPS were also collected for composite materials. The C 1s signal served as an internal reference. As shown in **Figure 6.25**, both bulk PtBi and OMC-PtBi-3nm exhibit a Bi4f<sub>7/2</sub> signal which can be deconvoluted into two components: the minor signal at 158.4 eV, is attributed to surface Bi<sub>x</sub>O<sub>y</sub> formed during transfer of the sample in air to the XPS chamber (an oxide component is also apparent in the Pt4f spectrum, **Figure 6.5b**). The major

component at 157.0 - 157.2 eV, lies at higher energy compared to that of pure Bi metal supported on OMC (156.7 eV), and is characteristic of PtBi as reported elsewhere [12]. It can be noted that nano-PtBi is also very slightly shifted to higher energy compared to bulk-PtBi.

To the best of my knowledge, this is the first time that PtBi intermetallic nanoparticles of 3 nm and less in diameter were prepared with extremely homogeneous distribution on carbon supports, especially in the voids of OMC.

### 6.3.8 Electrochemical studies of catalyzed formic acid oxidation reactions

The steady state cyclic voltammograms (CV) of formic acid oxidation on the different catalysts at a scan rate of 10 mV/s are presented in **Figure 6.26**. For OMC-Pt-2nm, the first current maximum at 0.68 V (vs. reversible hydrogen electrode (RHE)) in the anodic scan is assigned to the “direct path” reaction (path 1, see section 1.3.3.2) (**Figure 6.26 black**). The second current maximum at 0.94 V with a hysteresis corresponds to oxidation of CO<sub>ad</sub>, accumulated in the “CO path” (path 2, see section 1.3.3.2). The ratio between the two peaks’ intensity sheds light on the question of which path is adopted more during the catalysis process. With the poisoning species consumed in the anodic scan, the current attains a higher maximum in the subsequent cathodic scan. A CV of formic acid oxidation on conventionally prepared CMK-3/Pt carried out under the same conditions was also performed (**Figure 6.26a red**). OMC-Pt-2nm is clearly superior to CMK-3/Pt. It exhibits a lower onset potential, a higher current maximum for formic acid oxidation, and a higher <formic acid oxidation> vs. <CO oxidation> peak ratio. This demonstrates that the sulfur employed in the catalyst preparation is fully removed and does not contaminate or poison the surface.

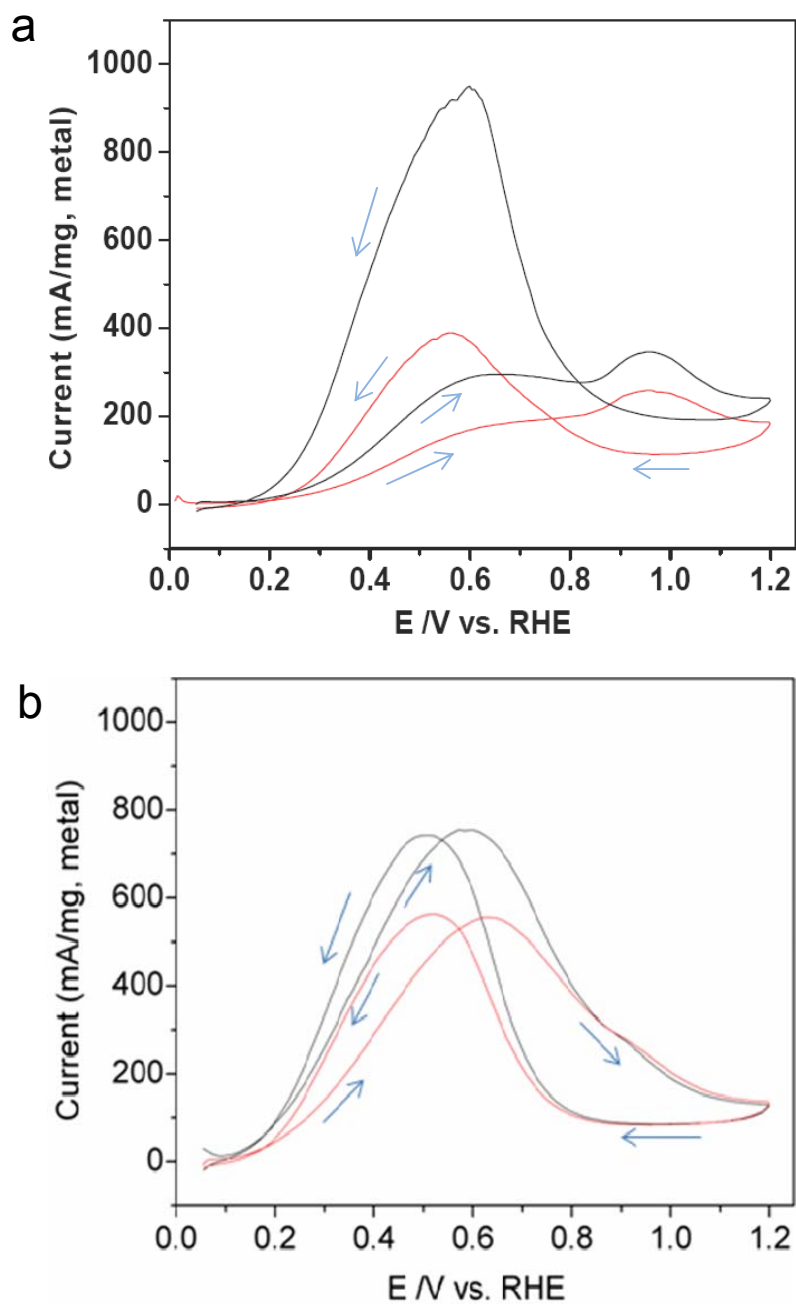


**Figure 6.26** Steady state cyclic voltammograms obtained for formic acid oxidation on a) CMK-3/Pt (red) and OMC-Pt-2nm (black) b) OMC-PtBi-1nm (red) and OMC-PtBi-3nm (black) in  $N_2$  saturated 0.5 M sulfuric acid plus 0.5 M formic acid solution. The scan rate is 10 mV/s. All catalysts were cleaned with faster scan at 50 mV/s for 3 cycles at a steady state.

**Figure 6.26b** shows the voltammograms of formic acid oxidation on OMC-PtBi-1nm and OMC-PtBi-3nm. The catalytic performance closely resembles the case of carbon/Pd catalyzed formic acid oxidation, where Pd is reported favourable to dehydrogenation of formic acid without the formation of CO [13]. The current behaviour of formic acid oxidation in scans on both directions is nearly identical, which is a significant improvement compared to the pure Pt case [14], or “large-nano” intermetallic PtBi materials in the literature [7,8]. The results indicate that the dehydrogenation path is completely eliminated on these OMC-PtBi catalysts. OMC-PtBi materials exhibit an onset potential of about 0.08 V, which is 0.12 V lower than that OMC-Pt-2nm, indicating that formic acid oxidation is catalyzed more easily on PtBi nanoparticles *vs.* pure Pt. OMC-PtBi-3nm displays superior properties than those of OMC-PtBi-1 nm. It exhibits both a higher current maximum and at a lower potential (0.57 V *vs.* RHE). The improved crystallinity of the 2-3 nm PtBi particles *vis a vis* the 1 nm PtBi explains their superior properties. Furthermore, OMC-PtBi-3nm exhibits a very high mass activity of 770 mA/mg at 0.57 V which is double that of Pt-decorated-Au nanoparticles (400 mA/mg) [15] and PtAg alloy nanoparticles (340 mA/mg) [16] recently reported under the same conditions used here.

Chronoamperometry (CA) was carried out at a practical operating voltage of 0.3 V *vs.* RHE to investigate the long term stability of OMC-PtBi-3nm for catalyzing formic acid oxidation. The CA curve is shown in **Figure 6.27**. It starts off with a very high activity (800 mA/mg) and experiences a deactivation process at a rate of ~ 5%/100s in the first 1000 seconds, and at the end of the first hour, a mass activity of 220 mA/mg is achieved (**Figure 6.27a**). This is quite comparable to that of Pd nanoparticles with a particle size of 3 nm

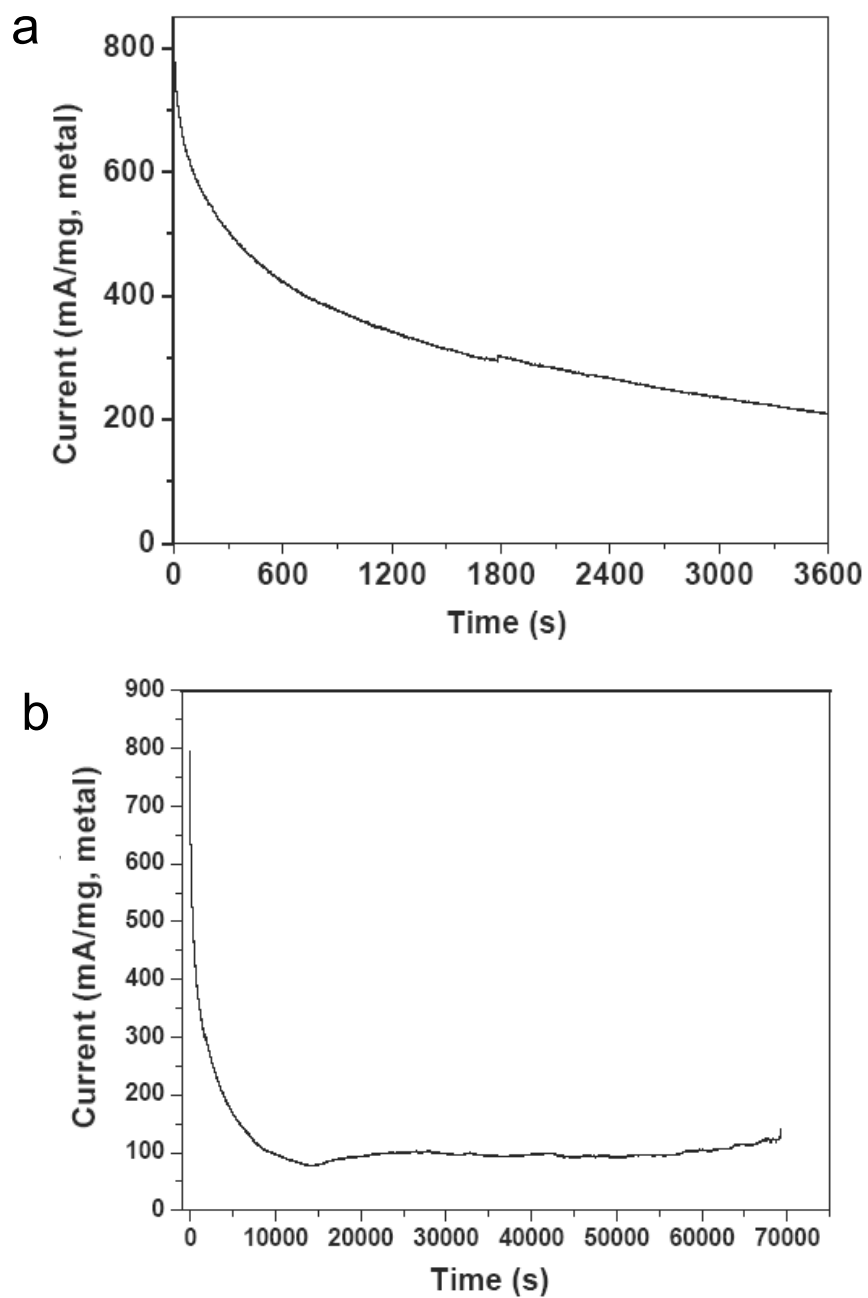


**Figure 6.27** CA curve of the OMC-PtBi-3nm with working electrode rotated at 200 rpm at a given potential of 0.3 V vs. RHE. a) I-t curve shown for the first an hour; b) I-t curve shown for whole 20 hrs.

which exhibits a deactivation rate of 4.5%/100s in the first 1000 seconds [13]. The current decay diminishes over the next 2 hrs to fully stabilize at 100 mA/mg for another 17 hrs until the measurement is manually stopped (**Figure 6.27b**). As expected, PtBi nano-intermetallic shows greatly improved performance including much higher mass activity and better resistivity to poisoning over a long term, compared to pure Pt case which typically loses 80% of its activity in the first 60 seconds [17]. To date, stability tests on bulk PtBi and PtBi nanoparticles have not been reported for comparison for our knowledge. Our OMC-PtBi is superior to the Pt<sub>80</sub>Ru<sub>20</sub> nanoparticles [18] and PtPd nanoparticles [19]. It exhibits a higher activity per gram at a same deactivation rate. The CA behaviour of OMC-PtBi is quite comparable to the carbon supported Pd nanoparticles (3 nm [13] and 6 nm [20]) which exhibit almost the same current fading rate and mass activity. To our best knowledge, except these nano-catalysts mentioned above, most the other catalysts reported either exhibit very low activity with higher stability [21] or suffer very fast current deactivation [22]. To date, to simultaneously achieve high stability and high activity of formic acid oxidation to a higher degree still remains as a challenge. This not only requires highly developed synthetic techniques for new catalysts but also more comprehensive understanding on the catalysis process.

#### **6.4 Conclusion**

In conclusion, I describe a novel, highly effective methodology for impregnating noble metal and bimetallic nanoparticles into OMC voids with precisely controlled particle size and ultra-high dispersion. The method is applicable to a wide range of catalysts, namely bimetallic PtBi but also including Pt, Ru, Rh and Pd. It is evident that intermetallics less than

3.5 nm in diameter can be formed in the channels of OMC with this approach. The method is also tailored for the deposition of single and binary catalysts on conventional fuel-cell carbon supports that are sulfur-modified. OMC-PtBi nanohybrids were investigated as catalysts for formic acid oxidation for the first time. OMC-PtBi catalysts show an absence of CO poisoning. By comparing our material to the other state-of-the-art catalysts with available stability performances, it is evident that our OMC-PtBi-3nm is one the most stable catalysts reported for formic acid oxidation with very high level of mass activity under similar conditions. The excellent catalytic properties can be attributed to the successful catalyst preparation and the faithful practice of the “ensemble effect” at the nanoscale level. Although the concept is illustrated here with nanocrystalline PtBi, the generality of this process dictates that a variety of intermetallics having at least one component that strongly interacts with sulfur could also be developed for bi and tri-metallic nanocrystallites. These can be supported on a variety of porous carbons using this approach, aimed at a broad set of applications including electrocatalysis and catalysis.

## Chapter 7

### **Agitation Induced Loading of Sulfur into Carbon CMK-3 Nanotubes: Scavenging of Pt Ions from Aqueous Solution**

#### **7.1 Introduction**

It is economically and ecologically important to recover platinum group metals (PGM) from dilute effluents [1] which include leached electronics or catalyst wastes, fission product solutions from nuclear reactors [2], and geothermal brines [3]. Recently, there has been a concern that Pt based catalysts in polymer electrolyte membrane fuel cells (PEMFC) suffer dissolution problem during operation, particularly at high output. This forms dilute Pt effluents, which potentially generates negative impact. Sorbents which can rapidly capture otherwise lost Pt from dilute solutions are highly desirable [4]. Extensive efforts have been devoted to chitosan based materials [5,6,7] that exhibit sorption mainly through the ion exchange mechanism, which is only effective to metal complex anions. It also takes hours or days to achieve an equilibrium sorption due to the nature of the ion exchange process, which limits their applications.

It is well known that elemental sulfur exhibits strong affinity to heavy metals through a soft acid/base interaction [8,9]. Sulfur impregnated activated carbon (SIAC), prepared by vaporizing sulfur onto activated carbons is used as a mercury sorbent [10]. However, bulk SIAC exhibits poor efficiency for the capture of Pt ions from dilute solutions, owing to poor porosity. Ordered mesoporous carbons (OMC) [11], in contrast, display various valuable characteristics, such as tunable pore structure/size and surface chemistry. These can be

employed to build nanostructured sorbents [12,13,14]. In *Chapter 5*, a melt-diffusion method has been introduced to deposit a (thin) coating of sulfur onto the channel surface of OMCs, while maintaining the structural order and porosity [15]. However, to achieve fast uptake of metal ions, the particle size of OMC (above 1  $\mu\text{m}$ ) still represents a longer diffusion path than the ideal case [16].

Herein, a unique and efficient scheme is presented for the preparation of sulfur functionalized CMK-3 [17] (a well studied OMC) nanorods (nano-CMK-3/S) and its application as a Pt sorbent in extremely dilute solutions is also discussed.

## 7.2 Experimental

Nano-CMK-3 and bulk CMK-3 rods are prepared by the nanocasting method (see **section 3.2.1**). In a typical agitation-friction process for the preparation of nano-CMK-3/S, solid elemental sulfur powder 0.1 g (or 0.11g) and nano-CMK-3 0.1 g are dispersed into 5 ml de-ionized water. The mixture was vigorously stirred for 24 hrs. The composite was collected by filtration and dried at 50°C.

For kinetics studies, sorbents (10 mg) was dispersed into dilute solution of  $\text{H}_2\text{PtCl}_6$  (100 ml, 5 mg Pt/L). After various time intervals, parts of the mixture were filtered to collect the filtrate for analysis. Solution concentration was determined by inductive coupled plasma mass spectrometry (ICP-MS) carried out by Galbraith Laboratories (Tennessee, USA). For total sorption capacity tests, sorbents (30 mg) were dispersed into an excessive  $\text{H}_2\text{PtCl}_6$  solution (3000 ml, 10 mg Pt /L).

## 7.3 Results and discussion

### 7.3.1 Characterizations of sulfur filtration

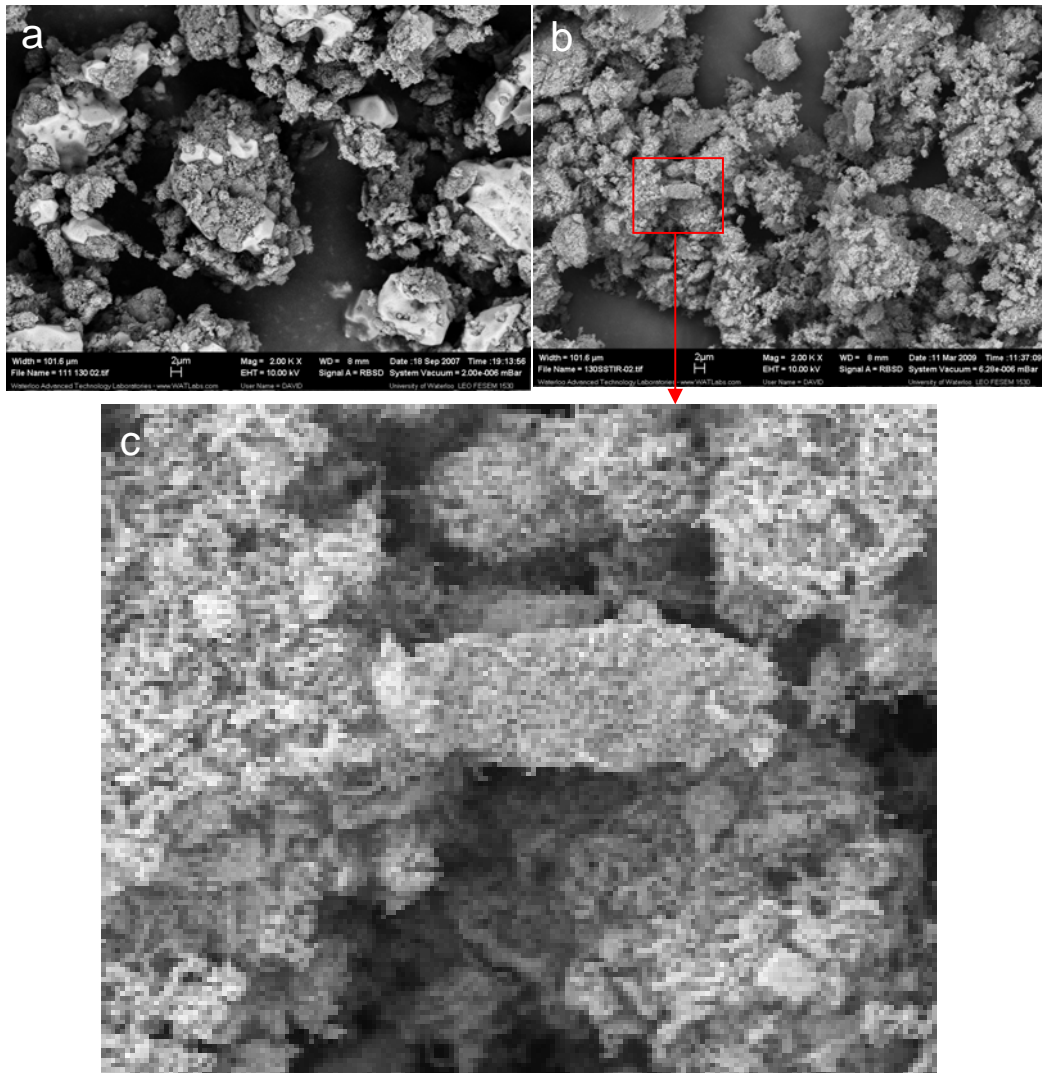


**Figure 7.1 SEM images of nano-CMK-3/S prepared by a) melt-diffusion method; b) agitation-friction method; c) image expansion of the area outlined by the red square in part b.**

To infiltrate sulfur into nano-CMK-3, a melt-diffusion method (see **section 5.2.2**) was first attempted. This was highly effective for the preparation of bulk-CMK-3/S composites which show excellent properties as cathodes in Li-S batteries [14]. A mixture of nano-CMK-3 and sulfur was ground together and heated to 155°C. As shown in **Figure 7.1a**, the resultant C/S sample (C/S 1:1 in weight), does not display the same complete encapsulation of sulfur within the nano-CMK-3 channels that is exhibited by bulk CMK-3 (see **Figure 5.6c**). This may result from the much weaker capillary force within these nanosized structures (nano-scaffolds), which is also evident in its N<sub>2</sub> adsorption and desorption isotherms, as shown in **Figure 3.10**. Nano-CMK-3 does not exhibit typical Type IV profiles of other mesoporous solids, and exhibits a very small hysteresis loop (see **section 3.2.2**).

To realize the sulfur filtration, an unusual method was developed. It relies on friction forces, and the hydrophobic attraction of the components. Typically, a mixture of elemental sulfur and mesoporous carbon (C/S 1:1 in weight) was simply dispersed into de-ionized water, and vigorously stirred for 24 hrs. The collision/friction with carbon forces sulfur into carbon nano-scaffolds. This approach is completely different from any conventional impregnation which requires the molecular mobility of guest phases (liquids [18,19] or vapour [20,21]).

The nano-CMK-3/S composite exhibits a strong sulfur signal in its EDX spectrum (**Figure 7.2c**), and a morphology (**Figure 7.1b, c, Figure 7.2b**) identical to empty nano-CMK-3 (**Figure 7.2a**). This is in sharp contrast to the composite prepared by the melt-

diffusion method that shows bulk sulfur masses. The intense peaks in the XRD pattern (Figure 7.2d i and ii) assigned to sulfur in the C/S mixture completely vanish after the agitation-friction process. The C/S mixture also exhibits a large decrease of its surface area from 543 to 137 m<sup>2</sup>/g, and decrease of the specific pore volume from 0.63 to 0.31 cm<sup>3</sup>/g, respectively. Taken together, this demonstrates that the nano-CMK-3 channels are effectively infiltrated with sulfur.

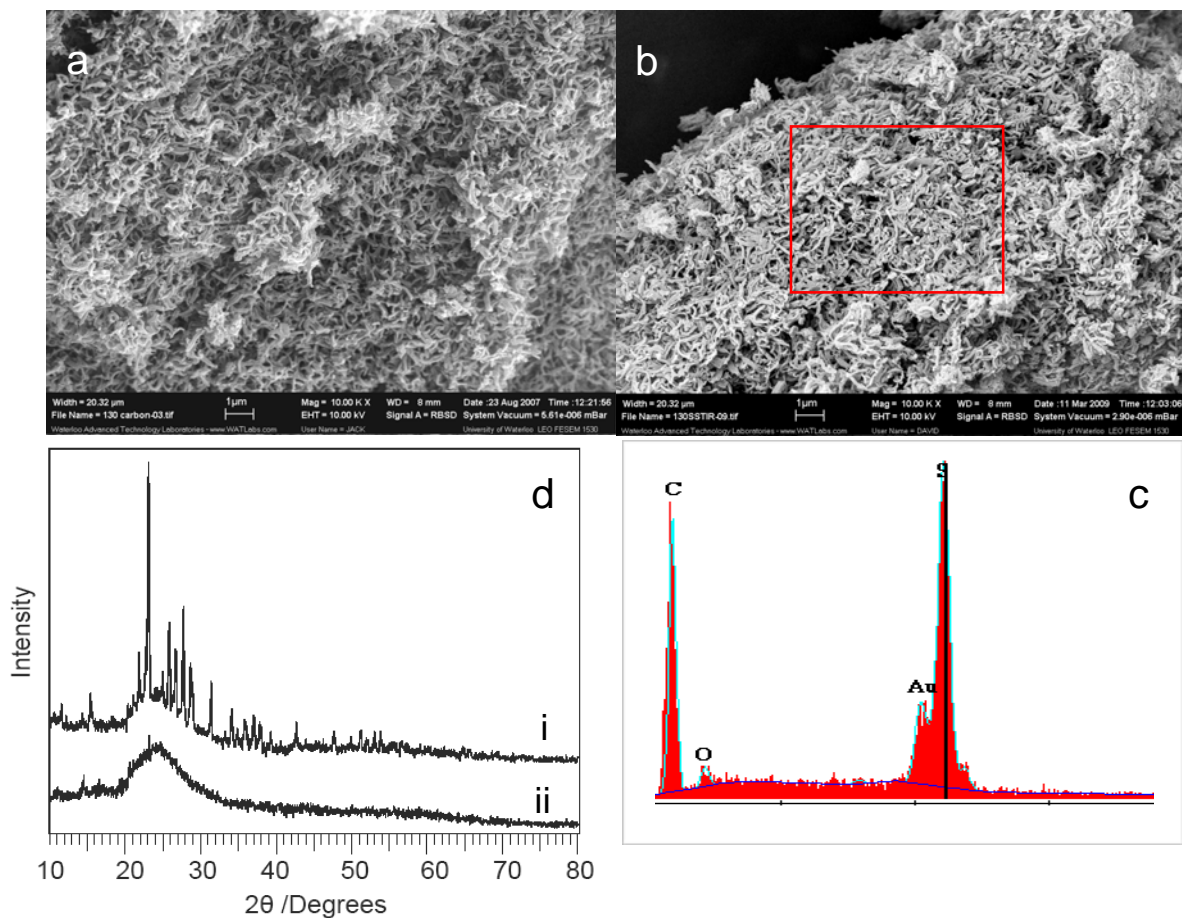


**Figure 7.2** SEM image of a) nano-CMK-3; b) nano-CMK-3/S prepared by agitation-friction method; c) corresponding EDX spectrum of inset area outlined by red square in part b; d) XRD patterns of (i) simple mixture of nano-CMK-3 and sulfur, (ii) nano-CMK-3/S prepared by agitation-friction.

### 7.3.2 Infiltration mechanisms

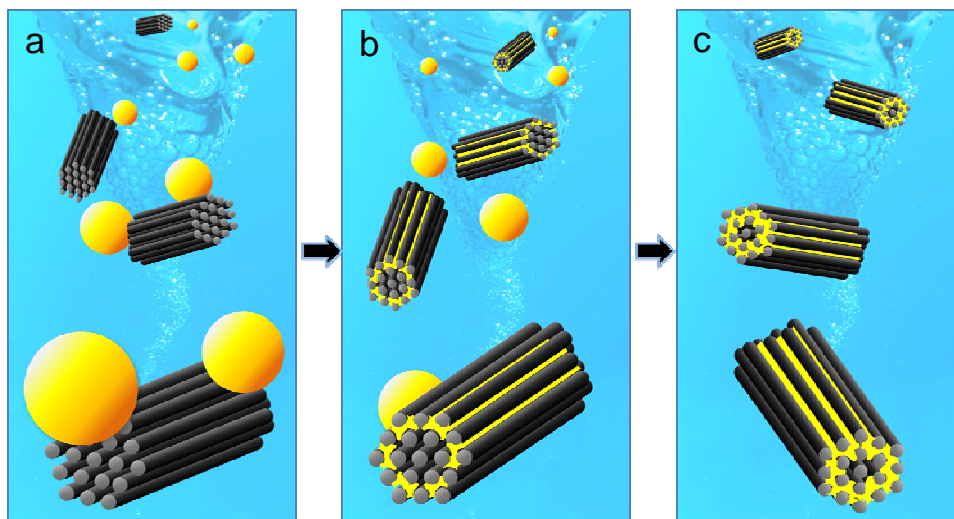


**Figure 7.3** Schematic diagram depicting the agitation-friction process a) initial mixture of nano-CMK-3 and sulfur; b) during infiltration; c) final stage with sulfur all infiltrated.

The mechanism takes place by a mechanical/chemical process, which is schematically illustrated in **Figure 7.3**. Since sulfur is a soft material bound together by weak van der Waals forces, with a hardness of only  $\sim 2$  (on the Mohs' scale) [22], the  $S_8$  molecules can be easily dislodged from the bulk particles by friction provided by the hard carbon nanoscaffolds, which are comprised mainly of  $sp^3$  carbon. Upon vigorous stirring in aqueous solution, the soft sulfur particles and carbon nanorods are provided with high kinetic energy and countless chances of collision. Thus, the sulfur mass is forced in between the gaps in parallel carbon nanofibers on the sides of carbon nanoscaffolds, as schematically shown in **Figure 7.3b**. The sulfur masses formed between the carbon nanofibers are pushed deeper into the interior structure by the force of the incoming sulfur. The process ceases when all of

the sulfur is incorporated into carbon nanoscaffolds as schematically shown in **Figure 7.3c** and as experimentally observed in **Figure 7.1b, c** and **Figure 7.2b**.

The solid-solid wetting can clearly only proceed when it is both thermodynamically and kinetically viable. First, the energy imparted to the system must be sufficient to overcome the cohesive energy of molecular sulfur. This is provided by frictional force. However, sulfur can not be incorporated into *siliceous* SBA-15 nanorods of exactly the same dimensions. The hydrophobicity of both sulfur and carbon is a prerequisite. This can be understood by the fact that in an aqueous medium, the interfacial tension  $\gamma_{cw}$  at carbon/water and  $\gamma_{sw}$  at sulfur/water is larger than  $\gamma_c$  and  $\gamma_s$  (in air), respectively. The surface energy of the system will decrease if both carbon and sulfur reduce their contact area with water, which favours infiltration [23].

The agitation-friction process was also attempted for bulk CMK-3 with sulfur (to a target of C/S 1:1 in weight). As shown in **Figure 7.4a, b**, The SEM image and corresponding sulfur EDX map show that the infiltration took place although the depth of sulfur penetration cannot be determined from a 2D map. The surface of sulfur infiltrated CMK-3 particle exhibits clear contrast, as shown in **Figure 7.4c**, which confirms that infiltrated sulfur are pushed *into* the mesoporous structure, instead of spreading on the surface. However, the infiltration to bulk CMK-3 is incomplete, as shown by the presence of bulk sulfur masses in the SEM (**Figure 7.4d**)

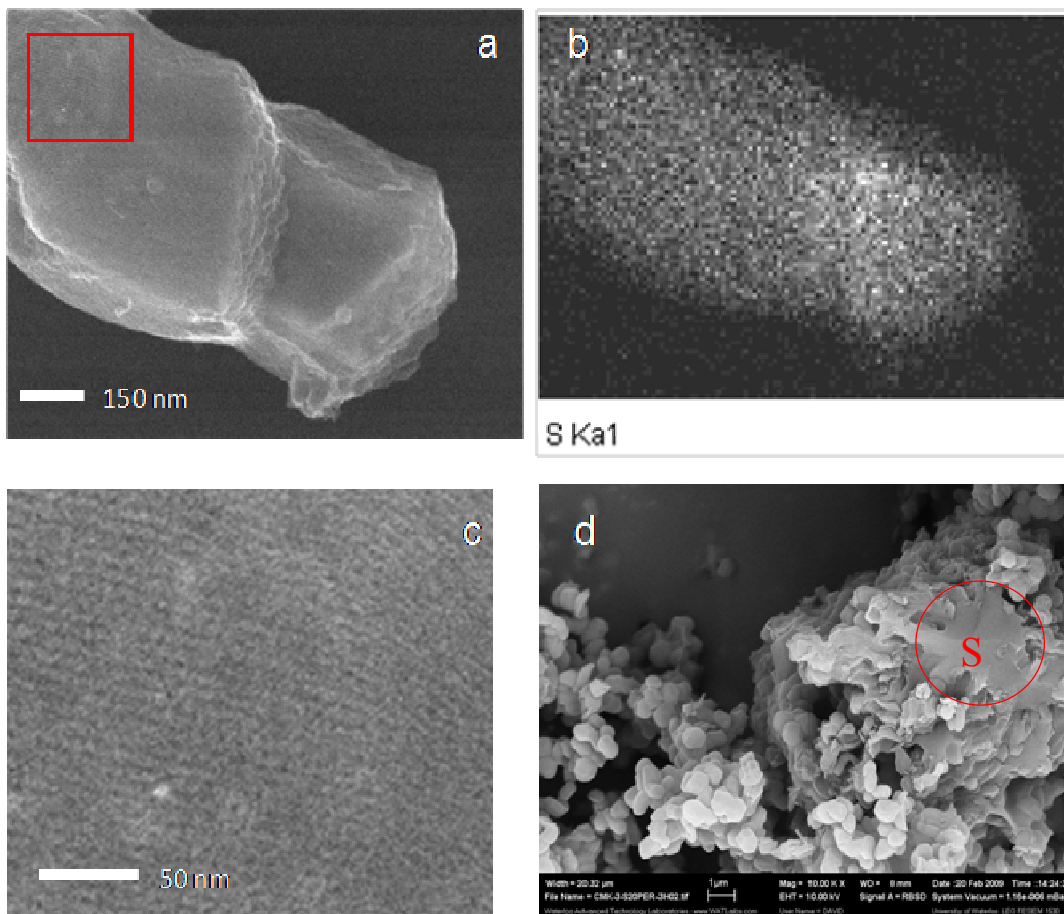


**Figure 7.4 SEM images and sulfur map of bulk CMK-3/S composite prepared with agitation-friction method a) high resolution image; b) corresponding EDX sulfur map to part a; c) enlarged image corresponding to the area outlined by the red square in part a; d) low resolution image.**

The size of mesoporous carbon particles is an important factor in an agitation-friction process. Note that nano-CMK-3 (diameter: 80 nm and pore volume: 1.1 cm<sup>3</sup>/g) has 43.9% of its pore volume within a depth of 10 nm, which is enough to accommodate an equivalent mass of sulfur (assuming infiltrated sulfur has a density of 2.07 g/cm<sup>3</sup> [24]). However, bulk

CMK-3 (1  $\mu\text{m}$  in diameter and pore volume 2.06  $\text{cm}^3/\text{g}$ ) has only 4% of its pore volume within a depth of 10 nm. To accommodate an equivalent sulfur/carbon ratio, the initial moving front has to be forced 62.5 nm into the bulk which leads to a higher activation energy (due to channel blockage) and less favourable kinetics.

### 7.3.3 Nano-CMK-3/S's uptake of aqueous Pt ions

To realize practical adsorption applications for nano-CMK-3/S, an optimized amount of sulfur (10wt%) was loaded into nano-CMK-3 by the agitation-friction method. BET data reveal reduced surface area (from 995 to 719  $\text{m}^2/\text{g}$ ) and reduced pore volume (from 1.1 to 0.92  $\text{cm}^3/\text{g}$ ) for the nano-CMK-3/S (C/S 9:1 in weight), compared to nano-CMK-3 itself. As shown in **Figure 7.5a, b**, the pore size decreases from 3.4 nm to 3.0 nm and the pore size distribution (PSD) gets broader upon the agitation-friction process as well. As known, the infiltrated sulfur mainly resides in the shallow space of the nanorods (10 nm in depth). For adsorption applications, it is favourable to have the infiltrated sulfur spread over the entire inner surface area of the nanorods. This can facilitate the diffusion path for adsorbates and maximize the adsorption active surface area as well. To realize this, the composite (C/S 9:1 in weight) prepared by agitation-friction was treated at 155°C for 12 hrs. As shown in **Figure 7.5c**, the heated composite exhibits a sharper PSD and a pore size of 2.6 nm. This is consistent with formation of thin sulfur layer on the carbon surface (0.8 nm in thickness). Bulk CMK-3/S composite (C/S 9:1 in weight) as a sorbent was also prepared by the melt-diffusion method for comparison.

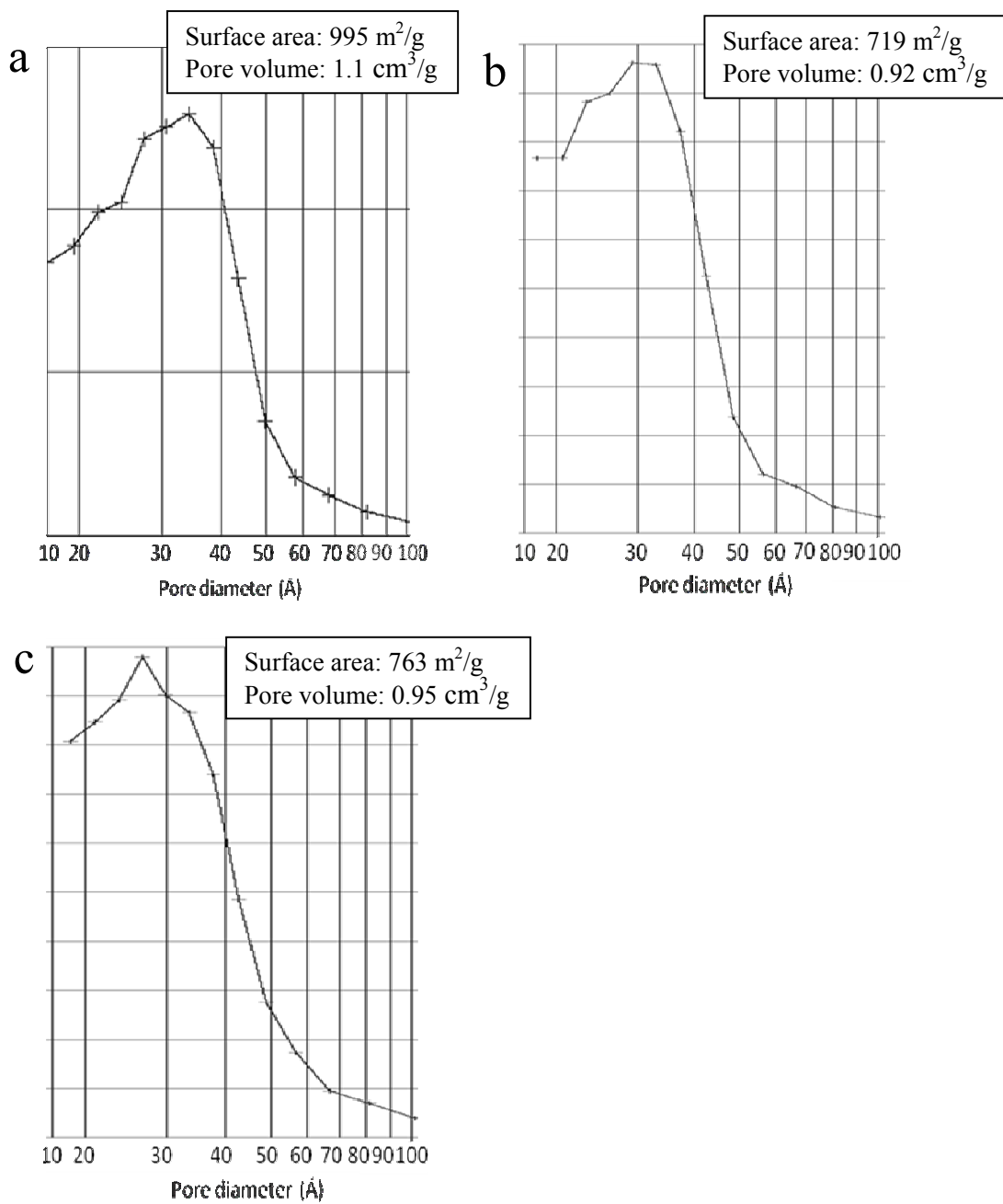


**Figure 7.5** Pore size distribution curves of a) nano-CMK-3; b) nano-CMK-3/S before sulfur melting; c) nano-CMK-3/S after sulfur melting.

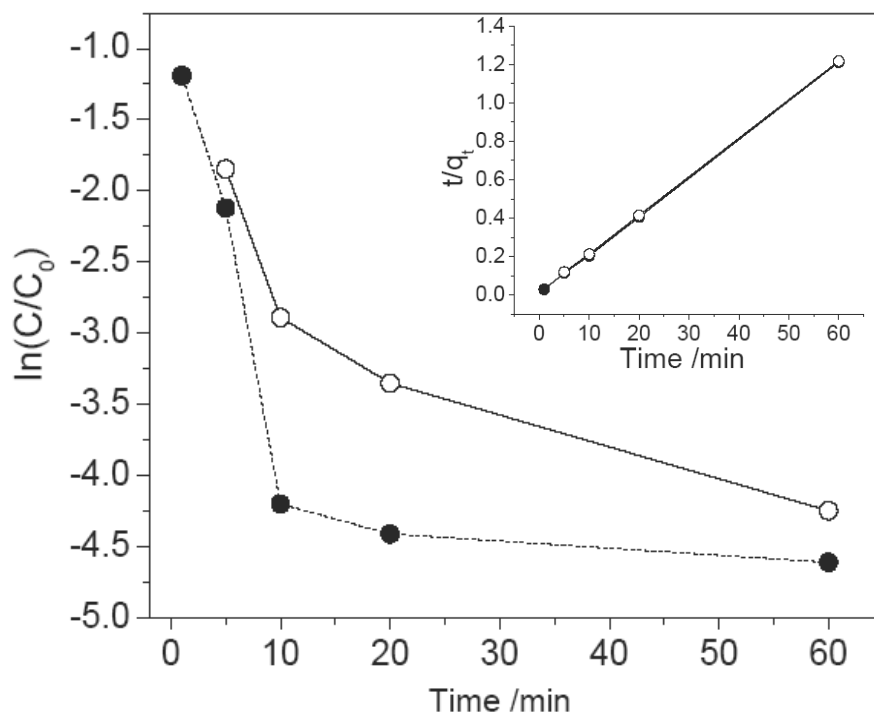


**Figure 7.6** Plots of  $\ln(C/C_0)$  vs.  $t$ , on Pt sorption kinetics, nano-CMK-3/S (solid black dots) and bulk CMK-3/S (hollow circle), inset: pseudo-second-order model fitting on sorption kinetics.

For kinetics studies, sorbents (10 mg) were dispersed in dilute solutions of  $H_2PtCl_6$  (100 mL, Pt: 5 mg/L). After various time intervals, portions of the mixture were filtered and the filtrate was analysed. During the sorption tests, it was observed that nano-CMK-3/S was initially much more readily dispersed in the solutions than its bulk counterpart. **Figure 7.6** shows the platinum sorption kinetics of nano-CMK-3/S (S: 10wt%) and bulk CMK-3/S (S: 10wt%) at pH 4.0. Rapid uptake took place after the dispersion of both sorbents, particularly for the nanomaterial. Within the first minute of contact, 70% of the Pt was immediately adsorbed in nano-CMK-3/S, and 99% within the first 10 min. This is more rapid compared to

bulk CMK-3/S (94.4% in the first 10 min, and 99% after one hour). The diffusion path in nano-CMK-3/S is only 1/10 of that in its bulk counterpart, which explains its faster kinetics.

Sorption controlled by chemical interactions typically fits the pseudo-second-order kinetics model [25] which can be expressed as:

$$dq_t/dt = k(q_e - q_t)^2 \quad (7-1)$$

where  $k$  is the rate constant for pseudo-second-order (g/mg/min) kinetics. Value  $q_t$  (mg/g) is the amount of solute captured by a sorbent at any time  $t$ . Sorption capacity  $q_e$  (mg/g) is the theoretical amount of solute adsorbed at equilibrium. After integration by applying boundary conditions ( $q_t = 0$  at  $t = 0$  and  $q_t = q_t$  at  $t = t$ ), Eq. [7-1] can be linearized as:

$$t/q_t = 1/(k \cdot q_e^2) + t/q_e \quad (7-2) [26]$$

**Table 7.1 Parameters calculated from the pseudo-second-order model and obtained from experiments.**

Sample	$q_e$	$R^2$	$k_2$	$q_{e \text{ exp.}}$
CMK-3/S	49.93	1.0	$2.71 \cdot 10^{-2}$	151
Nano-CMK-3/S	50.5	1.0	$5.35 \cdot 10^{-2}$	169

Sorbent dosage: 0.1g/L; stirring speed: 300 rpm;  $C_0 = 5$  mg/L;  $q$  is unit of (mg metal/g), and  $k$  is units of (g/mg/min);  $q_{e \text{ exp.}}$  is obtained from solutions concentrated at 10 mg/L.

A plot of  $t/qt$  vs.  $t$  (**Figure 7.6 inset**), confirms that sorption (both bulk and nano CMK-3/S) fits the pseudo-second-order kinetics model very well ( $R^2 = 1.0$ ). The rate constant for nano-CMK-3/S calculated from the slope and the intercept is nearly twice that of its bulk counterpart, as listed in **Table 7.1**. Under the similar conditions, the rate constant of nano-CMK-3/S is one order of magnitude higher than the recently reported chitosan sorbents which follow pseudo-second-order sorption kinetics as well [27]. Note that both the pseudo-first-order model and the intraparticle diffusion mode [28] do not fit the sorption data here as they fail to yield straight lines from their linearized model equations.

The capacity of a sorbent can be further quantified through the use of a mass-weighted partition coefficient ( $K_d$ ), which represents the distribution of noble metal in the absorbent vs. the solution ( $K_d = [(C_0 - C_f)/C_f] \cdot V/M$ ;  $C_0$  and  $C_f$  represent the initial and final concentrations of solute,  $V$  (ml) is the volume of solution and  $M$  (g) is the mass of a sorbent). This measure of a sorbent material's affinity for the metal yields a  $K_d$  of 990,000 for nano-CMK-3/S.  $K_d$  values of 100,000 are considered excellent, and values as high as 200,000 have been reported for Hg adsorption on heteroaromatic-functionalized mesoporous carbon [14]. However, Pt and Hg adsorption are not strictly comparable.

Equilibrium sorption capacity of sorbents was measured by employing an excessive solution with initial platinum concentration of 10 mg/L. Nano-CMK-3/S can uptake 169 mg Pt per gram of the sorbent, higher than the bulk CMK-3/S [151 mg Pt/(g sorbent)].

About 95% of loaded Pt can be desorbed by sonicating in an aqueous solution containing 0.1 M dithiooxamide for 1 hr. Dithiooxamide is a well-known chelating agent for metals [29]. By forming a complex most likely with two dithiooxamide molecules, Pt species can be effectively removed from the CMK-3/S sorbent into the eluent solution.

#### **7.4 Conclusions**

In summary, nano-CMK-3 rods were imbibed with solid sulfur simply by vigorously stirring the aqueous mixture at room temperature. The facile infiltration can be explained by a combination of chemical and mechanical schemes. This is the first example of a nanoporous material which can be infiltrated by another solid phase at room temperature. This fabrication strategy may be applied to prepare other nanostructured materials by using soft materials as the fillers. In terms of Pt uptake, nano-CMK-3/S not only exhibits better sorption kinetics than its bulk counterpart, but also a higher rate constant than the recently reported chitosan sorbents which follow the pseudo-second-order kinetics model as well. Nano-CMK-3/S is potentially applicable in collecting noble metals from dilute effluents of PEFCs or other sources.

## References

### References for Chapter 1

- 1 M. S. Dresselhaus and I. L. Thomas, *Nature*, **414**, 332, (2001).
- 2 *U.S. Annual Energy Review 2008*, Report No. DOE/EIA-0384 (2008).
- 3 C. A. Vincent and B. Scrosati, *Modern Batteries: An Introduction to Electrochemical Power Sources*, John Wiley & Sons, Inc., New York. (1997).
- 4 J. L. Sudworth and A. R. Tilley, *The Sodium Sulfur Battery*, Chapman & Hall, London, (1985).
- 5 M. S. Whittingham, *Science*, **192**, 1126, (1976).
- 6 E. A. Cellar, M. E. Manna, R. D. Wise, A. B. Gavrilo, M. J. Bastian, R. M. Brey and J. DeMatteis, *J. Power Sources*, **96**, 184, (2001).
- 7 S. Laruelle, S. Grugeon, P. Poizot, M. Dollé, L. Dupont, and J-M. Tarascon, *J. Electrochem. Soc.*, **149**, A627, (2002).
- 8 M. S. Whittingham, *Chem. Rev.*, **104**, 4271, (2004).
- 9 K. Mitzushima, P. C. Jones, P. J. Wiseman and J. B. Goodenough, *Mater. Res. Bull.*, **15**, 783, (1980).
- 10 G. G. Amatucci, J. M. Tarascon and L. C. Klein, *J. Electrochem. Soc.*, **143**, 1114, (1996).
- 11 J. M. Reimers, W. Li and J. R. Dahn, *Phys. Rev. B*, **47**, 8486, (1994).
- 12 A. Rougier, P. Graveau and C. Delmas, *J. Electrochem. Soc.*, **143**, 1168, (1996).
- 13 C. Delmas and I. Saadon, *Solid State Ionics*, **370**, 53, (1992).
- 14 J.-C. Grenier, M. Pouchard and A. Wettiaux, *Current Opinion in Solid State & Materials Science*, **1**, 233, (1996).
- 15 W. Li and J. C. Currie, *J. Electrochem. Soc.*, **144**, 2773, (1997).
- 16 S. B. Schougaard, J. Bréger, M. Jiang, C. P. Grey and John B. Goodenough, *Adv. Mater.*, **18**, 905, (2006).
- 17 Z. Liu, A. Yu and J. Y. Lee, *J. Power Sources*, **416**, 81, (1999).
- 18 T. Ohzuku and Y. Makimura, *Chem. Lett.*, 744, (2001).

- 19 T. Ohzuku and Y. Makimura, *Chem. Lett.*, 642, (2001).
- 20 M. M. Thackeray, W. I. F. David, P. G. Bruce and J. B. Goodenough, *Mater. Res. Bull.*, **18**, 461, (1983).
- 21 A. K. Padhi, K. S. Nanjundaswamy and J. B. Goodenough, *J. Electrochem. Soc.*, **144**, 1188, (1997).
- 22 A. K. Pahdi, K. S. Nanjundaswamy, C. Masquelier, S. Okada and J. B. Goodenough, *J. Electrochem. Soc.*, **144**, 1609, (1997).
- 23 H. Huang, S.-C. Yin and L. F. Nazar, *Electrochem. Solid State Lett.*, **4**, A170, (2001).
- 24 P. S. Herle, B. Ellis, N. Coombs and L. F. Nazar, *Nat. Mater.*, **3**, 147, (2004).
- 25 D. Peramunage and S. Licht, *Science*, **261**, 1029, (1993).
- 26 M. L. Rao, *US Patent*, No. 3413154, (1968).
- 27 D. Nole and V. Moss, *US Patent*, No. 3532543, (1970).
- 28 J. Wang, J. Yang, J. Xie and N. Xu, *Adv. Mater.*, **14**, 963, (2002).
- 29 W. Zheng, Y. Liu, X. Hua and C. Zhang, *Electrochim. Acta*, **51**, 1330, (2006).
- 30 X. Ji, K. T. Lee and L. F. Nazar, *Nat. Mater.*, **8**, 500, (2009).
- 31 R. D. Rauh, F. S. Shuker, J. M. Marston and S. B. Brummer, *J. Inorg. Nucl. Chem.*, **39**, 1761, (1977).
- 32 S.-E. Cheon, K.-S. Ko, J.-H. Cho, S.-W. Kim, E.-Y. Chin and H.-T. Kim, *J. Electrochem. Soc.*, **150** A800, (2003).
- 33 S. J. Visco and M. Y. Chu, *US Patent*, No. 6210832, (2001).
- 34 M.-S. Song, S.-C. Han, H.-S. Kim, J.-H. Kim, K.-T. Kim, Y.-M. Kang, H.-J. Ahn, S. X. Dou and J.-Y. Lee, *J. Electrochem. Soc.*, **151**, A791, (2004).
- 35 A. Gorkovenko, T. A. Skotheim, Z.-S. Xu, *US Patent*, No.6878488, (2005).
- 36 R. D. Rauh, K. M. Abraham, G. F. Pearson, J. K. Surprenant and S. B. Brummer, *J. Electrochem. Soc.*, **126**, 523, (1979).
- 37 M.-Y. Chu, *US Patent*, No. 5686201, (1997).
- 38 B. Jeon, J. Yeon, K. Kim and I. Chung, *J. Power Sources*, **109**, 89, (2002).
- 39 K. M. Abraham and Z. Jiang, *J. Electrochem. Soc.*, **143**, 1, (1996).

- 40 T. Ogasawara, A. Debart, M. Holzapfel, P. Novak and P. Bruce, *J. Am. Chem. Soc.*, **128**, 1390, (2006).
- 41 J. Yamaki and S. Tobishima, *Handbook of Battery Materials*, Wiley-VCH, Weinheim, (1999).
- 42 W. van Schalkwijk and B. Scrosati, *Advances in Lithium-ion Batteries*, Kluwer Academic/Plenum, New York, (2002).
- 43 J.-I. Yamaki, S.-I. Tobishima, Y. Sakurai, K.-I. Saito and K. Hayashi, *J. Appl. Electrochem.*, **28**, 135, (1998)
- 44 T. A. Skotheim, C. J. Sheehan, Y. V. Mikhaylik and J. Affinito, *US Patent*, No.6936381B2, (2005).
- 45 X. Yu, J. B. Bates, G. E. Jellison, Jr. and F. X. Hart, *J. Electrochem. Soc.*, **144**, 524, (1997).
- 46 J. J. Klaassen, *US Patent*, No.7211351B2, (2007).
- 47 G. Pistoia, *Lithium Batteries: New Materials, Developments and Perspectives*, Elsevier, Amsterdam, (1994).
- 48 M. Nakamizo and H. Honda, *Carbon*, **16**, 281, (1978).
- 49 P. G. Bruce, *Solid State Ionics*, **179**, 752, (2008).
- 50 E. Peled, *J. Electrochem. Soc.*, **126**, 2047, (1979).
- 51 A. Mabuchi, K. Tokumitsu, H. Fujimoto and T. Kasuh, *J. Electrochem. Soc.*, **142**, 1041, (1995).
- 52 M. Inaba, H. Yoshida, and Z. Ogumi, *J. Electrochem. Soc.*, **143**, 2572, (1996).
- 53 H. Zhou, S. Zhu, M. Hibino, I. Honma and M. Ichihara, *Adv. Mater.*, **15**, 2107, (2003).
- 54 M. Winter and J. O. Besenhard, *Electrochim. Acta*, **45**, 31, (1999).
- 55 K.-L. Lee, J.-Y. Jung, S.-W. Lee, H.-S. Moona and J.-W. Park, *J. Power Sources*, **130**, 241, (2004).
- 56 J. Li, R. B. Lewis and J. R. Dahn, *Electrochem. Solid-State Lett.*, **10**, A17, (2007).
- 57 P. Poizot, S. Laruelle, S. Grugeon, L. Dupont, and J. M. Tarascon, *Nature*, **407**, 496, (2000).

- 58 P. Poizot, S. Laruelle, S. Grugeon, L. Dupont, B. Beaudoin and J. M. Tarascon, *Ann. Isr. Phys. Soc.*, **3**, 681, (2000).
- 59 F. Badway, F. Cosandey, N. Pereira and G. G. Amatucci, *J. Electrochem. Soc.*, **150**, A1318, (2003).
- 60 S. Boyanov, J. Bernardi, F. Gillot, L. Dupont, M. Womes, J.-M. Tarascon, L. Monconduit and M.-L. Doublet, *Chem. Mater.*, **18**, 3531, (2006).
- 61 Q. Sun and Z. Fu, *Electrochim. Acta*, **54**, 403, (2008).
- 62 W. R. Grove, *Philos. Mag.*, **21**, 417, (1842).
- 63 W. Vielstich, A. Lamm and H. A. Gasteiger, *Handbook of Fuel Cells: Fundamentals, Technology, and Applications*, Wiley, West Sussex, UK, (2003).
- 64 M. Winter and R. J. Brodd, *Chem. Rev.*, **104**, 4245, (2004).
- 65 M. H. Nebrir, C. Wang and S.R. Shaw, *IEEE Pow. & Ener. Mag.*, **4**, 47, (2006).
- 66 A. S. Aricò, S. Srinivasan and V. Antonucci, *Fuel Cells*, **1**, 133, (2001).
- 67 M. Weber, J. T. Wang, S. Wasmus and R.F. Savinell, *J. Electrochem. Soc.*, **143**, L158, (1996).
- 68 C. Rice, S. Ha, R. I. Masel, P. Waszczuk, A. Wieckowski and T. Barnard, *J. Power Sources*, **111**, 83, (2002).
- 69 Y-W Rhee, S. Y. Ha and R. I. Masel, *J. Power Sources*, **117**, 35, (2003).
- 70 S. Park, Y. Xie and M. J. Weaver, *Langmuir*, **18**, 5792, (2002).
- 71 J. D. Lović, A. V. Tripković, S. Lj. Gojković, K. Dj. Popović, D. V. Tripković, P. Olszewski and A. Kowal, *J. Electroanal. Chem.*, **581**, 294, (2005).
- 72 A. Capon and R. Parsons, *J. Electroanal. Chem.*, **45**, 205, (1973).
- 73 O. Wolter, J. Willsau and J. Heitbaum, *J. Electrochem. Soc.*, **132**, 1635, (1985).
- 74 S. G. Sun and J. Clavilier, *J. Electroanal. Chem.*, **240**, 147, (1988).
- 75 S.-C. Chang, Y. Ho and M. J. Weaver, *Surf. Sci.*, **265**, 81, (1992).
- 76 M. J. Llorca, E. Herrero, J. M. Feliu and A. Aldaz, *J. Electroanal. Chem.*, **373**, 217. (1994).
- 77 E. Leiva, T. Iwasita, E. Herrero and J. M. Feliu, *Langmuir*, **13**, 6287, (1997).
- 78 S. P. E. Smith and H. D. Abruña, *J. Electroanal. Chem.*, **467**, 43, (1999).

- 79 T. J. Schmidt and R. J. Behm, *Langmuir*, **16**, 8159, (2000).
- 80 E. Casado-Rivera, Z. Gál, A. C. D. Angelo, C. Lind, F. J. DiSalvo and H. D. Abruña, *Chemphyschem.*, **4**, 193, (2003).
- 81 E. Casado-Rivera, D. J. Volpe, L. Alden, C. Lind, C. Downie, T. Vázquez-Alvarez, A. C. D. Angelo, F. J. DiSalvo and H. D. Abruña, *J. Am. Chem. Soc.*, **126**, 4043, (2004).
- 82 C. Roychowdhury, F. Matsumoto, P. F. Mutolo, H. D. Abruña and F. J. DiSalvo, *Chem. Mater.*, **17**, 5871, (2005).
- 83 C. Roychowdhury, F. Matsumoto, V. B. Zeldovich, S. C. Warren, P. F. Mutolo, M. Ballesteros, U. Wiesner, H. D. Abruña and F. J. DiSalvo, *Chem. Mater.*, **18**, 3365, (2006).
- 84 F. Matsumoto, C. Roychowdhury, F. J. DiSalvo and H. D. Abruña *J. Electrochem. Soc.*, **155**, B148, (2008).
- 85 J. C. Bauer, X. Chen, Q. Liu, T.-H. Phan and R. E. Schaak, *J. Mater. Chem.*, **18**, 275, (2008).
- 86 R. Ryoo, S. H. Joo and S. Jun, *J. Phys. Chem. B*, **103**, 7743, (1999).
- 87 K.-Y. Chan, J. Ding, J. Ren, S. Cheng and K. Y. Tsang, *J. Mater. Chem.*, **14**, 505, (2004).
- 88 A. Roucoux, J. Schulz and H. Patin, *Chem. Rev.*, **102**, 3757, (2002).
- 89 C. T. Kresge, M. E. Leonowicz, W. J. Roth, J. C. Vartuli and J. S. Beck, *Nature*. **359**, 710, (1992).
- 90 J. S. Beck, J. C. Vartuli, W. J. Roth, M. E. Leonowicz, C. T. Kresge, K. D. Schmitt, C. T.-W. Chu, D. H. Olson, E. W. Sheppard, S. B. McCullen, J. B. Higgins and J. L. Schlenkert, *J. Am. Chem. Soc.*, **114**, 10834, (1992).
- 91 T. Yanagisawa, T. Shimizu, K. Kuroda and C. Kato, *Bull. Chem. Soc. Jpn.*, **63**, 988, (1990).
- 92 K. Schumacher, P. I. Ravikovitch, A. D. Chesne, A. V. Neimark, and K. K. Unger, *Langmuir*, **16**, 4648, (2000).
- 93 K. Schumacher, P. I. Ravikovitch, A. D. Chesne, A. V. Neimark and K. K. Unger, *Langmuir*, **16**, 4648, (2000).

- 94 D. Zhao, J. Feng, Q. Huo, N. Melosh, G. H. Fredrickson, B. F. Chmelka and G. D. Stucky, *Science*, **279**, 548, (1998).
- 95 D. Zhao, Q. Huo, J. Feng, B. F. Chmelka, and G. D. Stucky, *J. Am. Chem. Soc.*, **120**, 6024, (1998).
- 96 M. Kruk and M. Jaroniec, *Chem. Mater.*, **12**, 1961, (2000).
- 97 R. Ryoo and C. H. Ko, *J. Phys. Chem. B*, **104**, 11465, (2000).
- 98 M. Imp rator-Clerc, P. Davidson and A. Davidson, *J. Am. Chem. Soc.*, **122**, 11925, (2000).
- 99 G. Wegner, *Acta Mater.*, **48**, 253, (2000).
- 100 B. Tian, S. Che, Z. Liu, X. Liu, W. Fan, T. Tatsumi, O. Terasaki and D. Zhao, *Chem. Commun.*, 2726, (2003).
- 101 D. Zhao, P. Yang, N. Melosh, J. Feng, B. F. Chmelka and G. D. Stucky, *Adv. Mater.*, **10**, 1380, (1998).
- 102 H. Miyata, T. Noma, M. Watanabe and K. Kuroda, *Chem. Mater.*, **14**, 766, (2002).
- 103 P. Y. Feng, X. H. Bu, G. D. Stucky and D. J. Pine, *J. Am. Chem. Soc.*, **122**, 994, (2000).
- 104 H. Yang, Q. Shi, B. Tian, S. Xie, F. Zhang, Y. Yan, B. Tu and D. Zhao, *Chem. Mater.*, **15**, 536, (2003).
- 105 D. Zhao, J. Sun, Q. Li and G. D. Stucky, *Chem. Mater.*, **12**, 275, (2000).
- 106 C. Boissiere, A. Larbot, A. van der Lee, P. J. Kooyman and E. Prouzet, *Chem. Mater.*, **12**, 2902, (2000).
- 107 P. Yang, D. Zhao, B. F. Chmelka and G. D. Stucky, *Chem. Mater.*, **10**, 2033, (1998).
- 108 P. Schmidt-Winkel, P. Yang, D. I. Margolese, B. F. Chmelka and G. D. Stucky, *Adv. Mater.*, **11**, 303, (1999).
- 109 C. Yu, J. Fan, B. Tian, D. Zhao and G. D. Stucky, *Adv. Mater.*, **14**, 1742, (2002).
- 110 A. Sayari, B.-H. Han and Y. Yang, *J. Am. Chem. Soc.*, **126**, 14348, (2004).
- 111 C. Yu, B. Tian, J. Fan, G. D. Stucky and D. Zhao, *J. Am. Chem. Soc.*, **124**, 4556, (2002).
- 112 C. Yu, J. Fan, B. Tian and D. Zhao, *Chem. Mater.*, **16**, 889, (2004).

- 113 F. Kleitz, S. Choi and R. Ryoo, *Chem. Commun.*, 2136, (2003).
- 114 L. Zhou, H. Li, C. Yu, X. Zhou, J. Tang, Y. Meng, Y. Xia and D. Zhao, *Carbon*, **44**, 1581, (2006).
- 115 F. Schüth, *Chem. Mater.*, **13**, 3184, (2001).
- 116 A. Monnier, F. Schüth, Q. Huo, D. Kumar, D. Margolese, R. S. Maxwell, G. D. Stucky, M. Krishnamurty, P. Petroff, A. Firouzi, M. Janicke and B. Chmelka, *Science*, **261**, 1299, (1993).
- 117 Q. Huo, D. Margolese, U. Ciesla, P. Feng, T. Gier, P. Sieger, R. Leon, P. Petroff, F. Schüth and G. D. Stucky, *Nature*, **368**, 317, (1994).
- 118 D. M. Antonelli and J. Y. Ying, *Angew. Chem., Int. Ed.*, **34**, 2014, (1995).
- 119 U. Ciesla, S. Schacht, G. D. Stucky, K. K. Unger and F. Schüth, *Angew. Chem., Int. Ed.*, **35**, 541, (1996).
- 120 M. Templin, A. Franck, A. Du Chesne, H. Leist, Y. Zhany, R. Ulrich, V. Schädler and U. Wiesner, *Science*, **278**, 1795, (1997).
- 121 Y. F. Lu, R. Ganguli, C. A. Drewien, M. T. Anderson, C. J. Brinker, W. L. Gong, Y. X. Guo, H. Soye, B. Dunn, M. H. Huang and J. I. Zink, *Nature*, **389**, 364, (1997).
- 122 P. Yang, D. Zhao, D. I. Margolese, B. F. Chmelka and G. D. Stucky, *Nature*, **396**, 152, (1998).
- 123 P. Yang, D. Zhao, D. I. Margolese, B. F. Chmelka and G. D. Stucky, *Chem. Mater.*, **111**, 2813, (1999).
- 124 B. Tian, X. Liu, B. Tu, C. Yu, J. Fan, L. Wang, S. Xie, G. D. Stucky and D. Zhao, *Nat. Mater.*, **2**, 159, (2003).
- 125 S. Tanaka, N. Nishiyama, Y. Egashira and K. Ueyama, *Chem. Commun.*, 2125, (2005).
- 126 Y. Meng, D. Gu, F. Zhang, Y. Shi, H. Yang, L. Zheng, C. Yu, B. Tu and D. Zhao, *Angew. Chem., Int. Ed.*, **44**, 7053, (2005).
- 127 F. Zhang, Y. Meng, D. Gu, Y. Yan, C. Yu, B. Tu and D. Zhao, *J. Am. Chem. Soc.*, **127**, 13508, (2005).

- 128 P. Llewellyn, M. Keung, S. Kallus, F. Schüth and K. K. Unger, *Stud. Surf. Sci. Catal.*, **84**, 2013, (1994).
- 129 R. Ryoo, S. H. Joo and S. Jun, *J. Phys. Chem. B*, **103**, 7743, (1999).
- 130 M. Kang, S. Yi, H. Lee, J. Yie and J. Kim, *Chem. Commun.*, 1944, (2002).
- 131 A. Lu, W. Schmidt, A. Taguchi, B. Spliethoff, B. Tesche and F. Schüth, *Angew. Chem., Int. Ed.*, **41**, 3489, (2002).
- 132 C. Yu, B. Tian and D. Zhao, *Curr. Opin. Solid State Mater. Sci.*, **7**, 191, (2003).
- 133 R. Ryoo, S. H. Joo, M. Kruk and M. Jaroniec, *Adv. Mater.*, **13**, 677, (2001).
- 134 S. Jun, S. H. Joo, R. Ryoo, M. Kruk, M. Jaroniec, Z. Liu, T. Ohsuna and O. Terasaki, *J. Am. Chem. Soc.*, **122**, 10712, (2000).
- 135 R. Ryoo, S. H. Joo, S. Jun, T. Tsubakiyama and O. Terasaki, *Zeolites and Mesoporous Materials at the Dawn of the 21st Century*, Elsevier, Montpellier, France, (2001).
- 136 S. H. Joo, S. J. Choi, I. Oh, J. Kwak, Z. Liu, O. Terasaki and R. Ryoo, *Nature*, **412**, 169, (2001).
- 137 S. Che, K. Lund, T. Tatsumi, S. Iijima, S. H. Joo, R. Ryoo and O. Terasaki, *Angew. Chem., Int. Ed.*, **42**, 2182, (2003).
- 138 J. Kim, J. Lee and T. Hyeon, *Carbon*, **42**, 2711, (2004).
- 139 X. Ji, P. S. Herle, Y. Rho and L. F. Nazar, *Chem. Mater.*, **19**, 374, (2007).
- 140 Y. Xia and R. Mokaya, *Adv. Mater.*, **16**, 1553, (2004).
- 141 Y. Xia, Z. Yang and R. Mokaya, *Chem. Mater.*, **18**, 140, (2006).
- 142 F. Jiao, K. M. Shaju and P. G. Bruce, *Angew. Chem., Int. Ed.*, **44**, 6550, (2005).
- 143 J. Luo, Y. Wang, H. Xiong and Y. Xia, *Chem. Mater.*, **19**, 4791, (2007).
- 144 Y. Zhao, D. Xia, Y. Li and C. Yu, *Electrochem. Solid-State Lett.*, **11**, A30, (2008).
- 145 S. Joo, S. Choi, I. Oh, J. Kwak, Z. Liu, O. Terasaki and R. Ryoo, *Nature*, **412**, 169, (2001).
- 146 J. B. Joo, P. Kim, W. Kim, J. Kim and J. Yi, *Catal. Today*, **111**, 171, (2006).
- 147 J.-H. Nam, Y.-Y. Jang, Y.-U. Kwon and J.-D. Nam, *Electrochem. Commun.*, **6**, 737, (2004).

- 148 L. Li, Z. H. Zhu, G.Q. Lu, Z. F. Yan and S. Z. Qiao, *Carbon*, **45**, 11, (2007).
- 149 J.-S. Yu, S. Kang, S. B. Yoon and G. Chai, *J. Am. Chem. Soc.*, **124**, 9382, (2002).
- 150 H. Liu, C. Song, L. Zhang, J. Zhang, H. Wang and D. P. Wilkinson, *J. Power Sources*, **155**, 95, (2006).
- 151 Z. Li, W. Yan and S. Dai, *Langmuir*, **21**, 11999, (2005).
- 152 Z. Guo, G. Zhu, B. Gao, D. Zhang, G. Tian, Y. Chen, W. Zhang and S. Qiu, *Carbon*, **43**, 2344, (2005).
- 153 L. Calvillo, M.J. Lázaro, E. García-Bordejéa, R. Moliner, P.L. Cabot, I. Esparbé, E. Pastor and J. J. Quintana, *J. Power Sources*, **169**, 59, (2007).
- 154 W. Choi, S. Woo, M. Jeon, J. Sohn, M. Kim and H. Jeon, *Adv. Mater.*, **17**, 446, (2005).
- 155 Z. Wen, J. Liu and J. Li, *Adv. Mater.*, **20**, 743, (2008).
- 156 S. Liu, W. Yu, C. Chen, A. Lo, B. Hwang, S. Chien and S. Liu, *Chem. Mater.*, **20**, 1622, (2008).

## References for Chapter 2

- 1 P. P. Ewald, *Fifty Years of X-ray Diffraction*, International Union of Crystallography, Utrecht, (1962).
- 2 L. V. Azaroff and M. J. Buerger, *The Powder Method in X-ray Crystallography*, McGraw-Hill Book company Inc., New York, (1958).
- 3 W. L. Bragg, *Proc. Camb. Phil. Soc.*, **17**, 43, (1913).
- 4 A. R. West, *Basic Solid State Chemistry*, John Wiley & Sons Ltd., (1999).
- 5 C. Suryanarayana and M. Grant Norton, *X-Ray Diffraction A Practical Approach*, Plenum Press, New York, (1998).
- 6 B. E. Warren, *X-Ray Diffraction*, Gneral Publishing Company, Ltd., North York, ON, (1990).
- 7 S. Brunauer, P. H. Emmett and E. Teller, *J. Am. Chem. Soc.*, **60**, 309, (1938).
- 8 E. P. Barrett, L. G. Joyner and P. P. Halenda, *J. Am. Chem. Soc.*, **73**, 373, (1951).
- 9 D. Wolverson, *Characterization of Semiconductor Heterostructures and Nanostructures*, Elsevier B. V., Amsterdam, Neth., (2008).
- 10 K. Siegbahn, C. Nordling, A. Fahlmann, R. Nordberg, K. Hamrin, J. Hedmann, G. Johansson, T. Bergmark, S.-E. Karlsson, I. Lindgren and B. Lindberg, *Nova Acta Regiae Soc. Sci.*, Ser. IV, **20**, (1967).

### References for Chapter 3

- 1 H. Yong, N. Coombs and G. Ozin, *Nature*, **386**, 692, (1997).
- 2 D. Zhao, J. Feng, Q. Huo, N. Melosh, G. H. Fredrickson, B. F. Chmelka and G. D. Stucky, *Science*, **279**, 548, (1998).
- 3 P. Yang, D. Zhao, B. Chmelka and G. D. Stucky, *Chem. Mater.*, **10**, 2033, (1998).
- 4 C. Boissiere, A. Larbot, A. van der Lee, P. J. Kooyman and E. Prouzet, *Chem. Mater.*, **12**, 2902, (2000).
- 5 C. Yu, B. Tian, J. Fan, G. D. Stucky and D. Zhao, *J. Am. Chem. Soc.*, **124**, 4556, (2002).
- 6 P. Feng, X. Bu, G. D. Stucky and D. J. Pine, *J. Am. Chem. Soc.*, **122**, 994, (2000).
- 7 C. Yu, J. Fan, B. Tian and D. Zhao, *Chem. Mater.*, **16**, 889, (2004).
- 8 A. Sayari, B. Han and Y. Yang, *J. Am. Chem. Soc.*, **126**, 14348, (2004).
- 9 K. Flodström, C. Teixeira, H. Amenitsch, V. Alfredsson and M. Lindén, *Langmuir*, **20**, 4885, (2004).
- 10 S. Ruthstein, J. Schmidt, E. Kesselman, Y. Talmon and D. Goldfarb, *J. Am. Chem. Soc.*, **128**, 3366, (2006).
- 11 K. Flodström, H. Wennerstrom and V. Alfredsson, *Langmuir*, **20**, 680, (2004).
- 12 X. Ji, S. Herle, Y. Rho and L. F. Nazar, *Chem. Mater.*, **19**, 374, (2007).
- 13 W. Stöber, A. Fink and E. Bohn, *J. Colloid and Interface Sci.*, **26**, 62, (1968).
- 14 Y. Xia, B. Gates, Y. Yin and Y. Lu, *Adv. Mater.*, **12**, 693, (2000).

#### References for Chapter 4

- 1 R. Ryoo, S. H. Joo and S. Jun, *J. Phys. Chem. B*, **103**, 7743, (1999).
- 2 S. Jun, S. H. Joo, R. Ryoo, M. Kruk, M. Jaroniec, Z. Liu, T. Ohsuna and O. Terasaki, *J. Am. Chem. Soc.*, **122**, 10712, (2000).
- 3 A. H. Lu, W. C. Li, W. Schmidt, W. Kiefer and F. Schuth, *Carbon*, **42**, 2939, (2004).
- 4 A. B. Fuertes and S. Alvarez, *Carbon*, **42**, 3049, (2004).
- 5 T. W. Kim, I. S. Park and R. Ryoo, *Angew. Chem., Int. Ed.*, **42**, 4375, (2003).
- 6 H. Yang, Y. Yan, Y. Liu, F. Zhang, R. Zhang, Y. Meng, M. Li, S. Xie, B. Tu and D. Zhao, *Phys. Chem. B*, **108**, 17320, (2004).
- 7 C. Vix-Guterl, S. Saadallah, L. Vidal, M. Reda, J. Parmentierb and J. Patarin, *J. Mater. Chem.*, **13**, 2535, (2003).
- 8 A. B. Fuertes and T. A. Centeno, *J. Mater. Chem.*, **15**, 1079, (2005).
- 9 J. Kim, J. Lee and T. Hyeon, *Carbon*, **42**, 2711, (2005).
- 10 S. Han, Y. Yun, K. W. Park, Y. E. Sung and T. Hyeon, *Adv. Mater.*, **15**, 1922, (2003).
- 11 M. Yoshio, H. Wang, K. Fukuda, T. Umeno, N. Dimov and Z. Ogumi, *J. Electrochem. Soc.*, **149**, A15983, (2002).
- 12 I. Gigoriant, L. Sominski, H. Li, H. Ifargan, D. Aurbach and A. Gedanken, *Chem. Commun.*, 921, (2005).
- 13 J. J. Auborn and Y. L. Barberio, *J. Electrochem. Soc.*, **134**, 638, (1987).
- 14 C. Yu, J. Fan, B. Tian and D. Zhao, *Chem. Mater.*, **16**, 889, (2004).
- 15 S. Zhu, H. Zhou, M. Hibino, I. Honma and M. Ichihara, *Mater. Chem. Phys.*, **88**, 202, (2004).
- 16 N. M. Rodriguez, A. Chambers and R. T. K. Baker, *Langmuir*, **11**, 3862, (1995).
- 17 H. P. Lin, S. T. Wong, C. Y. Mou and C. Y. Tang, *J. Phys. Chem. B*, **104**, 8967, (2000).
- 18 W. C. Choi, S. I. Woo, M. K. Jeon, J. M. Sohn, M. R. Kim and H. J. Jeon, *Adv. Mater.*, **17**, 446, (2005).
- 19 I. Mochida, Y. Korai, C. H. Ku, F. Watanabe and Y. Sakai, *Carbon*, **38**, 305, (2000).
- 20 A. C. Ferrari and J. Robertson, *Phys. Rev. B*, **63**, 121405, (2001).

- 21 A. Manthiram and C. Tsang, *J. Electrochem. Soc.*, **143**, L143, (1996).
- 22 F. Leroux, G. R. Goward and W. P. Power, *Electrochem. Solid-State Lett.*, **1**, 201, (1998).
- 23 P. Poizot, S. Laruelle, S. Grugeon, L. Dupont and J.-M. Tarascon, *Nature*, **407**, 496, (2000).
- 24 S. Laruelle, S. Grugeon, P. Poizot, M. Dollé, L. Dupont and J.-M. Tarascon, *J. Electrochem. Soc.*, **149**, A627, (2002).
- 25 H. Zhou, S. Zhu, M. Hibino, I. Honma and M. Ichihara, *Adv. Mater.*, **15**, 2107, (2003).

## References for Chapter 5

- 1 R. D. Rauh, K. M. Abraham, G. F. Pearson, J. K. Surprenant and S. B. Brummer, *J. Electrochem. Soc.*, **126**, 523, (1979).
- 2 J. Shim, K. A. Striebel and E. J. Cairns, *J. Electrochem. Soc.*, **149**, A1321, (2002).
- 3 J. A. Dean, *Lange's Handbook of Chemistry*, McGraw-Hill, New York (1985).
- 4 P. T. Cunningham, S. A. Johnson and E. J. Cairns, *J. Electrochem. Soc.*, **119**, 1448, (1972).
- 5 J.-W. Choi, J.-K. Kim, G. Cheruvally, J.-H. Ahn, H.-J. Ahn and K.-W. Kim, *Electrochim. Acta*, **52**, 2075, (2007).
- 6 R. D. Rauh, F. S. Shuker, J. M. Marston and S. B. Brummer, *J. Inorg. Nucl. Chem.*, **39**, 1761, (1977).
- 7 S.-E. Cheon, K.-S. Ko, J.-H. Cho, S.-W. Kim, E.-Y. Chin and H.-T. Kim, *J. Electrochem. Soc.*, **150**, A800, (2003).
- 8 J. H. Shin and E. J. Cairns, *J. Electrochem. Soc.*, **155**, A368, (2008).
- 9 L. X. Yuan, J. K. Feng, X. P. Ai, Y. L. Cao, S. Chen, and H. X. Yang, *Electrochem. Commun.*, **8**, 610, (2006).
- 10 H.-S. Ryu, H.-J. Ahn, K.-W. Kim, J.-H. Ahn, K.-K. Cho, T.-H. Nam, J.-U. Kim and G.-B. Cho, *J. Power Sources*, **163**, 201, (2006).
- 11 J. Wang, S. Y. Chew, Z. W. Zhao, S. Ashraf, D. Wexler, J. Chen, S. H. Ng, S. L. Chou and H. K. Liu, *Carbon*, **46**, 229, (2008).
- 12 M. Y. Chu, S. J. Visco, and L. C. De Jonghe, *US Patent*, No. 6402795, (2002).
- 13 Y. M. Lee, N. S. Choi, J. H. Park and J.-K. Park, *J. Power Sources*, **964**, 119, (2003).
- 14 K.-I. Chung, W.-S. Kim and Y.-K. Choi, *J. Electroanal. Chem.*, **566**, 263, (2004).
- 15 W. Zheng, Y. W. Liu, X. G. Hu and C. F. Zhang, *Electrochim. Acta*, **51**, 1330, (2006).
- 16 S.-E. Cheon, S.-S. Choi, J.-S. Han, Y.-S. Choi, B.-H. Jung and H. S. Lim, *J. Electrochem. Soc.*, **151**, A2067, (2004).
- 17 M.-S. Song, S.-C. Han, H.-S. Kim, J.-H. Kim, K.-T. Kim, Y.-M. Kang, H.-J. Ahn, S. X. Dou and J.-Y. Lee, *J. Electrochem. Soc.*, **151**, A791, (2004).

- 18 T. Kobayashi, Y. Imade, D. Shishihara, K. Homma, M. Nagao, R. Watanabe, T. Yokoi, A. Yamada, R. Kanno, and T. Tatsumi, *J. Power Sources*, **182**, 621, (2008).
- 19 J. Lei, J. Fan, C. Yu, L. Zhang, S. Jiang, B. Tu and D. Zhao, *Micro. Meso. Mater.* **73**, 121, (2004).
- 20 F. Kleitz, S. Choi and R. Ryoo, *Chem. Commun.*, 2136, (2003).
- 21 G. L. Miessler and D. A. Tarr, *Inorganic Chemistry*, Pearson Education, New Jersey, (2004).
- 22 K. Xu and C. A. Angell, *J. Electrochem. Soc.*, **145**, L70, (1998).
- 23 R. Ryoo, S. H. Joo and S. Jun, *J. Phys. Chem. B*, **103**, 7743, (1999).
- 24 J. Lee, J. Kim and T. Hyeon, *Adv. Mater.*, **18**, 2073, (2006).
- 25 M.V. Landau, L. Vradman, X. Wang and L. Titelman, *Micro. Meso. Mater.*, **78**, 117, (2005).
- 26 B. Meyer, *Chem. Rev.*, **76**, 367, (1976).
- 27 J. Kim, J. Lee and T. Hyeon, *Carbon*, **42**, 2711, (2004).
- 28 Y. Jung and S. Kim, *Electrochem. Commun.*, **9**, 249, (2007).
- 29 H. Yamin, A. Gorenshtein, J. Penciner, Y. Sternberg and E. Peled, *J. Electrochem. Soc.*, **135**, 1045, (1988).
- 30 Y. V. Mikhaylik and J. R. Akridge, *J. Electrochem. Soc.*, **150**, A306, (2003).
- 31 M. Choi and R. Ryoo, *Nat. Mater.*, **2**, 473, (2003).
- 32 L. A. Solovyov, A. N. Shmakov, V. I. Zaikovskii, S. H. Joo and R. Ryoo, *Carbon*, **40**, 2477, (2002).
- 33 R. Ryoo, S. H. Joo, M. Kruk and M. Jaroniec, *Adv. Mater.*, **13**, 677, (2001).

## References for Chapter 6

- 1 A. Capon and R. Parsons, *J. Electroanal. Chem.*, **45**, 205, (1973).
- 2 O. Wolter, J. Willsau and J. Heitbaum, *J. Electrochem. Soc.*, **132**, 1635, (1985).
- 3 C. Roychowdhury, F. Matsumoto, P. F. Mutolo, H. D. Abruña and F. J. DiSalvo, *Chem. Mater.*, **17**, 5871, (2005).
- 4 C. Roychowdhury, F. Matsumoto, V. B. Zeldovich, S. C. Warren, P. F. Mutolo, M. Ballesteros, U. Wiesner, H. D. Abruña and F. J. DiSalvo, *Chem. Mater.*, **18**, 3365, (2006).
- 5 F. Matsumoto, C. Roychowdhury, F. J. DiSalvo and H. D. Abruña *J. Electrochem. Soc.*, **155**, B148, (2008).
- 6 J. C. Bauer, X. Chen, a Q. Liu, T.-H. Phan and R. E. Schaak, *J. Mater. Chem.*, **18**, 275, (2008).
- 7 E. Casado-Rivera, Z. Gál, A. C. D. Angelo, C. Lind, F. J. DiSalvo and H. D. Abruña, *Chemphyschem.*, **4**, 193, (2003).
- 8 E. Casado-Rivera, D. J. Volpe, L. Alden, C. Lind, C. Downie, T. Vázquez-Alvarez, A. C. D. Angelo, F. J. DiSalvo and H. D. Abruña, *J. Am. Chem. Soc.*, **126**, 4043, (2004).
- 9 S. Jun, S. Joo, R. Ryoo, M. Kruk, M. Jaroniec, Z. Liu, T. Ohsuna and O. Terasaki, *J. Am. Chem. Soc.*, **122**, 10712, (2000).
- 10 I. Chen, *Phys. Rev. B*, **2**, 1053, (1970).
- 11 N. N. Zhuravlev and A. A. Stepanova, *Sov. Phys.-Crystallogr.*, **7**, 231, (1962).
- 12 D. R. Blasini, D. Rochefort, E. Fachini, L. R. Alden, F. J. DiSalvo, C. R. Cabrera and H. D. Abruña, *Surf. Sci.*, **600**, 2670, (2006).
- 13 J. Ge, W. Xing, X. Xue, C. Liu, T. Lu and J. Liao, *J. Phys. Chem. C*, **111**, 17305, (2007).
- 14 E. Casado-Rivera, Z. Gál, A. C. D. Angelo, C. Lind, F. J. DiSalvo and H. D. Abruña, *Chemphyschem.*, **4**, 193, (2003).
- 15 N. Kristian, Y. Yan and X. Wang, *Chem. Commun.*, 353, (2008).
- 16 J. B. Xu, T. S. Zhao and Z. X. Liang, *J. Phys. Chem. C*, **112**, 17362, (2008).
- 17 N. Tian, Z. Zhou, S. Sun, Y. Ding and Z. Wang, *Science*, **316**, 732, (2007).

- 18 M. A. Rigsby, W. P. Zhou, A. Lewera, H. T. Duong, P. S. Bagus, W. Jaegermann, R. Hunger and A. Wieckowski, *J. Phys. Chem. C*, **112**, 15595, (2008).
- 19 C. Rice, S. Ha, R. I. Masel and A. Wieckowski, *J. Power Sources*, **115**, 229, (2003).
- 20 Y. Huang, X. Zhou, J. Liao, C. Liu, T. Lu and W. Xing, *Electrochem. Commun.*, **10**, 621, (2008).
- 21 W. P. Zhou, A. Lewera, R. Larsen, R. I. Masel, P. S. Bagus and A. Wieckowski, *J. Phys. Chem. B*, **110**, 13393, (2006).
- 22 X. Yu and P. G. Pickup, *J. Power Sources* **182**, 124, (2008).

## References for Chapter 7

- 1 C. S. Brooks, *Metal Recovery from Industrial Wastes*, Lewis, Chelsea, MI, (1991).
- 2 H. Mimura, H. Ohta, K. Akiba, Y. Wakui and Y. Onodera, *J. Nucl. Sci. Technol.*, **39**, 1008, (2002).
- 3 D. L. Gallup and G. T. Ririe, *US patent*, No. 5290339, (1994).
- 4 S. Mitsushima, S. Kawahara, K. Ota and N. Kamiya, *J. Electrochem. Soc.*, **154**, B153, (2007).
- 5 E. Guibal, T. Vincent and R. Navarro-Mendoza, *J. Appl. Polym. Sci.*, **75**, 119, (2000).
- 6 P. Chassary, T. Vincent, J. S. Marcano, L. E. Macaskie and E. Guibal, *Hydrometallurgy*, **76**, 131, (2005).
- 7 A. Parodi, T. Vincent, M. Pilsniak, A. W. Trochimczuk and E. Guibal, *Hydrometallurgy*, **92**, 1, (2008).
- 8 I. Chen, *Phy. Rev. B*, **2**, 1053, (1970).
- 9 J. T. Miller and D. C. Koningsbergery, *J. Catal.*, **162**, 209, (1996).
- 10 W. Liu and R. D. Vidić, *Environ. Sci. Technol.*, **32**, 531, (1998).
- 11 R. Ryoo, S. H. Joo and S. Jun, *J. Phys. Chem. B*, **103**, 7743, (1999).
- 12 S. H. Joo, S. J. Choi, I. Oh, J. Kwak, Z. Liu, O. Terasaki and R. Ryoo, *Nature*, **412**, 169, (2001).
- 13 M. Choi, F. Kleitz, D. Liu, H. Y. Lee, W.-S. Ahn and R. Ryoo, *J. Am. Chem. Soc.*, **127**, 1924, (2005).
- 14 Y. Shin, G. Fryxell, W. Um, K. Parker, S. Mattigod and R. Skaggs, *Adv. Funct. Mater.*, **17**, 2897, (2007).
- 15 X. Ji, K. T. Lee and L. F. Nazar, *Nat. Mater.*, **8**, 500, (2009).
- 16 C. Yu, J. Fan, B. Tian, D. Zhao and G. D. Stucky, *Adv. Mater.*, **14**, 1742, (2002).
- 17 S. Jun, S. H. Joo, R. Ryoo, M. Kruk, M. Jaroniec, Z. Liu, T. Ohsuna and O. Terasaki, *J. Am. Chem. Soc.*, **122**, 10712, (2000).
- 18 B. Tian, X. Liu, H. Yang, S. Xie, C. Yu, B. Tu and D. Zhao, *Adv. Mater.*, **15**, 1370, (2003).

- 19 Y. F. Lu, R. Ganguli, C. A. Drewien, M. T. Anderson, C. J. Brinker, W. L. Gong, Y. X. Guo, H. Soyez, B. Dunn, M. H. Huang and J. I. Zink, *Nature*, **389**, 364, (1997).
- 20 H. Yang and D. Zhao, *J. Mater. Chem.*, **15**, 1217, (2005).
- 21 W. Zhang, C. Liang, H. Sun, Z. Shen, Y. Guan, P. Ying and C. Li, *Adv. Mater.*, **14**, 1776, (2002).
- 22 M. Prinz, R. Crespi, G. E. Harlow, A. Mottana, G. Liborio and J. Peters, *Guide to Rocks and Minerals*, Simon and Schuster, New York, (1978).
- 23 A. Aksay, C. E. Hoge and J. A. Pask: *J. Phys. Chem.*, **78**, 1178, (1974).
- 24 R. C. Weast, *Handbook of Chemistry and Physics*, Chemical Rubber Co., Cleveland, Ohio, 1972.
- 25 M. Y. Arica, G. Bayramoğlu, M. Yilmaz, S. Bektaş and Ö. Genç, *J. Hazard. Mater.*, **B109**, 191, (2004).
- 26 C. L. Mack, B. Wilhelmi, J.R. Duncan and J.E. Burgess, *Miner. Eng.*, **21**, 31, (2008).
- 27 F. Li, C. Bao, J. Zhang, Q. Sun, W. Kong, X. Han and Y. Wang, *J. Appl. Polym. Sci.*, **113**, 1604, (2009).
- 28 Y. Nacéra and B. Aicha, *Chem. Eng. J.*, **119**, 121, (2006).
- 29 F. Nastasi, F. Puntoriero, N. Palmeri, S. Cavallaro, S. Campagna and S. Lanza, *Chem. Commun.*, 4740, (2007).